

Mathematical Modelling of Vascular Development in Zebrafish

Sunny Modhara, BSc.

Thesis submitted to The University of Nottingham
for the degree of Doctor of Philosophy

September 2014

For Pritam Dass and Baba Amri

Abstract

The Notch signalling pathway is pivotal in ensuring that the processes of arterial specification, angiogenic sprouting and haematopoietic stem cell (HSC) specification are correctly carried out in the dorsal aorta (DA), a primary arterial blood vessel in developing vertebrate embryos. Using the zebrafish as a model organism, and additional experimental observations from mouse and cell line models to guide mathematical modelling, this thesis aims to better understand the mechanisms involved in the establishment of a healthy vasculature in the growing embryo.

We begin by studying arterial and HSC specification in the zebrafish DA. Mathematical models are used to analyse the dose response of arterial and HSC genes to an input Notch signal. The models determine how distinct levels of Notch signalling may be required to establish arterial and HSC identity. Furthermore, we explore how Delta-Notch coupling, which generates salt-and-pepper patterns, may drive the average gene expression levels higher than their homogeneous levels. The models considered here can qualitatively reproduce experimental observations. Using laboratory experiments, I was able to isolate DA cells from transgenic zebrafish embryos and generate temporal gene expression data using qPCR. We show that it is possible to fit ODE models to such data but more reliable data and a greater number of replicates at each time point is required to make further progress.

The same VEGF–Delta–Notch signalling pathway is involved in tip cell selection in angiogenic sprouting. Using an ODE model, we rigourously study the dynamics of a VEGF–Delta–Notch feedback loop which is capable of amplifying differences between cells to form period-2 spatial patterns of alternating tip and stalk cells. The analysis predicts that the feedback strengths of Delta ligand and VEGFR-2 production dictate the onset of patterning in the same way, irrespective of the parameter values used. This model is extended to incorporate feedback from filopodia, growing in a gradient of extracellular VEGF, which are capable of facilitating tip cell selection by amplifying the resulting patterns. Lastly, we develop a PDE model which is able to properly account for VEGF receptor distributions in the cell membrane and filopodia. Receptors can

diffuse and be advected due to domain growth, defined by a constitutive law, in this model. Our analysis and simulations predict that when receptor diffusivity is large, the ODE model for filopodia growth is an excellent approximation to the PDE model, but that for smaller diffusivity, the PDE model provides valuable insight into the pattern forming potential of the system.

Acknowledgements

Firstly, I would like to thank my supervisors at the School of Mathematics: Markus Owen, Helen Byrne and Etienne Farcot, for their continuous support, encouragement, and guidance over the last four years. A big thank you also goes to my supervisor Martin Gering in the School of Life Sciences for all his help and patience during my time spent in his laboratory.

I would also like to thank my internal assessor, Dov Stekel, for his support over the last couple of years; my external examiner, Nick Monk; and the University of Nottingham (School of Biosciences, Life Sciences and Mathematical Sciences) for providing funding for this project.

I also express my gratitude to Andrea Blackbourn, Dave Parkin, and the other administrative staff at the School of Mathematical Sciences for all their hard work.

Thank you to Karen Strung for initially formulating the ODE model of Chapter 3 and providing preliminary analysis.

I also thank the members of the Gering lab: Roshana Thambyrajah, Chris Moore, Aaron Savage, Maryam Jalili, Deniz Ucanok and Mohammad Al-Khamees for lending me their expert advice and helping me with the very early morning embryo sorts that allowed me to FAC sort during human hours!

I am very grateful to all the wonderful people I have met over the last few years, in particular, Heather Pettitt, Tom Wicks and Loic Le Merlus for being the very best of friends throughout the toughest stages of this research. The distractions of running; drinking copious amounts of coffee; and hours of gaming and television would not have been the same without you!

Thank you to my family for their love, encouragement and support from long before this project ever started. Although I have worked with the people above for the past few years, these are the people that have and will tolerate me for a lifetime.

Finally, thank you to Waheguru for being there every step of the way.

List of Abbreviations

hpf - hours post fertilisation
DA - dorsal aorta
PCV - posterior cardinal vein
gfp/GFP - green fluorescent protein
ODE - ordinary differential equation
PDE - partial differential equation
BC - boundary condition
HSC - haematopoietic stem cell
EHT - endothelial to haematopoietic transition
EC - endothelial cell
VEGF - vascular endothelial growth factor
VEGFR-2 - VEGF receptor 2
NICD - Notch intracellular domain
Dll4 - Delta like 4
HMEC - human microvascular endothelial cell line
NECD - Notch extracellular domain
YSE - yolk sac extension
PLM - posterior lateral mesoderm

Contents

1	Introduction	1
1.1	Biology background: Notch signalling	3
1.1.1	Notch signalling in sprouting angiogenesis and tip-cell selection	10
1.2	Mathematical modelling of biological systems	13
1.2.1	Models of juxtacrine cell signalling	14
1.2.2	Models of sprouting angiogenesis and tip cell selection	18
1.2.3	Models of Notch signalling in other contexts	19
1.2.4	Overview of models for studying gene regulatory networks	20
1.2.5	Model fitting and experimental data	22
1.3	Thesis overview and context	24
2	Systems Biology of Notch Signalling in Haematopoietic Stem Cell Specification	27
2.1	Notch signalling in arterial specification and HSC specification	27
2.2	Mathematical modelling	31
2.2.1	Model formulation	35
2.2.2	Quasi-steady state and dose response solutions	37
2.2.3	The effect of runx1 having a sigmoidal response to gata2	43
2.2.4	The effect of gata2 having a sigmoidal response to Notch	46
2.2.5	Summary	47
2.3	The potential role of cell coupling on HSC specification in arterial ECs	48
2.3.1	Modelling assumptions	50
2.3.2	Dimensionless model	51

2.4	Experimental techniques	61
2.4.1	Transgenic zebrafish lines	61
2.4.2	Embryo dissociation and preparation of cell suspension	61
2.4.3	Fluorescence-activated cell sorting (FACS)	62
2.4.4	RNA extraction, cDNA synthesis and real-time qPCR	63
2.5	Parameter estimation in a model for <i>efnb2a</i> and <i>runx1</i> activation by Notch signalling	66
2.6	Conclusions and further work	70
3	An Ordinary Differential Equation Model of VEGF–Delta–Notch Signalling in Angiogenic Tip Cell Selection	76
3.1	Introduction	76
3.2	Model overview	78
3.2.1	Initial and boundary conditions used in numerical simulations	81
3.3	Homogeneous and period-two steady states	82
3.4	Numerical bifurcation analysis	86
3.5	Bifurcation analysis of the homogeneous steady state	88
3.5.1	Stability to homogeneous perturbations	91
3.5.2	Stability to non-homogeneous perturbations	91
3.5.3	Patterning bifurcations are generated via purely real eigenvalues changing sign	94
3.6	Feedback strengths determine patterning regions	95
3.6.1	Lower-right quadrant ($A < 0, B > 0$ biologically relevant)	97
3.6.2	Lower-left quadrant ($A < 0, B < 0$)	99
3.7	Numerical simulations for a string of N cells	104
3.7.1	Zero flux BCs: single neighbour with $2 \times$ inhibition	105
3.7.2	Periodic BCs	105
3.7.3	Zero flux: single neighbour with regular inhibitor	105
3.7.4	Zero flux: cell sees itself	108
3.8	Travelling waves in the bistable system	108
3.9	Discussion	108

4 Modelling and Analysis of Filopodia Extension Regulated by VEGF-Delta-Notch Signalling in Angiogenic Tip Cell Selection	115
4.1 Model Overview	116
4.1.1 Filopodia growth	116
4.2 Steady state analysis	120
4.3 Two-cell analysis	123
4.3.1 Feedback through filopodia growth	125
4.3.2 Feedback through VEGF receptor production ($\theta > 0 = \psi$)	125
4.3.3 Feedback through VEGF gradient ($\psi > 0 = \theta$)	128
4.3.4 Feedback through combinations of filopodia growth, receptor production and VEGF gradient ($\theta, \psi > 0$)	133
4.4 Linear stability analysis	136
4.5 Modulation of stability regions by filopodia feedback	138
4.5.1 Loss of the black stable region	140
4.5.2 Loss of the grey patterning region	140
4.5.3 Numerical simulations	141
4.6 Discussion	144
5 A Partial Differential Equation Model for Intramembrane VEGF Receptor Transport-Regulated Filopodia Extension	146
5.1 PDE model framework and model equations	147
5.2 Domain growth laws	150
5.2.1 Local strain dependent on the local bound VEGFR-2 concentration	151
5.2.2 Local strain dependent on the global average bound VEGFR-2 concentration	152
5.2.3 Local strain dependent on the VEGFR-2 concentration at the proximal end of the cell ($x = 0$)	153
5.2.4 Filopodia length-dependent local bound VEGFR-2 dependent growth model	153
5.2.5 Filopodia length-dependent global average and proximal end VEGFR-2 dependent growth models	154

CONTENTS

5.3	Numerical simulation	155
5.3.1	Transforming PDEs to a fixed domain	157
5.3.2	Numerical solvers and numerical continuation methodology	158
5.4	Simulation of proximal end bound VEGFR-2 dependent filopodia growth	160
5.4.1	Simulation with algebraically defined velocity profile	160
5.4.2	Simulation with a coupled PDE for the strain rate	162
5.5	Simulation with growth dependent on local bound VEGFR-2 concentra- tion divided by the filopodia length	169
5.5.1	Small diffusion	169
5.6	Simulation with growth dependent on the locally-bound VEGFR-2 con- centration divided by the total domain size	172
5.7	Simulation for growth depending on the average bound VEGFR-2 con- centration	175
5.8	Growth depends on local VEGFR-2 concentration without scaling	178
5.9	Comparison of models with growth dependent on local, global average and proximal end VEGFR-2 concentrations	178
5.10	Conclusions and further work	180
5.10.1	Further work	185
6	Conclusions	187
A	Non-dimensionalisation and scalings for the model without filopodia growth: (3.2.10)-(3.2.14)	193
B	Non-dimensionalisation and scalings for the model considering filopodia growth: (4.1.3)-(4.1.5)	195
C	Routh Hurwitz conditions for the filopodia system	197
D	Parameter choices for the no-filopodia model	199
E	Parameter values for the filopodia model	201
	References	204

Introduction

As tissues grow beyond a certain size, their demand for nutrients, oxygen and waste removal cannot be met by diffusion alone. This necessitates the need for a transport system. For complex organisms with multiple organ systems, communication between organs and tissues is essential for the transport of hormones, for example, which regulate physiological behaviour. Cells, such as those required for an immune response or to heal injury, also need to be transported around the body. In the embryo, a transport system may not initially be necessary but the growing organism, in particular the adult, will require it due to the limitations of diffusive transport. Thus there comes a point in development where blood vessels start to form in a process called vasculogenesis. Once the initial vasculature has been established, its maintenance and remodelling are crucial for continued growth of the organism. Failure of the vasculature to remodel properly can lead to complications such as those caused by the drug thalidomide, (where abnormalities in newborn babies were caused by impaired blood vessel development [1]). Maintenance and remodelling of the vascular system is also crucial for wound healing and plays a role in a number of pathologies including diabetes, rheumatoid arthritis, cancer and neurodegeneration (dementia).

The growing embryo undergoes embryonic patterning into 3 distinct germ layers, one of which is the mesoderm. Angioblasts are mesodermally-derived cells and common progenitors of blood and endothelial cells (ECs) that take part in vasculogenesis, the *de novo* formation of blood vessels. During vasculogenesis angioblasts coalesce into a cord-like structure, and become recruited to the EC lineage where they subsequently undergo arterial and venous specification followed by lumenisation, a process in which the vascular cords are hollowed to allow blood to flow through them in due course [2]. Initially, the vessels formed through vasculogenesis are free of smooth muscle cells, pericytes and other associated cells which are later required for vessel stability and integrity.

One of the key ways in which the initial vasculature laid down by vasculogenesis remodels itself is via angiogenesis, which is defined as the outgrowth of new blood vessels from the pre-existing vasculature. The first step of angiogenesis is tip cell selection in which particular ECs, named tip cells, are chosen to leave their parent vessel and form new branches of blood vessels in a process called angiogenic sprouting. The sprouts are headed by tip cells but remain in contact with the parent vessel via proliferative stalk cells. Thus angiogenesis enables the existing vasculature to expand and provide tissues with an increased blood supply for the deliver of oxygen and nutrients. When angiogenesis is not properly regulated, tissues become starved of oxygen (hypoxic) and secrete growth factors which initiate angiogenesis in nearby blood vessels. Angiogenesis is also implicated in a number of diseases included diabetes, rheumatoid arthritis and cancer.

Vascular development is also coupled to haematopoiesis, the process by which mature blood cells form from the arterial blood vessels in a process called endothelial to haematopoietic transition (EHT) [3]. Haematopoiesis is maintained throughout life and the cells responsible for replenishing the blood system are haematopoietic stem cells (HSCs), immature progenitors that can self-renew, i.e. divide and remain in an undifferentiated, stem-cell state. They are also multipotent and, so, can give rise to mature cells of all blood lineages including myeloid cells, such as macrophages, and platelets and lymphoid cells, such as T-cells and B-cells. Together these two properties allow HSCs to reconstitute the blood system of hosts that have been exposed to irradiation or chemotherapy. Hence HSCs are the active components in bone marrow transplants performed in the clinic for patients suffering from cancer or acute radiation syndrome (radiation poisoning).

In vertebrates HSCs first form during embryogenesis from the haemogenic endothelium of the ventral wall of the dorsal aorta (DA), a major arterial blood vessel of the developing embryo [4]. During EHT, the ECs of the DA switch off endothelial marker genes, switch on haematopoietic genes and change their morphology from the long, flat shape associated with ECs to round cells characteristic of the blood system. The HSCs cells eventually leave the dorsal aorta and enter the blood circulation where they temporarily occupy intermediary organs before seeding the bone marrow from which they maintain the blood system of the adult organism [3, 5].

A shortage of HSCs, our limited ability to expand their numbers *ex vivo* and a lack of donors in certain ethnic groups mean that new sources of HSCs are being sought [6]. Such sources include pluripotent, embryonic stem (ES) cells, taken from the inner cell mass of blastula stage embryos, and also the recently discovered induced pluripotent

stem cells which are reprogrammed cells derived from adult body cells. Investigating the molecular programming of HSCs during embryogenesis will increase knowledge of the signalling pathways by which they are specified and may, thus, facilitate the reprogramming of such pluripotent cells to HSCs.

1.1 Biology background: Notch signalling

Notch signalling plays a key role in each of the three embryonic processes of arterial specification; the selection of tip cells in angiogenic sprouting; and the specification of HSCs. In arterial specification Notch is involved in establishing arterial gene expression marked by *efnb2a*. Loss of *efnb2a* or Notch pathway components in mice results in embryonic lethality due to angiogenic defects and a failure to intercalate arteries and veins [7, 8]. During angiogenic sprouting, Notch signalling is required for the correct specification of tip cells and in its absence severe vascular abnormalities are observed [9]. Finally, Notch signalling is required for the formation of HSCs. Since Notch deficient mice die at, or before, embryonic day 10.5 (E10.5), the time of HSC emergence, a direct test of their ability to repopulate the adult blood system is precluded. However, cell based assays using HSC progenitors at or just before the time of death have shown these cells to have reduced HSC activity [10–12]. Zebrafish embryos with impaired Notch signalling display similar vascular defects and a loss of HSC gene expression.

The requirement of Notch in the DA of vertebrate embryos to allow correct arterial specification, angiogenic sprouting and HSC specification, intimately unites these otherwise unrelated processes.

The Notch signalling pathway is an evolutionarily conserved mode of juxtacrine (direct cell-to-cell) signalling in metazoans (multi-cellular organisms). Signals are passed from cells to adjacent cells in direct contact when Delta or Jagged ligands interact with Notch receptors located in the cell membranes. In mammals there are 5 canonical DSL (Delta, Serrate, LAG-2) ligands: Delta-like 1 (Dll1), Delta-like 3 (Dll3), Delta-like 4 (Dll4), Jagged-1 (Jag1), Jagged-2 (Jag2) and four Notch receptors, Notch1 to Notch4 [13]. In canonical Notch signalling this interaction causes the ligand to be internalised by the signalling cell, taking with it the extracellular portion of the Notch receptor. Consequently there is a conformational change in the remaining receptor that facilitates proteolytic cleavages both outside and inside of the cell by ADAM/TACE and γ -secretase, respectively. This results in the release of the Notch intra-cellular domain (NICD), which translocates to the cell nucleus where it recruits the DNA binding protein CSL, and other co-activators, into a complex which activates Notch target genes.

In the absence of NICD, CSL forms part of a corepressor complex that actively inhibits transcription of Notch target genes. The NICD-CSL activating complex however regulates Notch target genes, many of which are transcriptional repressors of the Her/HRT/Hey families which in turn repress genes required for cell differentiation [14, 15].

In this way Notch signalling is able to control a variety of processes in both the developing embryo and adult organism, including neuronal cell differentiation [16] and T-cell specification and differentiation [17, 18]. In this thesis we focus specifically on its role during embryogenesis in the DA, specifically in arterial specification; tip cell specification in angiogenesis; and the specification of HSCs from the ventral wall of the DA. We use the zebrafish as a model organism to study these processes as the embryos are initially transparent, facilitating imaging and analysis of the developing vasculature. The embryos develop much faster than chick or mouse embryos and external development means that they are more easily accessible than mouse embryos and do not require the pregnant mother to be sacrificed. Lastly, the zebrafish's fully sequenced genome and the availability of mutants and genome editing tools makes identifying the roles of specific genes considerably easier. Although challenging, these advantages allow us to use the zebrafish embryo to collect quantitative gene expression data to study the Notch controlled processes of interest.

In the next few sections we review the role played by Notch signalling in arterial specification, angiogenic sprouting and HSC specification.

HSC formation has been reported in the DA, the umbilical and vitelline arteries but never in venous vessels [19]. Hence arterial identity may be an important pre-requisite for HSC specification. Previously, arterial identity was assumed to be determined by differences in blood flow through the vessels but studies in mouse and zebrafish have demonstrated that arterial specification is in fact genetically determined, before circulation initiates [20–23]. Notch plays a vital role in the genetic determination of arterial identity. Targeted deletion of many Notch components including CSL, the Notch 1 receptor, the Mindbomb protein or the ligand Dll4, leads to a loss of arterial specification identified by the expression of the gene *efnb2a*, which has been shown to be a direct target of Notch signalling in the human microvascular endothelial cell line, HMEC1 [24]. *Efnb2a* expression is lost in mouse and zebrafish embryos with impaired Notch signalling and ectopic expression of venous markers is observed in the DA [20, 21, 25, 26]. In venous ECs the venous transcription factor COUP-TF11 suppresses Notch signalling. In its absence, arterial genes are upregulated in venous ECs [27].

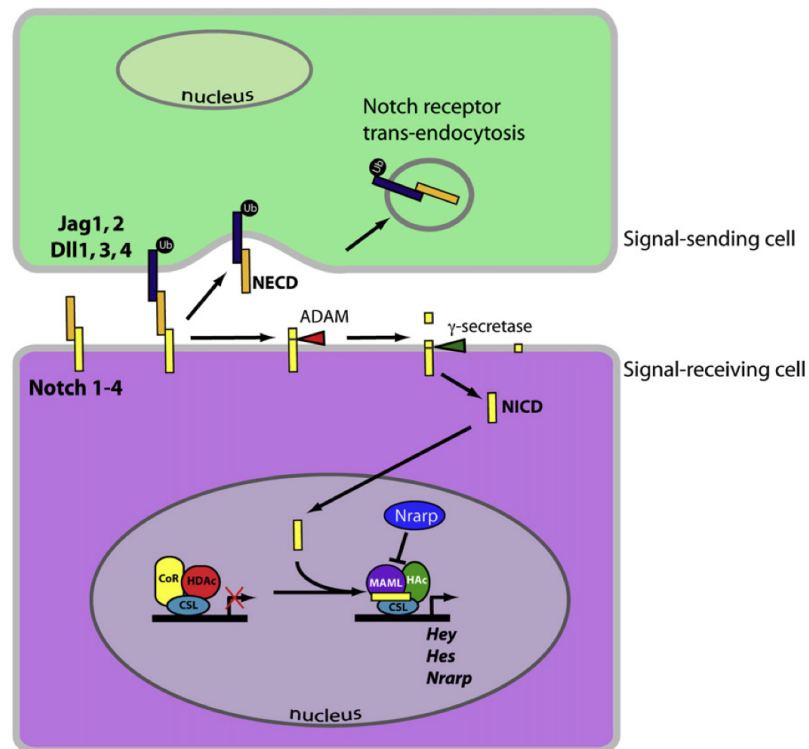


Figure 1.1: Figure from the review by Phng and Gerhardt, 2009 [13], showing the ligand–receptor interactions of Notch signalling and the downstream intracellular signal transduction pathway. DSL ligands on a signalling cell interact with Notch receptors on a signal receiving cell. This results in a conformational change in the receptor which allows cleavage of the Notch extracellular domain (NECD) by the enzyme ADAM. The extracellular domain is internalised into the signalling cell by the Ubiquitin ligase, Mind-bomb. Subsequently, there is a second cleavage of the intracellular domain by the enzyme γ -secretase, which cleaves the Notch intracellular domain (NICD) from the membrane, allowing it to translocate to the nucleus. In the absence of NICD, CSL forms part of a corepressor complex which inhibits Notch target genes such as the Her/HRT/Hey families of transcription repressors. NICD triggers the transcriptional activation of Notch target genes by displacing the corepressor complex with an activating one. Key: CoR=corepressor complex; NICD=Notch intracellular domain; NECD=Notch extracellular domain; Ub=Ubiquitin ligase (Mind-bomb).

In zebrafish, the activation of Notch receptors and ligands in the DA is induced by a cascade of signalling pathways as angioblasts (endothelial progenitors) migrate from the posterior lateral mesoderm (PLM) to the midline of the embryo to form the DA and posterior cardinal vein (PCV) (see Figure 1.2). Sonic Hedgehog signalling by the notochord induces expression of VEGFA by the adjacent somites (paired segments of mesoderm and precursors for bone and muscle in the adult organism). This activates Vascular endothelial growth factor (VEGF) receptors (VEGFR-2/flk1) on the migrating DA angioblasts, in turn, inducing them to express Notch ligands and receptors. As a result of Notch signalling between the angioblasts, *efnb2a* expression is induced at 18hpf [21] specifying them as arterial.

One hypothesis about the formation of the DA is that the first cells to arrive at the midline form the dorsal aorta angioblast chord, a precursor vessel to the DA. These cells experience the greatest VEGFA signal and thus initiate Notch signalling, becoming specified as arterial ECs whereas cells arriving subsequently form the PCV [22]. However, lineage tracing experiments by Zhong et al suggest that the identity of these cells is determined while they are still in the PLM and *gridlock/hey2* has a role, downstream of Notch, in recruiting angioblasts to an arterial fate, [20]. However *hey2* has been shown to be upstream of Notch and downstream of VEGF in a study by Rowlinson and Gering [28]. A recent study by Herbert and colleagues claims that formation of the PCV occurs by selective sprouting of progenitor cells from a common precursor vessel [29]. In summary the extent to which each of these mechanisms may be contributing to vasculogenesis remains unclear.

Zebrafish embryos express two ligands for Notch, Dll4 and DeltaC, and three receptors Notch 1a, Notch1b and Notch3 whose expression persists after initial arterial gene induction at 18hpf, through to the time when the HSC markers *runx1* and *gfi1.1* are first detected in the ventral wall of the DA [14, 25, 30].

Runx1 is the earliest detectable marker of HSC specification and can be visualised in the ventral wall of the DA at 24hpf by *in-situ* hybridisation [25, 30, 33]. A double fluorescent *in-situ* hybridisation (Gering lab unpublished data) shows that *runx1* is expressed in a subset of arterial ECs, identifiable by the co-localised expression of *runx1* with *efnb2a* and *flk1* (see Figure 1.4). Other markers of HSC specification in the zebrafish embryo include *gfi1.1* and *cmyb* which are detectable at 24hpf and 36hpf respectively in the DA [25, 28, 30] (and Gering lab unpublished data). The expression of *runx1*, *gfi1.1* and *cmyb* is either lost, for example in the *mindbomb* mutant, or reduced, such as in embryos treated with the γ -secretase inhibitor, DAPT, demonstrating a Notch requirement in HSC specification [25, 28, 30]. In addition, ubiquitous overactivation of Notch

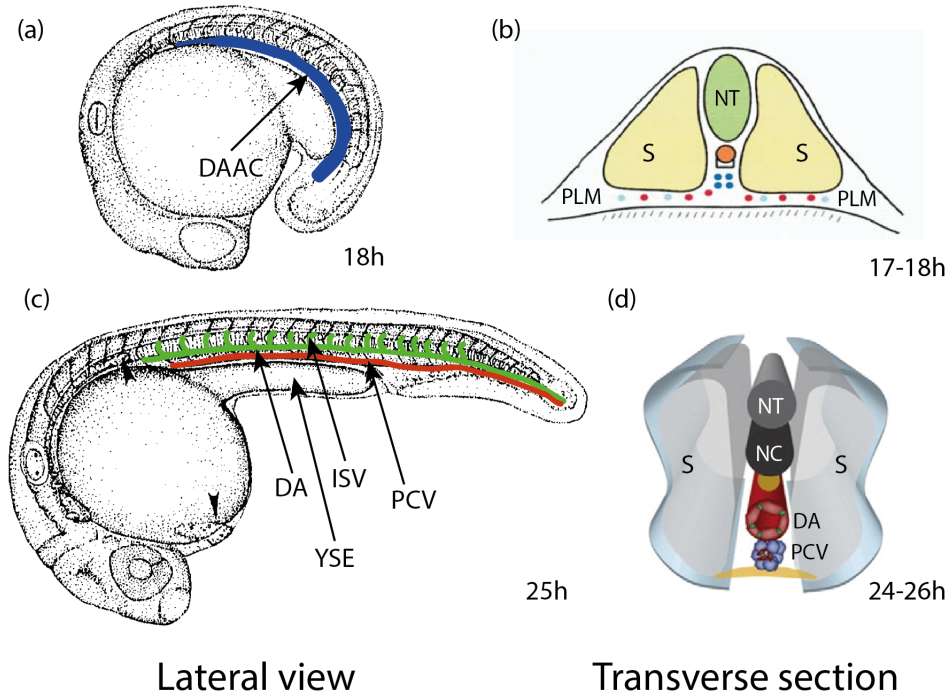


Figure 1.2: Schematic of the zebrafish embryo at 18 and 25hpf. The left panel shows lateral views (images modified from Kimmel et al [31]) and the right panel shows transverse sections taken at a position just above the yolk-sac extension (YSE) (images modified from [25, 32]). At 14-16hpf, angioblasts migrate from the posterior lateral mesoderm (PLM) to the midline (not shown). (a) and (b) By 17-18 hpf, differentiation into arterial (blue) and venous (sky blue) cells has already begun. The first cells to reach the midline experience the greatest VEGF signal, express Notch ligands and receptors and form cell-cell junctions to coalesce and form the dorsal aorta angioblast chord. Cells arriving subsequently are specified as venous ECs and primitive red blood cells (red). (c) By 25hpf, the primary axial vessels, the dorsal aorta (depicted in green) and posterior cardinal vein (depicted in red) are formed. (d) shows a transverse section of the embryo with the dorsal aorta in red and the posterior cardinal vein in blue. Blood circulation begins at this point. Key: DAAC=dorsal aorta angioblast chord; DA=dorsal aorta; ISV=intersomitic vessel; PCV=posterior cardinal vein; NT=neural tube; NC=notochord; S=somite; PLM=posterior lateral mesoderm.

leads to ectopic expression of both *runx1* and *efnb2a* in the PCV [28, 30] suggesting that high levels of Notch signalling promote haemogenic differentiation of ECs. Furthermore, Gering and Patient showed that Hedgehog is required at the same time for both arterial and HSC specification. This would suggest that Notch may be required twice, at low levels for *efnb2a* expression at 18hpf and at high levels for *runx1* expression at 24hpf. In chapter 3, we use mathematical modelling to explore this hypothesis, and present the supporting experimental evidence as motivation (see Figure 2.4).

CSL binding sites on the *runx1* promoter, which would indicate a direct activation of *runx1* by Notch signalling, have not yet been identified. However an (intronic) enhancer integrating inputs from Gata, Ets and Scl transcription factors has been located in the *runx1* gene in mouse embryos [34]. Since *gata2* has been identified as a direct target of Notch signalling, and an enhancer inside the *runx1* gene contains *gata2* binding sites, it is likely that *gata2* mediates Notch's effect on *runx1* [35, 36]. The role of *gata2* in HSC specification is further supported by a recent study in mouse embryos in which Guiu and co-workers demonstrate that *Hes1*, which is also a Notch target, represses *gata2* so that HSC precursors can form properly. Loss of repression by *Hes1* causes an increase in *gata2*, *runx1* and *cmyb* expression and a loss of HSC activity in the HSC precursors [36].

The Notch requirements for arterial and HSC specification mentioned thus far have been cell autonomous. A cell autonomous requirement demands the gene product be present in that cell for the process to occur. In our case this means that the DA ECs must receive a Notch signal to obtain the arterial and HSC phenotypes. A non-cell autonomous requirement is one for which the gene product is required in a different cell for the process to occur.

Such a non-cell autonomous Notch requirement has been identified by Clements et al. They demonstrated that a non-canonical *wnt16* signal is required for somitic¹ expression of the Notch ligands *DeltaC* and *DeltaD*. Their combined activity is required non-cell autonomously for the expression of the HSC marker genes *runx1* and *cmyb* whilst being dispensable for arterial specification and *efnb2a* expression [37].

In a recent paper, the same authors implicate the role of *jam1a-jam2a* interactions between migrating cells of the PLM and cells of the ventral somites in HSC specification. *Runx1* expression was lost in *jam1a* morphants but could be rescued by injection of *DeltaC* and *DeltaD* mRNA. It is suggested that the role of *jam1a-jam2a* signalling is to

¹Somites are dorsally located, paired segments of mesoderm which run along the longitudinally aligned notochord of vertebrate embryos and develop into muscle and bone (vertebrae) in the adult animal

Arterial-endothelial coexpression of runx1

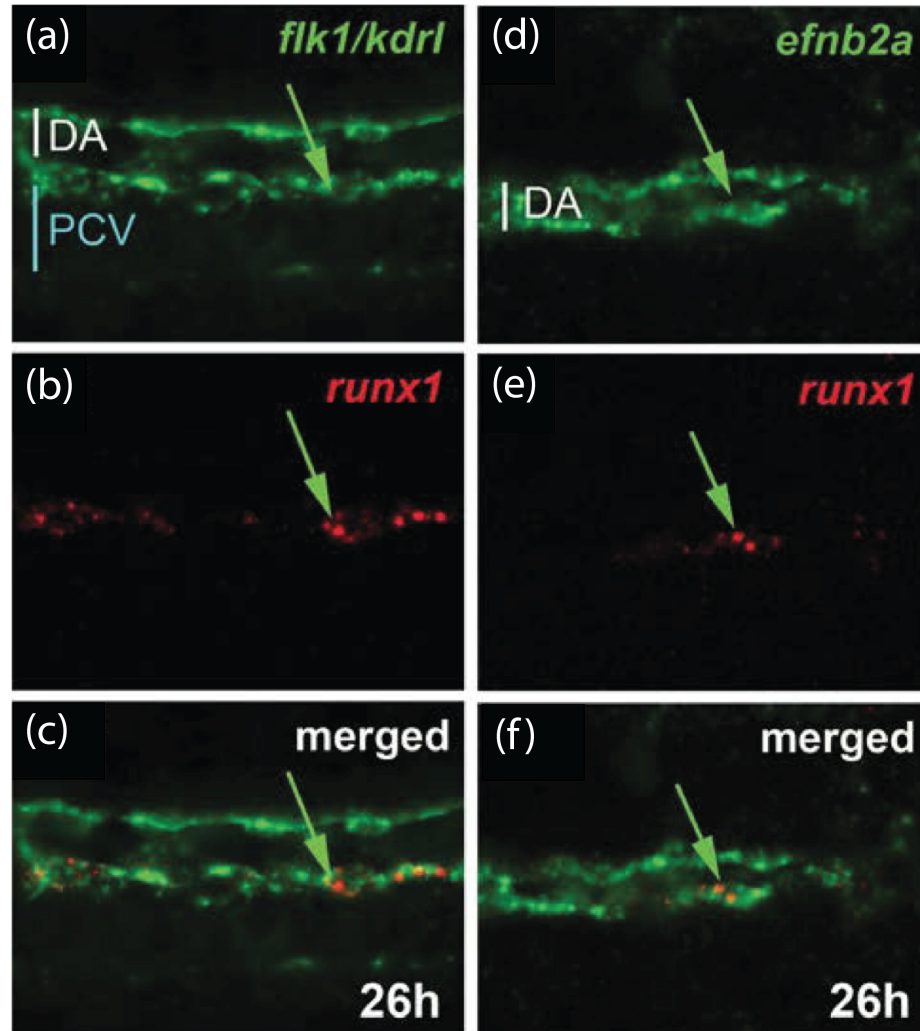


Figure 1.3: Double fluorescent *in-situ* hybridisation showing the localisation of runx1 mRNA in flk1 (a,b,c) and efnb2a (d,e,f) mRNA positive cells in the ventral wall of the DA. Single colour fluorescence shown in (a,b,d,e). Merges in (c,f) suggest that runx1 (red) is expressed in a subset of flk1 positive (green) and efnb2a positive (green) ECs since the two fluorescent markers are not localised together in every EC. (Figure is unpublished data of the Gering lab).

ensure effective Notch signal transduction in HSC precursors before the DA has formed [38].

1.1.1 Notch signalling in sprouting angiogenesis and tip-cell selection

Angiogenesis is the process by which new blood vessels form from pre-existing ones in response to external stimuli such as vascular endothelial growth factor (VEGF). It is essential that angiogenesis is carried out correctly so that a functional and perfused vasculature can be established to deliver oxygen and nutrients to tissues and remove waste products from them. Angiogenesis occurs in a number of physiological situations including embryonic development, wound-healing [39], in corpus luteum development and in bone morphogenesis. Aberrant regulation of angiogenesis can lead to lethality and diseased states in both the adult organism and during development. Examples of such pathologies in which angiogenesis occurs includes diabetes [40], rheumatoid arthritis [41], intraocular neovascular disorders [42] and cancer [43].

In both physiological and pathological cases, angiogenesis involves the same steps. ECs receive an angiogenic stimulus and establish a pattern of tip and stalk cells. The tip cells degrade a basement membrane and are then able to leave the parent vessel. Tip cells head the angiogenic sprout and migrate up gradients of growth factor by chemotaxis, followed by proliferative stalk cells which maintain contact with the parent vessel. The tip cells dynamically extend and retract filopodia which explore the surrounding environment and guide the tip cell towards the growth factor source. Eventually the tip-cell most likely anastomoses (reconnects) with other tip cells to form a circulatory loop. Lastly, mural cells, which are precursors for pericytes and smooth muscle cells, also play a role in guiding and stabilising vessel sprouts during angiogenesis [44]. Once the vasculature has matured, pericytes and smooth muscle cells continue to affect angiogenesis by influencing EC proliferation and stabilising the permeability of blood vessels. They also play roles in neovascularisation, the formation of microvascular networks in tissues, tumours and during wound-healing. The roles of pericytes and smooth muscle cells are reviewed in more detail elsewhere [45, 46]. In this thesis, we only concern ourselves with the first step of the angiogenic sprouting process, tip cell selection.

Notch signalling plays a pivotal role in sprouting angiogenesis and tip-cell selection as revealed by numerous studies using zebrafish intersomitic vessel (ISV) formation, mouse retina vascularisation, tumours and cell culture assays. Cross-talk with the VEGF signalling pathway has also been shown to be critically important in angiogenic sprouting responses. Hence, in this section, we review some of the consequences for

angiogenic tip cell selection of perturbing the Notch and VEGF pathways.

Tip cells are abundant in Dll4 expression and low in activated Notch expression whereas stalk cells characteristically have low Delta and high Notch [9] expression. A blockade of Notch signalling, for example in Dll4^{+/-} heterozygous mice, which only have one functional copy of a gene rather than the usual two, or in mice treated with a γ -secretase inhibitor, results in hypersprouting and hyperbranching defects with excessive fusion of the capillary network due to excessive tip cell formation. These physiological effects are accompanied by ectopic expression of genes usually expressed in tip cells, such as *flt4*, *flk1*, and *pdgfb* and widespread filopodia production [9, 47, 48]. Similar defects are seen in zebrafish Dll4 mutants and morphants. Furthermore, the hyperbranching defect is also observed in zebrafish embryos in which the expression of Notch1b and CSL have been knocked down [49, 50]. The requirement for Notch signalling was shown to be cell autonomous as cells with deficient CSL, that were transplanted into blastula stage wild type embryos and subsequently contributed to the endothelium, preferentially occupied the tip cell position compared to cells with activated Notch which did not. Similar observations are evident from studies in mice [9, 50]. This suggests that a cell's ability to send and receive a Notch signal plays a role in determining its fate as a tip or stalk cell and that tip and stalk cell fates are not stable, but may switch depending on the level of Notch activation received. Indeed, work by Jakobsson and colleagues suggests that ECs stimulated by VEGFA compete for the tip cell position in a shuffling or 'tug-of-war' manner [51]. Studies using mouse tumour models also support a role for Notch in suppressing the number of tip cells [52, 53].

How Notch limits the number of tip cells is less well understood although mounting evidence suggests that modulation of the VEGF pathway is involved. Notch appears to achieve EC quiescence by reducing the sensitivity of surrounding cells to the extracellular VEGF signal both in the DA and in stalk cells. By downregulating VEGF receptor levels, Delta-Notch signalling seems to modulate the response of surrounding ECs to extracellular VEGF. This prevents certain cells from adopting tip cell characteristics, ensures that a stable parent vessel remains behind and that contact is maintained between it and the stalk cells of the sprout. Each of the zebrafish VEGF receptors has been implicated in sprouting angiogenesis [13, 51].

There are 4 VEGF receptors in zebrafish: *Flt1* (VEGFR-1); *Flk1* and *kdr* (two alleles of VEGFR-2), which are functionally similar and bind to the ligand VEGFA; and *Flt4* (VEGFR-3) which binds to the ligand VEGFC. *flt4* is expressed in angioblasts from the 12 somite stage [54] but is downregulated in the DA from 24hpf in cells receiving a Notch signal, thereby decreasing the ability of the cells to respond to extracellular

VEGFC [50, 55, 56].

Flk1 is required for normal angiogenesis: the *plcg1* mutant, which has a mutation in a gene encoding a protein in the intracellular signalling transduction pathway acting downstream of *flk1*, fails to develop intersomitic vessels (ISVs) [57]. This phenotype (or observed effect) is copied when both alleles of *VEGFR-2*, *flk1* and *kdr*, are interfered with. The *flk1* mutant, *y17*, does not display the same phenotype as the *plcg1* mutant as it still exhibits some ISV sprouting. This is due to signalling via *kdr* since morpholino knockdown² of *kdr* in *flk1* mutant embryos reduces signalling through both *VEGFR-2* alleles to phenocopy the *plcg1* mutant, resulting in a failure to develop ISVs [55, 57].

Flt1, the decoy receptor, scavenges VEGFA ligand and hence reduces signalling through *flk1*. Consequently, loss of *flt1* results in ectopic angiogenic sprouting from the DA due to increased signalling via *flk1*. A recent study has shown that Semaphorin-PlexinD1 signalling induces soluble *flt1* (*sflt1*) expression in DA angioblasts and thereby blocks their angiogenic potential everywhere except at somite boundaries. Here the level of PlexinD1 activation, and hence the level of *sflt1*, is low, promoting angiogenesis via VEGF–*VEGFR-2* signalling [58]. Krueger et al, however, claim that the loss of *flt1* results in a downregulation of Notch receptor expression and hence a loss of Notch signalling in *flt1* morphants (embryos injected with a morpholino) suggesting that Notch may be upregulated by *flt1* [59]. However this reduction may be caused by an increase in VEGFA–*VEGFR-2* activity. Others have shown that Notch promotes *flt1* expression [60, 61] raising the possibility of a positive feedback loop in the network.

The complexity of the cross-talk between the Notch and VEGF signalling pathways is highlighted by the fact that VEGF induces *Dll4* expression via *flk1* in the mouse retina [47, 62] and EC cultures [63]. This forms part of a negative feedback loop in which,

- VEGF binds to *VEGFR-2* which leads to activation of *Dll4*,
- *Dll4* binds to Notch receptors in adjacent cells, and bound Notch receptors inhibit *VEGFR-2* production in those cells.

This negative feedback loop constitutes a mechanism termed lateral inhibition and characteristically forms salt-and-pepper patterns of tip and stalk cells which respectively have high and low levels of *Dll4*. Analysis of this negative feedback loop forms a major component of this thesis.

In the first half of this chapter we have reviewed the experimental work done by biologists studying the processes of arterial specification, angiogenic sprouting and HSC

²which interferes with mRNA splicing or translation

specification. These processes are all intimately connected by Notch signalling in the zebrafish DA and are summarised in Figure 1.4 (taken from the review by Gering and Patient [14]).

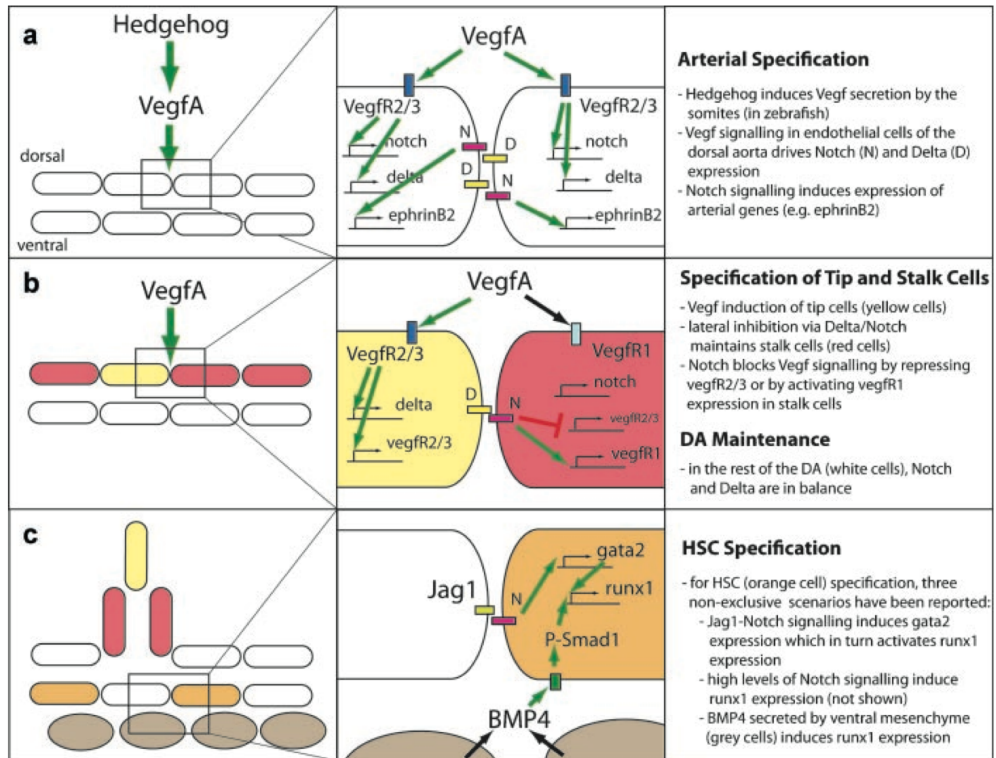


Figure 1.4: Figure taken from the review by Gering and Patient, 2010 [14], showing the role of Notch in (a) arterial specification of the DA; (b) tip cell specification in sprouting angiogenesis; (c) HSC specification in the ventral wall of the DA.

These insights will be essential for the formulation of mathematical models to study arterial specification, tip cell selection and HSC specification. Thus, in the next half of this chapter, we review the work done by mathematicians in studying the various aspects of Notch signalling such as ligand-receptor interactions, pattern formation in cells and the types of models use to study gene regulatory networks. This will give us a insight into where this thesis fits in amongst the work done by others.

1.2 Mathematical modelling of biological systems

Mathematical modelling is widely used to help scientists understand the mechanisms behind their experimental results. Beginning with a set of assumptions, or hypotheses about a particular biological process, mathematical models are used as invaluable tools to verify the consistency of these theories. They can be particularly useful in providing

insight into the mechanisms and dynamics underlying a system where experiments are either impossible, time-consuming or expensive to conduct. Modelling is an iterative process involving refinement of both the initial biological hypotheses and reformulation of the mathematical model. Modelling can also be useful for experimental design, for instance, in deciding which biological measurements to make and when to make them [64].

An example of where mathematical modelling has been successful in guiding experimental work is in the study by von Dassow and colleagues, who initially tried and failed to find a parameter set which could reproduce the characteristic periodic spatial pattern of segment polarity genes in the early *Drosophila* embryo. Adding two biologically feasible interactions to the genes in their original network allowed them to reproduce the observed expression pattern for a large number of parameter sets. They concluded that the network topology and interactions between genes were more important than the specific details of the interactions, such as the values of reaction rates. The insight gained herein was used to highlight the most valuable experiments to conduct [65, 66].

In this section some of the key published mathematical models of juxtacrine signalling, which include Notch signalling are reviewed, beginning with Collier et al's model of lateral inhibition [67]. This is then followed by reviews of more general models of juxtacrine cell signalling which can give rise to patterns of larger wavelengths in the contexts of TGF- α – EGF-R signalling and Delta-Notch signalling. Lastly, models of Notch signalling in other non-juxtacrine contexts are briefly discussed.

1.2.1 Models of juxtacrine cell signalling

Collier et al developed the first cell-based, ordinary differential equation (ODE), model of Notch signalling [67], to draw general conclusions about the pattern forming potential of Delta-Notch feedback loops. Their model used two variables per cell, p , one for each of Delta (d_p) and Notch (n_p) activity:

$$\frac{dn_p}{dt} = f(\bar{d}_p) - n_p \quad (1.2.1)$$

$$\frac{d\bar{d}_p}{dt} = \nu (g(n_p) - d_p) \quad (1.2.2)$$

where ν is the ratio of the decay rates for Delta and Notch activities. Production of Notch activity is an increasing function, $f(\cdot)$, of Delta activity in neighbouring cells, \bar{d}_p , and Delta production is a decreasing function, $g(\cdot)$, of Notch activity in the same cell. The authors showed that this feedback loop could amplify small scale differences in

Delta and Notch expression between neighbouring cells. This mechanism, involving cells with high Delta activity inhibiting their neighbours from delivering inhibition in turn, was termed lateral inhibition and was able to generate spatial patterns with a wavelength of two cells, provided that the feedback strength was sufficiently strong. The feedback strength is controlled using the parameters in Hill functions, which we cover later in this section. Their model was unable to generate longer wavelength patterns.

Owen and Sherratt (1998) explicitly incorporated ligand-receptor binding kinetics into a model of juxtacrine cell signalling. Their model consisted of three ODEs per cell, j :

$$\text{ligand: } \frac{da_j}{dt} = \overbrace{-k_a a_j \langle f_j \rangle}^{\text{binding}} + \overbrace{k_d \langle b_j \rangle}^{\text{unbinding}} - \overbrace{d_a a_j}^{\text{decay}} + \overbrace{P_a(b_j)}^{\text{production}}, \quad (1.2.3a)$$

$$\text{free receptors: } \frac{df_j}{dt} = -k_a \langle a_j \rangle f_j + k_d b_j - d_f f_j + P_f(b_j), \quad (1.2.3b)$$

$$\text{bound receptors: } \frac{db_j}{dt} = +k_a \langle a_j \rangle f_j - k_d b_j - \overbrace{k_i b_j}^{\text{internalisation}}, \quad (1.2.3c)$$

where ligand and receptor represented TGF- α and EGF-R levels. Positive feedback from bound receptors upregulated the production of both ligand and free receptor (P_a and P_f terms), making this model quite different to the Collier model which used both positive (f) and negative feedback (g) (see equations (1.2.1) and (1.2.2)). The key focus of this paper was to determine the range and extent to which a juxtacrine signal decays over a line of cells. The authors found that the decay rate for a wound-induced signal decreased with as feedback strength increased. For certain parameter choices this decay rate is not bounded below. The propagation of patterns with wavelength ≥ 2 is also demonstrated [68].

Owen et al. (2000) investigated the lateral induction mechanism from their previous model in which both receptor and ligand production are upregulated by bound receptors. The authors found that lateral induction can indeed generate spatial patterns with wavelengths longer than 2 cells. Fixing the receptor feedback strength and increasing the ligand induction strength generates longer wavelength patterns. In conclusion, the longest wavelength patterns were generated by the strongest ligand induction and the weakest receptor induction. The relative change in both the amplitude and wavelength of the pattern were robust to variations in the parameters of up to $\pm 20\%$ [69].

Wearing et al. (2000) further explored Owen and Sherratt's 1998 model, paying particular attention to how the range of unstable wavenumbers varied with model parameters as well as estimating the fastest growing patterning mode. Using linear analysis conditions for generating patterns were found in terms of the strengths of the feedback

functions for production of ligand and receptor. Linear analysis predicted that certain regions of parameter space could give rise to multi-mode patterns which occur when multiple wavenumbers become unstable but numerical simulations show little regular pattern [70].

Webb and Owen (2004) extended these previous models further by investigating the effect of lateral inhibition and induction of both ligand and free receptor on different cellular geometries (strings, squares and hexagons). The authors use linear analysis as done previously and find that unlike the Collier model, their model gives rise to spatial patterns with wavelengths greater than two cells for the case of lateral inhibition of ligand and receptor induction. Conversely ligand induction and receptor inhibition never generate patterns. Spatiotemporal oscillations are also predicted and seen in numerical simulations. Linear analysis predicts the onset of patterning well but fails to predict the observed wavelengths implying that the model's non-linearities are important. Lastly, under the assumption of slow binding kinetics and constant receptor expression a formal reduction can be made to the Collier model. When this isn't the case, a reduction cannot be made and the role of the cellular geometry is crucial [71].

Webb and Owen further extend previous models by including diffusive transport of ligands and receptors in and between individual membrane segments to determine the role of inhomogeneous distributions of ligands and receptors in juxtacrine signalling. The authors find that ligand transport is essential for generating long range patterns and without it the system cannot pattern in the case of lateral induction. A reduction to Owen and Sherratt's original model can be made by assuming diffusion of all species is large, however, this may not be a realistic assumption for bound ligand-receptor complexes as both species would be anchored in the cell membrane [72].

A common feature of the juxtacrine signalling models considered so far is that they rely on co-operativity to pattern. During the sequential binding of many ligands to a receptor, positive co-operativity occurs when the affinity of the ligand for the receptor increases with each bound ligand. This generates a sigmoid switch-like response for the receptor occupancy as a function of the ligand concentration: when there are small numbers of ligands, fractional receptor occupancy is also small but as the ligand concentration increases, receptors quickly become occupied. The fraction of occupied and free receptors are given by the Hill functions:

$$H_1(x) = \frac{x^n}{a^n + x^n} \quad \text{and} \quad H_2(y) = \frac{a^n}{a^n + y^n}. \quad (1.2.4)$$

The parameters associated with the Hill functions in equations (1.2.4), a and n , provide a measure of the ligand affinity for the receptor. Hill functions can be used to measure

the number of ligand molecules, n , required to bind the receptor to produce a functional effect. However this estimate only holds under the assumption of extremely positive co-operativity [73].

Both the Collier model [67] and the model of Owen and Sherratt [71], use co-operativity, characterised by Hill functions of the type given in equation (1.2.4) to model activating and inhibiting types of feedback. The functional form of $H_1(\cdot)$ and $H_2(\cdot)$ in equation (1.2.4) correspond to $f(\cdot)$ and $g(\cdot)$ in equations (1.2.1) and (1.2.2) of the Collier model and $H_1(\cdot)$ corresponds to the functions $P_a(\cdot)$ and $P_b(\cdot)$ in equations (1.2.3a) and (1.2.3b) of the Owen and Sherratt model. Linear analysis of the Collier and Owen models shows that the feedback strengths, which are proportional to the Hill coefficient (or co-operativity) determine the onset of patterning.

Recent work by Sprinzak and colleagues has shown that another mechanism, known as cis-inhibition, is capable of generating the salt-and-pepper patterns of lateral inhibition in the absence of co-operativity.

Cis-inhibition is the mechanism by which Delta and Notch on the same cell can bind and mutually inactivate each other. This competes with binding of Notch and Delta in trans (between adjacent cells). Sprinzak et al. show that in cells with more Notch than Delta, Delta becomes inactivated. Consequently, these cells, termed ‘receivers’, are only able to receive Notch signals but not send them. Conversely, cells with more Delta are unable to receive Notch signals and become known as ‘senders’. This effect results in a switch-like behaviour which can explain the sharp boundaries formed in *Drosophila* wing vein formation occurring along a gradient of Delta expression [74].

In a more recent paper, Sprinzak et al added cis-inhibition to a model of lateral inhibition (LI) and found that, compared to the model with LI alone, mutual inactivation of Delta and Notch decreases the time taken to reach the patterned state by increasing protein turnover when Delta and Notch are on the same cell. This decreases the response time of the system. The equation for Delta production in the LI model with cis-inhibition takes the following form:

$$\frac{dD_i}{dt} = \overbrace{\beta_D \frac{1}{1 + R_i^m}}^{\text{lateral inhibition}} - \overbrace{\gamma D_i}^{\text{decay}} - \overbrace{\frac{-D_i \langle N_j \rangle_i}{k_t}}^{\text{trans-binding}} - \overbrace{\frac{N_i D_i}{k_c}}^{\text{cis-inhibition}}, \quad (1.2.5)$$

where D_i and N_i are the concentrations of Delta and Notch on cell i , and k_t and k_c are binding interaction strengths. Compared to the LI model, the LI model with cis-inhibition was able to exhibit patterning in the absence of co-operativity because the mutual inactivation terms: $-\frac{D_i N_i}{k_c}$, provide the non-linearity required for the amplification of small differences between cells without the need for co-operativity. By mutually

inactivating Delta, Notch inactivation is also reduced, effectively upregulating Notch and increasing the intercellular feedback [75].

1.2.2 Models of sprouting angiogenesis and tip cell selection

Continuum models use PDEs to describe the large scale network behaviour in terms of EC densities. This was first done by Balding and McElwain in one dimensional simulations using PDEs to describe tip and sprout cell densities to chemotactic stimuli. Their solutions exhibit a wave-like behaviour of tip cells migrating towards the signalling source [76]. This model is extended by Byrne and Chaplain to include random and chemotactic fluxes to study angiogenesis in tumour neovascularisation [77]. The effect of fibronectin, an extracellular matrix protein (ECM), which induces a haptotactic flux, causing cells to migrate up gradients of fibronectin, was modelled by Orme and Chaplain in two dimensions [78]. Other models which further explore aspects of angiogenesis after tip cell selection such as the role of the ECM, matrix metalloproteases, growth factors, integrins and pericytes are reviewed in [79, 80]

Bentley and colleagues developed an agent-based model for the selection of endothelial tip cells in angiogenic sprouting. The model integrates the dynamics of the Notch and VEGF-signalling pathways to explore the effects that VEGF gradient, lateral inhibition and filopodia extension have on EC patterning and behaviour. The authors find that particular VEGF environments allow the cells to stabilise into a salt-and-pepper pattern of tip and stalk cells much faster. Low levels of VEGF generate little or no response and higher levels result in synchronised oscillations between the tip and stalk cell fates. Their model also predicts that patterns stabilise much faster in VEGF gradients as opposed to uniform environments and it is suggested that filopodia act as lateral inhibition amplifiers [81].

In a subsequent paper Bentley et al incorporated migration and fusion of tip cells into their existing model but not proliferation. The authors found that fusing tip cells inhibit each other causing neighbouring stalk cells to flip fate and also that if the average cell-cell junction size is inversely proportional to VEGF, then normal tip cell selection is possible regardless of the VEGF level [82].

Merks and Glazier used a cellular potts model coupled to a PDE representing the distribution of VEGF secreted by a population of endothelial cells to model vasculogenesis and angiogenesis. The cells both extend filopodia and migrate in the direction of chemoattractive gradient. The authors find two main mechanisms capable of driving vasculogenesis, cell shape changes and contact inhibition of motility, the latter of which

can also drive angiogenic sprouting. In the presence of VE-Cadherin binding at cell-cell junctions (required for adhesion), extracellular VEGF-A inhibits EC motility, proliferation and filopodia extension. This results in the suppression of chemotaxis at cell-cell junctions, an imbalance of chemotactic forces and directed cell migration culminating in angiogenic sprouting from initial blobs of cells [83].

Levine and colleagues devised a model of sprouting angiogenesis by coupling the theory of reinforced random walks, modelling cell migration, to Michaelis-Menten kinetics which model VEGF receptors as catalysts for transforming extracellular VEGF into a protease enzyme. The enzyme moves to the exterior of the cell membrane, and acts as a catalyst for fibronectin degradation, which consequently allows cell migration through the ECM [84, 85]. The authors propose inhibiting angiogenesis by inhibiting the growth factor, its receptor or the protease.

1.2.3 Models of Notch signalling in other contexts

Mathematical modelling of Notch signalling has been implemented in a number of contexts including filopodia signalling, boundary formation and oscillations. Although there are many examples one can choose from to demonstrate the diverse range of models in the literature, a select few are briefly reviewed here.

Cohen et al. modelled the pattern of bristle precursor cells on the *Drosophila* notum in which Delta-Notch signalling refines an initially disorganised pattern of bristle precursors into a well ordered one with a wavelength of approximately 4.6 cell diameters. The authors showed that the lateral inhibition mechanism of the Collier model, which exhibits period-2 patterns, is unable replicate wild-type precursor spacing. However the inclusion of filopodia into their model, which transmit Delta-Notch signals, allows communication between cells that are many cell diameters away and thus replicates the correct spacing of bristle precursors [86].

Momiji and Monk have incorporated delays into a simplified model of Delta-Notch signalling in the context of the neurogenic network, which determines the selection of neural cells from initially undifferentiated cells, previously studied by Meir et al [87]. Their DDE model extends the work of Collier et al. and investigates local and intercellular feedback loops in a coupled two-cell system. By sequentially reducing their full model they attribute its features, such as in- and out-of-phase oscillations and amplitude death (a zero amplitude solution), to the roles played by the intracellular and intercellular time delays in the simpler network motifs. In conclusion they attribute the behaviours exhibited by their full network to the local intracellular feed-

back loops[88] hence demonstrating that delays provide a mechanism for oscillatory behaviour in models of Notch signalling.

Ozbudak and Lewis investigated the role played by Notch signalling in the formation of somites in zebrafish embryos, which later give rise to structures such as vertebrae. The cells in the posterior presomitic mesoderm (PSM) oscillate in *her1/7* gene expression and, as result of growth and proliferation, pass into the anterior PSM where they are marked according to their clock phase and become somites upon leaving the anterior PSM. In this study, the authors block and overactivate the Notch pathway using DAPT and an inducible double transgenic zebrafish line, respectively, to show that only role of Notch signalling in the somites is to keep oscillations synchronised in the PSM. Following perturbation of Notch signalling, approximately 12 somites form normally before defective somites are deposited. This was replicated using the DDE model herein with oscillations drifting out of synchronisation in a similar time [89].

1.2.4 Overview of models for studying gene regulatory networks

In this section an overview of the types of models available for analysing the behaviour of GRNs is given as reviewed in [90], including a description of ODE models that we use to model HSC specification in the next chapter.

Logic-based models are the simplest type of framework, focussing on the network topology rather than changes in gene expression levels. Boolean networks are the most common type of logic-based models employed in which genes in the network, x_i , are represented by nodes which can be in either of two states, ‘on’ ($x_i = 1$) or ‘off’ ($x_i = 0$). Time is modelled using a series of discrete steps (t_1, t_2, \dots, t_n) at which the state of each gene is updated based on a set of rules which manifests itself as a Boolean function $f_i(\mathbf{x})$, such that,

$$x_i(t + 1) = f_i(\mathbf{x}(t)). \quad (1.2.6)$$

Boolean models have the advantage of being computationally inexpensive to simulate and require only qualitative information about the network structure for a model to be formulated. Although such models can be informative about network stability, they lack resolution in time and state, and thus may not always account for the way in which gene expression levels change continuously in time.

Since gene expression and its products are continuous rather than binary, with downstream effects occurring at different threshold levels of expression, ODE models are a good, alternative way of modelling GRNs. The state of an ODE model is described using continuous variables, x_i , representing gene expression levels. Transitions between

states are defined in terms of non-linear update functions, f_i , which give a coupled system of non-linear ODEs of the form

$$\dot{\mathbf{x}} = \mathbf{f}(\mathbf{x}). \quad (1.2.7)$$

Since Boolean models lack continuous parameters, an advantage of using ODE models, is that bifurcation theory, in particular, can be used to determine parameter values at which the system changes its qualitative behaviour [91]. Analysis of ODE models can give insight into how switches, oscillators and other complex behaviours are generated from network level features such as positive and negative feedback loops. In comparison to Boolean models, a disadvantage of ODE models is that they tend to have a large number of kinetic parameters, most of which are usually unknown and difficult to determine experimentally. In such cases, ODE models are restricted to qualitative analysis or computational methods for determining the unknown parameter values using fitting and learning algorithms, for example. Work by von Dassow and colleagues used this approach to infer parameter values in the segment polarity network in *Drosophila*. Later, the authors would go on to find that the model's dynamic behaviour was robust to variations in parameter values [65]. Meir and colleagues came to similar conclusions regarding the neurogenic network involving Delta-Notch signalling in *Drosophila* [87].

ODE models tend to make simplifying assumptions about the system under consideration, for example, assuming linearity between transcription factor concentrations and transcription rates, when in reality, the regulation is complex. This includes the processes of chemical and structural (epigenetic) modification of DNA, post-transcriptional modifications, transport and degradation of mRNA, translation and post-translational modifications. Including these assumptions in the non-linear function, f , allows us to model and subsequently analyse the effects of such processes.

The processes above may take some time to complete, for example, in the event that it takes time, T , to transcribe a molecule of mRNA, the concentration of mRNA about to undergo translation at a ribosome at time, t , is likely to be a reflection of the transcription factor concentrations at the promoter at time, $t - T$, rather than the concentration at the promoter at time, t . In the event that such delay times are known, GRNs can be studied using delay differential equations (DDEs). The disadvantage is that the inherent delays in these processes may affect the system dynamics, for instance, transforming steady states into oscillations. DDEs also require the specification of a history function just as ODEs require an initial condition. This makes them infinite dimensional dynamical systems, with discontinuous derivatives at the time points $t = 0, T, 2T, \dots$ which are known as knots. Since most DDEs don't have analytical solutions, one needs to be careful that the discontinuities do not compromise the algorithm used by the nu-

merical solver.

Both logic-based and continuous ODE models assume that the dynamics of the GRN are deterministic, when in reality the reactions taking place are subject to intrinsic and extrinsic noise. This becomes crucial to consider when the number of molecules in the system is small. In such cases, stochastic models can be used to model the GRN in which a master equation determines the update in gene expression levels and governs how the probability of the network being in a particular state evolves over time. This is difficult to solve and is usually studied using stochastic simulation algorithms (SSAs). Solving SSAs is computationally intensive due to the multiple runs required to estimate aggregate behaviour and the detailed experimental data required to fit the model compared to deterministic models.

1.2.5 Model fitting and experimental data

Mathematical models, such as the ODE models used in this thesis, require biological parameter values to generate realistic solutions. In cases where such data is not available, these models can be analysed using bifurcation analysis to give insight into the model behaviour for different parameter regimes. In order to reproduce experimental data, realistic parameter values are required. With the exception of simple organisms, GRNs are usually complex with multiples transcription factors and feedback loops determining the network behaviour. This makes it difficult to obtain accurate measurements for the required parameters. In such cases, these parameter values can be inferred mathematically by fitting the model to the experimental data. In general this is difficult to do as data is often only available for a subset of genes. Successfully fitting the model to the data is dependent on the type of biological data available and the mathematical method used to implement the fit.

Quantitative data is available for both protein and mRNA levels but in this thesis we focus on the methods used to obtain the latter. Quantitative PCR (qPCR) can be used to measure the absolute or relative levels of mRNA, with the latter being measured relative to a 'house-keeping' gene whose expression is assumed (temporally) constant and constitutive. This is discussed in more detail in §2.4.4. qPCR can be performed on whole embryos to establish how gene expression varies with developmental staging, but does not have any spatial resolution. Such information can be obtained by using *in-situ* hybridisation on whole embryos or transverse sections, for example, which results in coloured staining in tissues where specific mRNA transcripts are located. The limitation of *in-situ* hybridisation is that the data is not quantitative and can often be biased by overstaining and background staining.

There are a number of methods available to find an optimum parameter set which involve exploring an n -dimensional parameter space, either randomly or in some ‘efficient’ way which minimises the error between the experimental data and the model prediction. In most cases, the error is defined as a sum of squares

$$J(X_i^{\text{data}}, X_i^{\text{model}}) = \sum_{i=1}^N \left(X_i^{\text{data}} - X_i^{\text{model}} \right)^2 \quad (1.2.8)$$

where X_i^{data} are the experimental data points and X_i^{model} are the solution values from the model [92]. This sort of function assigns a larger error to data points of large magnitude compared to smaller data points. Thus a weighted function is often considered:

$$J(X_i^{\text{data}}, X_i^{\text{model}}) = \sum_{i=1}^N w_i \left(X_i^{\text{data}} - X_i^{\text{model}} \right)^2 \quad (1.2.9)$$

where $w_i = (1/X_i^{\text{data}})^2$ represents the weighting for the i th data point.

The parameter space can be explored using both local and global methods. Local methods start from an initial guess and search the parameter space in the immediate neighbourhood to converge to a parameter set which minimises the error to within some tolerance. Local methods converge quickly to the minimum error, however, there may be other minima which they fail to find. Thus global methods are used to search the entire parameter space, usually by incorporating some stochastic element so that different regions of parameter space can be explored. These methods, however, can be computationally expensive, involving long runs in order to search the entire parameter space well enough. An effective way to combine the advantages of both methods is to use a hybrid method. These methods explore the parameter space using a global search and when a ‘good’ region has been identified, they converge quickly using a local method. One such example is by Pan and Wu who combine the global simulated annealing method, first developed by Metropolis [93] with the local downhill simplex method, developed by Nelder and Mead [94], to estimate hydraulic parameters in a model of water flow through soil. Other efficient methods of parameter estimation include the global genetic algorithm [95, 96] and the local Levenberg-Marquardt algorithm [97]. However, in this thesis we minimise an error of the form (1.2.9).

Numerical bifurcation analysis for ODE models using XPPAUT

Biological systems usually contain a number of free parameters describing the system dynamics. An important aim in modelling such systems is to determine how their behaviour changes in response to varying the model parameters. Since there is no systematic way to explore a model as a function of all of its parameters, the first step

is usually to reduce the number of parameters by non-dimensionalisation, for instance and by fixing well established parameter values.

In this thesis, non-dimensionalisation of our ODE models is followed by steady state analysis. One way to achieve this is by using the software package XPPAUT which integrates the ODEs to steady state and furthermore, provides an interface to the continuation package, AUTO [98]. Continuation allows us to follow steady state solutions as functions of model parameters by utilising the implicit function theorem. In short, the theorem states that for a system of ODEs:

$$\frac{d\mathbf{u}}{dt} = \mathbf{G}(\mathbf{u}, \lambda), \quad (1.2.10)$$

under regularity assumptions on G , if there exists a steady state u^* , i.e. $\exists \lambda$ such that $G(\mathbf{u}^*, \lambda) = 0$ then there exists a locally unique family (or a branch) of steady state solutions, $\mathbf{u} = \mathbf{u}(\lambda)$ satisfying $\mathbf{G}(\mathbf{u}, \lambda) = 0$. For a small increment in the parameter value, AUTO is able to converge back to the solution branch by using an arclength-continuation method. The stability of these branches is automatically calculated by analysing the eigenvalues of the linearised system. This also allows automatic detection of bifurcation points in the system which correspond to changes in stability at particular points along solution branches.

1.3 Thesis overview and context

Chapter 2: This chapter aims to understand the timing of arterial specification at 18hpf followed by HSC specification at 24hpf in the zebrafish embryo. We present experimental observations, both our own and those of others, to form the hypothesis that Notch signalling is required twice: at 18hpf at a low level, which is sufficient for the induction of arterial gene expression, and at 24hpf, at a higher level, to induce HSC gene expression. Three initial feedforward ODE models with a prescribed input of NICD are explored and conditions on the parameters are derived such that arterial gene induction precedes HSC gene expression. One of these models is developed further to explore the effect of intercellular coupling. We show that for certain parameter values, salt-and-pepper patterning can also help drive higher HSC gene expression in alternating cells at 24hpf. Lastly we describe the experimental procedures used to obtain gene expression data from arterial ECs using qPCR and we demonstrate that parameters can be estimated by fitting the model to the qPCR data.

Chapter 3: In this chapter, we explore, using an ODE model, the VEGF–Delta–Notch feedback loop which has been implicated in tip cell selection during angiogenic sprout-

ing. The loop characteristically generates period-2 (salt-and-pepper) patterns of alternating tip and stalk cells for a range of parameter values. We use linear stability analysis and the Routh-Hurwitz conditions to define regions of parameter space, corresponding to the feedback strengths of Delta and VEGFR-2 production, for which the system admits patterning. A single generic picture, describing the onset of patterning, is obtained which is independent of the parameter values used. The predictions of the linear analysis are tested using numerical simulations in strings of cells with different boundary conditions. The system manifests period-2 spatial patterns, oscillatory behaviour and multiple homogeneous steady states with travelling wave behaviour.

Chapter 4: This chapter extends the ODE model of Chapter 3 by exploring the role of filopodia growth, in a gradient of VEGF, with the ability to enhance VEGFR-2 production. These model extensions correspond to three new parameters in the model whose effects are explored using steady state and bifurcation analysis. The analysis predicts that filopodia act to facilitate patterning by allowing the system to exhibit patterns for a wider range of parameter values, compared to the equivalent ODE model of Chapter 3. The filopodia-related parameters also give rise to a larger amplitude pattern capable for coexisting with the small amplitude pattern of Chapter 3. These predictions are confirmed using numerical simulations. Linear stability analysis predicts that increased filopodia feedback strength destroys the stable regions of parameter space to facilitate tip cell selection.

Chapter 5: This chapter aims to understand how sensible it was to use an ODE model, in Chapter 4, to study the effects of filopodia growth on tip cell selection. In this model we investigate the effects of VEGF receptor diffusion and advection in the cell membrane and filopodia, which grow into a gradient of extracellular VEGF. Advection is driven by a number of constitutive growth laws which are investigated numerically. We conduct numerical continuation of stable steady states of the PDE model by integrating the time-dependent model forward in time until it approaches steady state, modifying the parameters and initialising the next simulation using the previous state. The bifurcation diagrams for each PDE model variant (using different growth laws) are compared to the equivalent diagram for the ODE model of Chapter 4. All PDE models agree with their ODE counterparts when receptor diffusivity is large. When diffusion is small, the agreement breaks down.

The work in this thesis builds on and extends some of the key published works, discussed above.

The modelling work carried out in Chapter 2 is novel, to the best of our knowledge. The role of Notch signalling in arterial and HSC specification, using ODEs to model dose

response and intercellular Delta-Notch coupling, has not been investigated previously. The experimental procedures used to acquire fluorescent ECs from zebrafish embryos, isolation of RNA and the qPCR assay were performed according to standard procedures. The parameter fitting is performed by minimising a cost function representing the absolute value between experimental data points and ODE model predictions as done previously [92, 99, 100].

Collier et al.'s model of lateral inhibition provided the original framework of an ODE model with whole cell variables for Delta and Notch activity coupled to each other using one negative and one positive feedback function [67]. Owen and Sherratt, extended this work by, instead, modelling lateral induction of ligands. Their model also used binding kinetics to describe Delta-Notch interactions in terms of their concentrations [68]. The model of Bentley et al. is an agent based model which considers Delta-Notch signalling coupled to VEGF-VEGFR-2 signalling [81].

Our ODE model for tip cell selection, in Chapter 3, uses aspects of all three of these models. We study the VEGF-Delta-Notch feedback loop, modelled by Bentley et al in their agent based model, using ODEs for whole cell variables for the concentrations of Delta, Notch and VEGF receptors. The ODEs are formulated using binding kinetics and one positive and one negative feedback loop. To our knowledge, this is the first of this kind of ODE model for tip cell selection, which uses bifurcation and linear analysis to give further insight. Similarly, the ODE model of Chapter 4 is unique in its analysis of the role of filopodia in tip cell selection using dynamical systems theory.

The work in Chapter 5 considers the effect of domain growth on the pattern forming potential of the VEGF-Delta-Notch system. The effect of ligand diffusion in cell membranes has previously been modelled by Webb and Owen [72]. Others have investigated the effects of domain growth on pattern formation [101–103]. Using this as a basis, we allow both diffusive and advective transport of receptors in the cell membrane, where advection is defined by constitutive laws. The scheme for numerical continuation was developed by ourselves.

Systems Biology of Notch Signalling in Haematopoietic Stem Cell Specification

2.1 Notch signalling in arterial specification and HSC specification

Haematopoietic stem cells (HSCs) arise as the result of an endothelial to haematopoietic cell transition (EHT) which has been observed in arterial but not venous blood vessels [14]. Hence arterial identity may be an important pre-requisite for a HSC fate. The gene *efnb2a* has been identified as a direct target of Notch signalling in the human microvascular endothelial cell line (HMEC1) [24] and is a marker of arterial identity in zebrafish and mouse embryos. Embryos with impaired Notch signalling fail to express *efnb2a* at 18 hours post fertilisation (hpf) and also exhibit arteriovenous shunts (abberant connections between arteries and veins). These traits suggest that arterial/venous distinction is not maintained, implicating Notch signalling as being essential for arterial specification [20, 21, 25].

The expression of Notch ligands and receptors persists beyond initial arterial gene induction (18 hpf) and into the time window of HSC specification (see Figure 2.1) which can be recognised by the expression of the HSC marker gene *runx1* at 24 hpf. Embryos deficient in Notch signalling lack expression of the HSC markers *runx1*, *gf1.1* and *cmyb* in the ventral wall of the dorsal aorta DA, the site of EHT in zebrafish embryos ([25, 30] and Gering Lab unpublished data). Embryos treated with the γ -secretase inhibitor DAPT also lose *runx1* expression suggesting that Notch signalling is essential for HSC specification (see Figure 2.4).

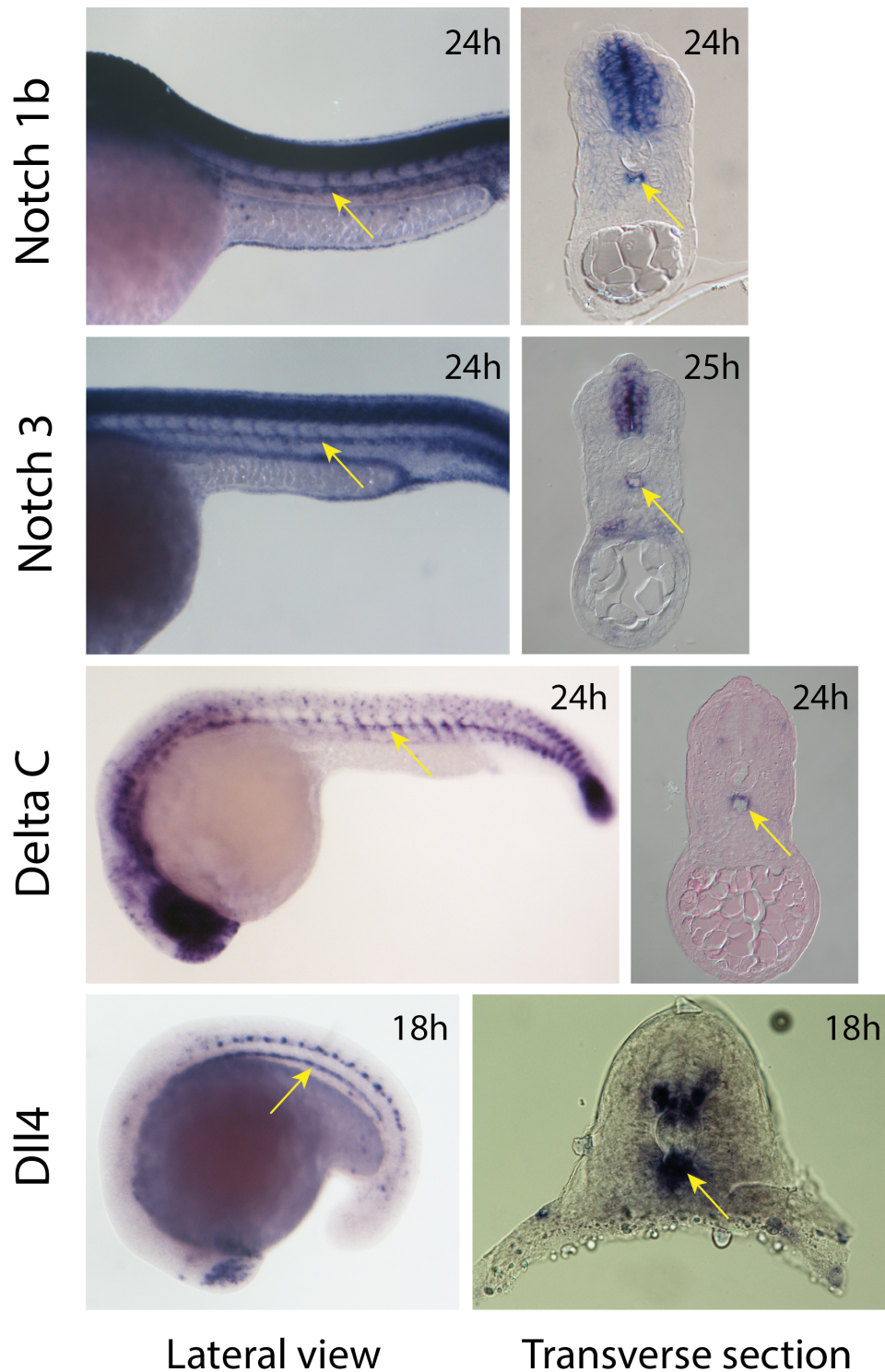


Figure 2.1: Expression of the Notch receptors, Notch 1b and Notch 3 at 24hpf, and ligands, Delta C and Delta-like 4 (Dll4) at 24 and 18hpf respectively, in the dorsal aorta of the zebrafish embryo. The location of mRNA transcripts in the embryo is visualised using the purple stain (see yellow arrows) as in the in-situ hybridisation assays shown. The left and right panes show lateral and transverse-sectional views of the embryo. Yellow arrows show expression in the DA. (These in-situ data are from the Gering lab).

Notch signalling is essential for normal angiogenesis in zebrafish (and mouse) embryos. At 21 hpf in zebrafish, tip cells are selected from endothelial cells comprising the DA by responding to Vascular Endothelial Growth Factor (VEGF). Selection happens due to a Notch-controlled process called lateral inhibition where a cell with high Delta expression prevents neighbouring cells from adopting the same (in this case the tip cell) fate by activating their Notch receptors. Tip cells lead angiogenic sprouts towards the source of growth factor, followed by stalk cells which allow the sprout to maintain contact with the parent vessel, the DA. Embryos with reduced Notch signalling display enhanced vessel branching, most likely due to reduced lateral inhibition. Notch represses expression of the VEGF receptors (VEGFR2/flk1 and VEGFR3/flt4) suggesting that its role in angiogenesis is to limit the ability of ECs to respond to extracellular VEGF, thus stabilising the angiogenic stalk and DA cells, stopping them from taking on the migratory behaviour of tip cells [14, 50, 54]. The retained expression of flt4 in the DA, due to a loss of Notch signalling can be seen in Figure 2.2 which was adapted from the work done by Siekmann and Lawson [50].

Since HSCs emerge from the DA after it has undergone arterial specification and angiogenesis, it is likely that the correct succession of these Notch-controlled processes (see Figure 2.3) needs to be carried out for successful HSC specification. Next we present and discuss the findings of our experimental work and conclude with a hypothesis which may explain the correct order in which events take place.

We utilise two different ways of knocking down Notch signalling: using the mindbomb mutant and by using the γ -secretase inhibitor, DAPT. Mindbomb is a protein required to successfully internalise the Delta-Notch extracellular domain complex into the signalling cell. As such, the mindbomb mutant has poor Notch signal transduction [104]. The DAPT inhibitor prevents effective cleavage of NICD, the Notch signalling effector, by inhibiting the cleaving enzyme γ -secretase. The inhibitor is dissolved in the solvent DMSO and its effectiveness, therefore, depends on a variety of factors including, permeability of the embryo's cell membranes, concentration required for inhibition and the length of time that embryos are incubated in the inhibitor.

In-situ hybridisation data from the Gering lab, shows that the expression of both runx1 and efnb2a is lost in the mindbomb mutant (see Figure 2.4b) whereas only runx1 is lost in DAPT treated embryos (see Figure 2.4a). Furthermore, the Notch reporter, 12 \times CSL:Venus, has very low Venus expression at 18hpf (see Figure 2.5), when efnb2a expression is first detected in the DA [21, 22]. However, the Venus expression is clearly visible at 24hpf, when runx1 expression is first detected in the ventral wall of the DA [25, 30, 33] and when flt4 is downregulated (see Figure 2.2) [50, 54]. This suggests that

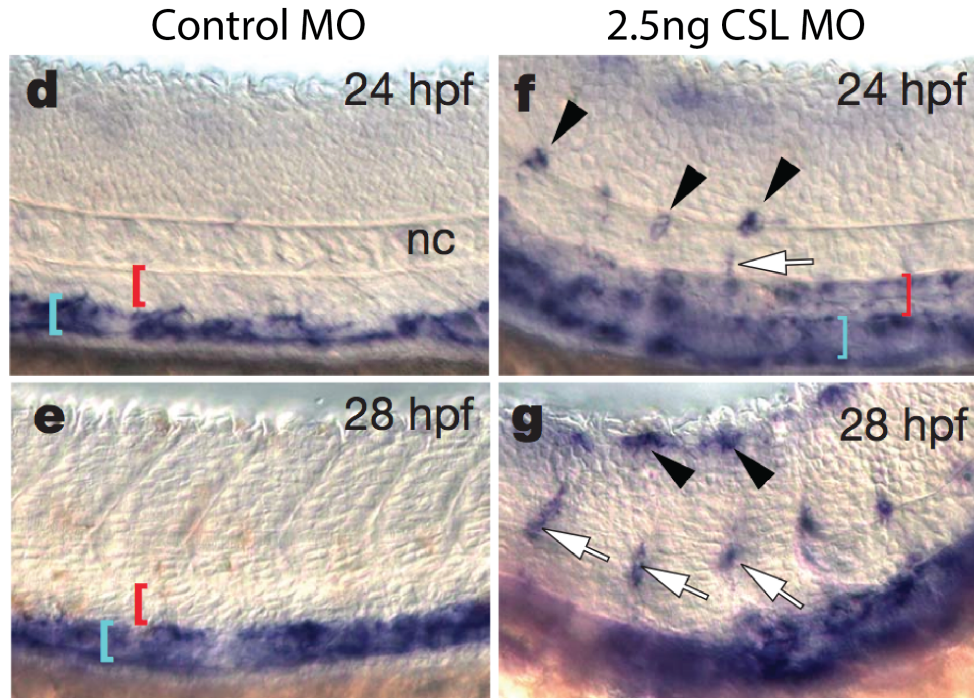


Figure 2.2: Figure adapted from Siekmanna and Lawson, 2007 [50]. Before 24 hpf *flt4* is a pan-endothelial marker (not shown). However by 24hpf VEGFR-3/*flt4* becomes suppressed in the DA and in intersomitic vessel sprouts at 24hpf and *flt4* becomes a marker of venous identity from this point onwards. This confirms the original finding by Thompson et al. 1998 [54]. Red and blue brackets mark the DA and PCV respectively. (d) and (f) show no DA expression of *flt4* in control morphants with expression in the PCV only. (e) and (g) show retained expression of *flt4* in the DA, stalk cells (white arrow in (f)) and the tip cells (black arrow heads) in the absence of Notch signalling. This suggests that the role of Notch is to downregulate VEGFR-3 in DA ECs. In (a) some expression of *flt4* is expected in the tip cells of control embryos, consistent with a role for VEGFC-*flt4* signalling in angiogenic sprouting [48], however, these cannot be seen as they are in a different focal plane (visible in the original Figure). Key: MO=morpholino; nc=notochord.

lower levels of Notch signalling are present at 18hpf than at 24hpf. At 18hpf this low level seems sufficient to drive *efnb2a* expression but is not sufficient to downregulate *flt4* or switch on *runx1*. Only at 24hpf are the levels high enough to achieve this (see Figure 2.3). As such, our in-situ hybridisation data in Figure 2.4 suggest that whilst Notch signalling is blocked, possibly completely, in the mindbomb mutant, DAPT treatment only eliminates Notch signalling partially.

In the next section we model the sensitivity of *efnb2a* and *runx1* to the received Notch signal.

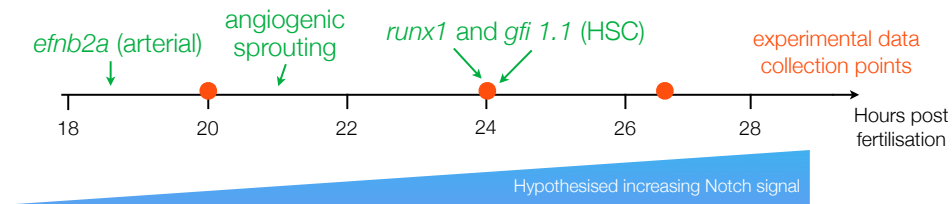


Figure 2.3: The timing of Notch controlled processes in the zebrafish DA, driven by a hypothesised increasing Notch signal. Arterial specification at 18 hpf is identified by *efnb2a* expression. This is followed by angiogenic sprouting at 21 hpf where lateral inhibition by Notch signalling is required for tip cell specification and stability of both the DA and the trailing stalk cells. Lastly, at 24 hpf, HSC specification is marked by *runx1* expression which is likely to be activated by high levels of Notch signalling.

2.2 Mathematical modelling

The aims of this chapter are to produce mathematical models that can correctly explain the timing of the experimentally observed expression of arterial and HSC marker genes in the DA. By combining our experimental observations from §2.1 with the observations made by others (see Table 2.1), we use Figure 2.6 to summarise the hypothetical interactions underlying the models that follow.

Initially we develop a simple feed-forward ordinary differential equation (ODE) model, with a prescribed input of Notch intracellular domain (NICD) to describe a homogeneous population of cells without Delta-Notch mediated cell-coupling as this gives a simple type of model with relatively few ODEs which we can later build on. The model will consider 3 different functional types of responses downstream of Notch and compare the sensitivity of *efnb2a* and *runx1* to the incoming Notch signal for each response type.

Following this, we extend our ODE model to account for cell-cell interactions, allowing

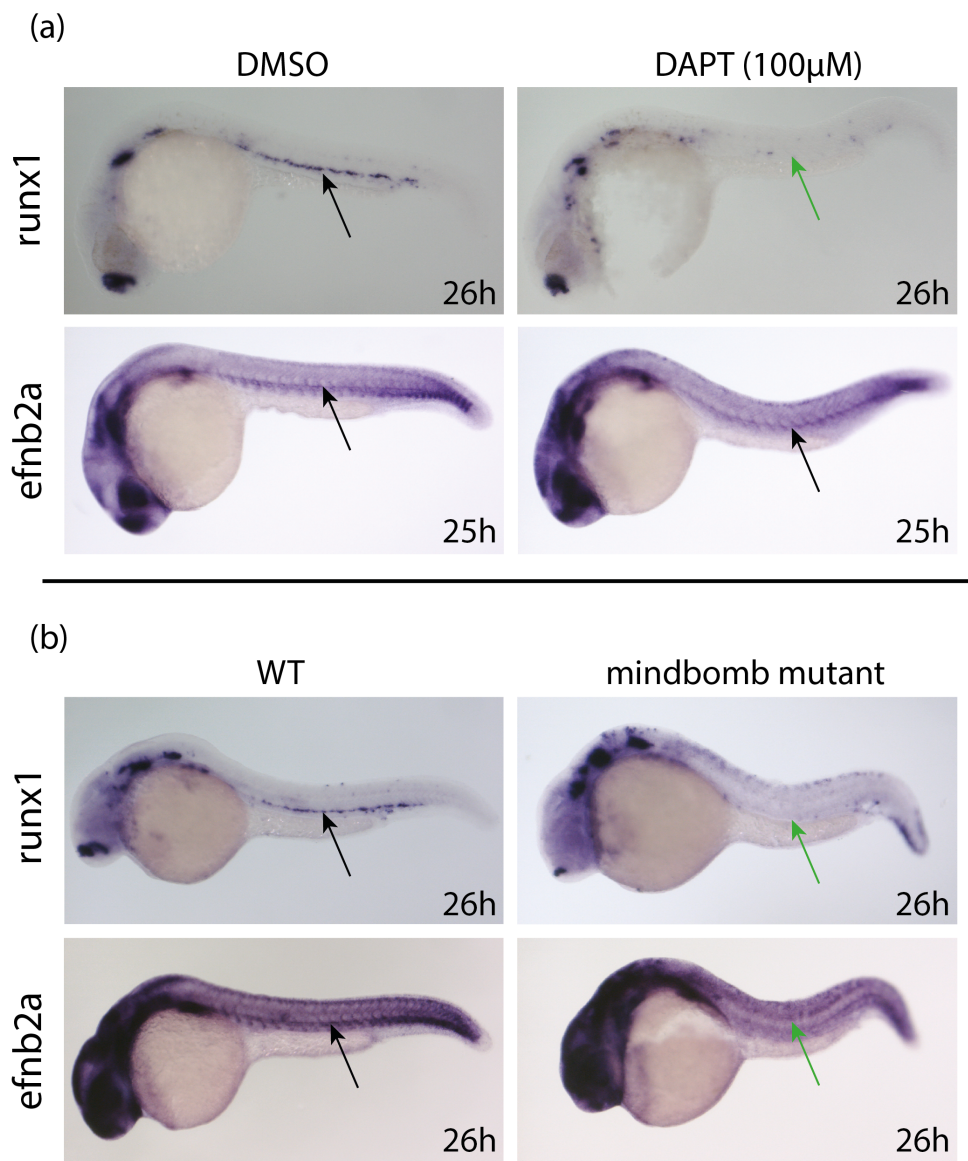


Figure 2.4: Expression of *efnb2a* and *runx1* as detected by in-situ hybridisation at 25-26hpf (a) after pharmacological treatment with the (γ -secretase) Notch signalling inhibitor DAPT and (b) in the *mindbomb* mutant. (b) shows loss of both *efnb2a* and *runx1* in the DA (green arrows) of the *mindbomb* mutant whereas (a) shows a loss of *runx1* (green arrow) but not *efnb2a* (black arrow) in DAPT treated embryos. (In-situ data is from the Gering lab).

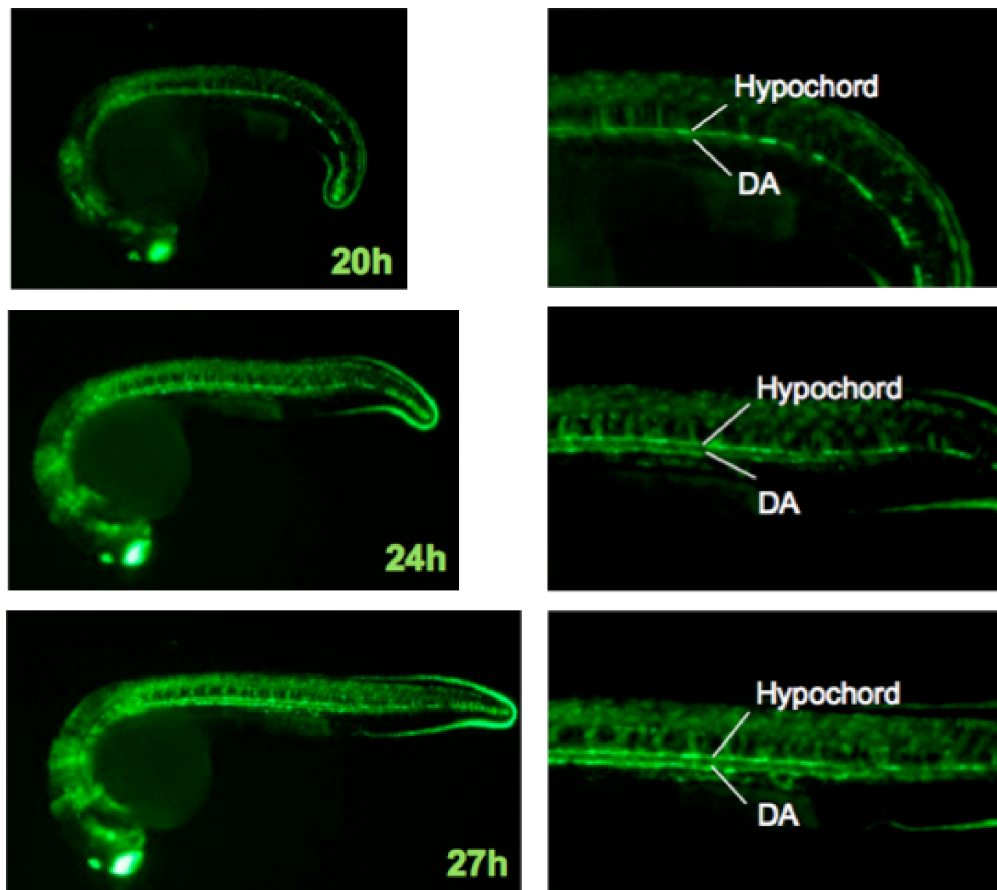


Figure 2.5: The 12×CSL:Venus line is a transgenic Notch reporter line of zebrafish. Cells receiving a Notch signal express the yellow fluorescent protein, Venus, which appears green when viewed using the FITC filter set on our microscope. Fluorescence of the Venus protein increases over time, suggesting that the DA cells receive a temporally increasing Notch signal.

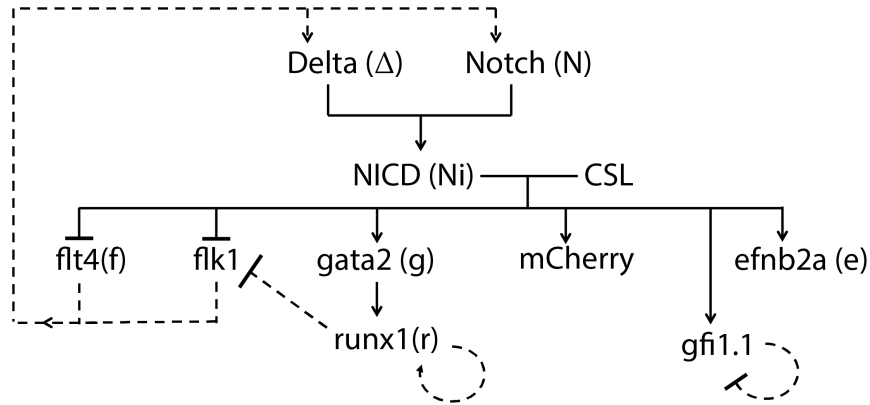


Figure 2.6: Gene regulatory network (GRN) in arterial ECs. Delta and Notch binding results in activation of *efnb2a* for arterial specification, and *runx1* and *gfi1.1* activation for HSC specification. Feedback from *flt4* and *flk1* may influence expression of Notch ligands and receptors. Arrows/bars represent activation/repression of gene expression respectively; Dotted lines: potential feedback loops.

cells to communicate via Delta-Notch signalling. In particular we investigate a system of two coupled cells with periodic boundary conditions i.e. a string of cells, $j = 1, 2$, in which the right-hand neighbour of cell $j = 2$ is identical to cell $j = 1$ and the left-hand neighbour of cell $j = 1$ is identical to cell $j = 2$. In terms of the cellular concentrations, u_j , periodic boundary conditions are equivalent to $u_3 = u_1$ and $u_0 = u_2$. Including Delta-Notch coupling allows us to investigate the effect of lateral inhibition feedback on *efnb2a* and *runx1* expression. This feedback loop, which is investigated in more detail in the next chapter, involves Notch inhibition of the VEGF receptors (*flk1* and *flt4*) which previously induced expression of Delta and Notch in all DA angioblasts at approximately 17hpf, just before the onset of arterial gene expression (see dashed lines in Figure 2.6 and Table 2.1 for references). In this chapter, we do not explicitly incorporate the effect of the VEGF receptors on Delta or Notch. Instead we allow the production rate of Delta ligand to be an increasing function of a prescribed extracellular VEGF concentration, multiplied by a decreasing function of NICD. Thus we determine whether Delta-Notch mediated cell coupling can qualitatively explain the experimental observations presented in §2.1.

Flt4 suppression by Delta-Notch signalling was originally considered in our models as its downregulation, reported by others [50, 54, 56], coincided with our hypothesised upregulation of Notch. However, we find that we cannot reliably isolate DA angioblasts in our experimental results. The cell population was contaminated, most likely, with PCV angioblasts. Thus we measure *flt4* expression in a wider population

of angioblasts in which *flt4* is not downregulated by Notch signalling. As such, we choose not to model the unreliable *flt4* data. The contamination does not seem to affect the *runx1* and *efnb2a* upregulation observed in the experimental results. This is likely due to the fact that, if contamination is indeed caused by the PCV angioblasts, since *runx1* and *efnb2a* are not normally detected in the PCV, the inclusion of some PCV angioblasts in the isolated population of cells is unlikely to make a large difference to the observed expression.

Interaction	Source of evidence	Direct?
NICD-CSL \rightarrow <i>efnb2a</i>	Human EC line (Grego-Bessa, 2007)[24]	Yes
NICD-CSL \rightarrow mCherry	Zebrafish (Our own unpublished data)	Yes
NICD-CSL \rightarrow <i>gfi1.1</i>	Zebrafish (Our own unpublished data)	No
NICD-CSL \rightarrow <i>gata2</i>	Mouse (Robert-Moreno, 2005; Guiu et al 2013)[35, 36]	Yes
<i>gata2</i> \rightarrow <i>runx1</i>	Mouse (Nottingham et al., 2007)[34], (Guiu et al 2013)[36]	Yes
NICD-CSL \nrightarrow <i>flt4</i>	Zebrafish (Siekman and Lawson, 2007; Gore et al., 2011; Thompson et al., 1998)[50, 54, 105]; Mouse (Tamella et al., 2008)[48]	No
NICD-CSL \nrightarrow <i>flk1</i>	Mouse (Suchting et al., 2007; Bentley et al., 2008) [47, 51, 81]	No
<i>flt4</i> \rightarrow Delta/(Notch)	Unknown - assuming interaction similar to <i>flk1</i> -Delta signalling	Unknown
<i>flk1</i> \rightarrow Delta/(Notch)	Lawson 2002 [22], Liu et al., 2003 [63], Bentley et al., 2008 [81]	Unknown
<i>runx1</i> \nrightarrow <i>flk1</i>	Mouse cell line (Hirai et al., 2005) [106]	Unknown
<i>runx1</i> \rightarrow <i>runx1</i>	Swiers et al 2010 [4]	Yes
<i>gfi1.1</i> \nrightarrow <i>gfi1.1</i>	-	Yes

Table 2.1: Evidence for the interactions in our models. These interactions are diagrammatically summarised in Figure 2.6

2.2.1 Model formulation

As a first step in exploring the responses of *efnb2a* and *runx1* to Notch signalling, we ignore the Delta-Notch binding processes and model the downstream dynamics using a prescribed input of NICD (see Figure 2.7). We analyse the effect of a linearly

increasing Notch signal (the simplest form of increasing function) on the expression of downstream genes. We are most concerned with the mechanism by which Notch activation may induce expression of *efnb2a* at 18hpf and expression of *runx1*, at 24hpf leading to arterial specification preceding HSC specification.

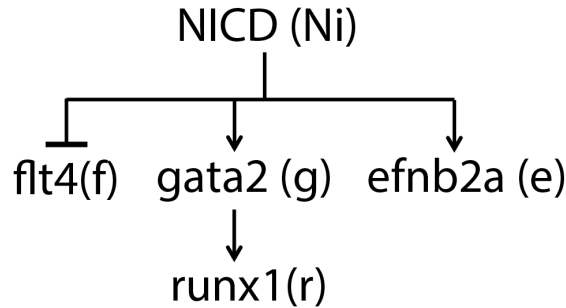


Figure 2.7: A reduced GRN which excludes Delta-Notch binding. A prescribed Notch input signal drives the expression of *efnb2a*, directly and expression of *runx1* via *gata2*. Model variables are in brackets.

One way in which this may be possible would be a difference in promoter sensitivities of each gene. The gene *efnb2a* has been identified as a direct target of Notch signalling in the human microvascular endothelial cell line, HMEC1 [24], whereas the effect of Notch on *runx1* expression is assumed to be mediated through the activation of *gata2* [35, 36]. Whether this mediation is responsible for the delayed activation of *runx1* is currently unclear. Other possible mechanisms contributing to the delay may be extra processing steps in the regulation, for example, transcriptional, translational and post-transcriptional modification related delays although we know of no experimental data confirming this.

In modelling the transcription of *gata2*, *efnb2a*, *runx1* and *flt4*, we make a number of assumptions:

- No basal transcription is assumed.
- The mRNA degradation rate is assumed to be identical for all transcripts.
- Proteins and translation are neglected for all genes.
- The input to the model is a linearly increasing NICD input signal over time, $Ni(t) = t$. The model is run for finite time as $Ni \rightarrow \infty$ as $t \rightarrow \infty$ may be unrealistic.

The following system of equations is used to model transcription downstream of Notch:

$$\text{gata2 mRNA: } \frac{dg}{dt} = \frac{c_1 Ni}{c_2 + Ni} - Dg, \quad (2.2.1a)$$

$$\text{Efnb2a mRNA: } \frac{de}{dt} = \frac{c_3 Ni}{c_4 + Ni} - De, \quad (2.2.1b)$$

$$\text{Runx1 mRNA: } \frac{dr}{dt} = \frac{c_5 g}{c_6 + g} - Dr, \quad (2.2.1c)$$

$$\text{Flt4/Flk1 mRNA: } \frac{df}{dt} = \frac{c_7}{c_8 + Ni} - Df. \quad (2.2.1d)$$

where c_1, c_3, c_5, c_7 are the maximal mRNA production rates for each gene and $c_2, c_4, c_8, (c_6)$ are the concentrations of NICD (gata2) at which the production rate of each mRNA species is at half of its maximum value. We use the following scalings to reduce the number of parameters and simplify the model:

$$g = \frac{c_1}{D} \hat{g}, \quad e = \frac{c_3}{D} \hat{e}, \quad r = \frac{c_5}{D} \hat{r}, \quad f = \frac{c_7}{D} \hat{f}, \quad (2.2.2)$$

where hats denote dimensionless variables. The equation for runx1 scales as follows

$$\frac{d\hat{r}}{dt} = D \left(\frac{\frac{c_1}{D} \hat{g}}{c_6 + \frac{c_1}{D} \hat{g}} - \hat{r} \right). \quad (2.2.3)$$

The final rescaled model is defined as

$$\text{gata2 mRNA: } \frac{d\hat{g}}{dt} = D \left(\frac{Ni}{c_2 + Ni} - \hat{g} \right), \quad (2.2.4a)$$

$$\text{Efnb2a mRNA: } \frac{d\hat{e}}{dt} = D \left(\frac{Ni}{c_4 + Ni} - \hat{e} \right), \quad (2.2.4b)$$

$$\text{Runx1 mRNA: } \frac{d\hat{r}}{dt} = D \left(\frac{\hat{g}}{\hat{c}_6 + \hat{g}} - \hat{r} \right), \quad (2.2.4c)$$

$$\text{Flt4/Flk1 mRNA: } \frac{d\hat{f}}{dt} = D \left(\frac{1}{c_8 + Ni} - \hat{f} \right), \quad (2.2.4d)$$

where $\hat{c}_6 = \frac{c_6 D}{c_1}$.

2.2.2 Quasi-steady state and dose response solutions

Dose response curves can be an insightful way to analyse how the steady states of a model change with respect to an input. By assuming that the Notch input varies slowly, we can make a quasi-steady state assumption for the genes in (2.2.4). The quasi-steady

states of the model in (2.2.4a)-(2.2.4d) are found by setting $\frac{d}{dt} = 0$, and are given by:

$$\hat{g}(Ni) = \frac{Ni}{c_2 + Ni}, \quad (2.2.5)$$

$$\hat{e}(Ni) = \frac{Ni}{c_4 + Ni}, \quad (2.2.6)$$

$$\hat{r}(Ni) = \frac{\hat{g}(Ni)}{\hat{c}_6 + \hat{g}(Ni)}, \quad (2.2.7)$$

$$\hat{f}(Ni) = \frac{1}{c_8 + Ni}. \quad (2.2.8)$$

Substituting (2.2.5) into (2.2.7) yields

$$\hat{r} = \frac{1}{\hat{c}_6 + 1} \frac{Ni}{\alpha + Ni}, \quad (2.2.9)$$

where

$$\alpha = \frac{\hat{c}_6 c_2}{\hat{c}_6 + 1}, \quad (2.2.10)$$

is the parameter specifying the value of Notch at which runx1 achieves its half-maximal concentration. After making the quasi-steady state assumption, the parameters c_2, c_4, c_8 correspond to the dose of NICD at which the steady state mRNA concentrations attain their half-maximal value and \hat{c}_6 corresponds to the sensitivity of runx1 to gata2. Thus, for runx1 expression to be less sensitive to NICD, we require

$$\alpha = \frac{\hat{c}_6 c_2}{\hat{c}_6 + 1} > c_4. \quad (2.2.11)$$

However, in the case where $Ni \ll 1$,

$$\hat{r} \approx \frac{1}{\hat{c}_6 + 1} \frac{Ni}{\alpha} = \frac{Ni}{\hat{c}_6 c_2} \quad \text{and} \quad \hat{e} \approx \frac{Ni}{4}. \quad (2.2.12)$$

These responses are linear and for efnb2a to grow faster we require

$$\frac{1}{c_4} > \frac{1}{\hat{c}_6 c_2}. \quad (2.2.13)$$

Figure 2.8 shows how varying c_2 , whilst keeping \hat{c}_6 fixed, modulate how quickly (relative to efnb2a) runx1 mRNA concentrations respond to low doses of Notch.

Henceforth, we assume that the NICD concentration is not small. Thus condition (2.2.11) determines the delayed onset of runx1 relative to efnb2a.

In this case, for fixed c_2 , when $\hat{c}_6 \ll 1$, $\alpha \sim \hat{c}_6 c_2$, and when $\hat{c}_6 \rightarrow \infty$, $\alpha \rightarrow c_2$. Thus α is an increasing, saturating function of \hat{c}_6 . However, for fixed \hat{c}_6 , the half-maximal concentration, α , is proportional to c_2 . Hence, α is always linearly proportional to c_2 whereas the dependence on $\hat{c}_6 = \frac{c_6 D}{c_1}$ is only significant when \hat{c}_6 is small. This implies

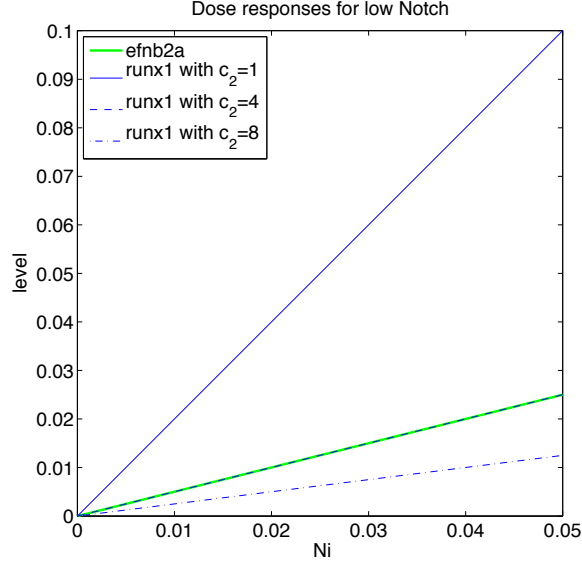


Figure 2.8: Dose response curves for *gata2*, *efnb2a* and *runx1* for low doses of NICD input using the parameter values in Table 2.2 unless otherwise stated. Responses are linear and are shown for $c_2 = 1, 4, 8$ by plotting equations (2.2.5)-(2.2.8). *Runx1* levels grow more slowly than *efnb2a* as c_2 is increased. Equation (2.2.13) is satisfied for the dash-dot curve, $c_2 = 8$, with equality shown in the dashed curve, $c_2 = 4$.

that the role of c_2 , *gata2*'s sensitivity to NICD, may be more important in achieving a delayed response to Notch signalling than *runx1*'s sensitivity to *gata2*, \hat{c}_6 . Using the parameter values in Table 2.2, where the half-maximal concentration parameter for *efnb2a*, $c_4 = 2$, and $\alpha = \frac{1}{3}, 2, 4$ by choosing $c_2 = 1, 6, 12$ respectively, we demonstrate in Figure 2.9, that we can induce *runx1* to respond earlier, at the same time and later than *efnb2a*. The plots therein use a linearly increasing Notch signal $Ni(t) = t$ and are normalised so that their maximum value on the interval $N \in [0, 30]$ is 1.

Although \hat{c}_6 , the sensitivity of *runx1* to *gata2*, has a small role in determining the *runx1* delay, it determines the level to which the *runx1* mRNA level saturates. Equation (2.2.5) implies that

$$\hat{g} \rightarrow G_{max} = 1, \quad (2.2.14)$$

where G_{max} is the maximum, quasi-steady state concentration of *gata2*. Thus, equations (2.2.5) and (2.2.9) both imply that *runx1*,

$$\hat{r} \rightarrow R_{max} = \frac{G_{max}}{\hat{c}_6 + G_{max}} = \frac{1}{\hat{c}_6 + 1} \quad \text{as } Ni \rightarrow \infty. \quad (2.2.15)$$

where R_{max} is the maximum, quasi-steady state concentration of *runx1*.

As $\hat{c}_6 \rightarrow 0$ then $R_{max} \rightarrow 1$ and when $\hat{c}_6 \rightarrow 1$, then $R_{max} \rightarrow 0.5$. For $\hat{c}_6 > 1$, $R_{max} < 0.5$

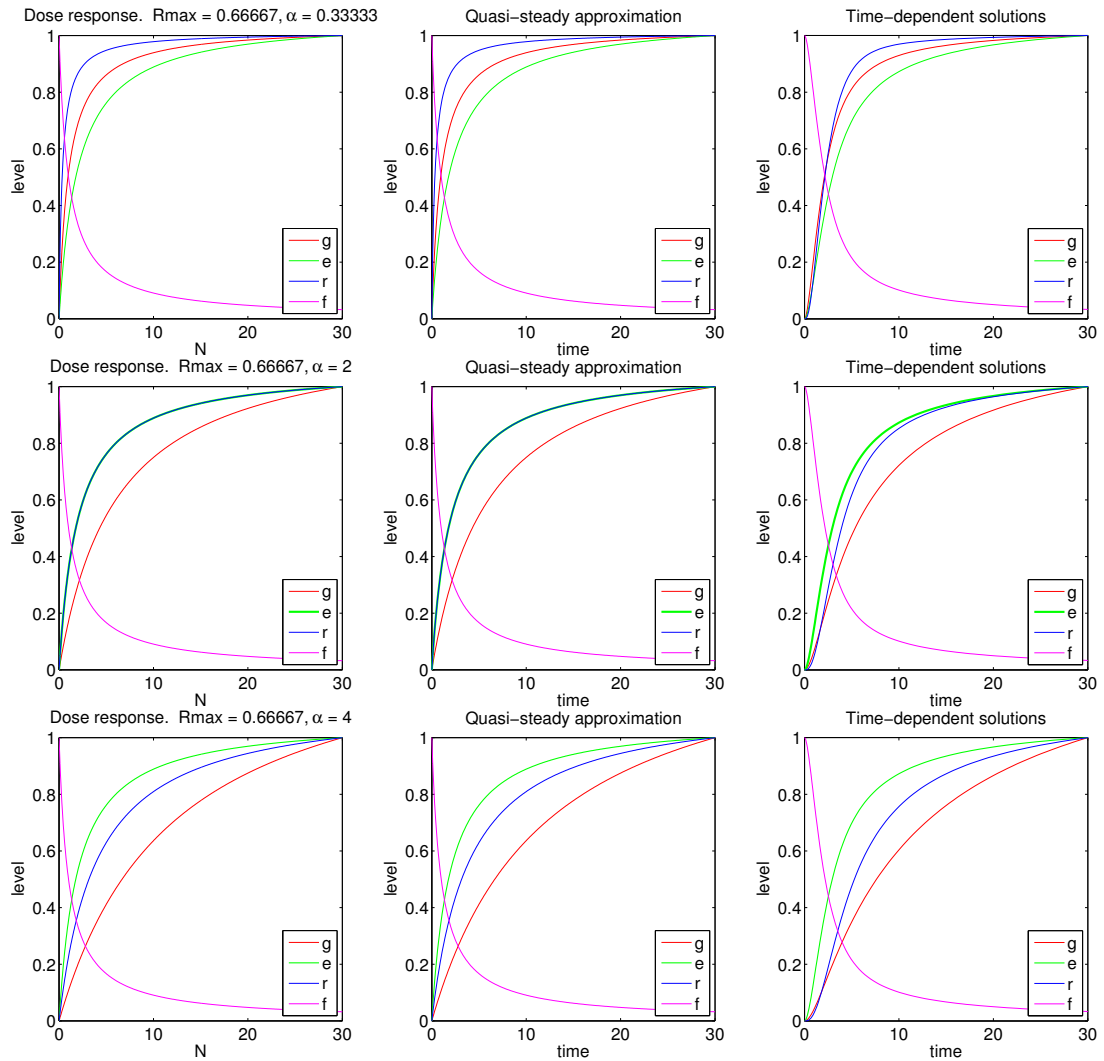


Figure 2.9: Dose response concentration curves, quasi-steady state approximations and numerical solutions to equations (2.2.5)-(2.2.8) using the parameters from Table 2.2. Row 1 has $c_2 = 1$ and $\alpha = 1/3$ for which runx1 is more sensitive to Notch than efnb2a. Row 2 has $c_2 = 6$ and $\alpha = 2$ for which runx1 and efnb2a have the same response (co-location of (thick) green and blue lines). Row 3 has $c_2 = 12$ and $\alpha = 4$ for which runx1 is less sensitive to Notch. We use an increasing Notch input signal, $N_i(t) = t$, and all curves are scaled by their maximum value, otherwise runx1 would saturate to $\frac{1}{1+1/2} = \frac{2}{3}$ making it difficult to determine whether its initial response is quicker than efnb2a's.

and tends to zero as $\hat{c}_6 \rightarrow \infty$. This is illustrated in Figure 2.10 which shows that for $\hat{c}_6 < 1$, runx1 quickly reaches its half-maximal concentration and saturates close to its R_{max} value, whereas for $\hat{c}_6 > 1$, runx1's sensitivity to gata2 is weak, such that R_{max} values greater than 0.5 are unattainable because gata2 has reached its maximum and can provide no more activation for runx1.

Parameter	Physical Meaning	Estimated value
c_1	Maximum rate of transcription for gata2	1
c_2	Concentration of Notch at which transcription of gata2 is half-maximal	-
c_4	Concentration of Notch at which transcription of efnb2a is half-maximal	2
c_6	Concentration of gata2 at which transcription of runx1 is half-maximal	0.5
c_8	Concentration of Notch at which transcription of flt4 is half-maximal	1
D	mRNA degradation rate	1 h^{-1}
\hat{c}_6	Dimensionless concentration of gata2 at which transcription of runx1 is half-maximal	$\frac{c_6 D}{c_1}$
α	Dimensionless concentration of Notch at which the response of runx1 is half-maximal	$\frac{c_2 \hat{c}_6}{\hat{c}_6 + 1}$

Table 2.2: Parameter values used for the model in equations (2.2.5)-(2.2.8) and (2.2.4a)-(2.2.4d).

Thus for runx1 to be detectable we require R_{max} to be 'large enough' which is obtained by increasing runx1's sensitivity to gata2 by making \hat{c}_6 'small enough'. For a reduced response to Notch, relative to efnb2a, we require c_2 to be large enough such that $\alpha > c_4$.

The time dependent behaviour of the model depends on the functional form taken by NICD. By assuming $Ni(t) = t$, both the quasi-steady approximation and the behaviour of the ODE model solutions closely match the dose responses. For this form of input signal the half-maximal concentrations can be viewed as characteristic times taken to reach the half-maximum concentration. Figure 2.11 illustrates a situation where runx1 reaches its half-maximal concentration 2 hours after efnb2a reaches its half-maximal concentration. This is done for parameter values corresponding to the blue curve in Figure 2.10.

In this section we have shown that when the genes downstream of Notch have Michaelis-

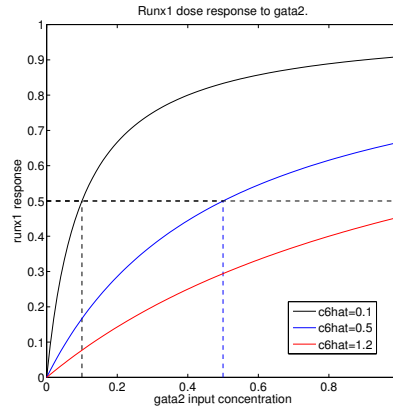


Figure 2.10: Dose responses of runx1 to a gata2 input for $\hat{c}_6 = 0.1, 0.5, 1.2$ calculated by plotting equation (2.2.7) for $\hat{g} \in [0, 1]$. Parameter values are as per Table 2.2. For $\hat{c}_6 > 1$, levels of runx1 greater than $\frac{1}{2}$ become unattainable (see red curve for example) because the maximum dose of gata2 can never exceed $\hat{g} = 1$. In this case the runx1 response is almost linear. When $\hat{c}_6 < 1$, runx1 is very sensitive to gata2 and reaches its half-maximal value before gata2 reaches $\hat{g} = 1$ (see black curve for example). Hence the runx1 response starts to saturate to a maximum value which approaches $R_{max} = 1$.

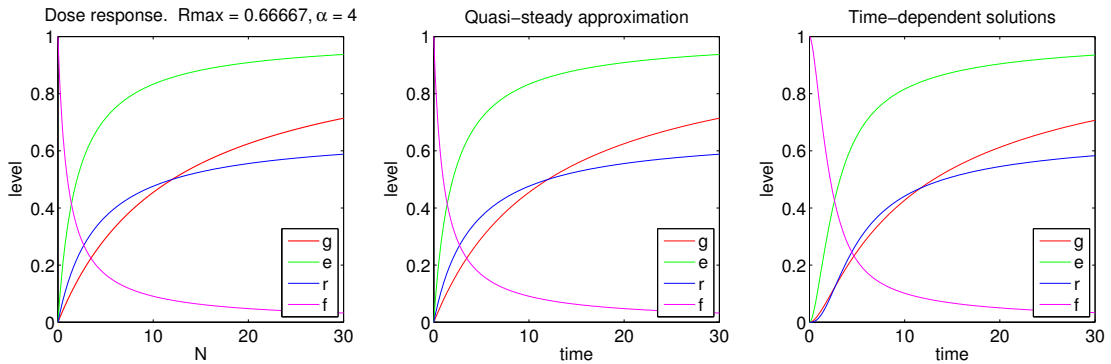


Figure 2.11: Dose response curves, quasi-steady and time-dependent solutions to the system in (2.2.5)-(2.2.8) using the parameters in Table 2.2 (corresponding to the blue curve in Figure 2.10) and $c_2 = 12$. These parameters can give efnb2a induction before runx1 induction as seen in experimental results.

Menten type responses to Notch (see equations (2.2.5)-(2.2.8)), runx1 's effective sensitivity to NICD, α , is proportional to gata2 's sensitivity to Notch, c_2 . Thus we manipulate c_2 until condition (2.2.11) is satisfied such that for a Notch input which increases linearly with time, $Ni(t) = t$, runx1 is effectively transcribed at a later time relative to efnb2a . We find that gata2 acts as a filter, only allowing runx1 to respond to NICD, once its expression levels are sufficiently high.

2.2.3 The effect of runx1 having a sigmoidal response to gata2

In this section we test whether changing the functional form of the responses can increase the delay in runx1 transcription. We do this by modifying equations (2.2.4a)-(2.2.4d) so that runx1 has a sigmoidal response to gata2 . In particular we replace equation (2.2.4c) with

$$\frac{d\hat{r}}{dt} = D \left(\frac{\hat{g}^m}{\hat{c}_6^m + \hat{g}^m} - \hat{r} \right), \quad (2.2.16)$$

where m is a coefficient controlling the sharpness of the runx1 response. The quasi-steady state of (2.2.16) is given by

$$\hat{r} = \frac{\hat{g}^m}{\hat{c}_6^m + \hat{g}^m} = \frac{\left(\frac{Ni}{c_2 + Ni} \right)^m}{\hat{c}_6^m + \left(\frac{Ni}{c_2 + Ni} \right)^m} \rightarrow \frac{1}{\hat{c}_6^m + 1} \quad \text{as } Ni \rightarrow \infty. \quad (2.2.17)$$

It is straightforward to show that $Ni_{1/2}$, the half-maximal response concentration for runx1 , is achieved at

$$Ni_{1/2} = \beta = \frac{c_2 \hat{c}_6}{(1 + 2\hat{c}_6^m)^{\frac{1}{m}} - \hat{c}_6}. \quad (2.2.18)$$

The form of β is similar to α . For instance, β is a linear function of c_2 for a fixed value of \hat{c}_6 and thus we vary it to manipulate the delay in runx1 .

Since runx1 is a sigmoid function of gata2 mRNA (see equation (2.2.17)), we begin by examining the response of runx1 to gata2 mRNA for $\hat{c}_6 = 0.1, 0.5, 1.2$ (see Figure 2.12). Similarly to the model in §2.2.2, when $\hat{c}_6 < 1$, $\hat{r} \rightarrow R_{max} > 0.5$. For $\hat{c}_6 > 1$, \hat{r} only traverses part of its sigmoid response curve and time-dependent solutions tend to $R_{max} < 0.5$.

By fixing $\hat{c}_6 = 0.5$, $m = 2$ and $c_2 = 12$, we observe the dose-response and time-dependent solutions corresponding to the blue curve in Figure 2.12 (see Figure 2.13). The Figure shows that the runx1 concentration tends to $R_{max} = \frac{1}{0.5^2 + 1} = 0.8$ and has a half-maximal concentration of $\beta = 8.2788$. Thus runx1 reaches its half-maximal concentration approximately 6.3 hours after efnb2a reaches its half-maximal concentration.

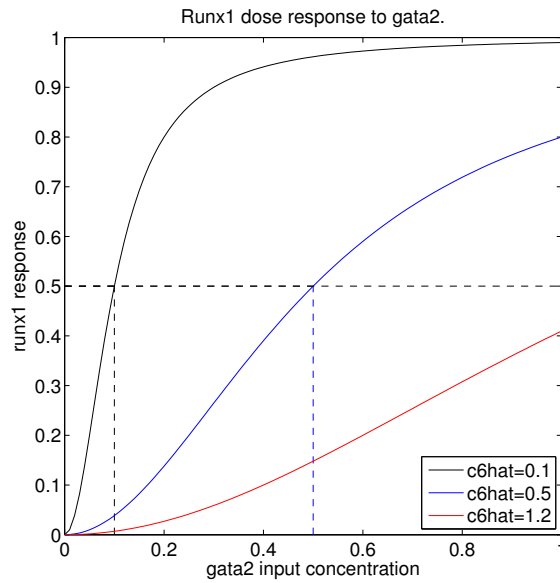


Figure 2.12: Dose responses of runx1 to a gata2 input for $\hat{c}_6 = 0.1, 0.5, 1.2$ and $m = 2$ calculated by plotting equation (2.2.17) for $\hat{g} \in [0, 1]$. The parameters used were as per Table 2.2. The gata2 mRNA concentration tends to 1 and therefore, when $\hat{c}_6 > 1$, levels of runx1 $> \frac{1}{1+1} = \frac{1}{2}$ become unattainable (see red curve for example). When $\hat{c}_6 < 1$, runx1 reaches its half-maximal value for a dose of gata2, corresponding to a value of \hat{c}_6 which is less than $\hat{g} = 1$ (see black curve for example). Hence the runx1 response saturates to a maximum value which approaches $R_{max} = 1$.

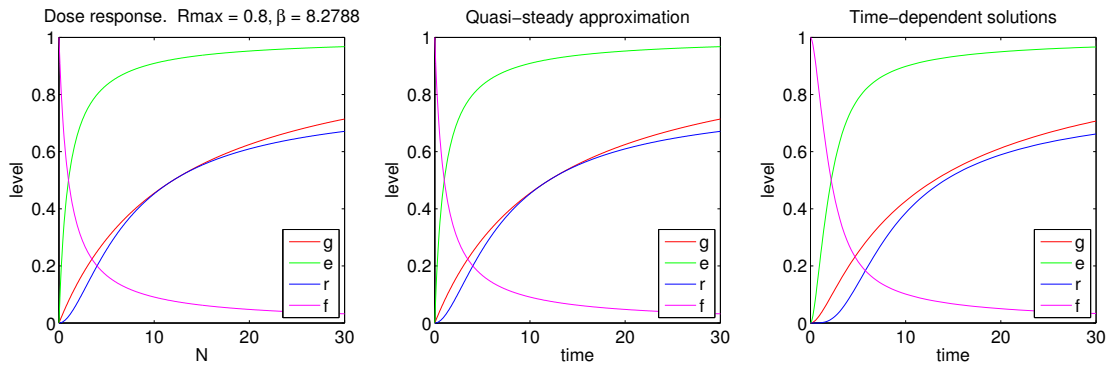


Figure 2.13: Dose response curves, quasi-steady and time-dependent solutions to the system in (2.2.5)-(2.2.8) using the parameters in Table 2.2 (corresponding to the blue curve in Figure 2.12) and $c_2 = 12$. The quasi-steady approximation gives a good approximation to the time-dependent ODE solutions. For a linearly increasing input $N_i(t) = t$, both quasi-steady and ODE solutions behave like the dose response curves. Our choice of parameters in this figure gives *efnb2a* induction before *runx1* induction with a larger delay in the induction of *runx1* in this model than the model from §2.2.2. For example, in the model of this section, *runx1* reaches its half maximal concentration at approximately 8.3h into the simulation whereas in the model of §2.2.2 *runx1* reaches its half maximal concentration after only 4h. The longer delay time is attributable to the functional form of *runx1*'s response to *gata2* which is sigmoidal for the model of this section.

Using the same parameter values, as those used in the model of §2.2.2, we find that runx1's sigmoidal response to gata2, reduces its sensitivity to Notch signalling. Comparison of the half-maximal Notch concentrations of this model, $\beta = 8.2788$, and those of the model in §2.2.2, $\alpha = 4$, demonstrates this.

2.2.4 The effect of gata2 having a sigmoidal response to Notch

In this section we model the system of equations (2.2.4a)-(2.2.4d) but instead allow gata2 to have a sigmoidal response to the NICD input. This involves replacing equation (2.2.4a) with

$$\frac{d\hat{g}}{dt} = D \left(\frac{Ni^m}{c_2^m + Ni^m} - \hat{g} \right), \quad (2.2.19)$$

for which the quasi-steady state is given by

$$\hat{g} = \frac{Ni^m}{c_2^m + Ni^m}. \quad (2.2.20)$$

This tends to

$$G_{max} = 1 \quad \text{as} \quad Ni \rightarrow \infty. \quad (2.2.21)$$

Thus, equations (2.2.20) and (2.2.7) both imply

$$\hat{r} \rightarrow R_{max} = \frac{G_{max}}{\hat{c}_6 + G_{max}} = \frac{1}{\hat{c}_6 + 1}, \quad (2.2.22)$$

which gives the same R_{max} value as the model in §2.2.2. Alternatively, substitution of (2.2.20) into (2.2.7) and refactorising the denominator gives

$$\hat{r} = \frac{1}{\hat{c}_6 + 1} \frac{Ni^m}{\gamma^m + Ni^m}. \quad (2.2.23)$$

where

$$\gamma = \left(\frac{c_2^m \hat{c}_6}{\hat{c}_6 + 1} \right)^{\frac{1}{m}} \quad (2.2.24)$$

Since runx1 responds to gata2 in the same way as per §2.2.2, the runx1–gata2 dose response curves are very similar to those observed in Figure 2.10 so are omitted for this model. Since the gata2 response to Notch is sigmoidal, the gata2–NICD dose response curves look similar to those observed for the runx1–gata2 dose response for the model in §2.2.3 (see Figure 2.12). These are also omitted here.

The effect of gata2's sigmoidal response to runx1 is shown in Figure 2.14 which shows that for fixed values of $\hat{c}_6 = 0.5$, $m = 2$ and $c_2 = 12$

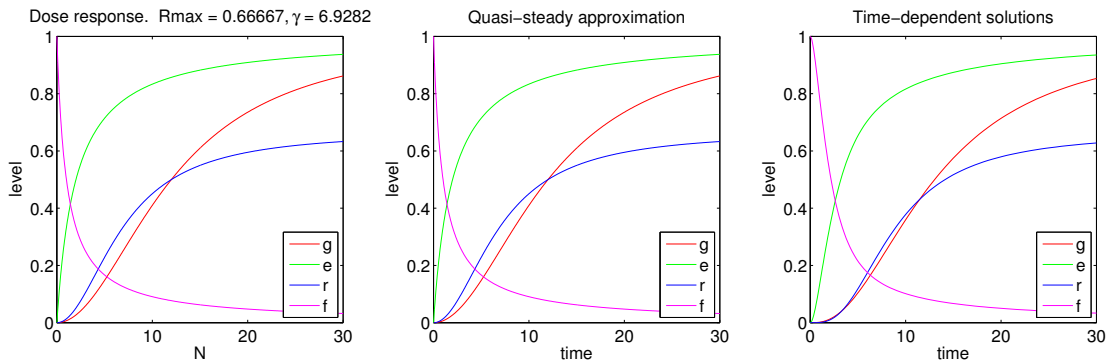


Figure 2.14: Dose response curves, quasi-steady and time-dependent solutions to the system in (2.2.6)-(2.2.8) and equation (2.2.20) using the parameters in Table 2.2 and $c_2 = 12$. The quasi-steady approximation gives a good approximation to the time-dependent ODE solutions. For a linearly increasing input $Ni(t) = t$, both quasi-steady and ODE solutions behave like the dose response curves. Our choice of parameters in this figure allow *efnb2a* induction before *runx1* induction with a delay in the induction of *runx1* ($\gamma \approx 6.9\text{h}$). This delay is larger than the delay in the first model in §2.2.2 which has $\alpha = 4$ and slightly smaller than the delay from the model in §2.2.3 which has $\beta \approx 8.3$ (compare with dose responses from Figures 2.11 and 2.13).

2.2.5 Summary

In summary, we have explored three different models in which *efnb2a* and *runx1* respond to Notch signalling for a linearly increasing Notch signal of the form $Ni(t) = t$. Each of these models has a characteristic time at which each gene reaches its half-maximal steady state concentration value. We find that the model in which the responses are all of Michaelis-Menten type has the shortest delay between the onset of *runx1* and *efnb2a* expression. The model with the next largest delay is the one in which *gata2* has a sigmoid response to Notch, with all other responses of Michaelis-Menten type. The model with the largest delay between the induction of *efnb2a* and *runx1* expression is the model in which *runx1* has a sigmoid response to *gata2* with all other responses being of Michaelis-Menten type. The larger delay time in the latter two models discussed here can be attributed to the sigmoid response functions included in them.

2.3 The potential role of cell coupling on HSC specification in arterial ECs

In this section, we extend the model in (2.2.1) to account for Delta-Notch mediated cell coupling upstream of the NICD input. The model remains continuous in time but contains a spatial aspect for which we use the discrete variable, j , to denote the cell index for a line of N cells: ($j = 1, 2, \dots, N$) [67]. For simplicity we focus on a two-cell system, with periodic boundary conditions so that $N = 2$ and we identify $u_3 = u_1$ and $u_0 = u_2$ where u_j represents the cellular concentrations of a species in cell j .

In this model Delta ligands reversibly bind Notch receptors on adjacent cells. The binding reaction can be summarised as follows:



where N_j and B_j represent the concentrations of unbound and bound Notch receptors in cell j , respectively, and $\Delta_{j\pm 1}$ represents the concentration of Delta ligand on cells adjacent to cell j . The Delta-Notch binding here is modelled in a similar way to how Owen and Sherratt modelled ligand-receptor binding [68]. Our model also assumes that the Notch receptors are conserved between bound and unbound forms. This assumption of a constant *number* of Notch receptors per cell is equivalent to assuming a constant *concentration* of Notch receptors, N_{tot} , if we also assume that the cell volume remains fixed.

The bound receptors undergo cleavage of their Notch intracellular domain (NICD), which translocates to the nucleus and directly activates *efnb2a*, *gata2* and *runx1* via *gata2* as per Figure 2.6. In practice, ligand-receptor binding leads to internalisation of the extracellular fragment of the Notch receptor into the signalling cell, followed by cleavage of the intracellular domain, NICD, leaving behind a non-functional intramembrane fragment. For simplicity, we ignore the details of the cleaving process and assume that the concentration of NICD is proportional to the concentration of bound receptors in cell j , as per [67],

$$Ni_j = k_2 B_j, \quad (2.3.2)$$

where k_2 is a dimensionless parameter representing the change in the concentration of Ni_j due to a change in bound Notch receptor concentration. It is important to note that equation (2.3.2) is only realistic if we assume that the production of Ni_j does not consume bound Notch receptors. This is equivalent to assuming that new NICD fragments are rapidly reattached to cleaved receptors, immediately yielding functional bound receptors.

The parameters herein and their physical meanings are given in Table 2.4. One of the key differences between this model and the model from §2.2.2 is that the NICD input is no longer prescribed. Instead NICD dynamics are governed by a combination of the feedback from the newly incorporated upstream Delta-Notch binding and an extracellular VEGF signal which acts to increase the production rate of Delta without explicitly incorporating VEGF receptor binding (see Figure 2.15).

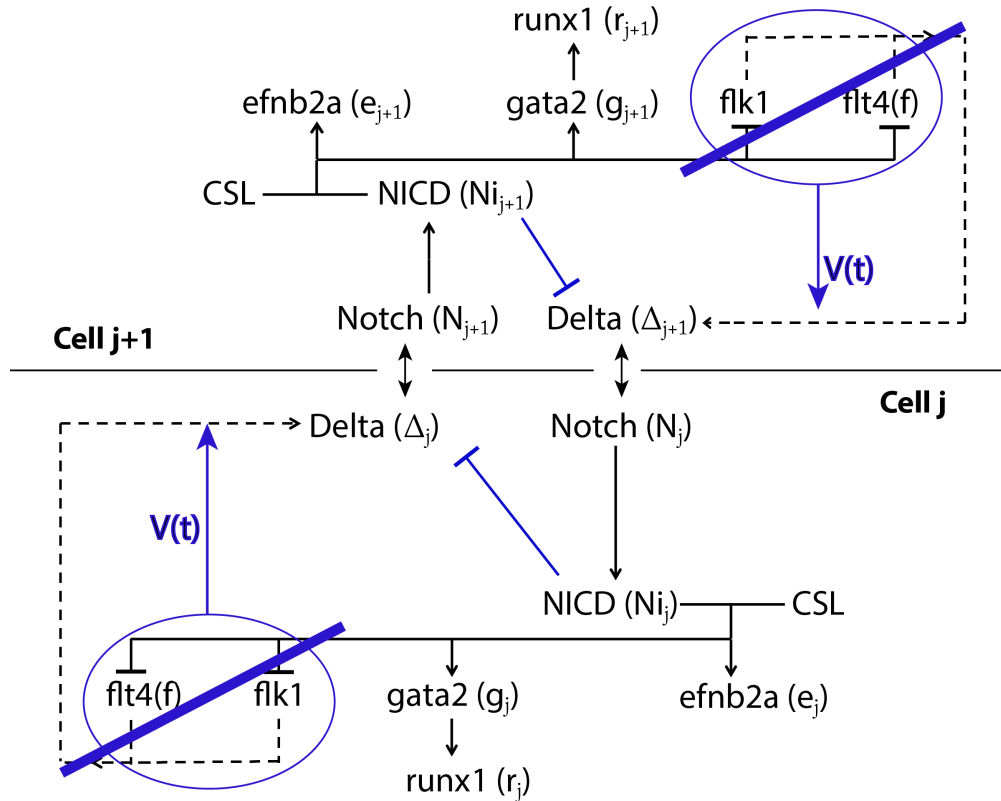


Figure 2.15: A two cell model of the GRN in Figure 2.6 which accounts for Delta-Notch binding without explicitly incorporating VEGF-VEGFR-2 binding. Instead Delta production is an increasing signal of extracellular VEGF, $V(t)$, which would otherwise activate Delta via flk1 and/or flt4, and a decreasing function of NICD in its own cell, which would inhibit Delta by down-regulating the production of flk1 and/or flt4. The regulation of efnb2a, gata2 and runx1 is the same as in Figure 2.7 except NICD is no longer prescribed in this model. The model input is the increasing, saturating VEGF signal $V(t)$. Model variables are in brackets.

Applying the law of mass action to the species in equation (2.3.1) we obtain the following system of equations:

$$\begin{aligned} \text{Delta: } \frac{d\Delta_j}{dt} &= k_D(Ni_j, V(t)) + k_{-B} \left(\frac{B_{j-1} + B_{j+1}}{2} \right) \\ &\quad - k_B \left(\frac{N_{j-1} + N_{j+1}}{2} \right) \Delta_j - \mu \Delta_j, \end{aligned} \quad (2.3.3a)$$

$$\text{Bound Notch: } \frac{dB_j}{dt} = k_B \left(\frac{\Delta_{j-1} + \Delta_{j+1}}{2} \right) N_j - k_{-B} B_j, \quad (2.3.3b)$$

$$\text{Unbound Notch: } N_j = N_{tot} - B_j, \quad (2.3.3c)$$

$$\text{NICD: } Ni_j = k_2 B_j. \quad (2.3.3d)$$

where

$$k_D(Ni_j, t) = \frac{\bar{\alpha} h^n}{h^n + Ni_j^n} V(t), \quad (2.3.4)$$

is the production rate of Delta which decreases with the level of NICD in cell j i.e. inhibition by neighbouring cells (see Figure 2.15). The parameters $\bar{\alpha}$, h and n represent the maximal production rate of Delta, the sensitivity of Delta production to NICD, and the strength of inhibition by NICD, respectively. As well as decreasing with NICD concentration, the Delta production rate also increases with the extracellular concentration of VEGF, which begins increasing at 17hpf:

$$V(t) = \frac{t - t_1}{h_1 + t - t_1} H(t - t_1) \rightarrow 1 \quad \text{as } t \rightarrow \infty, \quad (2.3.5)$$

where $t_1 = 17$. The parameter h_1 is the time after 17hpf at which the concentration of VEGF is at 0.5; and $H(\cdot)$ is the Heaviside switch function that initiates Delta production at 17hpf, defined as:

$$H(t) = \begin{cases} 0, & t < 0 \\ 0.5, & t = 0 \\ 1, & t > 0 \end{cases}. \quad (2.3.6)$$

2.3.1 Modelling assumptions

Our model averages the level of inhibition it receives from the neighbouring cells on either side. This is represented in equations (2.3.3) using the fractional terms. For a string of cells, this assumption may be unrealistic in cases where there is an asymmetric distribution of bound Notch receptors on cell j . In vivo, upon unbinding, unbound Notch receptors would be left on cell j and Delta ligand would be returned to the signalling cell. Our model, however, predicts that half of the Delta ligands would be

returned to cell $j - 1$ and the other half to cell $j + 1$. This may be problematic as one of the neighbouring cells would unrealistically generate Delta ligands which would have effectively been transferred from two cells away. A number of existing models take this averaging approach (see [68, 74] for example). Webb and Owen, explicitly account for the sides of the cell and only allow bound receptors to unbind to adjacent cell surfaces in their model. The authors find no significant qualitative differences between the models with and without explicitly defined sides, only minor quantitative differences [72].

2.3.2 Dimensionless model

We introduce the following scalings:

$$\Delta_j = N_{tot}\delta_j, \quad B_j = N_{tot}b_j, \quad N_j = N_{tot}n_j, \quad Ni_j = N_{tot}Ni_j^*, \quad (2.3.7)$$

where $N_{tot} = 1 \times 10^{-7}M$ is the total concentration of Notch receptors (calculated using cell size and Notch receptor data from [72, 81]) and lower case variables and Ni_j^* are dimensionless variables. The star is dropped for notational convenience. Equations (2.3.3) are coupled to the scaled equations for the genes downstream of Notch in equations (2.2.4). However since the model in §2.2.3 has the largest effective delay in runx1 transcription from all three of the previous models considered, we choose to replace equation (2.2.4c) with equation (2.2.16). Together these yield the following system of rescaled equations with dimensional time (in units of hours) and scaled NICD concentration expressed in units of $10^{-7} M$ ¹:

¹Assuming a cell with a $10\mu m$ diameter and 10,000 Notch receptors as per [72, 81].

$$\frac{d\delta_j}{dt} = k_D(Ni_j, t) + k_{-B} \left(\frac{b_{j-1} + b_{j+1}}{2} \right) - \bar{k}_B \left(\frac{n_{j-1} + n_{j+1}}{2} \right) \delta_j - \mu\delta_j, \quad (2.3.8)$$

$$\frac{db_j}{dt} = \bar{k}_B \left(\frac{\delta_{j-1} + \delta_{j+1}}{2} \right) n_j - k_{-B} b_j, \quad (2.3.9)$$

$$n_j = 1 - b_j, \quad (2.3.10)$$

$$Ni_j = k_2 b_j \quad (2.3.11)$$

$$\frac{d\hat{g}_j}{dt} = D \left(\frac{Ni_j}{c_2 + Ni_j} - \hat{g}_j \right), \quad (2.3.12)$$

$$\frac{d\hat{e}_j}{dt} = D \left(\frac{Ni_j}{c_4 + Ni_j} - \hat{e}_j \right), \quad (2.3.13)$$

$$\frac{d\hat{r}_j}{dt} = D \left(\frac{\hat{g}_j^m}{\hat{c}_6^m + \hat{g}_j^m} - \hat{r}_j \right), \quad (2.3.14)$$

$$\frac{d\hat{f}_j}{dt} = D \left(\frac{1}{c_8 + Ni_j} - \hat{f}_j \right), \quad (2.3.15)$$

where

$$k_D(Ni_j, t) = \frac{t - t_1}{h_1 + t - t_1} \frac{\bar{\alpha} \bar{h}^n}{\bar{h}^n + Ni_j^n} H(t - t_1), \quad (2.3.16)$$

with h_1 and t_1 defined as per equation (2.3.5). The parameter \bar{h} , is the NICD threshold for Delta inhibition and n is a coefficient controlling the feedback strength of the inhibition. In equations (2.3.8)-(2.3.16), the following parameter groupings are used:

$$\bar{\alpha} = \frac{\alpha}{N_{tot}}, \quad \bar{k}_B = k_B N_{tot}, \quad \bar{h} = h N_{tot}. \quad (2.3.17)$$

The half-maximal concentrations in the denominators of equations (2.3.12)-(2.3.15) have been scaled with N_{tot} as follows:

$$c_2^* = c_2 N_{tot}, \quad c_4^* = c_4 N_{tot}, \quad \hat{c}_6^* = \hat{c}_6 N_{tot}, \quad c_8^* = c_8 N_{tot}. \quad (2.3.18)$$

We drop the star on the dimensionless variables for convenience.

For the parameter values in Table 2.3, numerical simulations of equations (2.3.8)-(2.3.15) yield a patterning bifurcation at approximately 20hpf (see Figure 2.16). The homogeneous steady state is unstable and alternating cells express high and low concentrations of Delta and Notch. This leads to high and low expression of *efnb2a* and *runx1* mRNA. For the parameter values chosen here, patterning in *runx1* expression manifests after the homogeneous steady state has grown to a concentration of approximately 0.32.

Thus the model predicts that the concentration of runx1 initially increases homogeneously and then decreases in alternate cells due to patterning. To the best of our knowledge, this has not been observed in experiments although it is possible that the initial increase is undetectable by in-situ. If the average level of runx1 is measured using in-situ hybridisation or qPCR experiments, then the model suggests, that for these parameter values, the average runx1 concentration after patterning is no higher than the homogeneous steady state.

Ideally we would like the system to bifurcate whilst the homogeneous steady state is high for efnb2a and low for runx1 but retain similar solutions in alternating cells (a weak salt-and-pepper pattern) for efnb2a after the pitchfork but admit an asymmetrical, large amplitude pattern for runx1. This would mimic the early arterial specification in the whole of the DA and specification of HSCs in a subset of cells, albeit not in every other cell, as suggested by fluorescent in-situ hybridisation (see [21] and Figure 1.4).

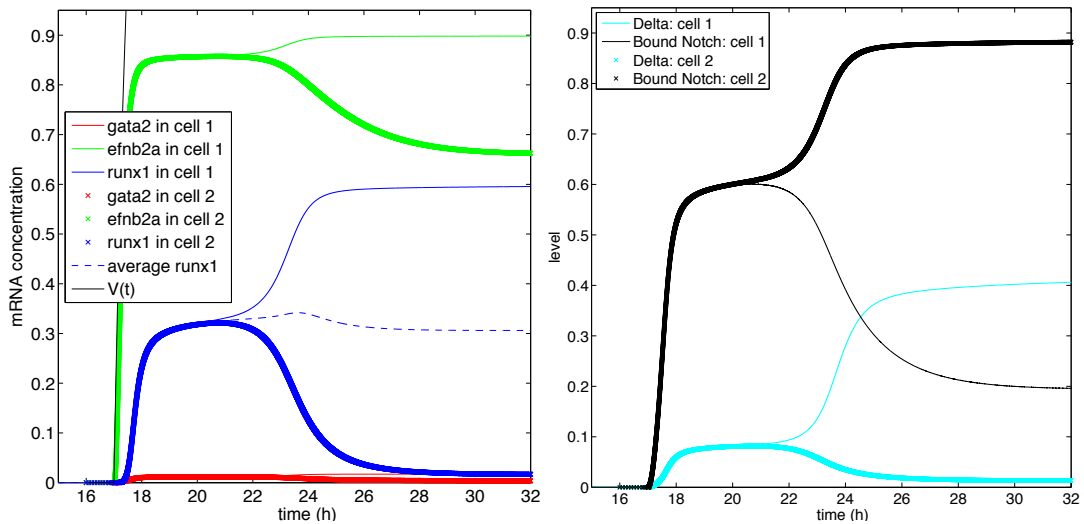


Figure 2.16: Numerical simulation of a two-cell system in which equations (2.3.8)-(2.3.16) are integrated using homogeneous initial conditions with all variables starting at 0 and parameter values as per Table 2.3. Since the model is at the homogeneous steady state when the VEGF signal switches on at $t = 17\text{hpf}$, any random perturbation added to the initial condition will have decayed back to the homogeneous steady state by the time the system reaches the pitchfork at 20hpf . Thus we add noise to the model solutions for $t < 21$ to allow the system to move away from the stable manifold of the homogeneous steady state. This simulation predicts that the two-cell model exhibits patterning due to lateral inhibition and that the homogeneous steady state for runx1 increases to approximately 0.32 before the pattern manifests significantly. The pattern is not capable of amplifying the average level of runx1 relative to the homogeneous steady state (blue dashed line).

Parameter	Physical Meaning	Estimated value
$\bar{\alpha}$	Maximum rate of Delta production	$2 \frac{\mu k_{-B}}{k_B} \times 4 = 3.13$
h	Concentration of NICD at which inhibition of Delta is half-maximal	0.5
h_1	Time at which the VEGF concentration is at half of its maximum level (shifted by 17h)	1
n	Strength of lateral inhibition from bound Notch receptors	6
m	Response strength of runx1 to gata2	3
k_{-B}	Dissociation rate for bound Notch receptors	$27.2 \times 4 \text{ h}^{-1}$
\bar{k}_B	Association rate of Delta and Notch	$0.5 \times 10^3 \times 4 \text{ h}^{-1}$
μ	Decay rate of Delta ligand	$1.8 \times 4 \text{ h}^{-1}$
k_2	NICD per bound Notch	1
c_1	Maximum rate of gata2 production	1×4
c_2	Concentration of Notch at which the transcription rate of gata2 is half-maximal	50.45
c_4	Concentration of Notch at which transcription of efnb2a is half-maximal	0.1
c_6	Concentration of gata-2 at which transcription of runx1 is half-maximal	0.001
D	mRNA degradation rate	$15.1 \times 4 \text{ h}^{-1}$
\hat{c}_6	Sensitivity of runx1 to gata2	$\frac{c_6 D}{c_1} = 0.0151$

Table 2.3: Parameter values used to numerically simulate equations (2.3.8)-(2.3.16) in Figure 2.16. (Concentrations are in units of $1 \times 10^{-7}\text{M}$).

By using a different parameter set (see Table 2.4), our model is able to exhibit such behaviour. If we assume that the VEGF dynamics are slow, relative to the Delta-Notch binding and the transcription of the downstream genes, we can vary $V(t) = V_0$, a constant, as a bifurcation parameter using XPPAUT (see §1.2.5 and [98] for details) and observe the downstream dose responses for NICD, *efnb2a* and *runx1* (see Figure 2.17).

Figure 2.17a shows how the steady state of NICD varies as the constant extracellular VEGF input, V_0 , is increased, using the parameter values in Table 2.4. The homogeneous steady state is stable and increases non-linearly with V_0 . A supercritical pitchfork bifurcation at $V_0 = 0.115$ causes the homogeneous steady state to become unstable and two new stable patterning branches emerge. For a system of N cells, odd and even cells would have steady state solutions located on each of the high and low patterning branches, respectively.

Figure 2.17b,c shows bifurcation diagrams for *efnb2a* and *runx1* mRNA concentrations using the same parameter values. These bifurcation diagrams qualitatively capture some of the key features seen in experimental data. Firstly the inclusion of Delta-Notch coupling allows salt-and-pepper patterning of *runx1* and *efnb2a* mRNA concentrations. The pattern is more exaggerated (solutions are very different in each cell) for the *runx1* response than for the *efnb2a* response. In other words, the stable, steady state mRNA concentrations, in each cell, for *efnb2a*, remain almost homogeneous after the pitchfork bifurcation, (approximately the same as the average concentration of the two cells) whereas the patterning branches for *runx1* are quite disparate (heterogeneous). This behaviour is consistent with experimental observations showing that all cells in the DA are specified as arterial from 18hpf onwards [21] whereas only certain cells are specified as *runx1*-positive HSC precursors at 24hpf (see Figure 1.4 for an example).

Secondly, due to the type of functional responses for *efnb2a* to NICD, and *runx1* to *gata2*, *efnb2a* is more sensitive to Notch than *runx1* is. Further, *efnb2a* requires a smaller dose of VEGF to saturate at its maximum steady state value *runx1*. The parameters controlling this sensitivity are c_4 and β (see equation (2.2.18)) which specify the dose of NICD required for *efnb2a* and *runx1* to reach their half-maximum concentrations. For the choice of parameter values in Table 2.4, these doses are $Ni_j = 0.1$ for *efnb2a* and $Ni_j = 5.4142$ for *runx1* (see the dose response curves for *efnb2a* and *runx1* in Figure 2.18). Figure 2.17a informs us that these NICD doses are attained at $V_0 = 0.0017$ and $V_0 = 0.16$. The time at which these doses of VEGF and, hence, NICD are obtained, however, depends on the functional form of $V(t)$.

These two features are summarised in the dose response curves for *gata2*, *efnb2a* and

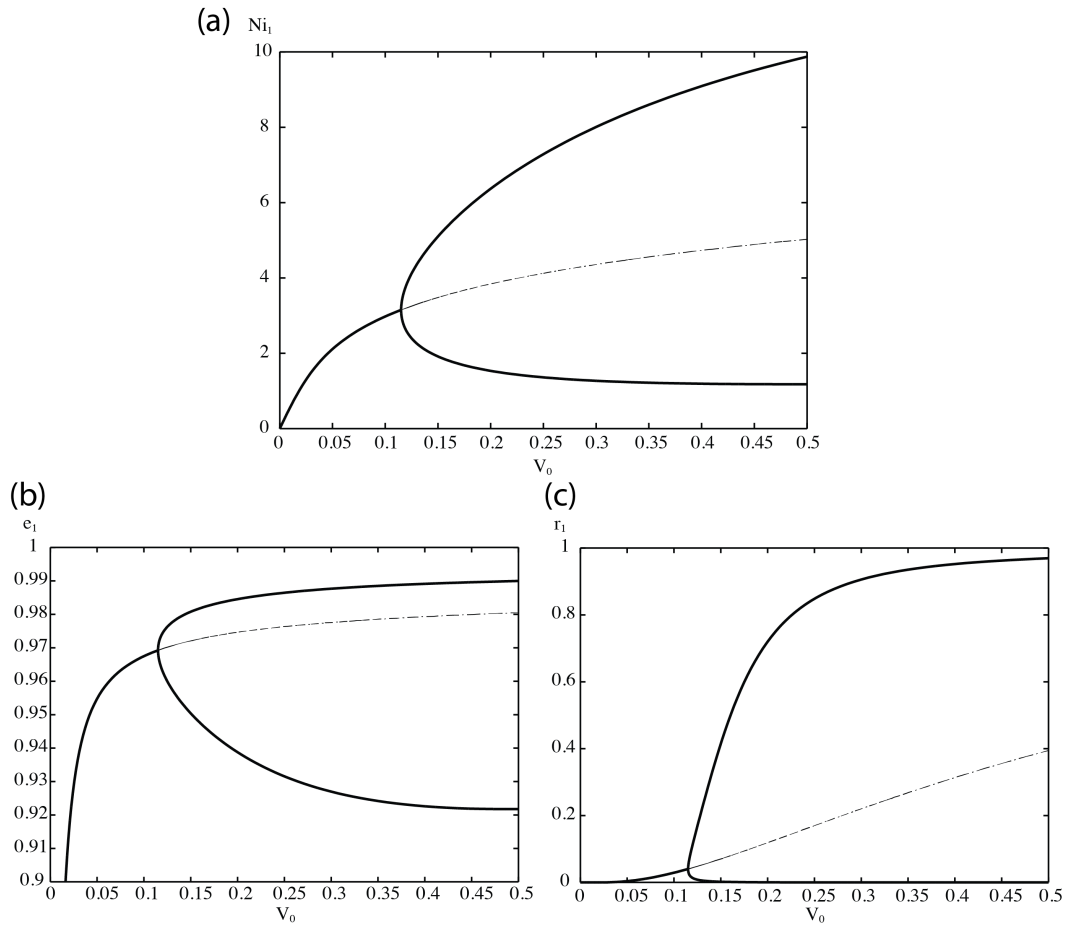


Figure 2.17: Bifurcation diagrams showing the steady state concentrations for (a) NICD, (b) *efnb2a* and (c) *runx1* mRNA in a two-cell system as the extracellular VEGF concentration, V_0 , is varied. The diagrams are produced using XPPAUT, by integrating the system of equations (2.3.8)-(2.3.15) to steady state using the parameters in Table 2.4 and then continuing the solutions for $V_0 \in [0, 0.5]$. Initial conditions for XPPAUT are $\delta_j = 0.1063, b_j = 0.5605, Ni_j = 0, g_j = 0.1, e_j = 1, r_j = 1, f_j = 0.3$ for $j = 1, 2$. A pitchfork bifurcation is found at $V_0 = 0.115$. (b) shows that after the pitchfork bifurcation the patterning branches for *efnb2a* are close together and remain approximately homogeneous as the VEGF dose is increased over time. (c) shows that in contrast, the patterning branches for *runx1* start close together (approximately homogeneous) but quickly separate (pattern) as the VEGF dose increases. Thus as time, and hence VEGF, increases, cell coupling and the functional forms for responses downstream of Notch, induce arterial identity homogeneously but assign the HSC fate differentially in a salt-and-pepper fashion.

runx1 in Figure 2.18. The Figure shows the steady state mRNA concentrations for *efnb2a* and *runx1* marked by green and blue markers respectively. These were taken at the last time point of a numerical simulation of a two-cell system in which equations (2.3.8)-(2.3.15) were integrated using constant VEGF inputs of $V_0 = 0.115$ (crosses) and $V_0 = 0.5$ (circles). For an extracellular VEGF concentration which increases continuously over time, this Figure qualitatively demonstrates that the model can replicate achieving homogeneous arterial identity at the early time point, 18hpf, followed by heterogeneous HSC specification.

In Figure 2.19 we integrate the system of equations (2.3.8)-(2.3.16) using the parameter values in Table 2.4 and initial conditions: $\delta_j = 0, b_j = 0, g_j = 0, e_j = 0, r_j = 0, f_j = 1$ for $j = 1, 2$. This corresponds to sweeping through the bifurcation diagrams in Figure 2.17 over time. When the VEGF level increases past $V(t) = 0.115$, the pattern can start to grow. However, the homogeneous steady state does not become unstable until approximately 25hpf. For the system to pattern, it requires a heterogeneous perturbation of the homogeneous steady state at approximately 25hpf. Such a perturbation cannot be provided via the initial conditions as it would decay back to zero. Thus, we add small random noise to the input signal $V(t)$ for $t < 25$. This seems to be sufficient to move solutions away from the homogeneous steady state.

The VEGF input signal, $V(t)$ (black line in Figure 2.19), saturates to $\bar{a} = 0.3$, a location inside the parameter window. Thus both *runx1* and *efnb2a* admit patterns here. The *runx1* homogeneous steady state bifurcates asymmetrically and splits into two branches of disparate solutions whose average is greater than that of the homogeneous steady state (see Figure 2.19 blue dashed line). The *efnb2a* homogeneous steady state, however, is already near its maximum when the system reaches the pitchfork. After the pitchfork bifurcation the patterning branches for *efnb2a* admit similar solutions, as required.

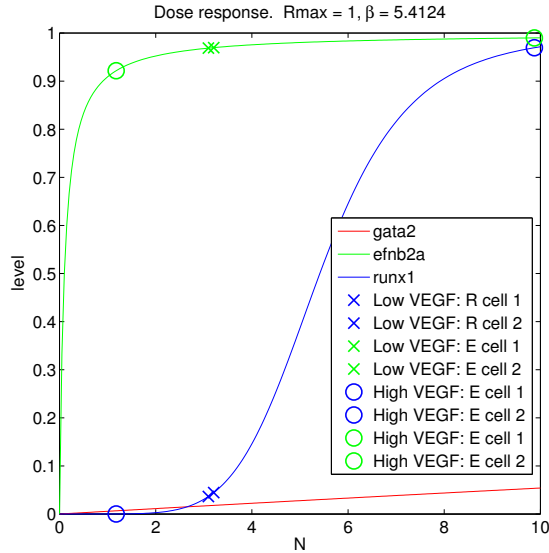


Figure 2.18: Dose responses of *gata2*, *efnb2a* and *runx1* mRNA concentrations to NICD for parameters as per Table 2.4. Overlaid are green (blue) crosses and circles marking the steady state concentrations of *efnb2a* (*runx1*) for low and high extracellular VEGF concentrations respectively, taken from the last time point of a two-cell simulation in which equations (2.3.8)-(2.3.15) were integrated. Parameters used were as per Table 2.4 and simulations were started at 0 for all variables except $Ni_1 = 0.1$. Since $V_0 \propto t$, The circles and crosses correspond to the extracellular VEGF concentration at early and late time points respectively. The green crosses show that for low VEGF signals, the steady state mRNA concentration for *efnb2a* in both cells is high and homogeneous whereas the blue crosses show that the steady state mRNA concentration for *runx1* is low in both cells. The circles show that in high VEGF concentrations which drive the high Notch signal from 24 hpf, the *efnb2a* concentration remains high and homogeneous (green circles) whereas the *runx1* concentration is patterned i.e. high in one cell and low in the other (blue circles). Hence this model qualitatively mimics early homogeneous arterial identity followed by differential HSC selection at 24hpf. An example of non-homogeneous *runx1* mRNA expression observed in the DA is shown in Figure 1.4, albeit not salt-and-pepper.

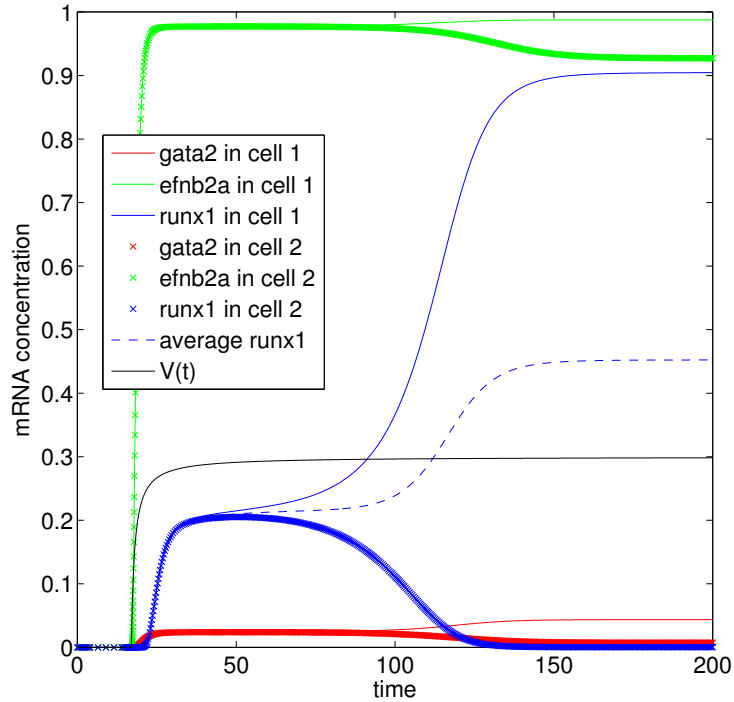


Figure 2.19: Timecourses for *gata2*, *efnb2a* and *runx1* mRNA concentrations in a two-cell system, calculated by integrating the system of equations (2.3.8)-(2.3.16) using initial conditions $\delta_j = 0, b_j = 0, g_j = 0, e_j = 0, r_j = 0, f_j = 1$ for $j = 1, 2$ and parameter values as per Table 2.4. We integrate the system to $t = 200\text{h}$ which allows $V(t)$ (black line) to saturate to $\bar{a} = 0.3$ such that the system comes to rest inside the patterning window seen in Figures 2.17. Although the pitchfork bifurcation is located at $V_0 = 0.115$, the pattern in *runx1* mRNA expression does not manifest until $V_0 \approx 0.2$. For the parameter values used here, patterning acts to amplify the average *runx1* mRNA concentration relative to the homogeneous steady state (blue dashed line). Solid lines and stars represent solutions in cells 1 and 2 respectively.

Parameter	Physical Meaning	Estimated value
$\bar{\alpha}$	Maximum rate of Delta production	0.3
h	Concentration of NICD at which inhibition of Delta is half-maximal	3.5
h_1	Time at which the VEGF concentration is at half of its maximum value (shifted by 17h)	1h
n	Strength of lateral inhibition from bound Notch receptors	6
m	Response strength of runx1 to gata2	3
k_{-B}	Dissociation rate for bound Notch receptors	0.25h^{-1}
\bar{k}_B	Association rate of Delta and Notch	1h^{-1}
μ	Decay rate of Delta ligand	1h^{-1}
k_2	NICD per bound Notch	15
c_1	Maximum rate of gata2 production	1
c_2	Concentration of Notch at which the transcription rate of gata2 is half-maximal	175
c_4	Concentration of Notch at which the transcription rate of efnb2a is half-maximal	0.1
c_6	Concentration of gata-2 at which the transcription rate of runx1 is half-maximal	0.03
D	mRNA degradation rate	1h^{-1}
\hat{c}_6	Sensitivity of runx1 to gata2	$\frac{c_6 D}{c_1} = 0.03$

Table 2.4: Parameter values used to numerically simulate equations (2.3.8)-(2.3.16) in Figure 2.19. (Concentrations are in units of $1 \times 10^{-7}\text{M}$).

2.4 Experimental techniques

In this section, the methodology for acquiring the quantitative experimental data to validate our models with is explained. We use quantitative PCR (qPCR) to measure the relative expression levels of *efnb2a*, *runx1* and *flt4* in ECs but there is a large amount of experimental work required before such data can be obtained.

2.4.1 Transgenic zebrafish lines

In order to identify cells in the embryo we use two transgenic zebrafish lines. The first is the *flk1:gfp* line which uses the endothelial specific promoter of the *flk1* gene to drive expression of green fluorescent protein (GFP) in endothelial cells (see Figure 2.20a).

The second zebrafish line is the Notch reporter, $12\times\text{CSL:mCherry}$, which consists of 12 CSL binding sites in front of a minimal promoter that drives expression of the red fluorescent protein, mCherry, in response to binding of the NICD-CSL complex in cells receiving a Notch signal. Figure 2.20(b) shows the expression pattern of the Notch reporter in the $12\times\text{CSL:Cerulean}$ line which has an identical expression pattern to the $12\times\text{CSL:mCherry}$ line except this line fluoresces in the blue cerulean protein instead of the red mCherry protein. A third Notch reporter line, also identical in expression level, is the $12\times\text{CSL:Venus}$ line shown in Figure 2.5.

Each fluorescent protein can only be detected after stimulation by the appropriate wavelength of light. Visualisation also requires a filter with an appropriate bandwidth to view the emitted wavelengths of light.

By crossing *flk1:gfp* fish with $12\times\text{CSL:mCherry}$ fish, double transgenic embryos which express both transgenes and hence both fluorescent proteins, are generated (see Figure 2.20(c)).

We aim to acquire ECs in which *runx1* will be expressed. These are located in the DA (arrow in Figure 2.20(a)) which has a higher *flk1:gfp* expression level than the PCV, thus making it appear more fluorescent.

2.4.2 Embryo dissociation and preparation of cell suspension

For each biological replicate, \mathcal{N} double transgenic *flk1:gfp*; $12\times\text{CSL:Cerulean}$ sections/embryos² are incubated in Liberase Blendzyme in $1\times$ Hanks Balanced Salt Solu-

²Using the trunk sections (without heads or tails) removes non-endothelial parts of the embryo which dilute the changes in the EC gene expression we are trying to detect

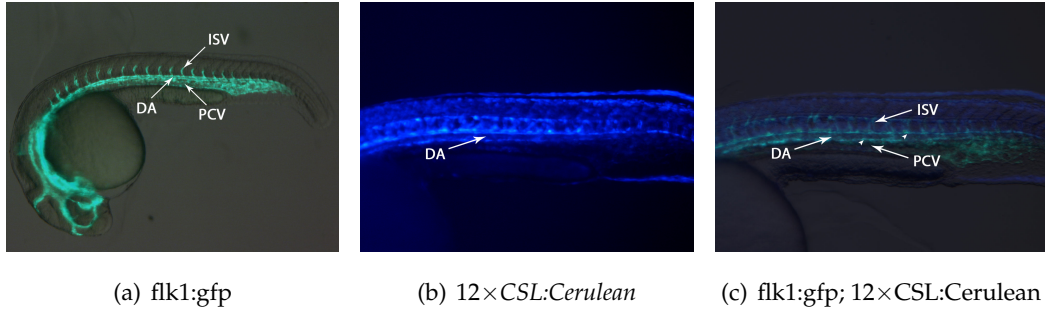


Figure 2.20: (a) Hybrid bright-field/dark-field image of a 24hpf *flk1:gfp* embryo shows *gfp* expression in ECs which comprise the trunk and head vasculature. The *gfp* expression is high in the DA and low in the PCV. We will take advantage of this to sort arterial ECs. Labelled: Dorsal Aorta - DA, Posterior Cardinal Vein - PCV, Intersomitic Vessel - ISV. (b) Notch reporter expression in the trunk: Cerulean expression marks cells receiving an active Notch signal. Arrow shows the DA which is Cerulean positive. (c) Double transgenic *flk1:gfp; 12×CSL:Cerulean* embryo. The DA expresses both GFP and Cerulean proteins. Arrowheads show the dorsolateral and ventral walls of the DA.

tion (HBSS) at 31 °C for 1 hour, where

$$\mathcal{N} \approx \begin{cases} 200 & \text{20hpf whole embryos} \\ 100 & \text{23 and 27hpf trunk sections} \end{cases} . \quad (2.4.1)$$

The embryos are dissociated by periodically macerating with a P1000 pipette whilst incubated in the Liberase Blendzyme. The resulting cell suspension is strained through a 40 μ m cell strainer and the cells are pelleted and washed three times by centrifugation in 5% fetal calf serum (FCS) in 0.9 \times phosphate buffered saline (PBS), at 1500 rpm for 5 mins. The final resuspension in 300 μ L of FCS/PBS is taken to the FAC sorter for cell sorting.

The same procedure is also repeated for 200 single transgenic *flk1:gfp* embryos, 200 single transgenic *12×CSL:mCherry* embryos and 200 wild type embryos which are not fluorescent. These are used as controls in the FAC sorting experiments described in the next section.

2.4.3 Fluorescence-activated cell sorting (FACS)

ECs are sorted using a FAC sorter as shown in Figure 2.21(a). We exploit the increased activity of the *flk1* promoter in the aortic endothelium which causes the DA to fluoresce at a higher level than the PCV. Using the control embryos we define cut-off points,

called *gates*, based on the background expression level of *gfp* and *mCherry* in control embryos. Gates define boundaries between gfp^{high} (assumed arterial) and gfp^{low} (assumed venous) cells. Cells identified as gfp^{high} are sorted into $350\mu L$ of extraction buffer.

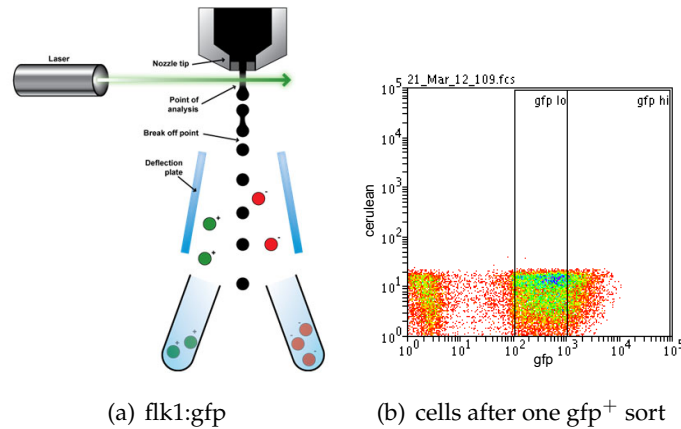


Figure 2.21: (a) A jet of liquid, to which the cell suspension is added, is ejected from a nozzle such that it splits into droplets, each containing a single cell from the suspension. A laser then examines each droplet. If the droplet contains a fluorescent cell, then the reflected light is analysed by a computer which applies an appropriate charge to the droplet. Charged deflection plates attract (or repel) the droplets into the appropriate collecting tubes. (Image in (a) from www.abcam.com) (b) A typical FACS plot in which the x and y axes represent *gfp* and cerulean fluorescence respectively. Cells in the gfp^{hi} region are identified as arterial ECs (although later we find that not all of these cells may be arterial) and are sorted for further downstream analysis (see §2.4.4). Cells from the gfp^{lo} region are identified as venous cells.

2.4.4 RNA extraction, cDNA synthesis and real-time qPCR

Using the RNeasy micro kit, the FAC-sorted gfp^{hi} cells are lysed and their messenger RNA (referred to as RNA) is extracted. During extraction, it is common for genomic DNA also to be carried over, resulting in an aqueous solution of RNA and some DNA. Therefore this solution is DNase treated to prevent contamination from genomic DNA at later stages of the procedure. During this step, the DNase enzyme digests and breaks down genomic DNA, removing it from the sample. Following DNase treatment, the assumed pure RNA is pelleted by centrifugation and resuspended in $14\mu L$ of nuclease-free H_2O . Approximately $2-3\mu L$ of this liquid is dead volume, leaving $10 - 12\mu L$ to be used in the reverse transcription step. Approximately $5\mu L$ is reverse transcribed to form double-stranded complementary DNA (cDNA). The remaining

5 μ L is used as a minus-RT control.³

cDNA is generated by placing solutions of individual nucleotides and RNA into a reverse transcription reaction with a reverse transcriptase enzyme. The enzyme adds complementary nucleotides to the RNA strand, converting it to a double-stranded cDNA molecule. The cDNA differs from double stranded, genomic DNA in that it only contains nucleotides comprising the exons of genes involved in processes further downstream such as translation into proteins. Genomic DNA, however, also contains nucleotides which code for introns. After transcription, introns are removed from the primary transcript in a process called splicing. Thus the cDNA obtained from a reverse transcription reaction is a double stranded representation of genes which are being actively transcribed.

The reverse transcription occurs in a 20 μ L reaction and both cDNA and minus-RT samples are diluted 1 in 3 to give a total volume of 60 μ L to be used as templates in qPCR reactions.

qPCR is the amplification of cDNA template in a three-step process inside a thermocycler which is able, rapidly, to heat (and cool) samples. Individual nucleotides, taq polymerase enzyme and short (approximately 20 base pair) specifically designed single stranded sequences called forward and reverse primers and a TaqMan probe are added to the reaction mixture (see 2.22a). The TaqMan probe has a fluorophore attached at one end and a quencher at the opposite end. The quencher prevents emission of fluorescence from the fluorophore whilst the two ends are in close proximity.

Step 1 is the denaturing or melting step. The temperature is raised to 94°C and the double stranded cDNA separates into two single strands (see Figure 2.22b). Step 2 is the annealing step and involves lowering the temperature to approximately 60°C so that the complementary taqman probe and forward and reverse primers can bind to their specific sequences (see Figure 2.22c). Step 3 is called elongation and involves increasing the temperature to approximately 70°C which is the optimum temperature for taq polymerase to extend the primers by successively adding the individual nucleotides (see Figure 2.22c). Elongation results in twice the number of cDNA molecules. During the elongation phase, the taq polymerase digests the taqman probe, which binds between the forward and reverse primers, releasing the fluorophore from the vicinity of the quencher. This allows the fluorescence to be detected by the thermocycler. These three steps constitute a cycle of amplification and are typically repeated 25-40 times.

The accumulation of fluorescence at each cycle, results in curves of fluorescence in-

³A minus-RT sample undergoes an identical reverse transcription reaction except the reverse transcriptase enzyme is replaced with H₂O

tensity vs cycle number such as those in Figure 2.23. The point at which the detected fluorescence is statistically significantly greater than the background fluorescence level, denoted *fluorescent threshold* in Figure 2.23, is called the cycle threshold value, C_t . The fluorescent threshold and C_t values are automatically calculated by the thermocycler's software. Initially, the cDNA template is limiting and the reagents are in excess, causing an exponential increase in fluorescence with cycle number. Once enough template has accumulated, the taq polymerase becomes saturated with template and the reaction enters the *linear phase* where the fluorescence increases proportionally to cycle number. After some time, the reagents, most likely the individual nucleotides, become used up and limiting and, hence, amplification stops, causing the fluorescence level to *plateau*.

Theoretically, different samples with the same fluorescence level contain the same number of molecules, thus the earlier a sample is detected on the plot, the greater the initial number of molecules and the smaller the C_t value.

The C_t value is inversely proportional to the inverse of the initial number of molecules, N_0 :

$$C_t \propto \frac{1}{\log_2 N_0} \quad (2.4.2)$$

$$\implies N_0 = \bar{k} 2^{-C_t}, \quad (2.4.3)$$

where \bar{k} is the number of molecules present after C_t cycles of amplification.

Figure 2.23 shows C_t values for samples identified on the basis of colour and each cDNA sample was derived by diluting the previous sample 1 in 2. Thus, assuming the red sample has concentration $a_0 \mu\text{g}/\mu\text{L}$, then the orange, lime green, green, cyan and indigo samples have concentrations given by $\frac{a_0}{2}$, $\frac{a_0}{4}$, $\frac{a_0}{8}$, $\frac{a_0}{16}$ and $\frac{a_0}{32} \mu\text{g}/\mu\text{L}$ respectively. Assuming the volume of each sample is the same, the number of molecules per sample is also half that of the previous sample in the sequence.

Suppose we want to find the ratio of initial copy numbers r_0 and o_0 of the red and orange samples which have C_t values given by C_{tr} and C_{to} respectively (see Figure 2.23), then from equation (2.4.3) it follows that

$$\frac{r_0}{o_0} = \frac{k_1 2^{-C_{tr}}}{k_2 2^{-C_{to}}}.$$

Since the number of molecules detected at the *fluorescence threshold* is theoretically the same, we must have $k_1 = k_2$. Thus the ratio of initial copy numbers is given by

$$\frac{r_0}{o_0} = 2^{C_{to}-C_{tr}} \equiv 2^{\Delta C_t}. \quad (2.4.4)$$

In 2.4.4, $C_{tr} - C_{to}$ is also known as the ΔC_t value. Figure 2.23 shows that $C_{to} - C_{tr} = 1$

(marked with *), and therefore

$$r_0 = 2o_0, \quad (2.4.5)$$

i.e. 1 in 2 dilutions correspond to a 1 cycle shift. It also follows that 1 in 4 dilutions result in a 2 cycle shift, etc (see ** in Figure 2.23 where $C_{tv} - C_{tm} = 2$). This is commonly referred to as the comparative ΔC_t method [107]. The qPCR data are analysed using the comparative CT method of [107] in Microsoft Excel.

The experimental procedures described here were carried out by myself in the Gering lab. In the next section, we demonstrate how a simple ODE model can be fitted to the ΔC_t values obtained from qPCR experiments.

2.5 Parameter estimation in a model for *efnb2a* and *runx1* activation by Notch signalling

In this section we fit our model to experimental qPCR data generated using the methods described above. We identify those parameter values which minimise the error between the experimental data from qPCR experiments and the output from the ODE model. In equations (2.2.4) we assume that the NICD input initiates at $t = 17$ hpf thereafter increases linearly over time so that

$$Ni(t) = C_n(t - 17)H(t - 17). \quad (2.5.1)$$

The parameters to be fitted are c_2, c_4, \hat{c}_6 and C_n , where C_n is the rate at which the NICD input signal increases.

The experimental data are presented in the form of ΔC_t values, as described above (see Table 2.5). They are the differences between C_t values for *flt4*, *runx1*, *efnb2a* and the housekeeping gene *ef1- α* .

Equation (2.4.4) shows that exponentiating the negative ΔC_t values converts them to concentrations relative to a particular gene, which in our case is the housekeeping gene, *ef1 α* that has a constitutive and constant expression pattern over the time course for which we have. We average the ΔC_t values at each time point and transform the data to give relative concentrations (see Table 2.6).

The data shows a temporal increase in the *flt4* gene expression which does not agree with the in-situ hybridisation experiments in [50, 54, 56]. Possible reasons for this discrepancy are discussed at the end of this chapter. Currently, we ignore the *flt4* experimental data and focus on fitting to the *efnb2a* and *runx1* data only.

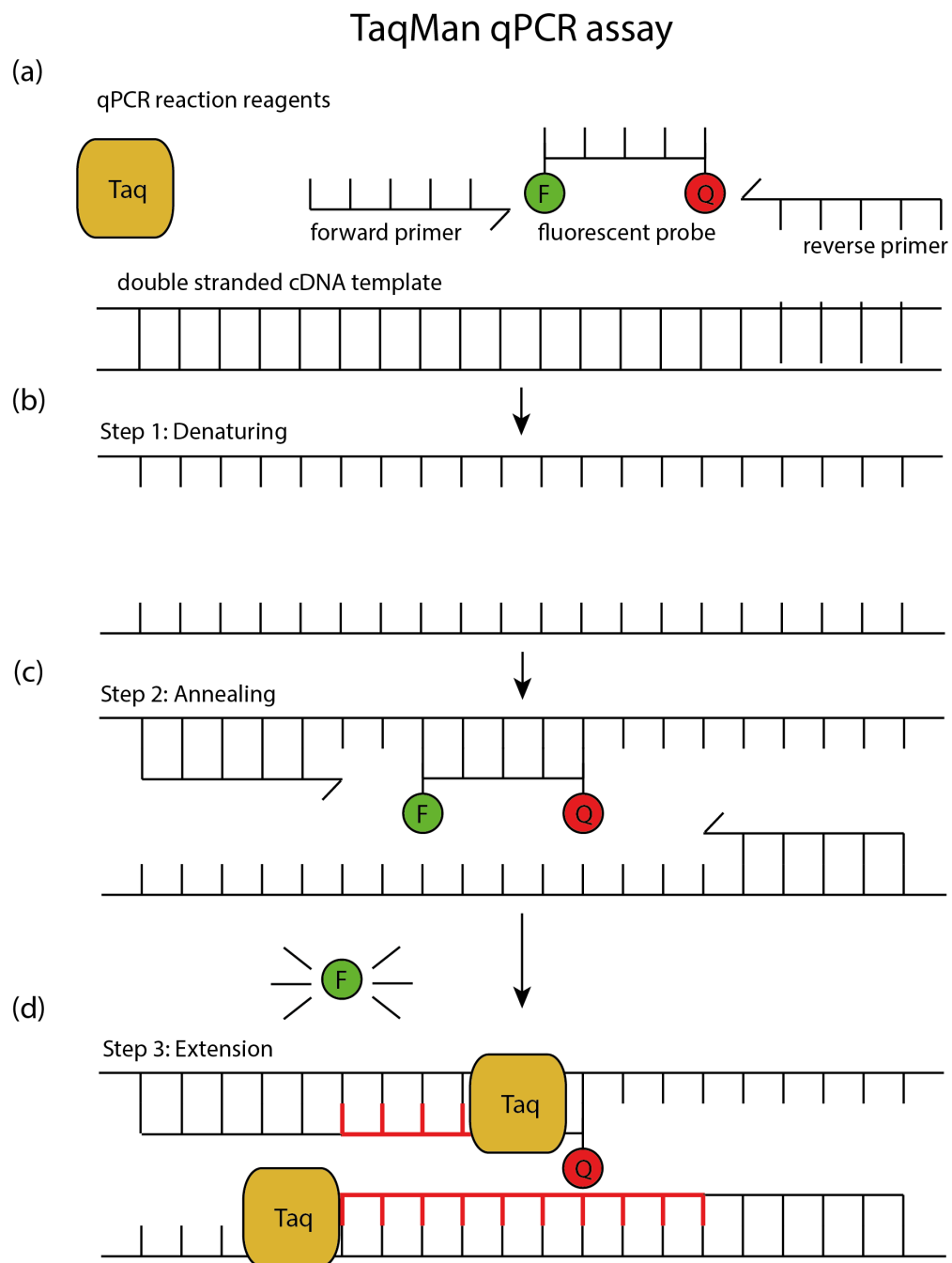


Figure 2.22: Figure showing the 3 steps of the TaqMan qPCR assay, as described in §2.4.4 of the text.

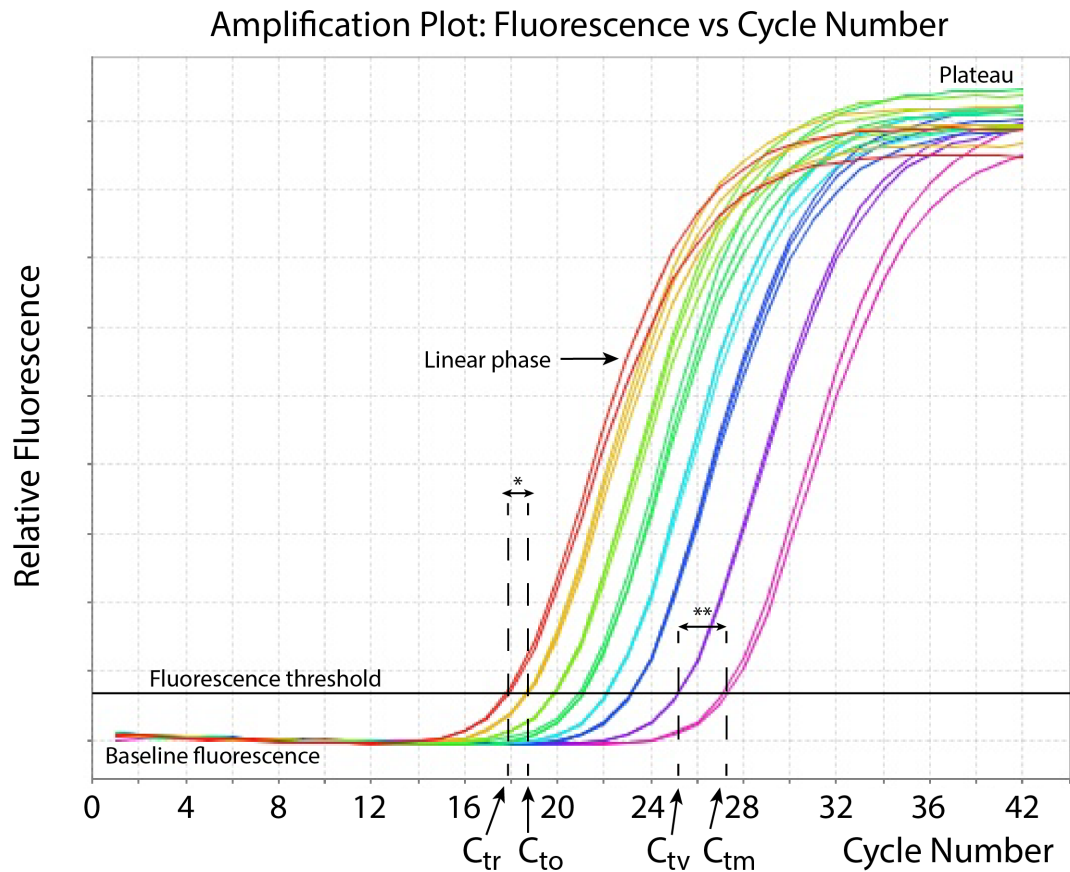


Figure 2.23: qPCR amplification plot of relative fluorescence vs cycle number for a dilution series of cDNA samples named after their colour. Each of the coloured curves correspond to cDNA samples obtained by sequentially diluting the red sample 1 in 2. For instance, let us assume the sample corresponding to the red curve has concentration $a_0 \mu\text{g}/\mu\text{L}$, then the orange, lime green, green, cyan and indigo curves have concentrations $\frac{a_0}{2}$, $\frac{a_0}{4}$, $\frac{a_0}{8}$, $\frac{a_0}{16}$ and $\frac{a_0}{32} \mu\text{g}/\mu\text{L}$ respectively. The violet and magenta samples were obtained by sequentially diluting the indigo sample 1 in 4. Thus 1 in 2 dilutions correspond to a 1 cycle change in C_t value and 1 in 4 dilutions correspond to a 2 cycle change (see equation 2.4.4).

Time point (hpf)	flt4	runx1	efnb2a
20	4.7575	11.1749	8.3005
20	5.0920	12.1763	8.5105
20	6.1923	11.3020	8.7884
23	4.0893	11.0295	7.4586
27	3.2540	10.4049	7.5120
27	3.1053	9.0639	7.5137

Table 2.5: ΔC_t values generated from qPCR experiments where. $\Delta C_t^i = C_t^i - C_t^{\text{efl}\alpha}$ and $i = \text{flt4}, \text{runx1}$ and efnb2a . There are three biological replicates at 20hpf, one replicate at 23hpf and two at 27hpf.

Time point (hpf)	flt4	runx1	efnb2a
20	0.024565	0.00033326	0.0026994
23	0.058749	0.00047840	0.0056851
27	0.11036	0.0011739	0.0054719

Table 2.6: $2^{-\Delta C_t}$ values generated for flt4, runx1 and efnb2a by using equation (2.4.4) and exponentiating the values in Table 2.5. Runx1 and efnb2a data both increase over time. Efnb2a data decrease slightly at the last time point. The increase in efnb2a data is initially large and then appears to saturate whereas runx1 data is initially low and increases quickly after 23hpf suggesting that efnb2a data reach high levels relatively quickly, compared to runx1. In contrast to other experimental results, flt4 data also increase over time, suggesting that FAC sorting cells using the flk1:gfp zebrafish line is not sufficient to reliably sort arterial ECs based on high gfp expression.

We note that the mRNA concentrations in (2.2.4) are scaled on the ratio of the maximal production rate to the mRNA decay rate. The experimental data, however, still has some scale. In other words, they are not measured relative to a reference value. Therefore, for each gene, we divide each data point by the largest data point and fit the ODE model parameters to this *normalised* data using a least squares approach. This is done using the *fmincon* function in MATLAB. The function to be minimised is

$$J(X_i^{\text{data}}, X_i^{\text{model}}) = \sum_{j=1}^M \sum_{i=1}^N w_{ij} \left(X_i^{\text{data}} - X_i^{\text{model}} \right)_j^2 \quad (2.5.2)$$

where $M = 2$ is the number of genes (efnb2a and runx1) and $N = 3$ is the number of data points (20,23,27hpf), subject to the constraints $c_2, c_4, \hat{c}_6, C_n > 0$. Figure 2.24 shows the lowest 80% of the optimal fits obtained for these four parameters using 400 random initial guesses, and also the top 15 of these which have the shortest minimised distance.

The fits show that the initial gradient of efnb2a is steeper than that of runx1 implying that efnb2a responds slightly faster to the Notch input signal than runx1. However the data points for runx1 at 20 and 23hpf are somewhat lower than the data point at 27hpf suggesting that fitting a sigmoid response function for runx1 to gata2 or gata2 to NICD may be more appropriate.

We note that our model assumes no basal transcription for gata2, efnb2a or runx1. Therefore their concentrations are always zero until Notch activation at 17hpf. The data suggest that there may be a baseline level of expression before Notch activation: by including this we will likely obtain better fits.

2.6 Conclusions and further work

The aim of this chapter was to increase our understanding of how Notch signalling controls arterial specification and HSC specification by using a combination of mathematical modelling and experimental data and observations. We began by presenting experimental evidence from the literature which supports the hypothesis that Notch signalling is needed twice during embryonic development: once, at low levels, to specify the arterial identity of ECs of the DA and later, at higher levels, to specify HSC identity. Arterial and HSC specification are characterised by the expression of efnb2a and runx1, respectively, in the embryo.

To test how different levels of NICD may influence the expression of efnb2a and runx1, we developed three ODE models, which can be applied to either a single cell or a homogeneous population of cells. In each model, efnb2a is a direct target of Notch signalling,

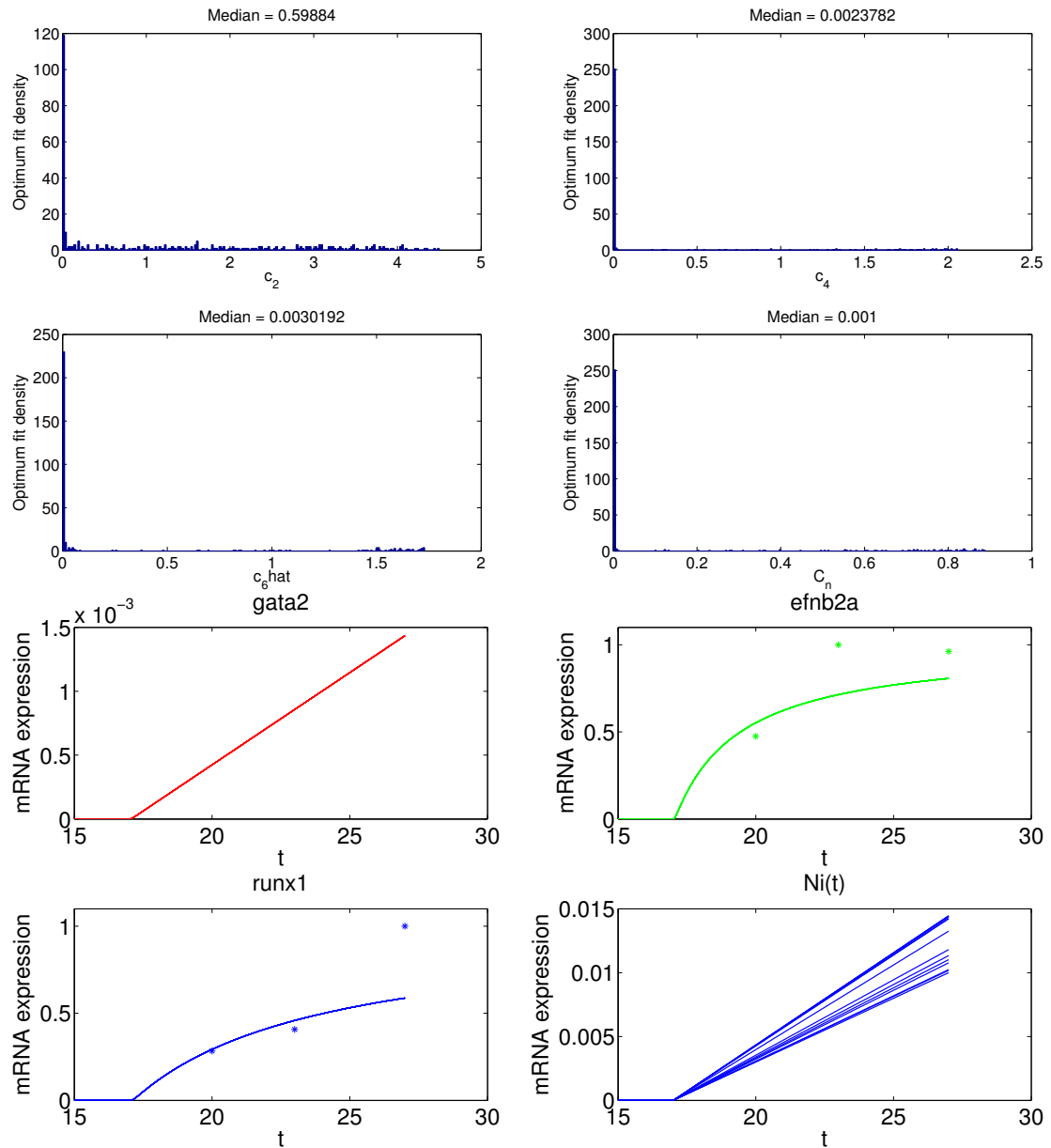


Figure 2.24: The upper 4 plots show histograms of the lowest 80% of optimally fitted parameter values for each of c_2, c_4, \hat{c}_6, C_n . Each plot is obtained by minimising the cost function in equation (2.5.2) 400 times, starting with a random initial guess. This was implemented using the *fmincon* function in MATLAB. The fits are sorted in ascending order (best fit to worst fit) and the ODE model solutions for the top 15 fits which have the smallest minimised errors are plotted in the lower 4 plots. We also note that the data for *flt4* have not been fitted here due to inconsistencies with previous experimental evidence.

as is the gene *gata2*, which in turn drives expression of *runx1*. These interactions are supported by evidence from experimental data in zebrafish, mouse and human endothelial cell lines [24, 34, 35]. For each ODE model, we considered dose responses of *efnb2a* and *runx1* to NICD and *runx1* to *gata2*. We also considered the behaviour of quasi-steady solutions for *efnb2a*, *gata2* and *runx1* and the full time-dependent system of ODEs, which are driven by a prescribed linearly increasing signal of NICD: $Ni(t) = t$.

In the first model, we considered the system of ODEs in equations (2.2.4) which used Michaelis-Menten kinetics, derived from Shea-Ackers type expressions, for transcriptional regulation. We demonstrated that, by satisfying the conditions associated with the half-maximal concentration parameters for *runx1* and *efnb2a*, *runx1* could be made to respond more slowly to the NICD input than *efnb2a*, in our model. For the linearly increasing Notch input, $Ni(t) = t$, high levels of Notch induced *runx1* mRNA expression at later times and low levels induced *efnb2a* expression at earlier times. The model predicted that *gata2*'s sensitivity to NICD was more important *runx1*'s sensitivity to *gata2* in determining the delay in *runx1* induction relative to *efnb2a*. This result is not entirely obvious as one would assume that *runx1*'s sensitivity to *gata2* is equally as important as *gata2*'s sensitivity to NICD. Further experimental work in zebrafish may need to investigate the role of *gata2* more closely in induction of *runx1* expression downstream of Notch.

In the second model (equations (2.2.4)), we also used Michaelis-Menten kinetics for transcription, however, *runx1* was modelled using a sigmoidal, Hill function type response to *gata2*. Similar conditions were derived as in the previous model to achieve a delayed *runx1* response to Notch, relative to *efnb2a*. For the same parameter values, this model achieves a larger transcriptional delay as the initial gradient of the response curve is shallower for Hill functions with Hill coefficients > 1 than for those with Hill coefficients equal to 1.

The third model assumed a sigmoidal response of *gata2* to NICD with the remaining responses as per the first model. For the same parameter values, the *runx1* delay in this model is longer than the delay from the first model and slightly shorter than the delay from the second model.

We also investigated the role of cell coupling on the downstream responses. Figure 2.6 indicates the presence of several feedback loops. We chose to model the feedback loop in which the VEGF receptors *flk1* and *flt4* activate Delta and Notch signalling without explicitly incorporating the binding processes into the model. Instead of NICD repressing *flk1* and *flt4*, which in turn are responsible for activating Delta and Notch

production, we introduce Delta and Notch binding in a two-cell system in which the production rate of Delta is a decreasing function of NICD and a temporally increasing, saturating function of extracellular VEGF. We show that this model exhibits salt and pepper patterns in which alternate cells express high and low levels of NICD leading to high and low levels of *efnb2a* and *runx1*.

Using parameter values from the literature (see Table 2.3), we varied the parameters whilst keeping them at the same order of magnitude to see if the lateral inhibition driven patterning mechanism of the model could recapitulate the gene expression seen in fluorescent in-situ data whereby *efnb2a* expression is homogeneously specified in all cells of the DA but *runx1* expression is only seen in a subset of cells (see Figure 1.4). A key difference between the model behaviour and the in-situ hybridisation is that the in-situ data does not show salt-and-pepper patterning for *runx1* expression. For the realistic parameter values used here, the solutions for *runx1* bifurcated symmetrically from a large value of *runx1* (see Figure 2.16). This meant that the pattern was unable to amplify the average mRNA concentration relative to the homogeneous steady state. Using a less physically realistic parameter set (see Table 2.4), *runx1* bifurcated asymmetrically and, as such, the pattern was able to contribute to an increase in the average level of *runx1* (see Figure 2.19). The latter parameter set also allowed induction of *efnb2a* before *runx1*.

The two-cell models considered here exhibit patterning driven by the lateral inhibition mechanism. We have assumed this to be mediated by VEGF–VEGF receptor binding although this is not explicitly included in our model (see Figure 2.15). Including VEGF–VEGF receptor interactions into the current model is another potential avenue for future work as the binding kinetics can generate their own interesting dynamics. These dynamics are explored more extensively, in the context of tip cell selection in Chapters 3 and 4.

Details of the experimental techniques used to acquire the mRNA from arterial ECs were also presented, followed by a detailed description of qPCR and the numerical output that it generated.

Lastly we fitted the parameters of the first model to qPCR data. In analysing the data we noticed that, contrary to in-situ hybridisation data from the literature [50, 54, 56], the *flt4* concentration was increasing in the DA EC population from 20 to 27hpf (see Table 2.6). Initially we sorted *gfp*⁺ cells from whole embryos and found that the increase in *flt4* expression was very large from 20-27hpf. We assumed that RNA from non-specific tissues may have been interfering with or overriding the expression from the DA, especially since there are many *gfp*⁺ cells in the head vasculature (see Figure

2.20a), which would have been sorted as gfp^{high} cells. Therefore we decided to remove the head region and the tail region of the embryo, as neither contribute to the central trunk region in which HSCs are specified. We managed to reduce the temporal increase in *flt4* but we never obtained qPCR data showing the temporal downregulation of *flt4* in the gfp^{high} cells.

One possible explanation is the presence of gfp^{high} cells in the PCV which are venous in identity. Herbert and colleagues argue that the PCV is formed as a result of selective sprouting of DA ECs. In this process, DA ECs leave the vessel from 21-24 hpf and migrate ventrally to contribute to the formation of the adjacent PCV [29]. However the authors do not specify the number of cells involved in ventral sprouting or the relative contribution of their proposed mechanism to the formation of the PCV. If this mechanism were to contribute a significant number of cells to the PCV then these cells would remain gfp^{high} in our transgenic *flk1:gfp* embryos because the *gfp* protein is relatively stable. Since these cells would have switched off arterial markers and switched on venous markers, *flt4* would not be downregulated in them. If this were the case, we could be misidentifying venous gfp^{high} ECs as arterial ECs, and we would need to rely on a transgene other than *flk1:gfp* to identify and sort the arterial ECs.

The *efnb2a* and *runx1* data, however, appeared to be increasing in the expected way. We fitted the model to their data points and the fits looked as expected. The *runx1* fit would likely be better if we modelled *runx1* or *gata2* using the sigmoidal responses of our second and third models, albeit a more phenomenological choice, rather than using a Michaelis-Menten type expression. Thus we propose that fitting this model to the data be left for future work. We also note that at 20hpf, the expression of both *runx1* and *efnb2a* is not zero. As such, other future work could involve incorporating basal transcription into these models and fitting them to the data.

Our experimental data was limited in terms of the number of time points and the number of replicates performed at each time point. Each experiment required us to grow approximately 800 embryos, including embryos used for fluorescent colour controls, to the age of 20, 23 or 27 hpf. We found it difficult to keep all 800 of these embryos growing at the same rate as embryo growth was sensitive to changes in temperature. This meant that, in a sample of 200 embryos, there were slight differences in the ages of individual embryos. Hence the experimental time points needed to be kept sufficiently apart or one sample, for example the 23hpf sample, may have contained embryos which fell into the category of another time point, the 20hpf sample for instance. Future modelling work may also need to take into account the variability in the time point being measured.

Lastly, the number of replicates is low because the FACS facility was not always available for us to use. There was the possibility of sorting our samples at another institution, for example, but this would bring about other complications such as transport of cell samples and cell viability.

An Ordinary Differential Equation Model of VEGF–Delta–Notch Signalling in Angiogenic Tip Cell Selection

3.1 Introduction

Angiogenesis is the outgrowth of new blood vessels from existing vessels and involves the processes of capillary sprouting, endothelial cell (EC) proliferation and vessel remodelling [23]. It is essential in reproduction, development and wound repair [39, 108, 109] and also plays a key role in tumour growth and metastasis [7, 23]. Angiogenesis proceeds when ECs respond to chemoattractants such as epidermal growth factor, fibroblast growth factor and transforming growth factor families. The best characterised chemoattractant is VEGF-A which is a member of the vascular endothelial growth factor (VEGF) family of growth factors. VEGF-A stimulates sprouting of tip cells from the parent vessel which lead the angiogenic sprout, migrating via chemotaxis, towards the source of growth factor. Tip cells further respond by extending long, thin extensions of the cell membrane called filopodia which locate areas of higher VEGF concentrations, allowing rapid capillary growth up spatial gradients of VEGF. [23, 110, 111]. We explore filopodia dynamics in more detail in the next chapter.

This work develops a simple ODE model of the first stage of angiogenesis, during which tip cells are selected from ECs lining existing blood vessels.

During the earliest stages of angiogenesis, before sprouting, in addition to responding

to VEGF, individual ECs are also regulated by interactions with neighbouring cells. In particular, differential selection for the tip cell fate is controlled by the interaction of Notch receptors with Delta ligands on adjacent ECs. Experimental observations reinforce the importance of VEGF and Notch pathway ligands and receptors in angiogenesis. In particular, knockout mice with a homozygous deletion for the genes encoding VEGF-A or any of the 3 mammalian VEGF receptors display embryonic lethality due to vascular malformations as do mice with a heterozygous deletion of VEGF-A [112]. Similarly, deletion of the Notch receptors, Notch1 and Notch4, is lethal as is, the heterozygous deletion of the Notch ligand Delta-like 4 (Dll4). These mice die due to vascular remodelling defects and arteriovenous malformations [11, 26, 113].

The key interactions between the VEGF and Notch signalling pathways during tip cell selection, can be summarised in two steps: (1) VEGF binds and activates its receptor, VEGFR-2, leading to up-regulation of Dll4; (2) Dll4 binds and activates Notch receptors on neighbouring cells to down-regulate VEGFR-2 expression in those cells. [9, 47, 49, 62, 109]. The resulting Delta-Notch lateral inhibition feedback generates a spatial pattern of cells where alternating cells are selected for different fates: a “salt and pepper” pattern of tip cells separated by one or two stalk cells [81, 109].

We here develop a system of ODEs which exhibits this feedback and subsequent patterning and accounts for similar outcomes as those modelled by Bentley et al. in their agent-based simulations [81]. Their model, which is defined on a 3D lattice, simulates a ten EC-long capillary whose cells can extend and retract filopodia. The filopodia and cells both contain VEGF receptors which can bind to VEGF in the surrounding environment and each cell communicates to its neighbours via Delta-Notch signalling. The model exhibits salt-and-pepper patterns and hypothesises phenomena such as oscillations between the tip and stalk cell fate in high VEGF environments. The authors assess the tip cell phenotype, pattern formation and pattern stability by scoring the system post-simulation. Being an agent based model, it is not amenable to much mathematical analysis. Such models lack the rigorous analytical tools that differential equation models have available to them, especially those from dynamical systems theory such as bifurcation analysis and linear stability analysis. These techniques are invaluable for understanding the mechanisms by which pattern formation occurs and in this chapter they are used to characterise the existence and stability of the model’s steady states.

In § 3 we consider a simple model of VEGF - Delta - Notch interactions while neglecting the growth of filopodia. By first examining a system of 2-cells in a spatially homogeneous distribution of VEGF, we show that if the feedback strengths for the activation of Delta and inhibition of VEGF Receptor-2 (VEGFR-2) are sufficiently strong then the

cells can enter a heterogeneous steady state where one cell has higher levels of bound VEGFR-2 and Dll4 and lower levels of bound Notch receptors, corresponding to the tip cell fate and the other cell has lower levels of VEGFR-2 and Dll4 but a high level of bound Notch, corresponding to the stalk cell fate. By performing numerical bifurcation analysis using xppaut, we show that a heterogeneous steady state will not occur if the level of extracellular VEGF ligand is either too high or low.

In §3.5, for purposes of tractability, we assume a quasi-steady state for bound VEGFR-2 and carry out linear stability analysis on this system to find its steady state bifurcations. This allows us to determine the growth rate of different perturbations and hence to identify any patterning modes. We use the Routh-Hurwitz stability criteria to define conditions which must hold for the model to exhibit the period-2, “salt and pepper” pattern and show that is the dominant unstable mode. We also identify regions of parameter space, corresponding to the strengths of Dll4 and VEGFR-2 production, in which the system admits the “salt-and-pepper” steady states. Linear stability analysis is then used to characterise their local stability.

3.2 Model overview

We consider a string of N endothelial cells (ECs) signalling via the VEGF–Delta–Notch system and with negligible filopodia growth (Figure 3.1). VEGF is assumed to be secreted by nearby tissues which may include hypoxic cells in the case of a tumour, macrophages in wound healing or somite cells during zebrafish development. We assume that the VEGF level is not depleted and that VEGF receptors (VEGFR-2) are uniformly distributed over the cell membranes. Any delays between VEGF binding to VEGFR-2 and production of Dll4 (Delta); between production of Dll4 and binding to a Notch receptor of an adjacent cell; between Delta–Notch binding and the down regulation of VEGFR-2 are ignored, as are recovery delays representing the time before gene expression returns to normal [81].

Denoting the j th EC in the string of cells by $j \in 1, 2, \dots, N$ the binding and unbinding reactions for VEGF with VEGFR-2 and Delta with Notch are the following



where

- V represents the concentration of extracellular VEGF molecules adjacent to the upper surface of the ECs,

- R_{Uj} – the concentration of unbound VEGFR-2 molecules on the surface of cell j ,
- R_{Bj} – the concentration of bound VEGFR-2 molecules on the surface of cell j ,
- Δ_j – the concentration of Dll4 ligand molecules on the surface of cell j ,
- N_j – the concentration of unbound Notch receptor molecules on the surface of cell j ,
- B_j – the concentration of bound Delta-Notch receptor complexes on the surface of cell j .

VEGF can also bind VEGF Receptor-1 (VEGFR-1) and its soluble form sFlt1, a “scavenger” receptor which sequesters VEGF and hence reduces signalling via VEGFR-2 [58]. By interpreting V as the number of VEGF molecules available to VEGFR-2 after VEGFR-1 binding has taken place, that is, $V = V_{\text{sink}} V_{\text{total}}$ where V_{total} is the total number of VEGF molecules and V_{sink} is the proportion of V_{total} left for VEGFR-2 binding [81], we decide to neglect explicit binding of VEGFR-1.

Reactions (3.2.1) and (3.2.2) and their interactions are illustrated in Figure 3.1 for a pair of adjacent cells.

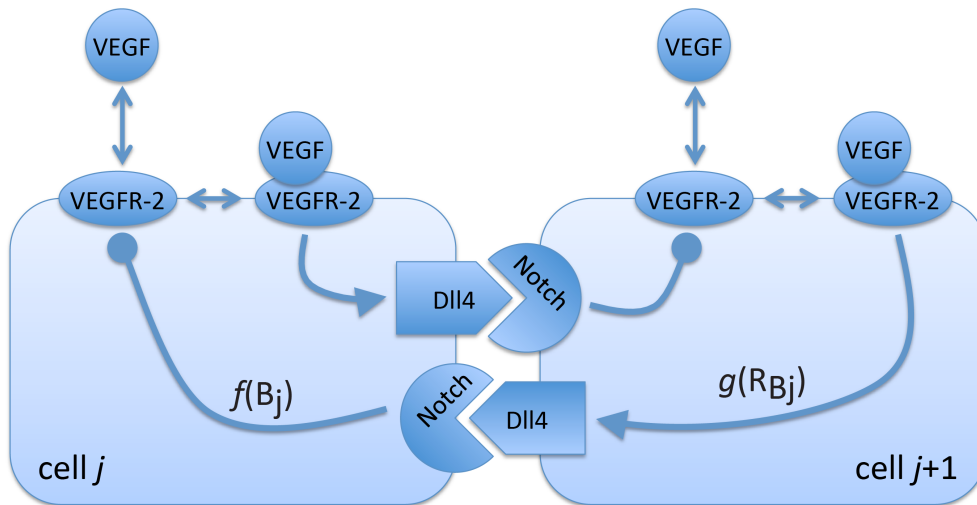


Figure 3.1: A self-made cartoon of the VEGF - Delta - Notch feedback loop in a string of N cells (shown for $N = 2$). VEGF binding to VEGFR-2 induces Dll4 expression, which in turn binds to Notch receptors on adjacent cells, suppressing VEGFR-2 expression. Interactions between Delta and Notch on the same cell or from bound VEGFR-2 onto Notch receptors is neglected for simplicity.

In this model cell j may interact with cells, $j \pm 1$ so that, for example, in reaction (3.2.2),

the Delta molecules from cells $j \pm 1$ interact with the Notch molecules from cell j . For simplicity we assume that Notch receptors on cell j cannot be bound and activated by Delta ligands on the same cell as is the case in other models [74]. We model the VEGF - VEGFR-2 and Delta - Notch binding processes in reactions (3.2.1) and (3.2.2) using the law of mass action. The activation of Dll4 by bound VEGFR-2 and the inhibition of VEGFR-2 by bound Notch receptor complexes constitute two types of feedback in the model and define the rates of production for Dll4 and VEGFR-2 which we model using the functions g and f respectively. We also assume that Dll4 and unbound VEGFR-2 are linearly degraded. No production or decay is assumed for Notch receptors and hence they are conserved in the model.

Using these principles, the following system of ODEs is used to describe the concentrations of ligands/receptors in cell j :

$$\frac{dR_{Uj}}{dt} = \underbrace{f(B_j)}_{\text{down-regulation of VEGFR-2}} + k_{-VR}R_{Bj} - k_{VR}VR_{Uj} - \underbrace{\lambda R_{Uj}}_{\text{internalisation}}, \quad (3.2.3)$$

$$\frac{dR_{Bj}}{dt} = k_{VR}VR_{Uj} - k_{-VR}R_{Bj}, \quad (3.2.4)$$

$$\frac{d\Delta_j}{dt} = \underbrace{g(R_{Bj})}_{\text{increase in Dll4 production}} + k_{-B} \left(\frac{B_{j-1} + B_{j+1}}{2} \right) - k_B \Delta_j \left(\frac{N_{j-1} + N_{j+1}}{2} \right) - \underbrace{\mu \Delta_j}_{\text{decay}}, \quad (3.2.5)$$

$$\frac{dN_j}{dt} = k_{-B}B_j - k_B \left(\frac{\Delta_{j-1} + \Delta_{j+1}}{2} \right) N_j, \quad (3.2.6)$$

$$\frac{dB_j}{dt} = k_B \left(\frac{\Delta_{j-1} + \Delta_{j+1}}{2} \right) N_j - k_{-B}B_j. \quad (3.2.7)$$

The total concentration of Notch receptors is denoted by N_{tot} . We assume a fixed cell volume so that the concentration, N_{tot} , is proportional to the number of Notch receptors. Thus N_{tot} is given by the sum of bound and unbound receptor concentrations at any given point in time. Initial and boundary conditions used in numerical simulations are given in §3.2.1.

We choose f to be a positive, monotonically decreasing function of bound Notch receptors representing its down-regulation of VEGFR-2 and we choose g to be a positive, monotonically increasing function of bound VEGFR-2, representing its activation of Dll4. In our numerical simulations, we use the following functional forms for $f(\cdot)$ and $g(\cdot)$:

$$f(x) = \frac{R_{U0}}{1 + (x/b)^m} \quad \text{and} \quad g(x) = g_{max} \frac{x^n}{x^n + a^n}. \quad (3.2.8)$$

In (3.2.8) the parameters R_{U0} and g_{max} are the maximal production rates of VEGF receptor and Dll4 respectively; b and a are the concentrations of bound Notch and bound VEGF receptor at which the production rates of VEGF receptor and Dll4 are at half of their maximal values, R_{U0} and g_{max} ; and m and n are the associated Hill coefficients controlling the sharpness of the switching action of f and g respectively. Thus $\lim_{m \rightarrow \infty} f(x) = 1 - H(x - \beta)$ and $\lim_{n \rightarrow \infty} g(x) = H(x - \alpha)$ where $H(x)$ is the Heaviside step function defined by

$$H(x) = \begin{cases} 0 & \text{if } x < 0 \\ \frac{1}{2} & \text{if } x = 0 \\ 1 & \text{if } x > 0 \end{cases} . \quad (3.2.9)$$

To facilitate the subsequent analysis, the variables are scaled using typical concentration values that they exhibit, for example, the concentrations of Dll4 and Notch receptors are scaled with the total concentration of Notch receptors; VEGF receptors are scaled with the ratio of their maximal production rate to their dissociation rate; and time is scaled with the inverse of the dissociation rate for VEGF-VEGFR-2 binding. Thus equations (3.2.3)-(3.2.7) have the following non-dimensional forms:

$$\frac{dr_{Uj}}{dt} = f(b_j) + r_{Bj} - V^*r_{Uj} - \lambda r_{Uj}, \quad (3.2.10)$$

$$\frac{dr_{Bj}}{dt} = V^*r_{Uj} - r_{Bj}, \quad (3.2.11)$$

$$\frac{d\delta_j}{dt} = g_{max}g(r_{Bj}) + k_{-B} \left(\frac{b_{j-1} + b_{j+1}}{2} \right) - k_B \left(\frac{n_{j-1} + n_{j+1}}{2} \right) \delta_j - \mu \delta_j, \quad (3.2.12)$$

$$\frac{db_j}{dt} = k_B \left(\frac{\delta_{j-1} + \delta_{j+1}}{2} \right) n_j - k_{-B} b_j, \quad (3.2.13)$$

$$n_j = 1 - b_j. \quad (3.2.14)$$

For a full derivation of the dimensionless system (3.2.10) - (3.2.14), including relevant scalings for the Hill functions, f and g , see Appendix A.

3.2.1 Initial and boundary conditions used in numerical simulations

For numerical simulations of equations (3.2.10) - (3.2.14), we use initial conditions close to the homogeneous steady state which are equivalent to perturbing the homogeneous steady state. Perturbations are either homogeneous (spatially uniform) where all solutions start at the same small distance from the steady state or heterogeneous where a small, randomly generated number is added to each steady state variable. The boundary conditions are periodic such that cell $j = N$ has neighbours $j = N - 1$ and $j = 1$ and cell $j = 1$ has neighbours $j = 2$ and $j = N$. The specific forms used for $f(\cdot)$ and

$g(\cdot)$ in numerical simulations are as per (3.2.8). In most cases we refer to and observe the solutions of a two-cell system in which we numerically integrate (3.2.10)-(3.2.14) for $j = 1, 2$ and periodic boundary conditions that identify $j = 0 = 2$ and $j = 1 = 3$.

3.3 Homogeneous and period-two steady states

We set the left hand side of equations (3.2.10)-(3.2.13) to zero and find homogeneous steady state solutions for which all cells express the same concentration of ligands and receptors, and period-two spatially patterned (salt-and pepper) steady states where alternate cells express the same levels of ligands and receptors. At the homogeneous steady state we have that

$$u_j = u_e \quad \forall j, \quad \text{where} \quad u_j = r_{Uj}, r_{Bj}, \delta_j, n_j, b_j.$$

With $\frac{d}{dt} = 0$, equation (3.2.10) + (3.2.11) gives

$$r_{Ue} = \frac{1}{\lambda} f(b_e),$$

which on substitution into (3.2.11) gives

$$r_{Be} = \frac{V^*}{\lambda} f(b_e). \quad (3.3.1)$$

With $\frac{d}{dt} = 0$, substitution of n_e from (3.2.14) into (3.2.13) gives

$$\delta_e = \frac{k_{-B} b_e}{k_B (1 - b_e)}. \quad (3.3.2)$$

Substituting (3.3.1) and (3.3.2) into (3.2.12) + (3.2.13), with $\frac{d}{dt} = 0$, gives

$$g_{max} g \left(\frac{V^*}{\lambda} f(b_e) \right) = \frac{\mu k_{-B} b_e}{k_B (1 - b_e)}, \quad (3.3.3)$$

or equivalently $b_e = h(b_e)$, where

$$h(x) = \frac{\hat{g}_{max} g(\hat{V} f(x))}{1 + \hat{g}_{max} g(\hat{V} f(x))}, \quad (3.3.4)$$

with $\hat{g}_{max} = \frac{g_{max} k_B}{\mu k_{-B}}$ and $\hat{V} = \frac{V^*}{\lambda}$.

For period-2 patterning solutions in strings of even numbered cells with periodic boundary conditions we have $u_{j-1} = u_{j+1}, \forall j$ which allows us to combine the concentrations of variables in adjacent cells together into a single variable:

$$u_{j-1} = u_{j+1} = u_{j\pm 1} \quad \text{for} \quad u_j = r_{Uj}, r_{Bj}, \delta_j, n_j, b_j. \quad (3.3.5)$$

We then solve for $b_{j\pm 1}$ in terms of b_j , in the same way as above, to give

$$b_{j\pm 1} = h(b_j). \quad (3.3.6)$$

Thus the concentration of bound Notch in neighbouring cells can be expressed as a function, $h(\cdot)$, of the concentration in cell j . Applying h to both sides of (3.3.6) allows us to find period-2 patterning solutions:

$$b_{j\pm 2} = h(b_{j\pm 1}) = h \circ h(b_j) = b_j. \quad (3.3.7)$$

In summary, for the system of equations in (3.2.10)-(3.2.14), the fixed points of $h(\cdot)$ determine the spatially homogeneous steady states and the fixed points of $h \circ h(\cdot)$ determine the period-2 patterning steady states. Since the fixed points of $h \circ h(\cdot)$ also include the fixed points of $h(\cdot)$, period-2 solutions, in particular, are fixed points of $h \circ h(\cdot)$ but not of $h(\cdot)$.

When $f(x)$ and $g(x)$ are positive, monotonically decreasing and increasing functions respectively, (see (3.2.8)), $h(x)$ is positive and monotonically decreasing with a unique fixed point (and hence a unique homogeneous steady state) $x_0 \in [0, h(0)]$ whereas $h \circ h(x)$ is positive and monotonically increasing on this interval. Originally, Collier and colleagues found a similar result where a composition of their production functions for Delta and Notch activity, $fg(\cdot)$, determined steady state levels in neighbouring cells [67]. This function is analogous to our decreasing function $h(\cdot)$ (see 3.3.4) which is also a composition of increasing and decreasing production functions, albeit for Dll4 and VEGFR-2 production.

In general patterning requires

$$h'(b_e) < -1, \quad (3.3.8)$$

where $b_e = x_0$ is the homogeneous steady state value for bound Notch and $h(\cdot)$ is the function defined in (3.3.4). This is because

$$(h \circ h)'(b_e) = h'(h(b_e))h'(b_e) = h'(b_e)^2, \quad (3.3.9)$$

where $'$ denotes differentiation. When condition (3.3.8) holds, $(h \circ h)'(b_e) > 1$. Consequently $h \circ h(x)$ has two distinct fixed points (not fixed points of $h(x)$) corresponding to period-2 patterns. The slope at the fixed point, $h'(b_e)$, can be changed by manipulating the parameters comprising $h(\cdot)$.

Using specific forms for f and g (see §3.2.1) we show that it is possible to construct a system with $-1 < h'(b_e) < 0$ which exhibits a solitary homogeneous steady state (see Figure 3.2a) or one with $h'(b_e) < -1$, which exhibits period-2 spatial patterns (see

Parameter	Numerical Value
V^*	0.12
λ	0.5
g_{max}	1
k_{-B}	0.25
k_B	3
μ	1
α	0.5
β	0.33
m	2
n	2

Table 3.1: Table of dimensionless parameter values for the model without filopodia

Figure 3.2b). By using the same parameter values as in Figure 3.2b we reinforce these results using numerical simulations of a two-cell system (defined in §3.2.1) (see Figure 3.3) and show that, for $m = n = 2$, perturbing the homogeneous steady state causes the solutions to diverge to the period-2, spatially patterned steady state. This demonstrates that the homogeneous steady state becomes unstable when $h'(b_e) < -1$.

In Figure 3.3a, simulations are started at the homogeneous steady state and we apply a small positive perturbation to r_{U1} . The system tends to the spatially-patterned steady state with period-2 where cell 1 has a high level of Delta (tip cell state) and cell 2 has a low level of Delta (stalk cell state). In Figure 3.3b we perturb r_{U2} and find that the system tends to the opposite period-2 spatially-patterned steady state, with cell 2 having high Delta and cell 1 having low Delta.

By applying a homogeneous perturbation to any pair of variables of the two-cell system, all variables remain on the stable manifold of the unstable steady state (not shown). This suggests that given $h'(b_e) < -1$, patterning occurs when the symmetry of the system is broken.

For a system exhibiting a solitary homogeneous steady state only, with $-1 < h'(b_e) < 0$, numerical simulations of a two-cell system (see §3.2.1) decay back to the steady state (not shown) suggesting that it is stable.

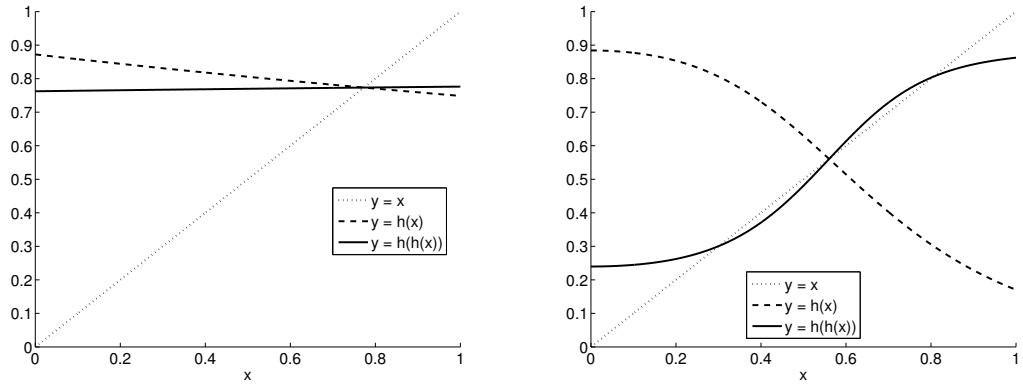


Figure 3.2: Plot showing the fixed points of $h(x)$ and $h \circ h(x)$ (for h defined in (3.3.4)) using the parameter values in Table 3.1 except for $V^* = 0.33$. (a) shows that when $m = n = 1$, $-1 < h'(b_e) < 0$, and $h(x)$ has a unique fixed point corresponding to a system which exhibits a single homogeneous steady state at $b_j = 0.7734$. Consequently, $h \circ h(b_e) < 1$ and $h \circ h(\cdot)$ has no distinct fixed points meaning patterning cannot occur. Figure 3.2 (b) shows that when $m = n = 2$ and $h'(b_e) < -1$, $h \circ h(\cdot)$ has two distinct fixed points at $b_j \approx 0.301$ and $b_j \approx 0.806$ corresponding to a pair of period-2, spatially patterned steady states. The common fixed point of $h(\cdot)$ and $h \circ h(\cdot)$ at $b_j \approx 0.5605$ determines the homogeneous steady state.

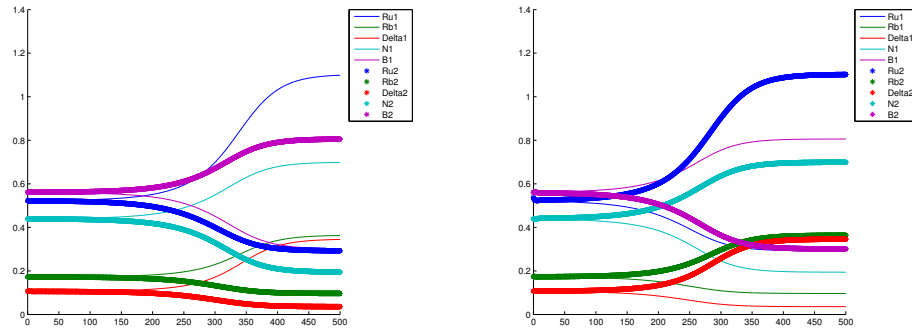


Figure 3.3: Numerical simulation of a two-cell system obtained by numerically integrating equations (3.2.10)-(3.2.14) using the parameters in Table 3.1 except $V^* = 0.33$. Initial and boundary conditions are as outlined in §3.2.1. Initial conditions are perturbed using a heterogeneous perturbation. (a) Positive perturbation of r_{U1} only. The system tends to the period-2 steady state where cell 1 has a high level of Delta and cell 2 has a low level. (b) Positive perturbation of r_{U2} only. The system tends to the opposite period-2 steady state where cell 1 has a low level of Delta.

3.4 Numerical bifurcation analysis

In this section we aim to characterise the parameter space in terms of the existence and stability of solutions, most notably by identifying regions that give rise to stable, period-2 patterning solutions. We use numerical bifurcation analysis to determine the stability of the homogeneous and period-2 spatial patterning steady states and the bifurcations by which they are created and disappear as key model parameters vary. Since period-2 spatial patterns are determined by fixed points of $h \circ h(x)$ so we focus on varying the parameters \hat{V} and \hat{g}_{max} which appear in the definition of $h(\cdot)$ (see (3.3.4)).

The model exhibits patterning for a range of values of V^* (recall $\hat{V} = \frac{V^*}{\lambda}$). Figure 3.4a shows that the homogeneous steady state becomes unstable via a supercritical pitchfork bifurcation at $V^* \approx 0.0977$ where two stable branches emerge, representing a stable period-2 spatial patterning solution. Here, alternating cells express high (low) levels of bound Notch receptor and the other ligands/receptors. We say that the system is bistable here as there are two steady state values for each value of the bifurcation parameter. The patterning region terminates at another supercritical pitchfork bifurcation where the period-2 branches coincide with the unstable homogeneous steady state. For larger values of V^* the stable branches disappear and the homogeneous steady state becomes stable again. We remark that increasing the total concentration of Notch receptors, N_{tot} , (see Appendix A) widens the range of values of \hat{V} for which the system is bistable, (see Figure 3.4b).

If we fix $V^* = 0.12$ (so that $\hat{V} = 0.24$ again), use the parameters from Figure 3.4b, but allow g_{max} to vary, we see a similar bifurcation diagram (see Figure 3.5a), with bistability for a range of values of \hat{g}_{max} . Pitchfork bifurcations again mark the endpoints of this patterning region and the stability of the steady states is identical to that described for Figure 3.4. The two-parameter bifurcation diagram for \hat{V} and \hat{g}_{max} (see Figure 3.5b) shows that if \hat{g}_{max} is made small enough, the pitchforks coalesce, thereby terminating the bistable region. For larger values of \hat{g}_{max} it is unclear whether the pitchforks ever coalesce, however, the system is bistable for a smaller range of \hat{V} values here than it is for lower values of \hat{g}_{max} . Hence the model predicts that it is harder for the system to pattern for large values of either parameter and this may be important for clinical purposes.

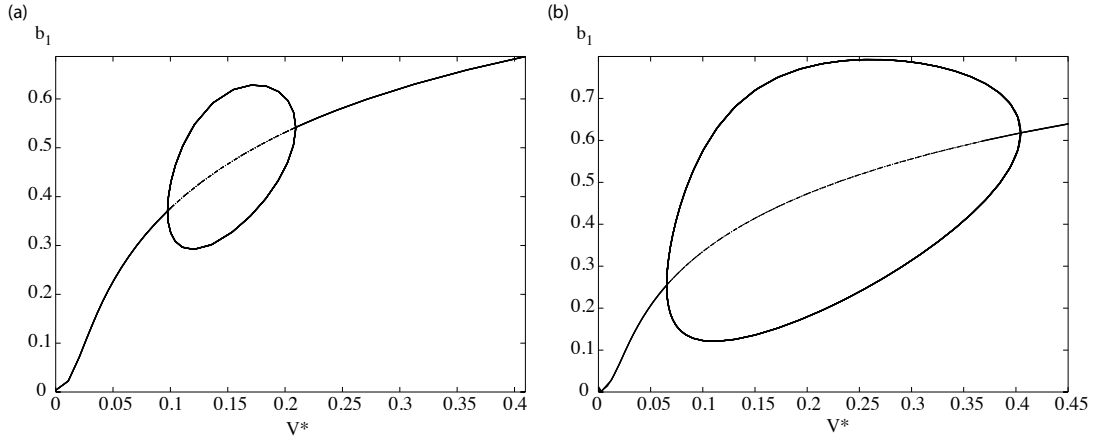


Figure 3.4: Bifurcation diagram for the system (3.2.10)-(3.2.14) showing how the steady state of bound Notch, b_j , changes with V^* . Solid (dashed) lines are stable (unstable) solutions as categorised by xppaut continuation software. (a) For parameters in Table 3.1 with the exception of $\{g_{max}, k_B, \beta\} = \{1.3129, 2.285, 0.4376\}$, period-2 spatial patterns exist for $0.09765 \leq V^* \leq 0.210$. (b) For parameters in Table 3.1 with the exception of $\{g_{max}, k_B, \beta\} = \{1.0526, 2.85, 0.3509\}$ (corresponding to an increase in the total number of Notch receptors), the system can now pattern for $0.0640 \leq \hat{V} \leq 0.406$.

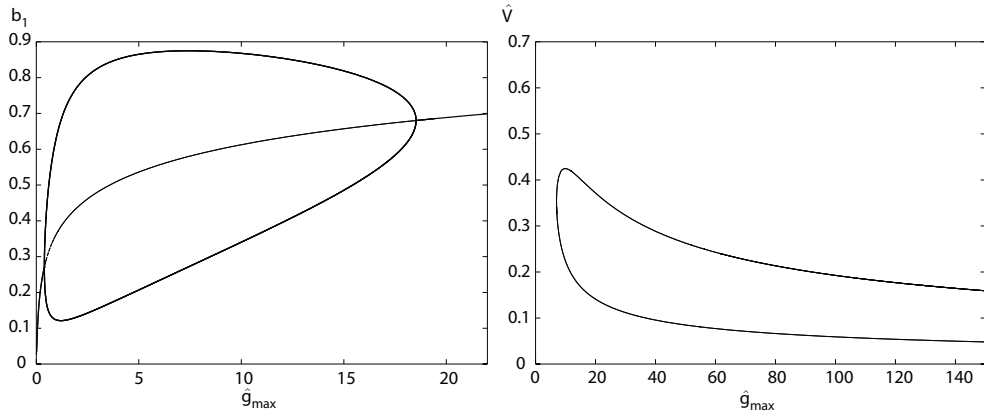


Figure 3.5: (a) Bifurcation diagram for the system (3.2.10)-(3.2.14) showing how, when $V^* = 0.12$, the steady state of bound Notch, b_j , varies with g_{max} . The parameter values are the same as those used in Figure 3.4b. Key: Solid (dashed) lines represent stable (unstable) solutions as categorised by xppaut continuation software. (b) Diagram highlighting regions of $\hat{V} - \hat{g}_{max}$ parameter space in which the system admits patterning and was produced using two-parameter continuation in xppaut and parameter values as per Figure 3.4a. The lines show the position of the pitchfork bifurcations and hence the boundary of the pattering region in $\hat{V} - \hat{g}_{max}$ parameter space.

3.5 Bifurcation analysis of the homogeneous steady state

In the previous section we used numerical bifurcation analysis to show that the system in (3.2.10)-(3.2.14) exhibits period-2 spatial patterns for a range of \hat{V} and \hat{g}_{max} values. In this section we characterise the pattern forming potential of the system by analytically determining the linear stability of the homogeneous steady state and using the Routh-Hurwitz stability criteria, derive necessary conditions for patterning.

To begin we make a few simplifications. Firstly, we make the quasi-steady state assumption that VEGF-VEGFR-2 binding is rapid so that $dr_{Bj}/dt = 0$ in equation (3.2.11) which gives $r_{Bj} = V^*r_{Uj}$. To simplify notation, we let $\langle b_j \rangle = \frac{b_{j-1} + b_{j+1}}{2}$ and $\langle \delta_j \rangle = \frac{\delta_{j-1} + \delta_{j+1}}{2}$ denote the coupling between the cells. For each cell, j , (3.2.10)-(3.2.14) reduce to give:

$$\frac{dr_{Uj}}{dt} = f(b_j) - \lambda r_{Uj}, \quad (3.5.1)$$

$$\frac{d\delta_j}{dt} = g_{max}g(V^*r_{Uj}) + k_{-B}\langle b_j \rangle - k_B(1 - \langle b_j \rangle)\delta_j - \mu\delta_j, \quad (3.5.2)$$

$$\frac{db_j}{dt} = k_B\langle \delta_j \rangle(1 - b_j) - k_{-B}b_j. \quad (3.5.3)$$

Following Webb and Owen [71], we perform linear stability analysis of the homogeneous steady state which is given by the $O(1)$ terms (r_{Ue}, δ_e, b_e) . We substitute $r_{Uj} = r_{Ue} + \epsilon\hat{r}_{Uj}$, $\delta_j = \delta_e + \epsilon\hat{\delta}_j$ and $b_j = b_e + \epsilon\hat{b}_j$ (for $0 < \epsilon \ll 1$) into (3.5.1)-(3.5.3), and retain $O(\epsilon)$ terms which gives

$$\frac{d\hat{r}_{uj}}{dt} = f'(b_e)\hat{b}_j - \lambda\hat{r}_{uj}, \quad (3.5.4)$$

$$\frac{d\hat{\delta}_j}{dt} = g_{max}V^*g'(V^*r_{Ue})\hat{r}_{uj} - (k_B(1 - b_e) + \mu)\hat{\delta}_j + (k_{-B} + k_B\delta_e)\langle \hat{b}_j \rangle, \quad (3.5.5)$$

$$\frac{d\hat{b}_j}{dt} = k_B(1 - b_e)\langle \hat{\delta}_j \rangle - (k_B\delta_e + k_{-B})\hat{b}_j. \quad (3.5.6)$$

We seek solutions of the form $\hat{u} = \tilde{u} \cdot \exp(ikj + \sigma t)$, where \tilde{u} are constants and σ is the growth rate of perturbations with wavenumber k . We consider an infinite line of cells with periodic boundary conditions and note that

$$\langle \hat{u}_j \rangle = \frac{\hat{u}_{j-1} + \hat{u}_{j+1}}{2} = \tilde{u} \cdot e^{ikj + \sigma t} \cdot \cos(k). \quad (3.5.7)$$

Substituting this ansatz into equations (3.5.4)-(3.5.6) gives $\sigma \mathbf{v} = M \cdot \mathbf{v}$ where $\mathbf{v} = [\hat{r}_{uj}, \hat{\delta}_j, \hat{b}_j]^T$,

$$M = \begin{bmatrix} -\lambda & 0 & A \\ g_{max}V^*B & -(k_B(1 - b_e) + \mu) & (k_{-B} + k_B\delta_e)K \\ 0 & k_B(1 - b_e)K & -(k_B\delta_e + k_{-B}) \end{bmatrix}, \quad (3.5.8)$$

$$K = \cos(k),$$

$$A = f'(b_e) \quad \text{and} \quad B = g'(V^*r_{Ue}). \quad (3.5.9)$$

Now the strengths of inhibition/activation of VEGF-R2 and Dll4 ligand respectively are measured by the two gradients of f and g at the homogeneous steady state. The stability of the linearized system is determined by the eigenvalues of M , which are the roots of the characteristic polynomial: $P(\sigma; K) = \sigma^3 + a_1\sigma^2 + a_2\sigma + a_3 = 0$ where

$$a_1 = k_{-B} + k_B\delta_e + \mu + k_B(1 - b_e) + \lambda, \quad (3.5.10)$$

$$a_2(K) = (\mu + k_B(1 - b_e))(k_{-B} + k_B\delta_e) - k_B(1 - b_e)(k_{-B} + k_B\delta_e)K^2 + \\ + \lambda(k_{-B} + k_B\delta_e + \mu + k_B(1 - b_e)), \quad (3.5.11)$$

$$a_3(K) = \lambda(k_{-B} + k_B\delta_e) (\mu + k_B(1 - b_e) - k_B(1 - b_e)K^2) \\ - ABg_{max}V^*k_B(1 - b_e)K. \quad (3.5.12)$$

For a patterning instability, we require the homogeneous steady state to be stable to homogeneous perturbations (for which $K = 1$) and unstable to non-homogeneous perturbations. This is analogous to a Turing instability in which the homogeneous steady state is stable to spatially uniform perturbations but unstable to spatially varying perturbations [114]. The steady state is stable to homogeneous perturbations if all roots of $P(\sigma; K = 1) = 0$ have $\Re(\sigma(K = 1)) < 0$. It is unstable to spatially varying perturbations if one or more roots of $P(\sigma, K) = 0$ have $\Re(\sigma(K)) > 0$ for $K \in [-1, 1)$ [71].

The roots of $P(\sigma, K) = 0$ are, in general, difficult to determine analytically, so we determine which modes generate patterning instabilities in the linearised system by fixing $K = \cos(k) \in [-1, 1]$, numerically identifying the eigenvalues of M , and plotting $\Re(\sigma_i(K))$ $i = 1, 2, 3$ vs K for different values of \hat{V} (see Figure 3.6). This is done for a range of values of $\hat{V} \in [0.18, 0.43]$ which span the bistable region in Figure 3.4. We find that the maximum of the real parts, $\Re(\sigma_i(K))$, always becomes positive at $K = -1$, or equivalently for wavenumber $k = \pi$, corresponding to a period-2 spatial pattern. We see similar dispersion relations for the parameters used in Figure 3.4b and Figure 3.5a (not shown). Hence the observed pitchfork bifurcations correspond to $\Re(\sigma_i(-1)) = 0$.

To understand how $\Re(\sigma_i(K))$ change sign, in particular at $K = -1$, we look to the Routh-Hurwitz stability criteria which state that the roots of $P(\sigma; K) = 0$ will all have $\Re(\sigma_i(K)) < 0$ if and only if the coefficients satisfy the following conditions, which for a cubic polynomial, are

$$a_1 > 0, \quad (3.5.13)$$

$$a_3(K) > 0, \quad (3.5.14)$$

$$a_1 \cdot a_2(K) - a_3(K) > 0. \quad (3.5.15)$$

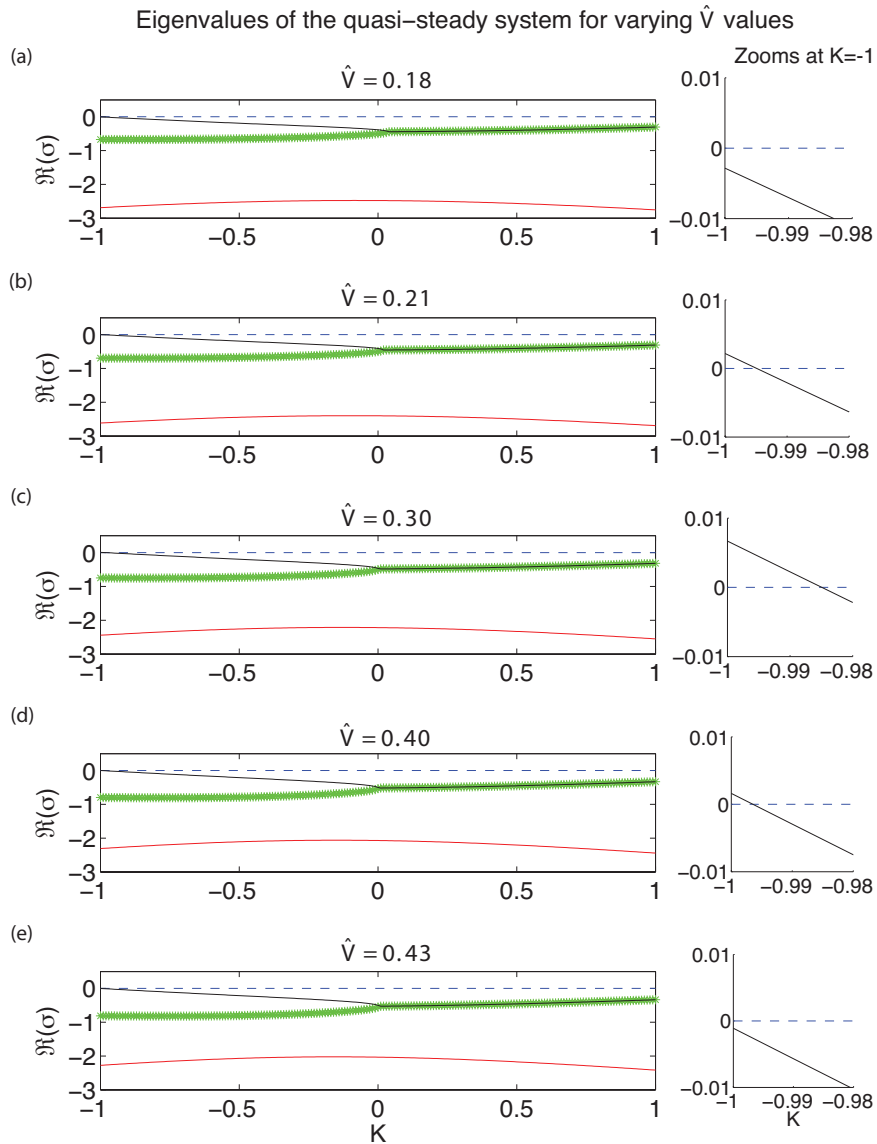


Figure 3.6: Dispersion relation plotting the eigenvalues, $\sigma_i(K), i = 1, 2, 3$ of M (3.5.8) for the linearised system (3.5.4)-(3.5.6) for different values of the parameter \hat{V} which lie at the centre of the bistable region and on either side of the two pitchfork bifurcations in Figure 3.4a. Parameters used are as per Figure 3.4a. The patterning instability occurs when the maximum of the three eigenvalues becomes positive. This always happens at $K = -1$ for those values of \hat{V} which lie inside the bistable region in Figure 3.4a. This suggests that the dominant unstable mode for this system is the one corresponding to the period-2, “salt and pepper” spatial pattern.

Inequality (3.5.13), is satisfied for all values of the model parameters whereas a_2 and a_3 are quadratic equations in $K = \cos(k)$.

3.5.1 Stability to homogeneous perturbations

For stability to homogeneous perturbations we require $a_3(1) > 0$ and $a_1 \cdot a_2(1) - a_3(1) > 0$ [71]. Substituting $K = 1$ into (3.5.12) and simplifying, gives

$$a_3(1) = \lambda\mu(k_B\delta_e + k_{-B}) - ABV^*g_{max}k_B(1 - b_e).$$

All parameter values are positive and $0 \leq b_e \leq 1$, so $a_3(1) > 0$ if and only if

$$AB < \frac{\lambda\mu(k_B\delta_e + k_{-B})}{g_{max}V^*k_B(1 - b_e)} = W. \quad (3.5.16)$$

Similarly, substituting $K = 1$ into (3.5.15) gives

$$a_1 \cdot a_2(1) - a_3(1) = (a_1 - \lambda) \cdot [(k_{-B} + k_B\delta_e)\mu + a_1\lambda] + ABV^*g_{max}k_B(1 - b_e).$$

wherein $a_1 - \lambda = k_B\delta_e + k_{-B} + k_B + \mu > 0$. Hence $a_1 \cdot a_2(1) - a_3(1) > 0$ if and only if

$$AB > -\frac{1}{V^*g_{max}k_B(1 - b_e)}(a_1 - \lambda)[(k_{-B} + k_B\delta_e)\mu + a_1\lambda] = -X. \quad (3.5.17)$$

3.5.2 Stability to non-homogeneous perturbations

For a spatial instability, we require at least one root of $P(\sigma; K) = 0$ to have $\Re(\sigma(K)) > 0$ for some $K \in [-1, 1)$ whilst $\Re(\sigma(1)) < 0$. Since a_1 is independent of K , the instability may only arise if $\exists K \in [-1, 1)$ such that $a_3(K) < 0$ or $a_1 \cdot a_2(K) - a_3(K) < 0$. Since both conditions are quadratics in K with negative leading coefficient, and we impose $a_3(1) > 0$ and $a_1 a_2(1) - a_3(1) > 0$ for stability to homogeneous perturbations, the only possibility for a patterning bifurcation occurs when either condition has a single root at $K = -1$. Figure 3.7 shows sketches of the quadratic Routh-Hurwitz conditions and demonstrates how $K = -1$ is the first wavenumber at which the violation occurs, giving rise to a patterning instability.

We also illustrate the transition from homogeneity to patterning in Figure 3.8 using the parameter values from Table 3.1. We vary \hat{V} whilst keeping all other parameters fixed at the values used in Figure 3.4a. The bifurcation point is observed at $\hat{V} \approx 0.195$ or equivalently $V^* \approx 0.0977$ in accordance with Figure 3.4a.

Since we know that the Routh-Hurwitz conditions are first violated at $K = -1$, a system which patterns must have either $a_3(-1) < 0$ or $a_1 \cdot a_2(-1) - a_3(-1) < 0$ as shown in

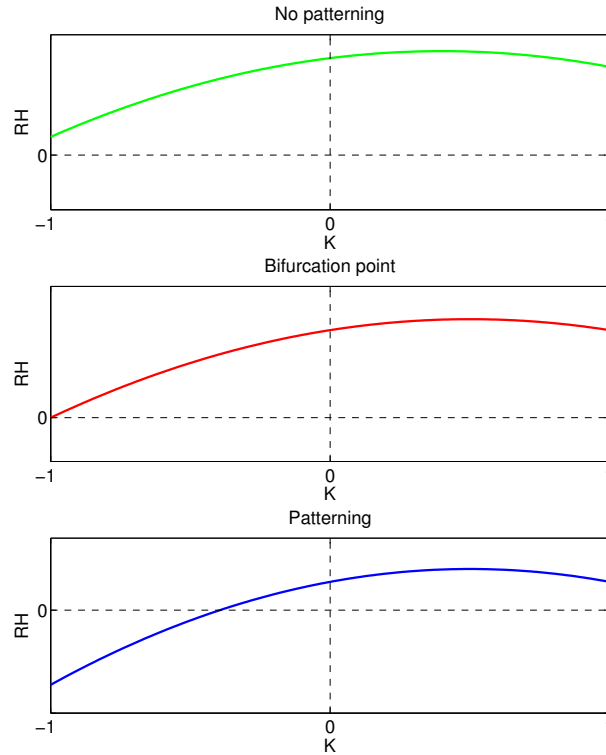


Figure 3.7: A sketch of the quadratic Routh-Hurwitz conditions with negative leading coefficient, (either $a_3(K)$ or $a_1 \cdot a_2(K) - a_3(K)$) showing the transition from no patterning to patterning. (a) The Routh-Hurwitz conditions in (3.5.14) and (3.5.15) are satisfied when the quadratic is positive for all values of $K \in [-1, 1]$ which produces no patterns. (b) The bifurcation point is where the Routh-Hurwitz condition is equal to zero at $K = -1$. (c) The Routh-Hurwitz conditions in (3.5.14) and (3.5.15) are violated for a range of $K \in [-1, 1]$ in which the quadratic is negative, thus giving rise to patterns. The wavelength of the pattern is determined by the mode with the most negative real part which is $K = -1$ in this case (period-2 spatial patterns).

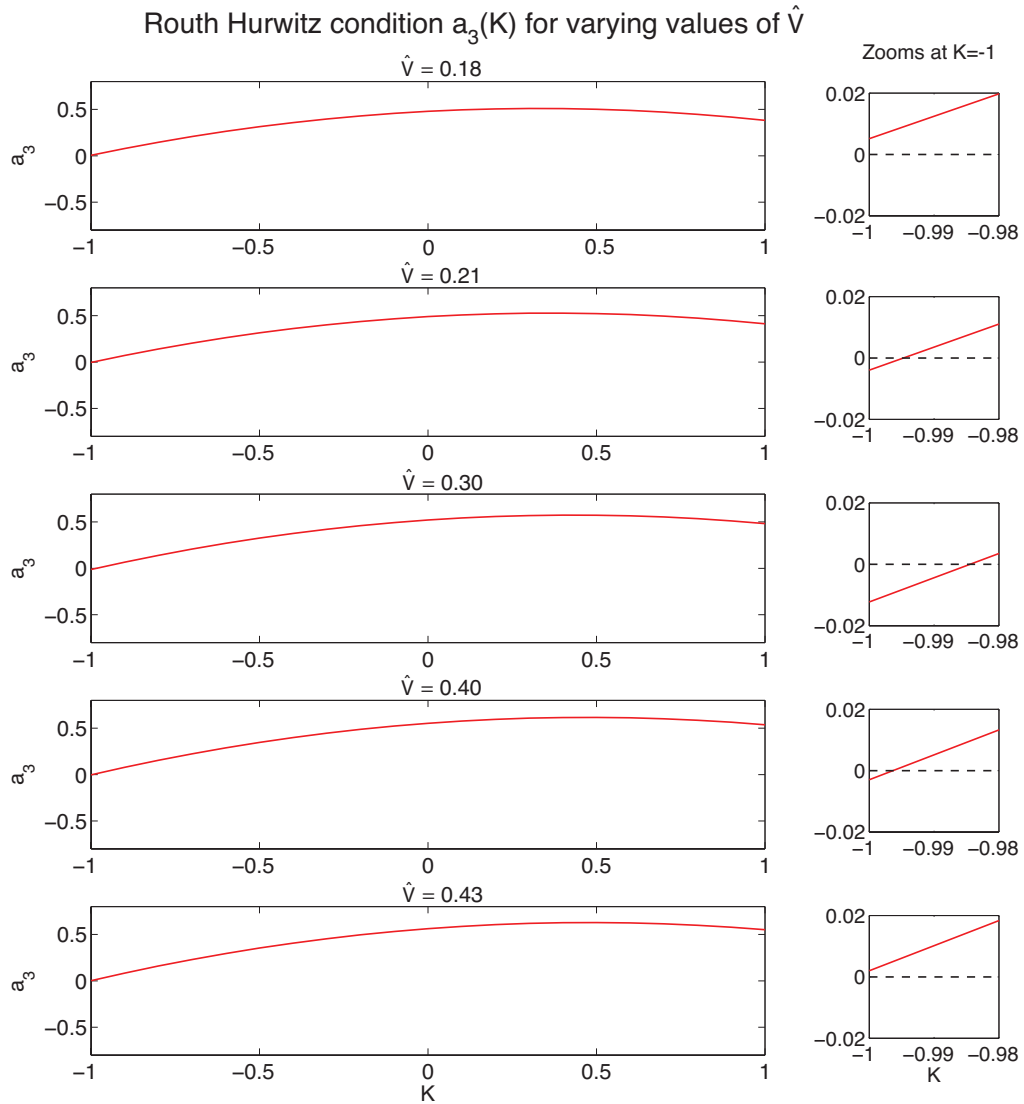


Figure 3.8: Routh-Hurwitz condition $a_3(K)$ plotted as a function of K for values of $\hat{V} = 0.18, 0.21, 0.30, 0.40, 0.43$, which are on either side of the bifurcation points marking the ends of the patterning window. Remaining parameters values: as per Table 3.1, except $\{g_{max}, k_B, \beta\} = \{1.31, 2.29, 0.438\}$. The right hand column shows a zoomed-in view of the Routh-Hurwitz condition at $K = -1$. A period-2 patterning bifurcation occurs when the Routh-Hurwitz condition $a_3(K)$ has a single root at $K = -1$ causing the homogeneous steady state to become unstable (see the plots for $\hat{V} = 0.21, 0.30, 0.40$). Varying \hat{V} keeps $a_3(1) > 0$, hence the homogeneous steady state remains stable to homogeneous perturbations.

Figure 3.7c. By substituting $K = -1$ into (3.5.15) and (3.5.14), $a_3(-1) < 0$ if and only if

$$AB < -\frac{\lambda\mu(k_{-B} + k_B\delta_e)}{g_{max}V^*k_B(1 - b_e)} = -W, \quad (3.5.18)$$

and $a_1a_2(-1) - a_3(-1) < 0$ (Figure 3.7c) if and only if

$$AB > \frac{1}{V^*g_{max}k_B(1 - b_e)}(a_1 - \lambda)[(k_{-B} + k_B\delta_e)\mu + a_1\lambda] = X. \quad (3.5.19)$$

Stability to homogeneous perturbations and instability to non-homogeneous perturbations requires satisfying both (3.5.16) and (3.5.17) and either one of (3.5.18) or (3.5.19). These conditions define hyperbolae in the A - B plane which delimit stability regions discussed in §3.6.

3.5.3 Patterning bifurcations are generated via purely real eigenvalues changing sign

Sign changes in the real parts of the eigenvalues of M (3.5.8) occur on the four curves, $AB = \pm W, \pm X$ (illustrated in the A - B plane in Figure 3.9), where

$$W = \frac{\lambda\mu(k_B\delta_e + k_{-B})}{g_{max}V^*k_B(1 - b_e)} \quad \text{and} \quad X = \frac{1}{V^*g_{max}k_B(1 - b_e)}(a_1 - \lambda)[(k_{-B} + k_B\delta_e)\mu + a_1\lambda].$$

Patterning instabilities occur on curves corresponding to $K = -1$:

$$\begin{aligned} A &= -\frac{W}{B} \quad \text{sign change in } \sigma \text{ with } \Im(\sigma) = 0 \text{ (patterning/real instability),} \\ A &= \frac{X}{B} \quad \text{sign change in } \Re(\sigma) \text{ for } \Im(\sigma \neq 0) \text{ (patterning/Hopf instability),} \end{aligned}$$

whereas instabilities to homogeneous perturbations occur on the curves corresponding to $K = 1$:

$$\begin{aligned} A &= -\frac{X}{B} \quad \text{sign change in } \Re(\sigma) \text{ for } \Im(\sigma \neq 0) \text{ (homogeneous/Hopf instability),} \\ A &= \frac{W}{B} \quad \text{sign change in } \sigma \text{ with } \Im(\sigma) = 0 \text{ (homogeneous/real instability).} \end{aligned}$$

Only curves $AB = \pm W$ correspond to bifurcations as they are the locus of points in the A - B plane at which the first eigenvalue(s) of (3.5.1)-(3.5.3) take positive real part. Moreover, only $AB = -W$ corresponds to a patterning *bifurcation* since traversing it maintains stability of the homogeneous steady state to homogeneous perturbations. Hence the homogeneous/Hopf instability always occurs “after” the patterning/real instability, for example, whilst moving along the path p_2 (see Figure 3.9), $AB = -X$ is always crossed after $AB = -W$. This is because $W < X$ for all realistic choices of

parameter values. This can be proved by contradiction: if $W > X$, then after some lines of algebra, we arrive at the following inequality:

$$(k_{-B} + k_B \delta_e) [\lambda k_B (1 - b_e) + \lambda^2 + \lambda + \mu] + (\mu + k_B (1 - b_e)) [\mu (k_{-B} + k_B \delta_e) + a_1 \lambda] < 0,$$

which cannot hold since the sum of positive parameter values cannot be negative. Hence the patterning bifurcation always occurs when a purely real eigenvalue changes sign and never due to a pair of complex conjugate eigenvalues crossing the imaginary axis.

The patterning instability at $AB = X$ does not correspond to a patterning *bifurcation* as the homogeneous steady state has already lost stability via a purely real eigenvalue changing sign on $AB = W$. This curve corresponds to a transcritical bifurcation in which the homogeneous steady state exchanges its stability with another steady state (see Figure 3.14) to become unstable.

3.6 Feedback strengths determine patterning regions

For general choices of the functions f and g , the stability of the homogeneous steady state to homogeneous and heterogeneous perturbations and the ability to produce patterning is determined by the values of their slopes at the homogeneous steady state, $A = f'(b_e)$ and $B = g'(r_{Be}) = g'(V^* r_{Ue})$. Positive (negative) values of A and B represent production (inhibition) of VEGF receptors and Dll4 ligand by the relevant proteins, whilst their magnitude provides information about the strength of activation/repression.

We characterise the stability of the homogeneous equilibrium in the A - B plane using the Routh-Hurwitz conditions, formulated in the previous section, which correspond to four hyperbolae in the A - B plane. We also interrogate the real parts of the eigenvalues of the Jacobian matrix of the quasi-steady system (3.5.8) for different choices of A and B to confirm our analysis. Both approaches are collated in Figure 3.9 and neither one makes any prior assumptions about the homogeneous steady state value or the forms of f and g .

In practice, changing A and B can be achieved by changing the values of α , β , m and n which are associated with our choices of f and g . In general this will also change the value of the underlying homogeneous steady state and/or the positions of the Routh-Hurwitz hyperbolae relative to the axes. In Appendix D we explain how it is possible to choose 3 model parameters such that A and B can be varied by manipulating the Hill coefficients, m and n , without altering the underlying steady state and hence without

changing the positions of the hyperbolae. These parameter choices (summarised in the non-shaded rows of Table E.1) are used for all analyses of the A - B plane (Figure 3.9) unless otherwise stated and thus allow for comparisons of N -cell systems with different feedback strengths.

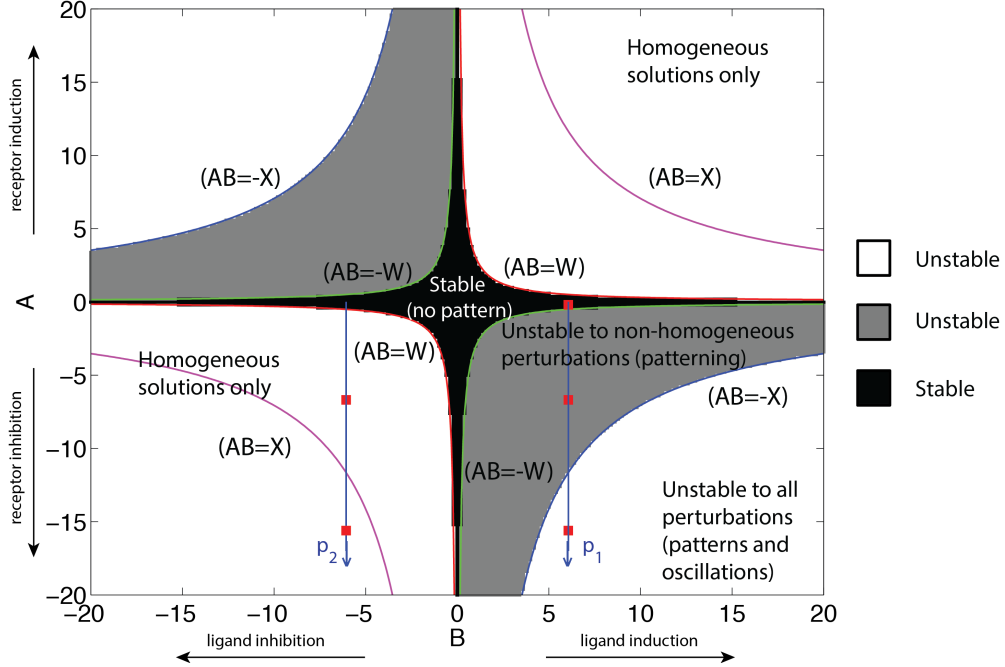


Figure 3.9: Stability of the homogeneous steady state for the quasi-steady state model (3.5.1)-(3.5.3). Parameter values chosen as in Appendix E and Table E.1. Postive (negative) values of A represent VEGFR-2 induction (inhibition) due to bound Notch receptors, and positive (negative) values of B represent Dll4 ligand induction (inhibition) due to bound VEGFR-2. Colours indicate the stability of the homogeneous steady state for a particular choice of values for A and B and are assigned by evaluating the sign of the real parts of the eigenvalues of M in equation (3.5.8) (see Table 3.2). Overlaid are the Routh-Hurwitz conditions corresponding to $AB = \pm W$ (in red and green) and $AB = \pm X$ (in blue and magenta). These correspond to equations (3.5.16)-(3.5.19). The arrows, p_1 and p_2 , are paths in parameter space along which we continue solutions (see Figures 3.12 and 3.14). Red squares lower-right: $m = 15, n = 8$ (grey region); $m = 35, n = 8$ (white region). Lower-left: $m = 15, n = -8$; $m = 35, n = -8$.

In Figure 3.9 we sketch the Routh-Hurwitz hyperbolae (3.5.16)-(3.5.19) in the A - B plane. Stability to homogeneous perturbations demands that both (3.5.16) and (3.5.17) are satisfied corresponding to points lying between the two red hyperbolae, (on which $a_3(1) = 0$), and the two blue hyperbolae, (on which $a_1a_2(1) - a_3(1) = 0$). Instability to non-homogeneous perturbations requires satisfying either (3.5.18), which corresponds

Region	Stability to		Sign of $\sup_i \Re(\sigma_i(K))$ ($i = 1, 2, 3$)	
	Hom pert	Het pert	$K = \cos(0) = 1$	$K = \cos(\pi) = -1$
Black	Stable	Stable	–ve	–ve
Grey	Stable	Unstable	–ve	+ve
White	Unstable	Unstable	+ve	+ve

Table 3.2: Table summarising the stability of the homogeneous steady state to homogeneous (Hom) and non-homogeneous (Het) perturbations and the signs of the maximum of the real parts of the three eigenvalues of M (3.5.8) in each of the coloured regions of the stability plot in Figure 3.9.

to points lying outside of the two green hyperbolae $a_3(-1) = 0$ or (3.5.19), which corresponds to points lying outside of the two magenta hyperbolae $a_1a_2(-1) - a_3(-1) = 0$. The intersection of these conditions are the two grey regions which is the set of points, $\{A, B\}$, satisfying (3.5.16), (3.5.17) and (3.5.18) for which we have a patterning instability.

In the black region, we have $a_3(1) > 0$ and $a_1a_2(1) - a_3(1) > 0$ which make the homogeneous equilibrium stable to homogeneous perturbations and $a_3(-1) > 0$ and $a_1a_2(-1) - a_3(-1) > 0$ giving stability to non-homogeneous perturbations for $K \in [-1, 1)$. Hence the steady state is stable in this region.

In the white region neither Routh-Hurwitz condition is satisfied and the homogeneous steady state is unstable.

The Routh-Hurwitz hyperbolae lie precisely on the boundaries to the coloured stability regions marking the steady state bifurcation points of the system in the A - B plane. This is demonstrated in Figure 3.10 by plotting both the Routh-Hurwitz conditions and the real parts of the eigenvalues as functions of A (moving along the path p_2) for a fixed value of B corresponding to $n = 8$.

3.6.1 Lower-right quadrant ($A < 0, B > 0$ biologically relevant)

To understand better the types of solutions and bifurcations that the system exhibits in the A - B plane, we use continuation methods (Figure 3.12a). In this section we investigate how patterning instability arises when we choose specific Hill function forms for the feedback functions f and g . In the next section we investigate the behaviour of the system in the lower left quadrant in which the homogeneous steady state destabilises via a transcritical bifurcation.

Firstly we continue solutions along the path, p_1 , in the lower-right quadrant of Figure

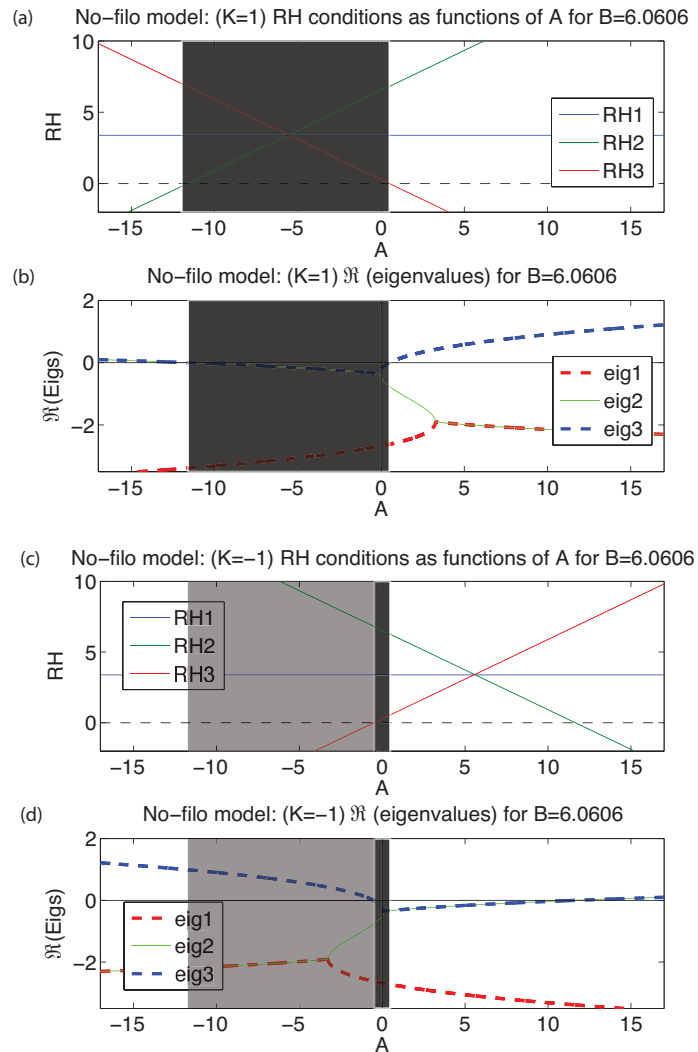


Figure 3.10: Plots of the Routh-Hurwitz conditions and the $\Re(\sigma_i(K))$ for $i = 1, 2, 3$ when $K = -1, 1$ and $B = 6.0606$ ($n = 8$). A (or equivalently m) varies along the path p_2 in Figure 3.9. Parameter values are as per Table 3.1 except for $V^* = 0.33$. Plots (a) and (b) show that the homogeneous steady state is stable to homogeneous perturbations when all Routh-Hurwitz conditions are positive i.e. all eigenvalues have negative real part (black region). Plots (c) and (d) show where a patterning instability occurs (grey region), meaning that the ($K = -1$) mode grows whilst the $K = 1$ mode decays. (Colours in (c) and (d) are consistent with those used in Figure 3.9)

3.9 where A (and hence m) is varied for a fixed B and fixed values of the remaining parameters (see Table E.1). A stable homogeneous steady state (black region) becomes unstable via a pitchfork bifurcation which breaks symmetry. As the black/grey boundary is traversed, the slope of $h(x)$ decreases through $h'(x) = -1$ and the slope of $h \circ h(x)$ increases through $\frac{d}{dx}h \circ h(x) = 1$, causing the number of crossing points to increase from 1 to 3 at the pitchfork bifurcation (see supplementary plots in Figure 3.12a). The period-2 spatial patterning solutions (grey region) are stable but these solutions are truncated in Figure 3.12a when the lower branch of solutions becomes extremely small. As the feedback strengths are increased further, a Hopf bifurcation at the grey/white boundary gives rise to an unstable limit cycle (see Figure 3.11). The system exhibits identical behaviour in the upper left quadrant.

3.6.2 Lower-left quadrant ($A < 0, B < 0$)

Solutions are also continued along the path p_2 (Figure 3.14). The stable homogeneous steady state loses stability via a transcritical bifurcation to an unstable steady state arising from a saddle node bifurcation (see supplementary plots in Figure 3.14). While the outer branches resemble those of the pitchfork bifurcation, they are two separate branches of stable, homogeneous solutions. There are no period-2 solutions in the lower-left and upper-right quadrants because the slopes of f and g have the same sign, in which case $h(x)$ is monotonically increasing on $[0, 1]$. In this case, it is possible to show that all fixed points of $h \circ h(x)$ are also fixed points of $h(x)$ and therefore correspond to homogeneous solutions.

Lemma 1. *Given a monotonically increasing function $y = h(x)$ with n fixed points, with gradient $h'(x_i)$ at the i th fixed point (for $1 \leq i \leq n$), then $y = h \circ h(x)$ has the same fixed points as $h(x)$ with gradient $h'(x_i)^2$ there.*

Proof Suppose $x = x_i$ is a fixed point of $h(\cdot)$. Then

$$x_i = h(x_i) \Rightarrow h(x_i) = h \circ h(x_i) = x_i. \quad (3.6.1)$$

Hence any fixed point of $h(x)$ is also a fixed point of $h \circ h(x)$. At such a fixed point,

$$\frac{d}{dx}(h \circ h(x_i)) = h'(h(x_i))h'(x_i) = h'(x_i)^2.$$

The result of Lemma 1 then implies

$$(h \circ h(x_i))' \begin{cases} < h'(x_i), & 0 < h'(x_i) < 1 \\ > h'(x_i), & h'(x_i) > 1 \end{cases}, \quad (3.6.2)$$

CHAPTER 3: AN ORDINARY DIFFERENTIAL EQUATION MODEL OF VEGF-DELTA-NOTCH SIGNALLING IN ANGIOGENIC TIP CELL SELECTION

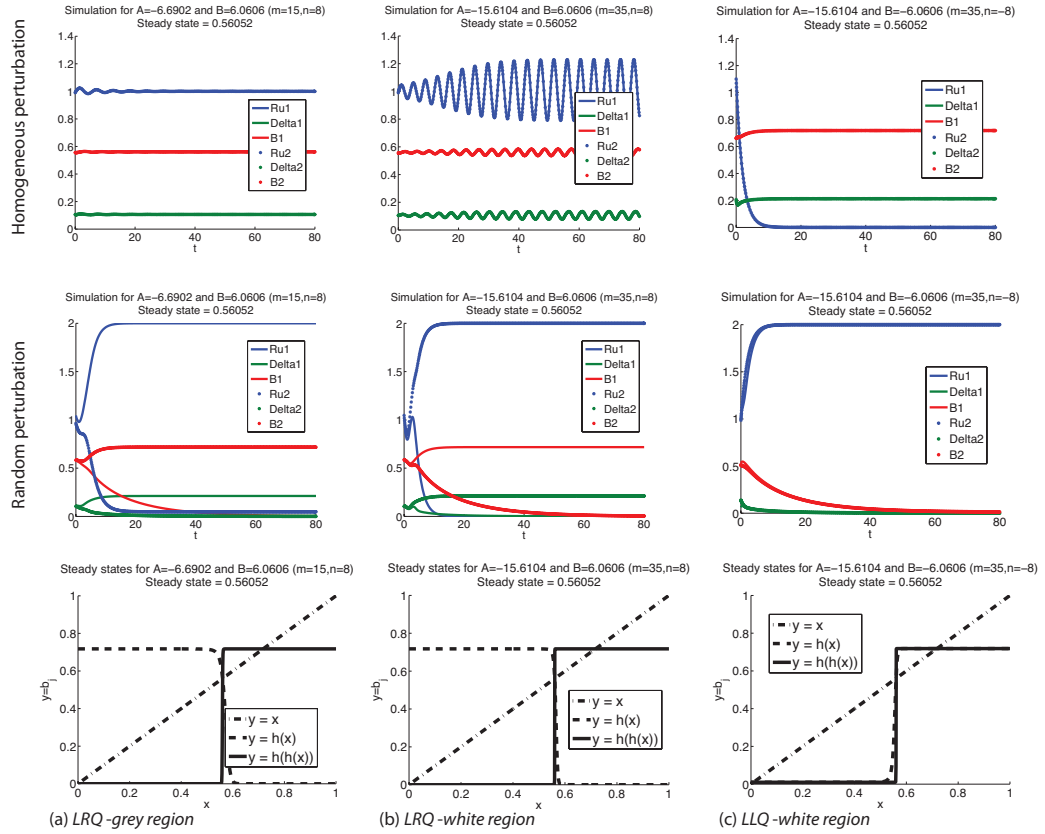


Figure 3.11: Numerical simulations of the quasi-steady two-cell system in (3.5.1)-(3.5.3) starting close to the homogeneous steady state. Rows 1 and 2 perturb the homogeneous steady state with homogeneous and random (non-homogeneous) perturbations respectively. The last row shows fixed points of $h(x)$ and $h \circ h(x)$ marking the existence of homogeneous and period-2 spatial patterning solutions respectively. Columns (a)-(c) use parameters from distinct regions of the A - B plane: (a) $m = 15, n = 8$ (b) $m = 35, n = 8$ (red markers in the grey and white regions of Figure 3.9 on the path p_1 in parameter space). (c) $m = 35, n = -8$ (Red marker in the white region on the path p_2). Parameters from Appendix D and Table E.1. In the grey region of the lower right quadrant, homogeneous perturbations decay back to the steady state and non-homogeneous perturbations grow to a period-2 spatial pattern. In the white region, homogeneous perturbations grow to a limit cycle and non-homogeneous oscillations grow to the period-2 spatial pattern. In the white region of the lower left quadrant, the homogeneous steady state is unstable and both homogeneous and non-homogeneous perturbations cause the solutions to move to one of two new homogeneous steady states.

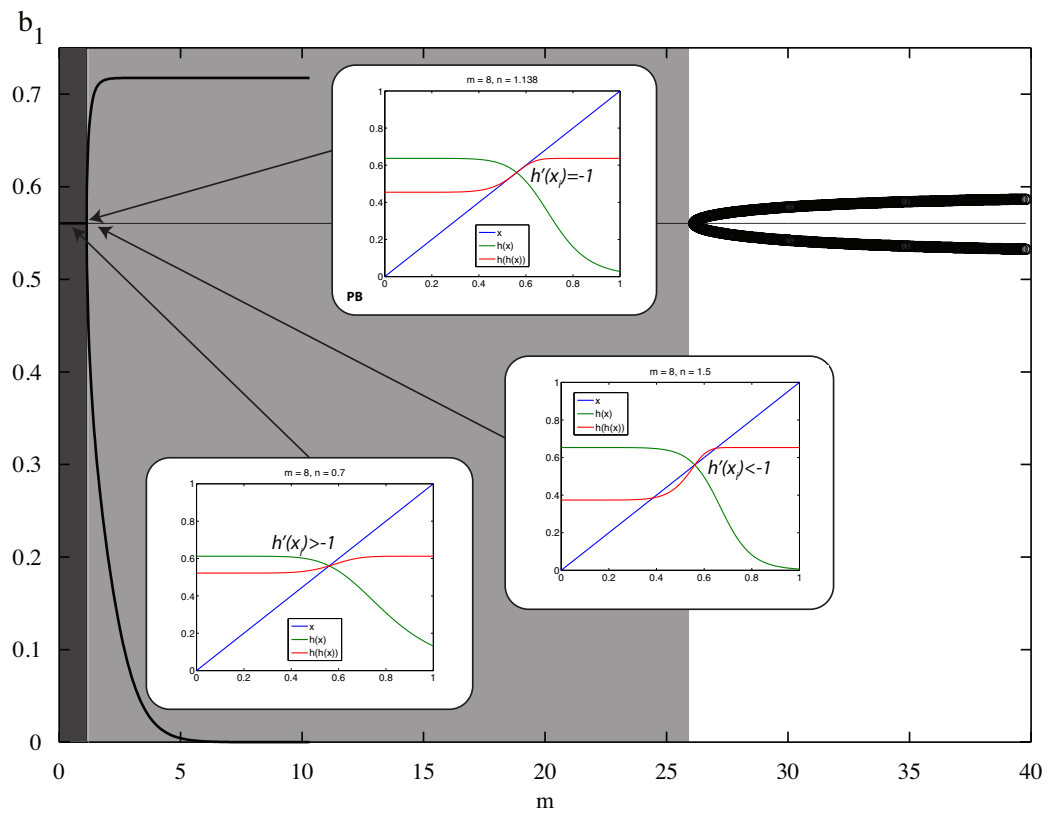


Figure 3.12: (a) Continuation of solutions to the quasi-steady two-cell system in (3.5.1)-(3.5.3) for a fixed value of $n = 8$ ($B = 6.0606$) and the remaining parameters whilst varying m , and hence A , along the path, p_1 , of Figure 3.9. (a) Colours are consistent with those used in Figure 3.9. There is a single, stable homogeneous steady state for $m \in [0, 1.138)$ which loses stability at $m \approx 1.138$ where a pitchfork bifurcation occurs and a pair of stable branches representing a period-2 spatial pattern emerge. The pitchfork bifurcation corresponds to a sign change in the Routh-Hurwitz condition $a_3(-1)$ as illustrated by the co-location of the pitchfork bifurcation with the colour change from black to grey. Open circles indicate an unstable limit cycle emerging from the Hopf bifurcation at $m \approx 26.12$ which corresponds to a sign change in the Routh-Hurwitz condition $a_1 a_2(1) - a_3(1)$ as shown by the colour change from grey to white. Supplementary plots show how the slope of $h(x)$ around the pitchfork relates to the number of crossings points of x , $h(x)$ and $h \circ h(x)$. **PB** - pitchfork bifurcation

such that, in quadrants $A < 0, B < 0$ and $A > 0, B > 0$, $h(x)$ is always sandwiched between the curves $y = h \circ h(x)$ and $y = x$. A period-2 patterning solution in these quadrants would require $h \circ h(x)$ to be of the form shown in Figure 3.13 which violates (3.6.2). Hence only homogeneous solutions exist in these quadrants and period-2

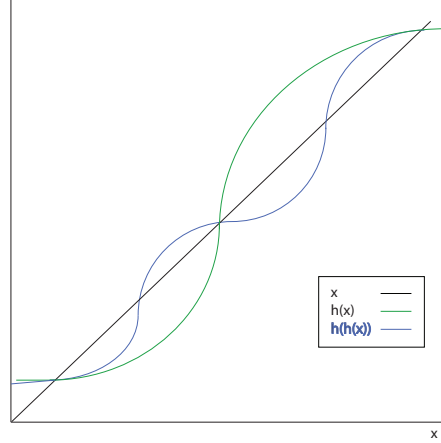


Figure 3.13: A sketch of the form $h \circ h(\cdot)$ would be required to take for the system in equations (3.5.1)-(3.5.3) to exhibit a period-2 pattern in the quadrants $A, B < 0$ and $A, B > 0$. When $h \circ h(\cdot)$ has distinct fixed points it violates the result (3.6.2) following from Lemma 1 and no longer sandwiches $y = h(x)$ between itself and the line $y = x$. Hence there can be no period - 2 patterns in these quadrants.

patterning solutions cannot occur.

For stronger feedback strengths in this quadrant, an unstable limit cycle emerges from a Hopf bifurcation but we never see this numerically. The same behaviour arises for $A > 0, B > 0$.

Although the biologically relevant region of the A - B plane is the lower-right quadrant, our analysis suggests that a patterning instability can only occur when the slopes of f and g are of opposite signs (lower-right and upper-left quadrants). Changing the system parameters may shift the Routh-Hurwitz hyperbolae but their positions, relative to each other, remain unchanged. As such, the qualitative behaviour of the model in the upper-left and lower-right quadrants remains unchanged for any choice of physically realistic parameter values. The analysis here also holds regardless of the types of feedback functions, f, g , used. In these quadrants, traversing the boundary between the stable (black) and unstable (grey) regions allows the system to exhibit spatial instabilities corresponding to a pattern with a wavelength of 2 cells.

By continuing solutions for negative m (corresponding to an *increasing* saturating feedback function f), a single bifurcation diagram in the left half-plane, $B < 0$, summarises

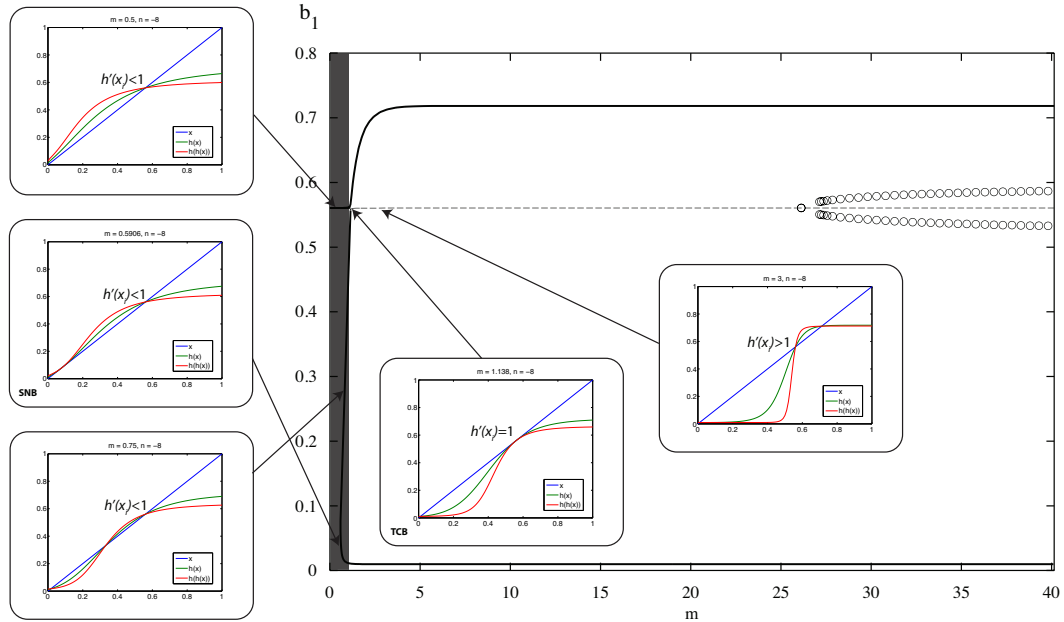


Figure 3.14: Continuation of solutions to the quasi-steady, two-cell system in (3.5.1)-(3.5.3) with $n = -8$ ($B = -6.0606$) whilst varying m , and hence A , along the path p_2 in Figure 3.9. Parameters are chosen as in Appendix D. Colours are consistent with those used in Figure 3.9. There is a single, stable homogeneous steady state for $m \in [0, 0.5906)$ which loses stability at $m \approx 0.5906$ when a pair of steady states is created (one stable, one unstable) in a saddle node bifurcation. So for $m \in (0.5906, 1.138)$ there are two, stable steady states (outer crossing points) and an unstable one (middle crossing point). At $m \approx 1.138$ there is a transcritical bifurcation at which the steady state at $b_j = 0.5605$ exchanges stability with the unstable steady state created in the saddle node bifurcation at $m \approx 0.5906$. The upper and lower branches represent two distinct, stable homogeneous solutions. Open circles indicate an unstable limit cycle emerging from a Hopf bifurcation at $m \approx 26.12$. Supplementary plots show how the slope of $h(x)$ around the bifurcation points relates to the number of crossings points of x , $h(x)$ and $h \circ h(x)$. **SNB** - saddle node bifurcation; **TCB** - transcritical bifurcation.

the system dynamics (see Figure 3.15).

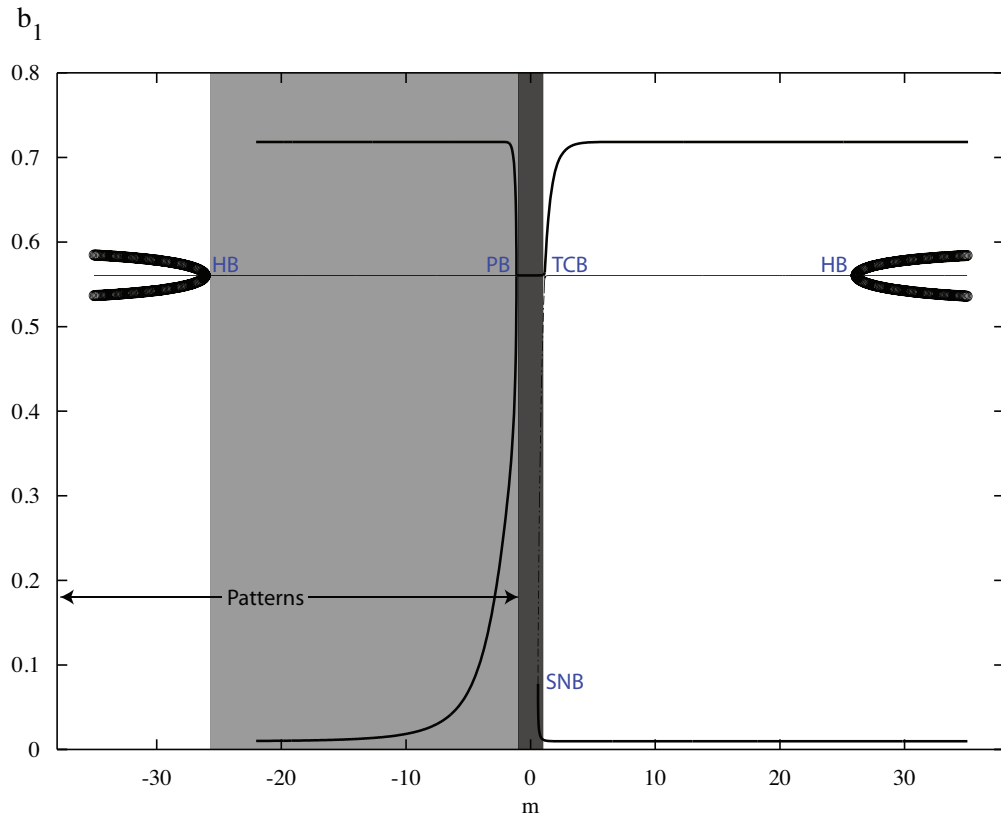


Figure 3.15: Bifurcation diagram produced by continuation of steady state solutions in the half-plane $B < 0$ showing how the existence and stability of solutions changes as m (and hence A) varies along the line $B = -6.0606$ ($n = -8$) in Figure 3.9. Solid lines represent stable steady states, thin/dotted lines represent unstable steady states and open circles represent limit cycle solutions. **SNB** - saddle node bifurcation; **TCB** - transcritical bifurcation; **HB** - Hopf bifurcation; **PB** - pitchfork bifurcation. Colours are consistent with those of Figure 3.9.

3.7 Numerical simulations for a string of N cells

In the following subsections, we numerically integrate the model in (3.2.10)-(4.1.16) using the *ode45* solver in MATLAB for a string of $N = 20$ cells. Parameter values are as outlined in Table E.1. Initial conditions are homogeneous and random perturbations about the homogeneous steady state. Each cell, j , Delta-Notch signals with its two neighbouring cells, $j \pm 1$, except for cells $j = 1$ and $j = N$ at each end of the spatial domain whose signalling is determined by the boundary conditions specified in a coupling matrix (not shown). We show numerical solutions for four different types of

boundary conditions.

3.7.1 Zero flux BCs: single neighbour with $2 \times$ inhibition

In this case, cells $j = 1$ and $j = N$ have a single neighbour, namely, cell $j = 2$ and $j = N - 1$ respectively, which deliver twice the regular level of Delta inhibition so that cells $j = 1$ and $j = N$ experience the same level of inhibition as the non-boundary cells. Numerical simulations of the string show that the system admits patterning in the grey region of the A - B plane when disturbed by spatially varying perturbations but not when disturbed by spatially uniform perturbations (see Figure 3.16(a)-(c)). The system is unstable to both homogeneous and inhomogeneous perturbations in the white region of the $A < 0, B > 0$ quadrant (see Figure 3.16(d)-(h)). In particular, all cells oscillate in synchrony when the homogeneous equilibrium is perturbed homogeneously (see Figure 3.16(d)). This is consistent with our linear analysis (see Figure 3.9) and previous numerical simulations of two-cell systems (see Figure 3.11).

3.7.2 Periodic BCs

In the case of periodic boundary conditions, cell $j = 1$ has neighbouring cells $j = 2$ and $j = N$ and cell $j = N$ has neighbouring cells $j = 1$ and $j = N - 1$. Applying periodic boundary conditions to a string of cells is equivalent to modelling a ring of cells. Simulations of the ring are shown in Figure 3.17. These are, again, consistent with our numerical observations in two-cell systems (see Figure 3.11).

3.7.3 Zero flux: single neighbour with regular inhibition

The boundary conditions in this section are another type of zero flux condition in which cells $j = 1$ and $j = N$ have a single neighbour, namely, cells $j = 2$ and $j = N - 1$ respectively which each deliver their normal level of inhibition. Therefore the cells at the boundary receive only half of the level of inhibition received by the other cells. The boundary conditions generate an inhomogeneity which allows the pattern to spread inwards from the boundaries, even when the homogeneous steady state is perturbed with a homogeneous perturbation. Cells at the centre of the domain continue to behave according to local influences until the inhomogeneity reaches them. Hence these are the last cells to pattern. For parameters from the grey region these cells transition from the homogeneous steady state to a pattern (see Figure 3.18a) and for parameters from the white region these cells transition from oscillating about the homogeneous steady state

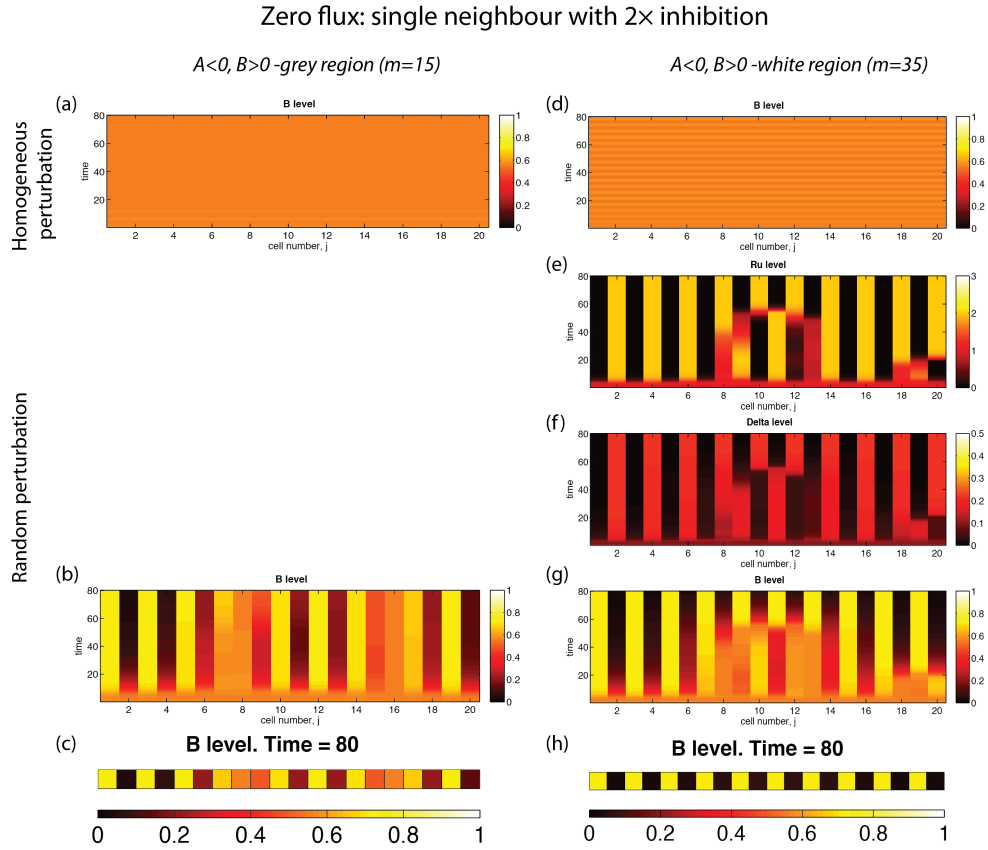


Figure 3.16: Numerical simulations of equations (3.5.1)-(3.5.3) for a string of $N = 20$ cells using zero flux boundary conditions. Initial conditions are perturbations of the homogeneous steady using: a small spatially uniform perturbation in (a) and (d); a randomly generated, spatially varying perturbation in (b)-(h). For $m = 15, n = 8$ (red square in the grey region on the path p_1 in Figure 3.9) the space-time plot in (a) shows stability to homogeneous perturbations; (b) shows instability to non-homogeneous perturbations; (c) shows the levels of bound Notch, b_j , in the string of cells at the end of the simulation in (b). For $m = 35, n = 8$ (red square in the white region on the path p_1 in Figure 3.9) (d) shows synchronised oscillations of bound notch in all cells when the homogeneous steady state is homogeneously perturbed; (e), (f), (g) show solutions for r_{Uj} , δ_j and b_j for the system with a randomly perturbed homogeneous steady state. (h) shows the solutions for b_j at the end of the simulation in (g).

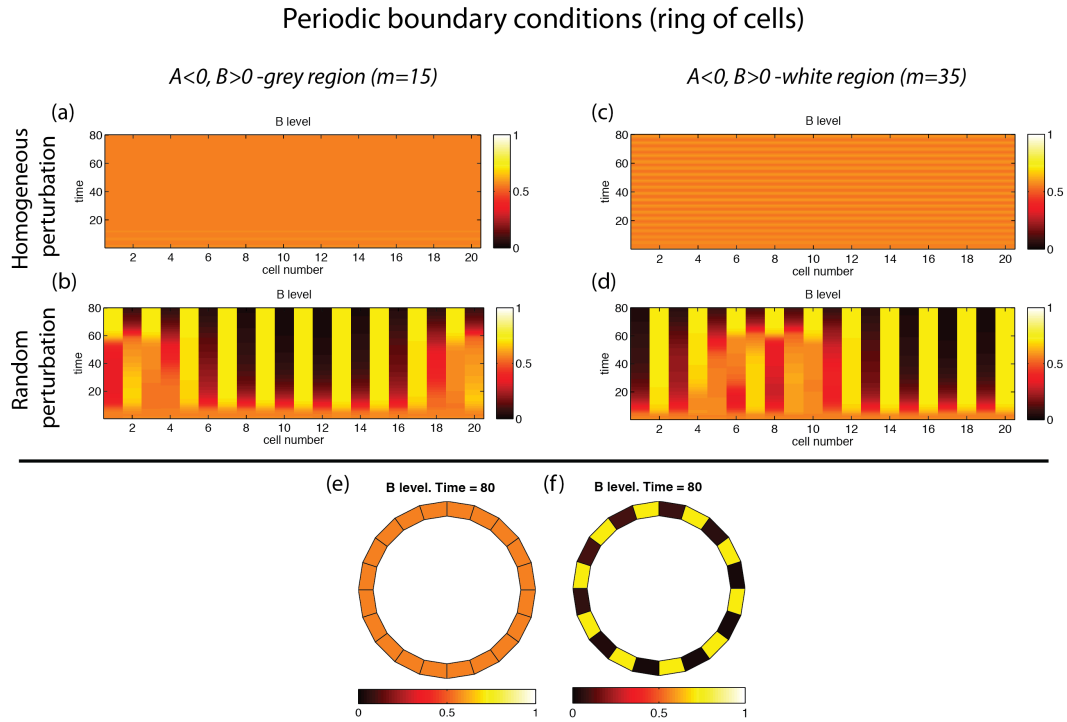


Figure 3.17: Numerical simulation of a ring of $N = 20$ cells using periodic boundary conditions in which cells $j = 2$ and $j = N$ neighbour cell $j = 1$ and cells $j = 1$ and $j = N - 1$ neighbour cell N . The left and right columns show simulations from the red square markers in the grey and white regions of Figure 3.9 which have $m = 15, n = 8$ and $m = 35, n = 8$ respectively. Homogeneous perturbations decay to the homogeneous steady state in the grey region in (a) and oscillate synchronously in all cells in (c). (b) and (d): In both grey and white regions, random/non-homogeneous perturbations of the steady state diverge to the period-2 spatial pattern. (e) and (f) show solutions at the end of the simulations in (a) and (d).

into a period-2 pattern (see Figure 3.18c). Random perturbations of the homogeneous steady state cause inhomogeneities to develop randomly across the domain and initiate formation of the period-2 pattern locally (see Figure 3.18b,d).

3.7.4 Zero flux: cell sees itself

In this section the cell at the boundary receives signals from both its single neighbouring cell as well as itself. Therefore cell $j = 1$ sees cells $j = 2$ and $j = 1$ adjacent to itself, and cell $j = N$ sees cells $j = N - 1$ and $j = N$. For a homogeneous perturbation, the boundary cells have two neighbours which are perturbed in the same way. Therefore the system is stable to homogeneous perturbations in the grey region (see Figure 3.19a) and oscillates about the steady state in the white region (see Figure 3.19c). Randomly perturbing the homogeneous steady state, causes the system to pattern in both the grey and white regions (see Figure 3.19b,d). However, boundary cells adopt a different steady state to the other cells in the domain as the inhibition they receive from themselves is different to that received from their other neighbour.

3.8 Travelling waves in the bistable system

In this section we simply acknowledge the presence of travelling waves exhibited by the system in particular regions of parameter space where there are multiple homogeneous steady states. Wave behaviour is not explored in this thesis, however, it has been extensively investigated in strings of cells by others [68, 115–117].

For $A, B < 0$ and $A, B > 0$ we have an unstable homogeneous steady state and a pair of stable homogeneous steady states. We expect the unstable and stable steady states to be connected by travelling waves. The waves can be seen moving in both directions in Figure 3.20. Cell $j = 50$ experiences a locally heterogeneous perturbation causing its solutions to fall into the basin of attraction of one of the stable steady states and a wave to be initiated. The remaining cells effectively experience a locally homogeneous perturbation until the moving wave causes their solutions to fall into the basin of attraction of one of the stable steady states.

3.9 Discussion

In this chapter we have investigated a discrete-space mathematical model of angiogenic tip cell selection in a string of cells. Using an ODE framework we have studied

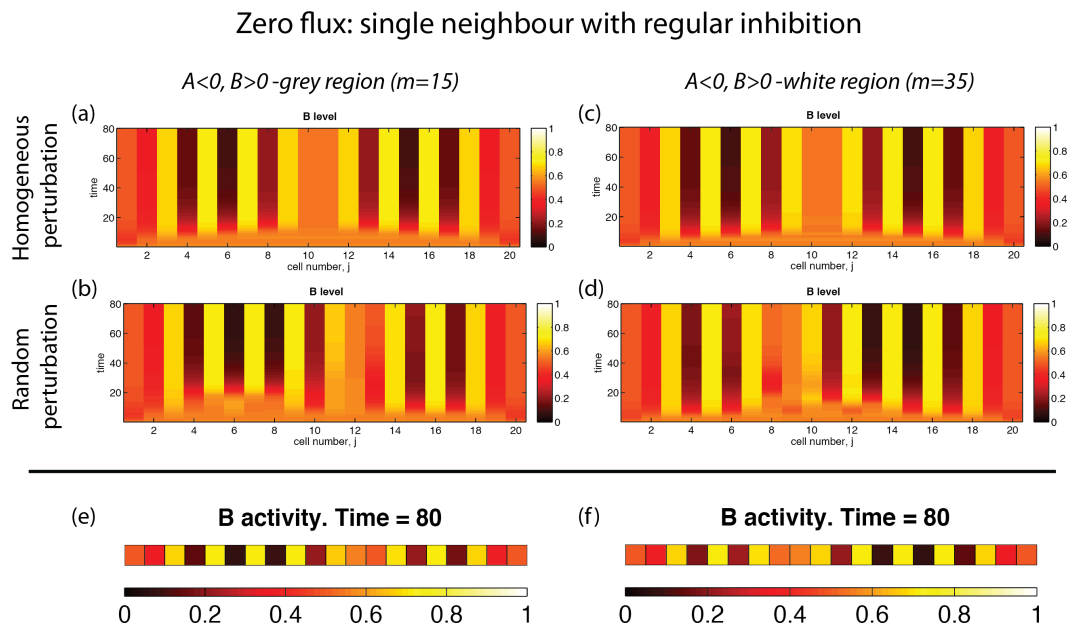


Figure 3.18: Numerical simulation for a string of 20 cells using boundary conditions in which the boundary cells, $j = 1$ and $j = N$, have a single neighbour, cell $j = 2$ and $j = N - 1$ respectively, that delivers the regular amount of inhibition. Hence cells $j = 1$ and $j = N$ only receive half of the amount of inhibition compared to other cells in the domain which have two neighbours. The left and right columns show simulations from the red square markers in the grey and white regions of Figure 3.9 which have $m = 15, n = 8$ and $m = 35, n = 8$ respectively. Homogeneous perturbations ((a) and (c)), including no perturbation (not shown) of the homogeneous steady state result in patterning. The boundary conditions cause an inhomogeneity from which the pattern spreads inwards. Hence cells at the centre of the domain either remain at the homogeneous steady state (a) or oscillate about it, (c), until the wave of patterning reaches them. (b) and (d) show similar behaviour in both grey and white regions where random/non-homogeneous perturbations of the steady state diverge to the period-2 spatial pattern. However, this pattern is induced by local inhomogeneities rather than a wave carrying the pattern inwards from the boundaries. (e) and (f) show solutions at the end of the simulations in (b) and (d).

Zero flux: cell sees itself

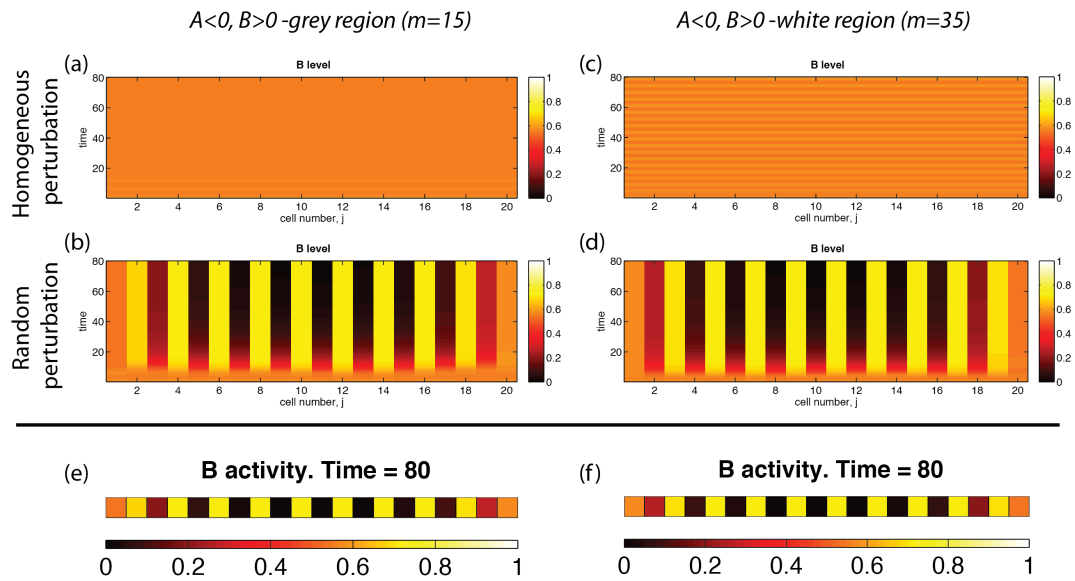


Figure 3.19: Numerical simulation for a string of 20 cells using boundary conditions in which cell $j = 1$ has neighbours $j = 1$ and $j = 2$ and cell $j = N$ has neighbours $j = N$ and $j = N - 1$. The left and right columns show simulations from the red square markers in the grey and white regions of Figure 3.9 which have $m = 15, n = 8$ and $m = 35, n = 8$ respectively. Homogeneous perturbations decay to the homogeneous steady state in the grey region in (a) and oscillate synchronously in all cells in the white region, (c). (b) and (d): In both grey and white regions, random/non-homogeneous perturbations of the steady state diverge to the period-2 spatial pattern but cells at the boundary settle to a different steady state. (e) and (f) show solutions at the end of the simulations in (b) and (d).

Travelling wave solutions connect stable homogeneous steady states

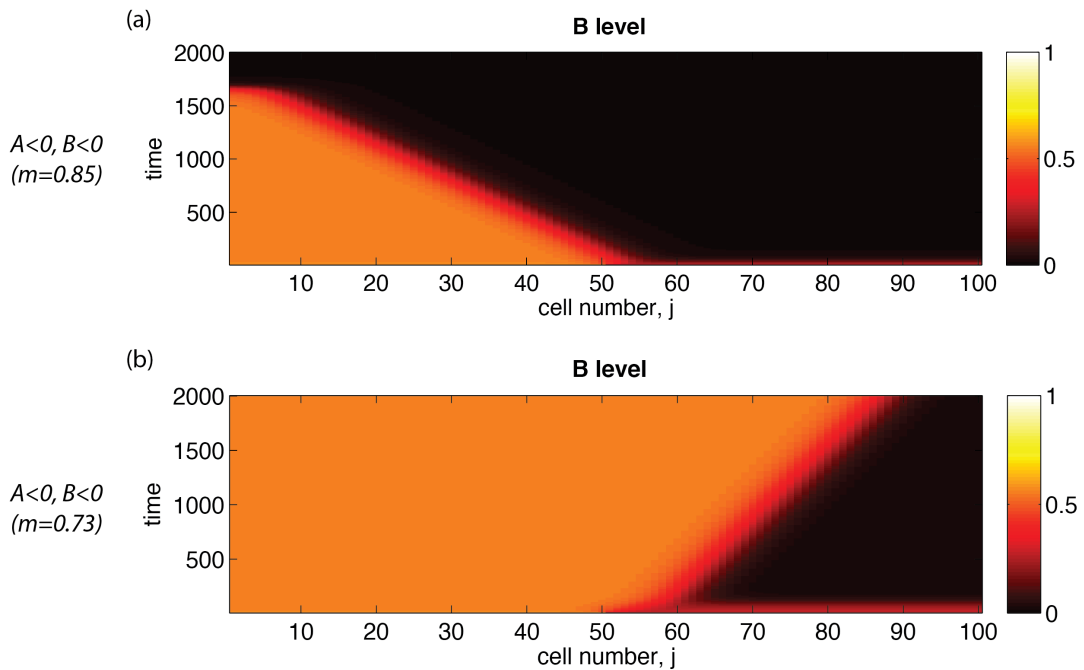


Figure 3.20: Numerical simulation for a string of 100 cells using zero flux boundary conditions as per Figure 3.16. Parameters are as per Figure 3.14 with $m < 1.138$ as specified within the figure. Hence there are two outer, stable homogeneous steady states and one unstable one between these. Initial conditions are the stable steady state at $b_e = 0.5605 + 0.1$ for $1 \leq j \leq 50$ and $b_e = 0.5605 - 0.3$ for $51 \leq j \leq 100$. (a) For $m = 0.85$, we see a travelling wave moving to the left and all solutions tend to the lower steady state near $b_e \approx 0$. (a) For $m = 0.73$, we see a travelling wave moving to the right and all solutions tend to the upper steady state at $b_e \approx 0.5605$.

the properties of an intracellular VEGF–Delta–Notch signalling pathway determining the emergence of a salt-and-pepper spatial pattern from an initially homogeneous population of ECs, where every other cell is fated to become a sprouting tip cell. Bentley and colleagues originally studied this system using a hierarchical agent-based modelling framework and we here make various comparisons to their work [81]. By using a dynamical systems approach we were able to use mathematical tools such as linear stability analysis and bifurcation theory to analyse our model. No such analytical methods exist for agent-based models.

We focus only on the initial process of tip cell selection in metazoan development, unlike other models of angiogenesis, some of which model processes such as the enzymatic breakdown of the primary vessel wall, tip cell migration, sprout elongation and proliferation, interactions with the extracellular matrix, anastomosis and remodelling [79, 84].

Our model exhibits the period-2 (“salt-and-pepper”) spatial pattern, previously seen in both the Bentley and Collier models [67, 81], and predicts that it is the dominant mode. This suggests that longer wavelength patterns may require additional mechanisms. These could include, for example, the inclusion of cell growth, proliferation or long range filopodia growth, in the lateral direction, transmitting Delta-Notch signalling between ECs further afield [86].

We used numerical simulations and bifurcation analysis, to confirm the pattern forming potential of our model. By linearising a reduced system of equations ((3.5.1)-(3.5.3)), which assume a quasi-steady state for bound VEGFR-2 and Notch receptor conservation, we were able to use the Routh-Hurwitz stability criteria to determine when the system would admit a patterning instability in terms of parameters representing the feedback strengths of VEGFR-2 production, A , and Dll4 ligand production, B . This gave a single generic picture (Figure 3.9) which is always of the same form regardless of parameter choices or the functional forms of ligand and receptor production. This allows strong statements to be made about the model behaviour, for example, the system exhibits period-2 spatial (salt-and-pepper) patterns which can only occur if the type of feedback for VEGFR-2 and Dll4 production are different (one activating, one inhibiting). The analysis also suggests that the system always admits patterning via an instability in which a real eigenvalue changes sign and never via a Hopf instability.

In numerical simulations of our model, the feedback strengths, A and B , are proportional to the Hill coefficients, m and n , of the Hill functions used to model the production of ligands and receptors. Thus, in a similar way to the Collier model, our model relies on co-operativity in order to exhibit period-2 patterns [67]. This is in contrast to the

recent work by Sprinzak and colleagues in which the mutual inactivation of Delta and Notch on the same cell, due to binding, provides the non-linearity needed to exhibit period-2 patterns in the absence of co-operativity [75]. When the feedback strengths in our model are either both activating or both inhibiting, the system is bistable with a pair of stable homogeneous solutions and one unstable homogeneous solution. By studying our model for an N -cell system, we were able to verify that the same linear analysis holds for strings of cells. For appropriate choices of initial conditions, we also see travelling wave solutions moving in both directions which connect the unstable and stable homogeneous steady states (see Figure 3.20). Travelling wave behaviour between homogeneous steady states was also seen in Monk’s model of juxtacrine signalling [115].

Our model, like the Collier model, has two feedback loops, one positive and one negative. However the Collier model only considers two species per cell: Delta activity and Notch activity. This is in contrast to our model which incorporates two extra equations for unbound and bound VEGF receptors per cell. Another difference is that our model explicitly considers Delta–Notch and VEGF–VEGFR-2 binding and uses concentrations to describe the species rather than the measures of activity used in the Collier model.

A feature of our model is that the “salt-and-pepper” patterning window exists for a finite range of values for \hat{V} , which can be interpreted as the EC’s perception of VEGF in the environment and \hat{g}_{max} , which can be interpreted as the strength of inhibition delivered to neighbouring cells. At high concentrations of extracellular VEGF, our model exhibits a solitary homogeneous steady state whereas the Bentley model exhibits oscillations [81]. The oscillations in their model may be due to a delay caused by the “passing of actin tokens” between the memAgents comprising the filopodia in their model. Our model, however, does not account for such delayed effects.

Incorporating delays into our model is a possible avenue for future work that may allow our model to exhibit stable limit cycle solutions. Interestingly our model, given by equations (3.5.1)-(3.5.3), which uses parameter choices from Appendix D, also exhibits oscillations but these emerge via a Hopf bifurcation when the feedback strength is sufficiently strong (see grey-white transition in Figure 3.9). This limit cycle was found to be unstable and was only detected in numerical simulations when perturbing the homogeneous steady state homogeneously. Oscillatory feedback loops in cells communicating via Notch signalling are crucial in other contexts such as attaining the correct spacing of somites by the vertebrate segmentation clock [89, 118, 119].

Cells at different locations in the embryo may be located in different regions of parameter space. For instance, ECs in the dorsal wall of the zebrafish DA sprout to form

secondary intersomitic blood vessels whereas ECs in the ventral wall, which hours later become specified as HSC precursors, remain relatively quiescent. Cells in the ventral wall do not sprout or migrate but instead maintain the integrity of the vessel, a trait likely due to the closer proximity of the dorsal wall to the (somatic) VEGF source. Our model could be extended to incorporate both vessel walls, including the ECs of the ventral wall. This may allow us investigate how the signalling is different in each wall and whether the differential VEGF signal sensed by the cells of each wall could account for their distinct behaviour. The ECs of the ventral wall may, for example, lie at a location in parameter space in which there is a single stable homogeneous steady state rendering them unable to pattern, whereas cells in the dorsal wall may lie inside the patterning window (see Figure 3.4). Another possibility is that perhaps both walls exhibit patterning but there are extra mechanisms, that we have not accounted for, which suppress tip cell selection in the ventral wall. In Chapter 2, we showed how, for some parameter values, patterning could amplify the average concentration of *runx1*, relative to the homogeneous steady state. Patterning could, in theory, amplify the average level of a factor suppressing tip cell selection in the ventral wall.

The inclusion of transcriptional, translational and recovery delays is one way of extending this work as they have been shown to be important in other models of Delta-Notch signalling [81, 89]. Our model inevitably overlooks the effect of other pathways involved in angiogenesis and vessel morphogenesis, for instance, the connections between the Notch pathway and others such as $TGF\beta$, Hedgehog, or Wnt signalling may need to be considered [23]. However the analysis that we have presented here would be much more difficult, if not impossible, to carry out in the presence of these other signalling pathways. Another interesting way to develop this work would be to extend the existing model to n -dimensional arrays of squares and/or hexagons in a fashion similar to Webb and Owen [71].

In the next chapter we extend the ODE model of this chapter by incorporating filopodia growth in a gradient of extracellular VEGF, and feedback from filopodia length onto VEGFR-2 production, into our current ODE model.

Modelling and Analysis of Filopodia Extension Regulated by VEGF–Delta–Notch Signalling in Angiogenic Tip Cell Selection

In this Chapter we extend our model to investigate how filopodia extension can influence, and be influenced by VEGF receptor production. The assumption of a constant extracellular VEGF concentration is relaxed and, as in the Bentley model [81], we allow filopodia to grow in linear gradients of extracellular VEGF, perpendicularly away from the cell. In multi-cellular simulations using strings of ECs, the VEGF concentration is kept homogeneous in the direction parallel to the string. As the maximal growth rate parameter of filopodia tends to zero, the system reduces to the model analysed in Chapter 3. We consider the effect of filopodia growth on spatial patterning in both spatially homogeneous and linearly increasing gradients of VEGF. This is done for the two cases where filopodia extension enhances VEGFR-2 production or where there is no such effect. We show that whilst filopodia growth is coupled to the reactions from the model in Chapter 3, both enhancement of VEGF receptor production by filopodia extension and linear gradients of VEGF are mechanisms that facilitate pattern formation in strings of ECs. This is demonstrated using appropriate numerical simulations and bifurcation analysis. Moreover, our analysis in this chapter suggests that VEGF gradients (as opposed to the absolute VEGF concentration) may not be required to achieve the salt-and-pepper pattern. In such cases patterning can be achieved via positive feedback from filopodia length onto VEGFR-2 production or via the signalling processes alone which are discussed in Chapter 3.

4.1 Model Overview

We extend our VEGF-Delta-Notch model of Chapter 3 (see equations (5.3.4)-(3.2.7)) to investigate how filopodia growth modulates pattern formation in populations of ECs. Filopodia are membrane protrusions formed by the recruitment and polymerisation of actin in response to a chemoattractant [81]. Actin levels are increased in response to VEGF - VEGFR-2 binding leading to filopodia extension. Filopodia are also able to retract when there is insufficient VEGF available [81, 110, 111].

Thus far we have only considered a constant concentration of extracellular VEGF. However experimental work by Ruhrberg and colleagues, shows that the local gradient of VEGF is important for EC sprouting and migration [111]. Hence we also incorporate a VEGF gradient into our model. For simplicity, we consider a *linear* gradient. In the presence of a VEGF gradient, filopodia extend in the direction of higher VEGF concentration [110, 111] and thus a longer filopodium will allow a cell to access more VEGF via VEGFR-2 located along its length (see Figure 4.1). In our model, filopodia grow by sensing the average concentration of bound VEGFR-2. Therefore, even in a constant field of VEGF, longer filopodia expose a greater surface area of cell membrane to the environment, allowing the cell access to more extracellular VEGF. Hence the growth of filopodia introduces a positive feedback to the model: the binding of VEGF allows for the extension of filopodia, which in turn allow for further binding of VEGF. Thus, cells with longer filopodia can quickly gain an advantage in acquiring a tip cell fate. This ultimately accelerates and facilitates pattern formation in ECs.

The notation used for the variables is the same as that used in §3. However, due to the inclusion of a spatially varying extracellular VEGF concentration, the variables are now interpreted as spatially averaged concentrations rather than concentrations alone. We revisit this in Chapter 5, where we present a PDE model of this system in which VEGF receptors are transported along filopodia. We show that in the limit of large receptor diffusivity, the concentrations of receptors become homogeneous and this ODE model, which uses spatially averaged variables, is a good approximation with reasonable assumptions.

4.1.1 Filopodia growth

We assume that each cell, j , extends a single filopodium from its upper surface which is characterised by its time-dependent length, $F_j(t)$. The length of the periphery of cell j is given by $L_0 + F_j(t)$ where L_0 is the fixed length of the cell body membrane and is considered to be constant for all cells (see Figure 4.1). Note that $F_j(t) \geq 0, \forall t \in \mathbb{R}, j \in \mathbb{Z}$.

Another assumption is that the growth of filopodia is a direct consequence of VEGFR-2 activation [81, 110] and the details of actin accumulation are ignored. Filopodia growth is then determined by the following ODE:

$$\frac{dF_j}{dt} = \phi w(\bar{R}_{Bj}) - \gamma F_j(t), \quad (4.1.1)$$

where the production term $w(\bar{R}_{Bj})$ is assumed to be a positive, monotonically increasing Hill function of the *average* VEGFR-2 concentration of cell j , \bar{R}_{Bj} . This is given by

$$w(\bar{R}_{Bj}) = \frac{\bar{R}_{Bj}^q}{C^q + \bar{R}_{Bj}^q}, \quad (4.1.2)$$

where q represents the strength of response to bound VEGFR-2, ϕ represents the maximal extension rate of the filopodium and C represents the average bound VEGF receptor concentration at which the extension rate is half-maximal, $\frac{\phi}{2}$. This is analogous to a threshold level of bound VEGF receptors required for filopodial elongation. Lastly, γ represents the rate of retraction of the filopodium. This choice of feedback function is phenomenological as the exact mechanism by which bound VEGF receptors cause filopodia extension is unclear.

The following system of equations is formulated by coupling (4.1.1) to equations (3.2.10)-(3.2.14), which have been modified to account for enhanced VEGFR-2 production due to filopodia growth and a non-constant extracellular VEGF distribution:

$$\frac{dF_j}{dt} = \phi w(\bar{R}_{Bj}) - \gamma F_j(t), \quad (4.1.3)$$

$$\frac{d\bar{R}_{Uj}}{dt} = (1 + \hat{\theta}F_j(t))f(\bar{B}_j) + k_{-VR}\bar{R}_{Bj} - k_{VR}\bar{R}_{Uj} \frac{\int_0^{L_0+F_j(t)} V(x)dx}{L_0 + F_j(t)} - \lambda\bar{R}_{Uj}, \quad (4.1.4)$$

$$\frac{d\bar{R}_{Bj}}{dt} = k_{VR}\bar{R}_{Uj} \frac{\int_0^{L_0+F_j(t)} V(x)dx}{L_0 + F_j(t)} - k_{-VR}\bar{R}_{Bj}, \quad (4.1.5)$$

$$\frac{d\bar{\Delta}_j}{dt} = g(\bar{R}_{Bj}) + k_{-B} \left(\frac{\bar{B}_{j-1} + \bar{B}_{j+1}}{2} \right) - k_B \bar{\Delta}_j \left(\frac{\bar{N}_{j-1} + \bar{N}_{j+1}}{2} \right) - \mu\bar{\Delta}_j, \quad (4.1.6)$$

$$\frac{d\bar{N}_j}{dt} = k_{-B}\bar{B}_j - k_B \left(\frac{\bar{\Delta}_{j-1} + \bar{\Delta}_{j+1}}{2} \right) \bar{N}_j, \quad (4.1.7)$$

$$\frac{d\bar{B}_j}{dt} = k_B \left(\frac{\bar{\Delta}_{j-1} + \bar{\Delta}_{j+1}}{2} \right) \bar{N}_j - k_{-B}\bar{B}_j. \quad (4.1.8)$$

The new terms representing the modifications (filopodia growth terms) are shown in red. Moreover

$$V(x) = \begin{cases} V_0 & 0 \leq x \leq L_0 \\ V_0 + \psi(x - L_0) & L_0 \leq x \leq L_0 + F_j(t) \end{cases}, \quad (4.1.9)$$

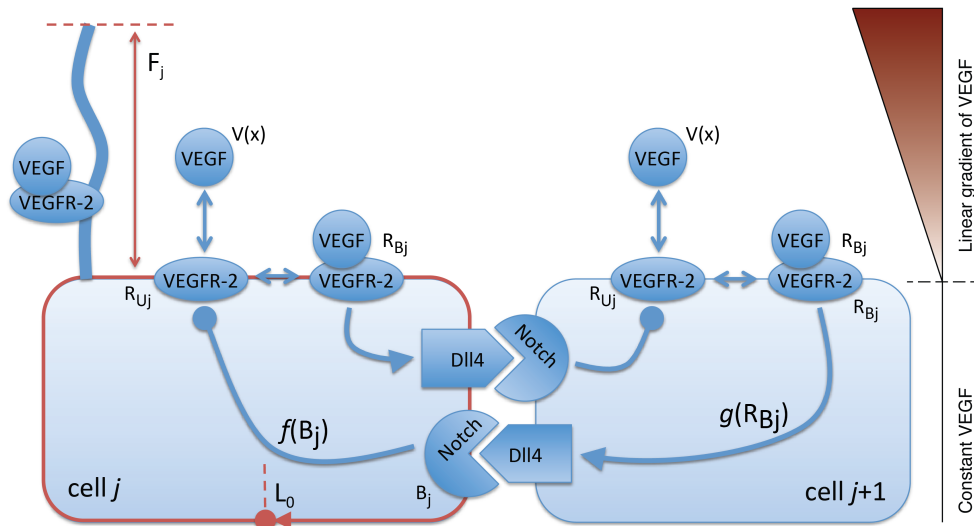


Figure 4.1: Sketch of a two-cell system for the model including filopodia growth. The ECs communicate via Delta-Notch signalling and the interactions between Delta and Notch, VEGF and VEGFR-2, rates of turnover and the feedback functions are identical to the model neglecting filopodia growth (3.2.10)-(3.2.14). Each cell body has a constant membrane length L_0 and extends a single filopodium of length $F_j(t)$ on which bound and unbound VEGF receptors are located. We consider the effect of linear gradients of VEGF on the pattern forming potential of our model in which the cell bodies are situated in a constant concentration of VEGF and the filopodia extend into the gradient of VEGF. The corresponding VEGF profile is shown on the right hand side.

is the spatial VEGF profile. The cell bodies, which have a fixed length, L_0 , are located in a constant concentration of VEGF, V_0 , and the filopodia grow perpendicularly away from the cell, into the linear gradient of VEGF which initiates at the upper membrane of the cell and increases linearly away from it with gradient ψ (see Figure 4.1).

The term $f(B_j)$ is a decreasing function of bound Notch receptors representing inhibition of VEGFR-2 production as in the model neglecting filopodia growth in §3 (see also Figure 4.1). The term $(1 + \hat{\theta}F_j(t))$ represents enhanced VEGFR-2 production in cells with longer filopodia lengths.

Since we are assuming spatially averaged concentrations for VEGFR-2, we incorporate a non-constant extracellular VEGF concentration, $V(x)$, into our existing model by considering a spatial *average* of VEGF seen by the cell. This is accomplished by integrating out the spatial dependence in equation (4.1.9) and dividing by the total domain length, $L_0 + F_j$, as shown by the VEGF–VEGFR-2 binding terms in equations (4.1.4) and (4.1.5). The integral is evaluated as follows:

$$\begin{aligned}
 \int_0^{L_0+F_j(t)} V(x)dx &= \int_0^{L_0} V_0 dx + \int_{L_0}^{L_0+F_j(t)} (\psi(x - L_0) + V_0) dx \\
 &= L_0V_0 + \frac{\psi}{2}x^2 \Big|_{L_0}^{L_0+F_j(t)} + (V_0 - \psi L_0)x \Big|_{L_0}^{L_0+F_j(t)} \\
 &= L_0V_0 + \frac{\psi}{2} (F_j(t)^2 + 2L_0F_j(t)) + (V_0 - \psi L_0)F_j(t) \\
 &= V_0 (L_0 + F_j(t)) + \frac{\psi}{2}F_j(t)^2.
 \end{aligned} \tag{4.1.10}$$

The $\frac{\int_0^{L_0+F_j(t)} V(x)dx}{L_0+F_j}$ terms with numerator as per equation (4.1.10) replace the constant concentration of VEGF, V , used in the ODE model without filopodia binding (compare equations (4.1.4) and (4.1.5) in §3 with (3.2.3) and (3.2.4)).

We non-dimensionalise this expression for the VEGF concentration and rescale equations (4.1.3)-(4.1.5) noting that the filopodia length, $F_j(t)$, is scaled with the length of the membrane, L_0 (see Appendix B for details of scalings and parameter groupings), whereas equations (4.1.6)-(4.1.8) are non-dimensionalised in the same way as for the model neglecting filopodia growth (see Appendix A).

The dimensionless system is given as follows,

$$\frac{dF_j}{dt} = \phi w(r_{Bj}) - \gamma F_j, \quad (4.1.11)$$

$$\frac{dr_{Uj}}{dt} = (1 + \theta F_j) f(b_j) + r_{Bj} - r_{Uj} \left(V_0 + \frac{\psi}{2} \frac{F_j(t)^2}{1 + F_j(t)} \right) - \lambda r_{Uj}, \quad (4.1.12)$$

$$\frac{dr_{Bj}}{dt} = r_{Uj} \left(V_0 + \frac{\psi}{2} \frac{F_j(t)^2}{1 + F_j(t)} \right) - r_{Bj}, \quad (4.1.13)$$

$$\frac{d\delta_j}{dt} = g_{max} g(r_{Bj}) + k_{-B} \left(\frac{b_{j-1} + b_{j+1}}{2} \right) - k_B \left(\frac{n_{j-1} + n_{j+1}}{2} \right) \delta_j - \mu \delta_j, \quad (4.1.14)$$

$$\frac{db_j}{dt} = k_B \left(\frac{\delta_{j-1} + \delta_{j+1}}{2} \right) n_j - k_{-B} b_j, \quad (4.1.15)$$

$$n_j = 1 - b_j. \quad (4.1.16)$$

Boundary conditions used in numerical simulations of (4.1.11)-(4.1.16) are identical to those used for the no-filopodia model (see §3.2.1). Initial conditions used in simulations are either a homogeneous or random perturbation about the homogeneous steady state.

4.2 Steady state analysis

Steady states of the model in equations (4.1.11) - (4.1.16) are found by setting the time derivatives of these equations to zero. We begin by looking for homogeneous solutions for which

$$u_j = u_e \quad \forall j, \quad \text{where} \quad u_j = F_j, r_{Uj}, r_{Bj}, \delta_j, n_j, b_j.$$

With $\frac{d}{dt} = 0$, equation (4.1.12) + (4.1.13) gives

$$r_{Ue} = \frac{1}{\lambda} (1 + \theta F_e) f(b_e), \quad (4.2.1)$$

and equation (4.1.11) gives

$$F_e = \frac{\phi}{\gamma} w(r_{Be}). \quad (4.2.2)$$

Substituting both (4.2.1) and (4.2.2) into equation (4.1.13), with $\frac{d}{dt} = 0$, gives

$$r_{Be} = \frac{1}{\lambda} \left(1 + \frac{\theta \phi}{\gamma} w(r_{Be}) \right) f(b_e) \left(V_0 + \frac{\psi}{2} \frac{\frac{\phi^2}{\gamma^2} w(r_{Be})^2}{1 + \frac{\phi}{\gamma} w(r_{Be})} \right). \quad (4.2.3)$$

Since equations (4.1.14)-(4.1.16) are identical to equations (3.2.12)-(3.2.14) from the model without filopodia growth, we repeat the steps taken therein which yield

$$g_{max} g(r_{Be}) = \frac{\mu k_{-B} b_e}{k_B (1 - b_e)}. \quad (4.2.4)$$

This is comparable to equation (3.3.3) except in this model we cannot express r_{Be} , inside the argument of $g(\cdot)$, in terms of b_e due to the heavy coupling between equations (4.1.11)-(4.1.13). Thus equation (4.2.4) rearranges to

$$b_e = \frac{\hat{g}_{max}g(r_{Be})}{1 + \hat{g}_{max}g(r_{Be})} \quad (4.2.5)$$

where \hat{g}_{max} is the dimensionless parameter defined as $\hat{g}_{max} = \frac{g_{max}k_B}{\mu k_{-B}}$. Substitution of (4.2.5) into (4.2.3) gives one non-linear equation to solve for the homogeneous steady state for bound VEGFR-2:

$$r_{Be} = \frac{1}{\lambda} \left(1 + \frac{\theta\phi}{\gamma} w(r_{Be}) \right) f \left(\frac{\hat{g}_{max}g(r_{Be})}{1 + \hat{g}_{max}g(r_{Be})} \right) \left(V_0 + \frac{\psi}{2} \frac{\frac{\phi^2}{\gamma^2} w(r_{Be})^2}{1 + \frac{\phi}{\gamma} w(r_{Be})} \right). \quad (4.2.6)$$

Solutions to this equation can be visualised by plotting the fixed points of the right-hand side for varying values of the new filopodia growth parameters (see Figure 4.2). The homogeneous steady state is no longer unique in this model since, unlike $h(b_j)$ in the model without filopodia growth (see equation (3.3.4)), the right-hand side of equation (4.2.6) is not necessarily a monotonically decreasing function for all realistic parameter choices. Therefore there is not necessarily a unique fixed point and hence a homogeneous steady state. For $\psi = 0$, equation (4.1.11) decouples and this model is equivalent to the model without filopodia growth. In this case, the right-hand side of equation (4.2.6) is a decreasing function of r_{Bj} and the homogeneous steady state is unique. As ψ increases, the number of homogeneous steady states increases from 1 to 3. Non-zero receptor feedback via $\theta > 0$ is also likely to generate more homogeneous solutions.

Next we look for period-2 spatially patterned steady states which have $u_{j-1} = u_{j+1}, \forall j$. We denote this as a common variable $u_{j\pm 1}$ which replaces the averaged terms in equations (4.1.14)-(4.1.16). Setting the time derivatives to zero, and solving in the same way as for the homogeneous steady state, equations (4.1.11)-(4.1.13) yield equation (4.2.6) again, whereas solving equations (4.1.14)-(4.1.16) gives

$$b_{j\pm 1} = \frac{\hat{g}_{max}g(r_{Bj})}{1 + \hat{g}_{max}g(r_{Bj})}.$$

Thus the equations for period-2 patterning solutions are given by

$$r_{B1} = \frac{1}{\lambda} \left(1 + \frac{\theta\phi}{\gamma} w(r_{B1}) \right) f \left(\frac{\hat{g}_{max}g(r_{B2})}{1 + \hat{g}_{max}g(r_{B2})} \right) \left(V_0 + \frac{\psi}{2} \frac{\frac{\phi^2}{\gamma^2} w(r_{B1})^2}{1 + \frac{\phi}{\gamma} w(r_{B1})} \right), \quad (4.2.7)$$

$$r_{B2} = \frac{1}{\lambda} \left(1 + \frac{\theta\phi}{\gamma} w(r_{B2}) \right) f \left(\frac{\hat{g}_{max}g(r_{B1})}{1 + \hat{g}_{max}g(r_{B1})} \right) \left(V_0 + \frac{\psi}{2} \frac{\frac{\phi^2}{\gamma^2} w(r_{B2})^2}{1 + \frac{\phi}{\gamma} w(r_{B2})} \right). \quad (4.2.8)$$

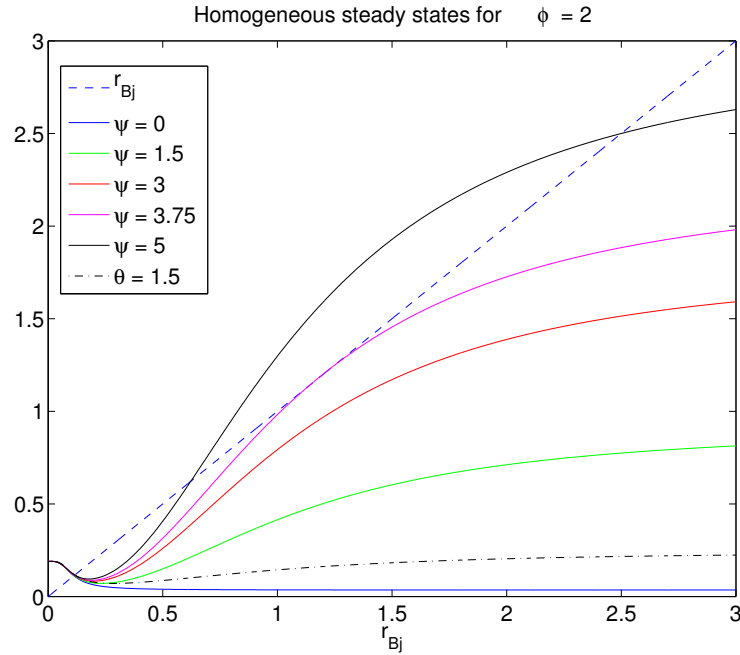


Figure 4.2: Homogeneous steady states of the ODE model with filopodia growth in equations (4.1.11)-(4.1.16) for filopodia growth parameter, $\phi = 2$, and increasing VEGF gradient, $\psi = 0, 1.5, 3, 3.75, 5$. Homogeneous steady states of the model correspond to fixed points of the right-hand side of equation (4.2.6) and intersections of the coloured curves with the line $r_{Bj} = r_{Bj}$. There is a single homogeneous steady state for $\psi = 0$ (solid blue line). Increasing ψ further increases the number of homogeneous steady states exhibited by the model from 1 to 3. The bifurcation point is located at approximately $\psi = 3.75$ (magenta line). The dash-dot line corresponds to $\psi = 0, \theta = 1.5$ and is also not a strictly decreasing function, suggesting that the system is also likely to have more homogeneous steady states for larger values of θ whilst keeping ψ fixed.

These can be visualised in the $r_{B1} - r_{B2}$ plane for $\psi = 0.38$ (see Figure (4.3)). This picture, however, changes dynamically as ψ is changed and this is explored in more detail in the next section where numerical bifurcation analysis is used to analyse the behaviour of the model's steady states.

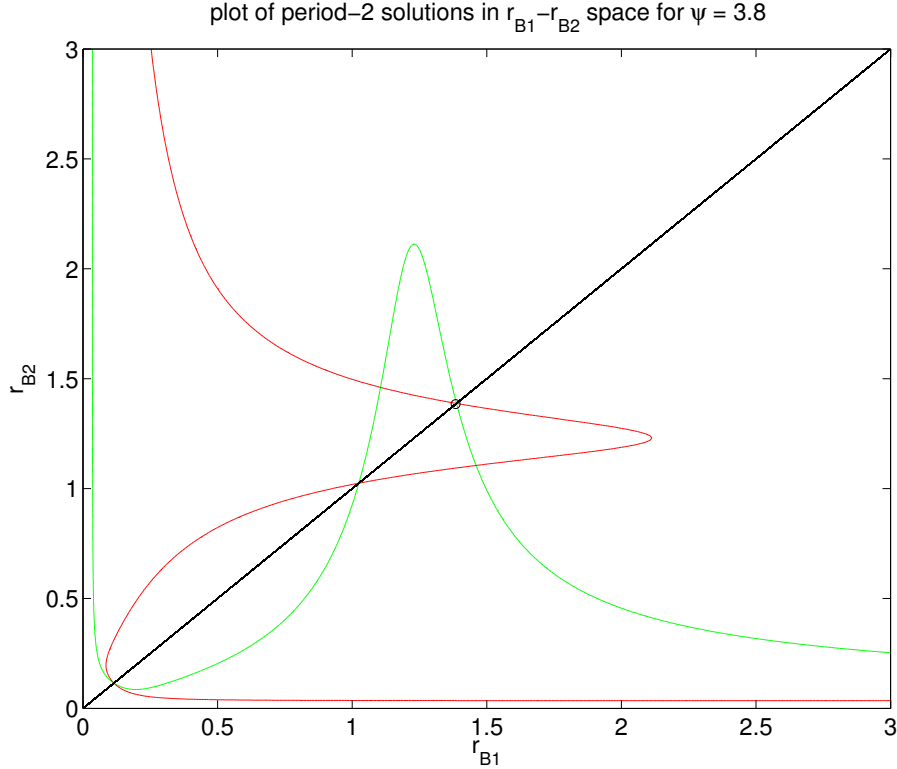


Figure 4.3: Figure showing how the period-2 steady states of the ODE model with filopodia growth in equations (4.1.11)-(4.1.16) for linear VEGF gradient $\psi = 3.8$, which is just after the bifurcation shown by the magenta curve in Figure 4.2. The green and red curves are plots of equations (4.2.7) and (4.2.8) respectively. Intersections of the curves represent solutions to this pair of equations, in particular, homogeneous solutions are located on the line $r_{B1} = r_{B2}$ and the remaining intersections represent period-2 patterning solutions. For $\psi = 3.8$ there are three homogeneous solutions in a agreement with Figure 4.2 and two pairs of period-2 patterning solutions. One is located at $r_{B1} = 1.4605, r_{B2} = 1.1052$ and the other (not visible) is located at $r_{B1} = 12.06, r_{B2} = 0.03489$.

4.3 Two-cell analysis

Our model with filopodia growth, (4.1.11)-(4.1.16), includes three new parameters, which determine how filopodia growth modulates and is modulated by the system

Parameter	Numerical Value	Physical meaning
V_0	0.095	Constant level of VEGF seen by cell body
λ	0.5	Decay rate of unbound VEGFR-2
g_{max}	1.3129	Maximum production of Dll4
k_{-B}	0.25	Dissociation rate of bound Delta-Notch complexes
k_B	2.285	Association rate of Delta and Notch
μ	1	Decay rate of Delta ligand
α	0.5	Response threshold for Dll4 production
β	0.4376	Response threshold for VEGFR-2 production
m	2	Response strength for VEGFR-2 production
n	2	Response strength for Dll4 production
γ	0.5	Retraction rate of filopodia
C	1	Response threshold for filopodia production
q	2	Response strength for filopodia growth
ϕ	2	Maximum growth rate for filopodia
ψ	Variable	Gradient of VEGF
θ	Variable	Effect of filopodia on VEGFR-2 production

Table 4.1: Table of dimensionless parameter values for the filopodia model and their physical meaning. Shaded rows indicate new parameters of the model with filopodia growth

dynamics. These key parameters are:

- ϕ - the maximum growth rate of filopodia
- θ - the extent to which filopodia regulate the production of unbound VEGFR-2
- ψ - the gradient of extracellular VEGF

To investigate the effect of each of these we first run numerical simulations of a two-cell system defined by equations (4.1.11)-(4.1.16) using combinations of the 3 new coupling parameters, whilst keeping the remaining parameters fixed (see Table 4.1). We then perform bifurcation analysis using *xppaut* numerical continuation software on the same two-cell system to verify our numerical observations. We show that in the presence of filopodia growth, ($\phi > 0$), the parameters, θ and ψ , can induce or amplify patterning.

4.3.1 Feedback through filopodia growth

We remark that as the concentration of r_{Bj} at which the filopodia growth is half of its maximum value, $C \rightarrow \infty$, or if $\phi = 0$ in (4.1.11) then the homogeneous steady state value of filopodia length is $F_e = 0$ and there is no contribution from filopodia growth to the production of unbound VEGF receptors or to the integrals in equations (4.1.12) and (4.1.13). In this case the model reduces back to the model neglecting filopodia growth (see equations (3.2.10)-(3.2.14)). Since $\phi > 0$ is a necessary condition for the existence of a non-zero, steady state filopodia length, all subsequent analysis is performed with $\phi > 0$.

Thus we first incorporate the effect of filopodia growth due to VEGF binding ($\phi > 0$), in the absence of receptor feedback ($\theta = 0$) and a VEGF gradient ($\psi = 0$). In this case equation (4.1.11) decouples and the steady state value for the filopodia length is given by

$$F_e = \frac{\phi}{\gamma} \cdot \frac{r_{be}^q}{C^q + r_{be}^q}. \quad (4.3.1)$$

In this case the steady states and the criteria for period-2 spatial patterns are identical to those for the system without filopodia, illustrated in Figure 3.5. We have confirmed this with numerical simulations of a two-cell system with $\phi = 0$ and $\phi = 2$ (not shown).

4.3.2 Feedback through VEGF receptor production ($\theta > 0 = \psi$)

In this section we consider the effect of feedback via VEGFR-2 production, ($\theta > 0$), whilst neglecting the effect of spatial variations in extracellular VEGF ($\psi = 0$). Figure 4.4 shows that as θ is increased, the patterning window gets both taller and wider as the pitchforks move apart. Thus there are parameter sets which allow patterning for $\theta = 0$ but give a more exaggerated pattern for $\theta > 0$ and others that will not allow patterning with $\theta = 0$ but will for $\theta > 0$. This gives rise to two types of patterning behaviour: pattern amplification and pattern induction, which can both be observed in numerical simulations of the two-cell system defined by equations (4.1.11)-(4.1.16). (see Figure 4.5(a)-(c) and (a)-(b)). Pattern amplification and induction can be explained in terms of the positive feedback generated by $\theta > 0$. Longer filopodia give rise to increased levels of VEGFR-2, which in turn allow more VEGF to bind, further increasing the length of the filopodia.

Lastly we fix $V_0 = 0.12$, and analyse the effect that varying θ has on the existence and stability of steady states. The bifurcation diagram in Figure 4.6(a), for a two-cell system defined by equations (4.1.11)-(4.1.16), shows the steady state of bound Notch in cell 1

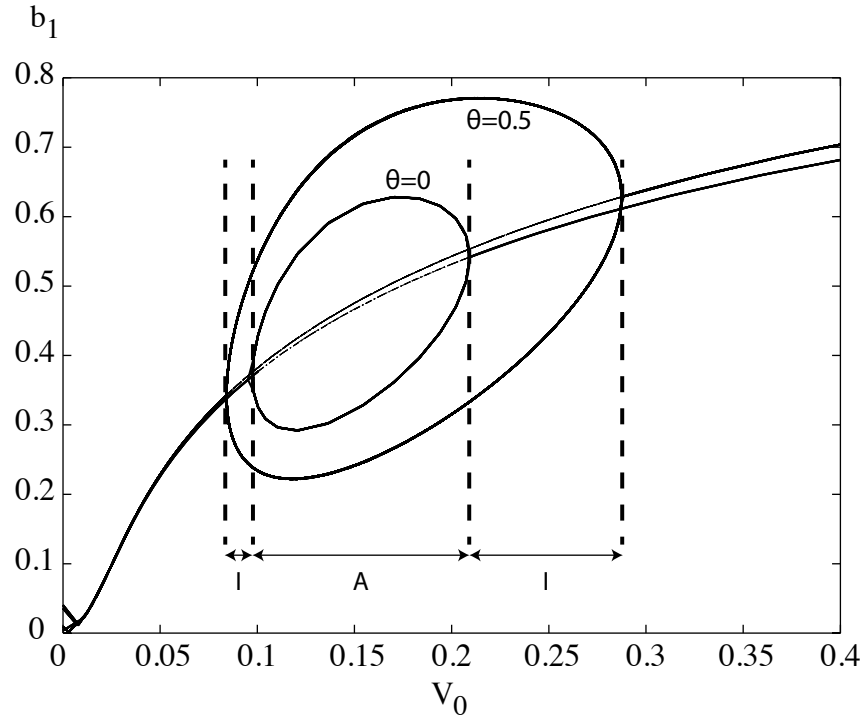


Figure 4.4: Bifurcation diagrams in V_0 -space for the system in (4.1.11)-(4.1.16) with parameters as per Table 4.1 for $\theta = 0$ (inner) and $\theta = 0.5$ (outer) showing a dilation of the patterning window in response to increasing feedback via increased VEGF receptor production, θ . Solid (thin/dotted) lines indicate stable (unstable) steady states. Changing θ from 0 to 0.5, causes the pitchforks to move further apart. Consequently, the stable period-2 patterning solutions also move away from the homogeneous steady state. This creates regions of parameter space where patterns can be induced or amplified by changing the value of θ . These regions are marked with I (induction region) and A (amplification region) and are delimited by vertical, dashed lines.

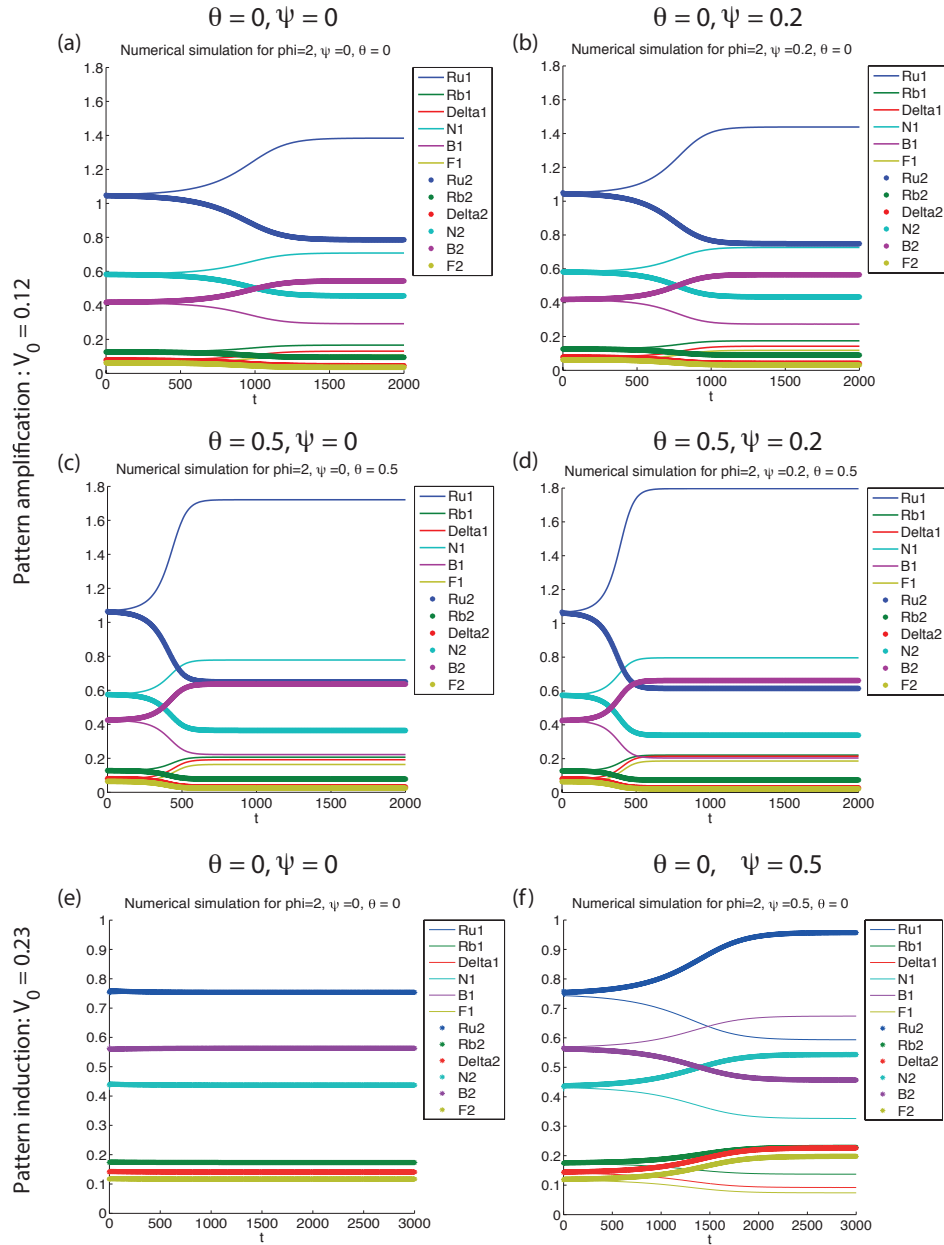


Figure 4.5: A demonstration of pattern amplification and induction using numerical simulations of the two-cell system in equations (4.1.11)-(4.1.16) with periodic boundary conditions and initial conditions corresponding to a random perturbation about the homogeneous steady state. Parameters are as per Table 4.1 unless otherwise specified. Lines - solutions in cell 1. Asterisks - solutions in cell 2. (a)-(d) show that one or both of θ and ψ are able to amplify the period-2 pattern. (e)-(f) show that patterning can be induced by activating the effect of the VEGF gradient ψ . Similar solutions for pattern induction are obtained when θ is made non-zero (not shown - but see induction regions in Figure 4.4).

against θ . As θ is increased, the system undergoes a pitchfork bifurcation at $\theta \approx 0.0712$ where the stable branch for the unique homogeneous steady state becomes unstable. At $\theta \approx 2.13$ the branches lose stability at a pair of fold bifurcations. At $\theta \approx 2.10$ these branches again turn stable and plateau to $b_1 \approx 0.0574$ and $b_2 \approx 0.921$.

We fix $\theta = 2.11$ which places the system in a quad-stable region and vary V_0 to get the bifurcation diagram in Figure 4.6(b). This is similar to the bifurcation diagram in Figure 3.4(a) and (b) except it has extra fold bifurcations which show the existence of a second patterning solution for $V_0 \in (0.0946, 0.0957)$ and for $V_0 \in (0.488, 0.498)$.

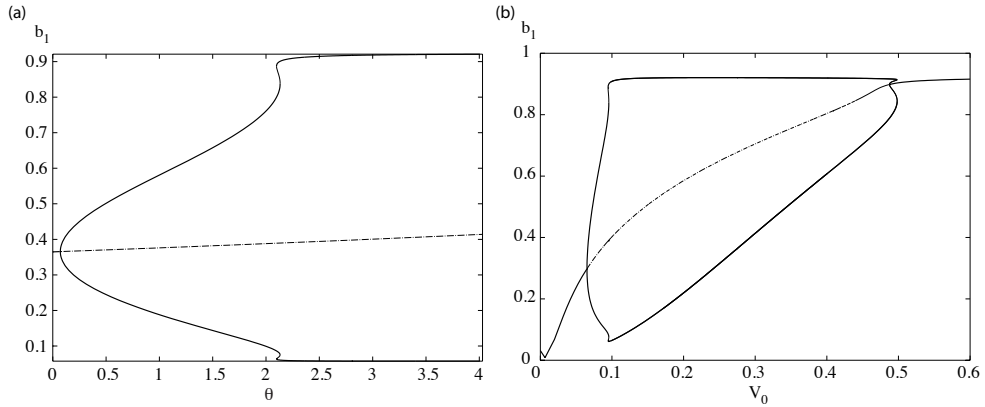


Figure 4.6: (a) Steady state bifurcation diagram for the system in (4.1.11)-(4.1.16) showing the branches of the homogeneous and period-2 spatially patterned steady states for bound Notch whilst varying θ . Produced using the parameters in Table 4.1. There are 4 regions of stability. We have mono-stability for $0 < \theta < 0.07123$, bi-stability for $0.07123 < \theta < 2.099$, quad-stability for $2.099 < \theta < 2.132$ and another region of bistability for $\theta > 2.132$. (b) Bifurcation diagram of b_1 vs V_0 for $\theta = 2.11$ and the remaining parameters as per Table 4.1. As we vary V_0 the system passes through the quadstable region. This occurs between the two pairs of fold bifurcations at $V_0 \approx 0.0946$ and $V_0 \approx 0.0957$ and again between $V_0 \approx 0.488$ and $V_0 \approx 0.498$. In these regions there are two types of patterned steady states, with one type having a more exaggerated pattern than the other

4.3.3 Feedback through VEGF gradient ($\psi > 0 = \theta$)

Next, we fix the feedback via VEGFR-2 production (set $\theta = 0$) and consider the effect of a spatially varying field of VEGF ($\psi > 0$). The filopodia equation no longer decouples as ψ modulates the steady state of unbound and bound VEGF receptors (see equations (4.1.12)-(4.1.13)), which in turn feed back into the equation for filopodia growth (see (4.1.11)). The bifurcation diagram in Figure 4.7(a) shows the steady state of bound

Notch receptors in cell 1 whilst varying ψ .

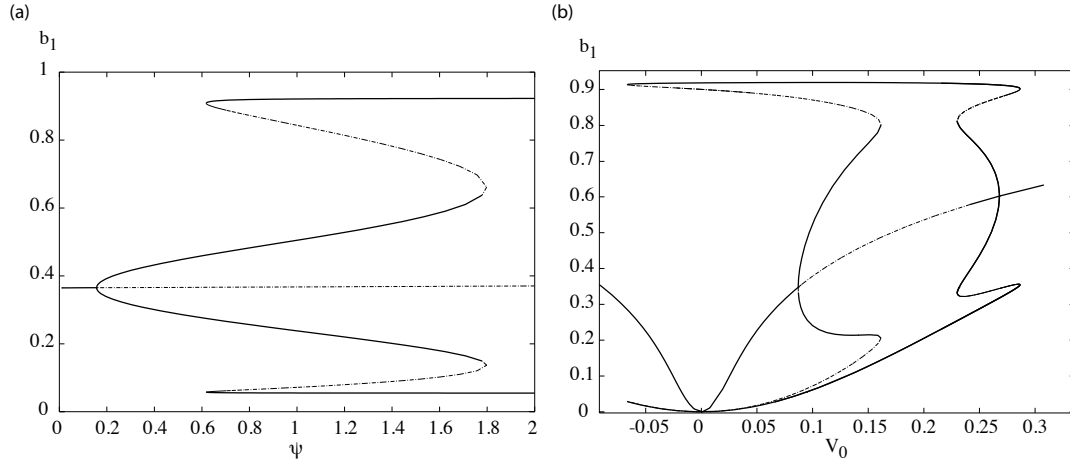


Figure 4.7: Steady state bifurcation diagram for equations (4.1.11)-(4.1.16) showing the branches of the homogeneous and period-2 spatially patterned steady states for bound Notch, b_1 , whilst varying the VEGF gradient, ψ . There are four distinct regions of stability: a mono-stable region for $0 < \psi < 0.157$, where there is a single, stable homogeneous steady state; a bistable region for $0.157 < \psi < 0.618$ where there is a single period-2 patterning solution; a quadstable region for $0.618 < \psi < 1.80$ where there are two stable, period-2 patterning solutions (one solution exists on the inner pair of stable branches and the second on the outer pair). Lastly, there is another bistable region for $\psi > 1.80$ consisting of the outer pair of period-2 patterning branches. (b) Bifurcation diagram of b_1 against V_0 for $\psi = 0.8$. As V_0 varies, there are two pairs of fold bifurcations at $V_0 \approx -0.0668$ and $V_0 \approx 0.162$ and again between $V_0 \approx 0.230$ and $V_0 \approx 0.287$. Since V_0 is a concentration, results for $V_0 < 0$ are physically unrealistic. Parameter values are as per Table 4.1 unless otherwise stated.

The homogeneous steady state becomes unstable via a pitchfork bifurcation at $\psi \approx 0.157$ and the period-2 spatial pattern branches supercritically from this such that in a line of cells, alternating cells exhibit steady states on each of the two patterning branches. These lose stability at a pair of fold bifurcations at $\psi \approx 1.80$ and then become stable again at $\psi \approx 0.618$. Between the two pairs of fold bifurcations in Figure 4.7(a) the system is quad-stable and has two stable patterning solutions. When the system lies on the inner pair of branches, the filopodia are of comparable length. However, the outer pair of branches corresponds to a large amplitude pattern where one of the filopodia is relatively large (see Figure 4.8)

In the quadstable region, the system exhibits hysteresis which may be important to consider if the gradient varied over time. This could, for instance, force the system onto

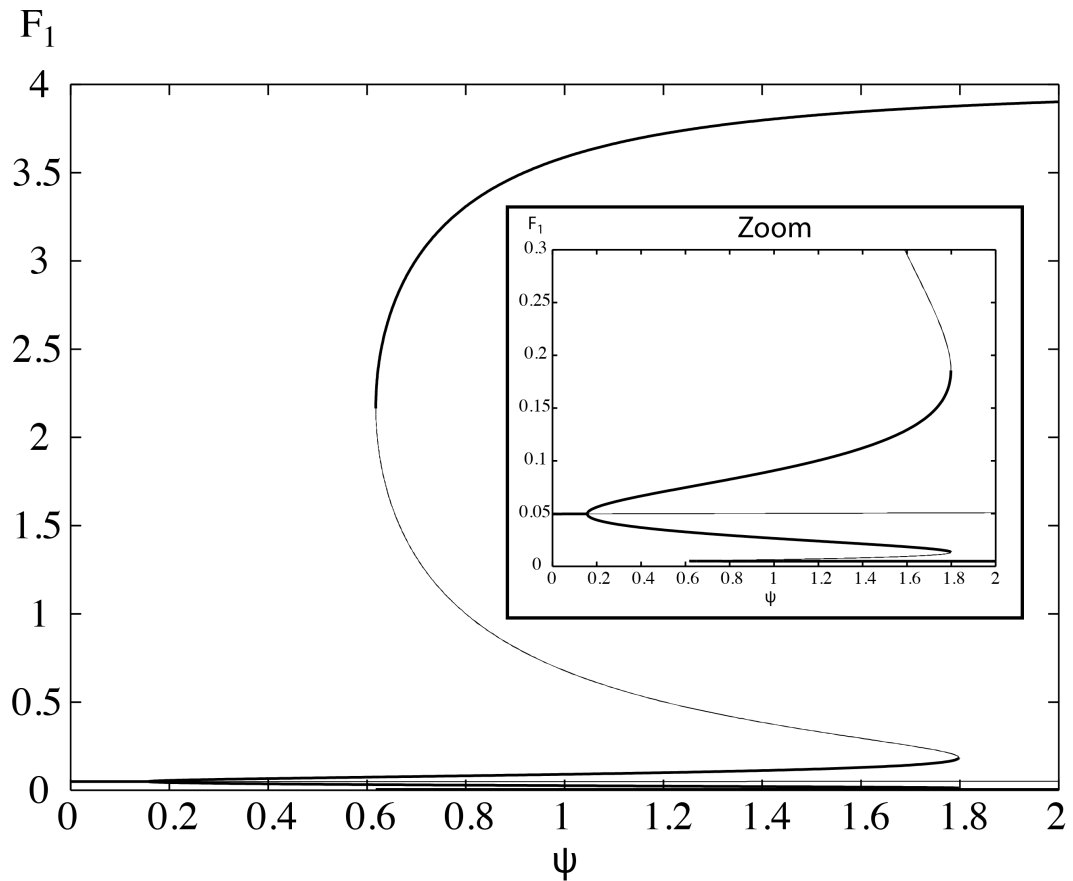


Figure 4.8: Bifurcation diagram for equations (4.1.11)-(4.1.16) showing how the steady state filopodia lengths in a two-cell system change as the extracellular VEGF gradient, ψ , is varied. Parameters used are as per Table 4.1. This figure shows that the large amplitude pattern corresponding to the outer pair of branches in Figure 4.7(a) has one very large filopodia tending to length $F_1 \approx 4.00$ and one very small one tending to length $F_1 \approx 0.00491$ as $\phi \rightarrow \infty$.

the outer pair of stable patterning branches. Since one of these corresponds to having a very long filopodium, being in this parameter regime could be a potential mechanism by which a cell can use its filopodium to explore the surrounding environment before, for example, migrating.

In the previous section we observed that at $\psi = 3.8$ the system has multiple homogeneous and period-2 patterning solutions (see Figure 4.3). By continuing the diagram in Figure 4.7(a) for $\psi > 2$, we are also able to capture the system's non-unique homogeneous steady states (see Figure 4.9). These extra homogeneous steady states are due to a fold bifurcation at $\psi = 22.36$. This diagram also shows an unstable patterning solution which branches subcritically from a pitchfork bifurcation at $\psi \approx 3.754$. For large ψ , these branches most likely connect to the outer patterning branches which are established at the fold bifurcation located at $\psi \approx 0.6179$. However XPPAUT was unable to identify a bifurcation joining these two pairs of branches together.

In §3.3, we observed that the pitchfork bifurcation occurred when the condition in equation (3.3.8) was satisfied. For this model, we analyse the behaviour of equations (4.2.7) and (4.2.8), which correspond to the green and red curves respectively in Figures 4.10 and 4.11. Their intersections determine the period-2 steady states, and we observe their behaviour as we vary $\psi \in [0, 24]$ in the parameter space in Figure 4.9.

Figure 4.10(a) outlines the location of bifurcations in ψ parameter space. We begin at the pitchfork bifurcation at $\psi = 0.1568$ where there is a single intersection of the two curves on the line $r_{B1} = r_{B2}$, with gradient -1 , corresponding to a stable homogeneous steady state becoming unstable (arrow in Figure 4.10(b)). As ψ is further increased, the green curve attains gradient < 1 and the red curve attains gradient > 1 at the intersection point. This results in two new intersections (marked with '+'s in Figure 4.10(c)). These correspond to the stable period-2 pattern on the inner pair of branches. At $\psi = 0.6179$, the green and red curves intersect at two new locations (marked with arrows in (d)) which correspond to fold bifurcations. Here the stable period-2 patterning solution and the unstable branches connecting them to the inner pair of patterning branches, is born. These are marked with '+'s and squares, respectively. Figure 4.10(e) shows these two solutions moving apart as ψ is further increased until, at $\psi = 1.798$, the unstable branches (squares) and the inner patterning branches ('+'s) annihilate each other at another fold/limit point bifurcation. This leaves a single homogeneous steady state coexisting with the large amplitude, outer branch patterning solution at $\psi = 2$ (see Figure 4.10(g)).

Further increasing ψ stretches the 'bumps' in the green and red curves upwards and to the right, respectively, until they lie tangent to the line $r_{B1} = r_{B2}$ at $\psi = 3.745$. This

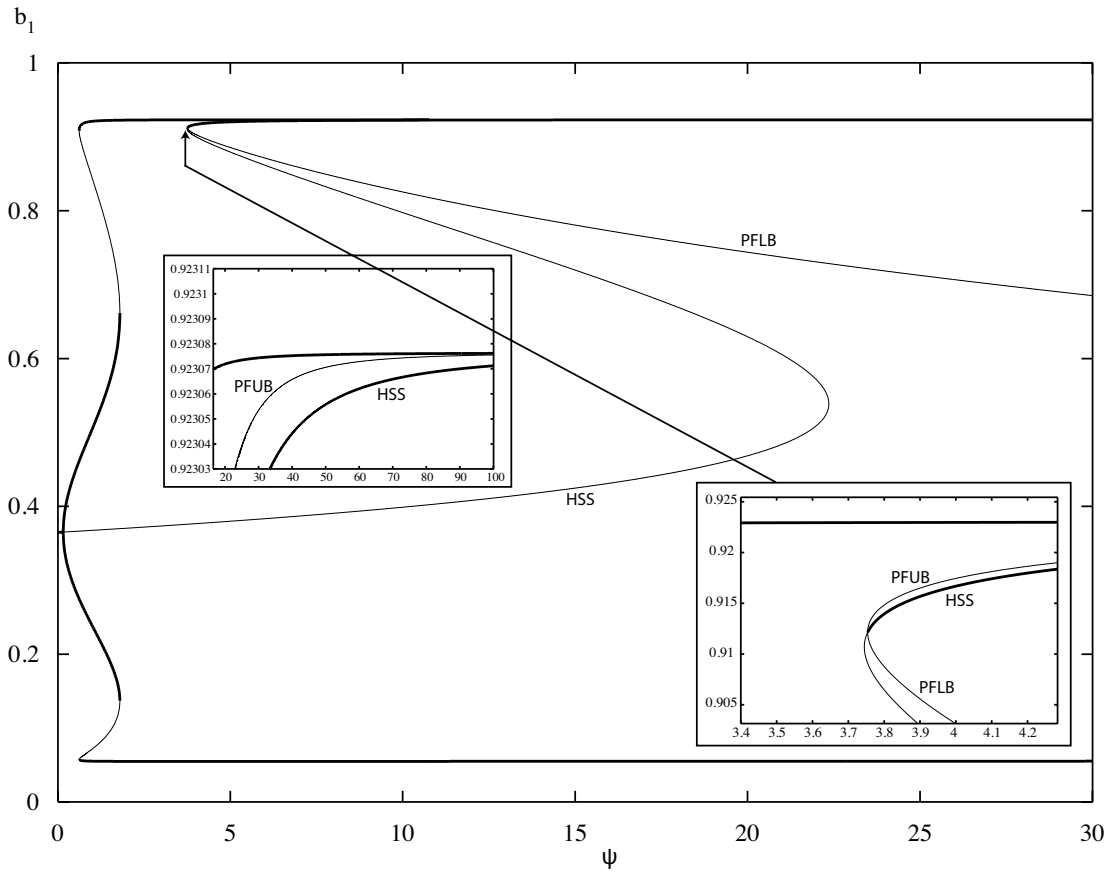


Figure 4.9: Bifurcation diagram showing how the steady states of the ODE model with filopodia growth in equations (4.1.11)-(4.1.16) change whilst varying the linear VEGF gradient ψ . The unstable homogeneous steady state branch folds back at a saddle node at $\psi = 22.36$ and folds again at $\psi = 3.745$. Hence there are 3 homogeneous steady states for $3.745 < \psi < 22.36$. The homogeneous steady state becomes stable at a subcritical bifurcation at $\psi = 3.754$. The unstable patterning branches from this pitchfork appear to connect to the outer patterning branches, however, xppaut was unable to identify a saddle node bifurcation for ψ as large as $\psi = 150$. Key: HSS = homogeneous steady state; PFLB = pitchfork lower branch; PFUB = pitchfork lower branch (the unstable patterning branches emerging from the subcritical pitchfork).

corresponds to a limit point bifurcation where two new unstable homogeneous steady states are born (arrow in Figure 4.11(a)). At $\psi = 3.754$, the system goes through a subcritical pitchfork bifurcation. The gradient of the curves at the upper crossing point (arrow in Figure 4.11(b)) traverses through -1 . This gives rise to an extra pair of unstable period-2 patterning solutions (see Figure 4.11(c): marked with triangles) whilst simultaneously allowing the homogeneous solution corresponding to the upper crossing point on the diagonal to become stable. As ψ is further increased, the unstable period-2 solutions move towards the axes (corresponding to the two patterning branches converging for large ψ) whilst along the line $r_{B1} = r_{B2}$, the middle crossing point (unstable homogeneous solution) moves towards and annihilates the lower crossing point at a fold bifurcation at $\psi = 22.36$. For $\psi > 22.36$, there is a single stable homogeneous solution, 1 stable pair of patterning solutions and 1 unstable pair of patterning solutions (see Figure 4.11(d)). The bifurcation points in Figure 4.10b,d,f and Figure 4.11a,b correspond to the bifurcation in Figure 4.9.

We fix $\psi = 0.8$, placing the system in the quadstable region, and vary V_0 to get the bifurcation diagram in Figure 4.7(b). This is similar to the bifurcation diagram in Figure 3.4(a) and (b) except it has extra fold bifurcations which show the existence of a second patterning solution for $V_0 \in (0.230, 0.287)$. A second quad-stable region exists for $V_0 \in (-0.0668, 0.162)$.

We find that changes in ψ can also act to both amplify (see Figure 4.5(a) and (b)) or induce patterns (numerical simulations of the two-cell system are qualitatively similar to Figure 4.5(e)-(f) and are therefore omitted). The pitchfork and fold bifurcations in Figure 4.7 correspond to the same pitchfork and fold bifurcations in Figure 4.6(a) except they occur at different numerical values in each parameter space. This will be confirmed in the next section when conducting two-parameter bifurcation analysis.

4.3.4 Feedback through combinations of filopodia growth, receptor production and VEGF gradient ($\theta, \psi > 0$)

In the previous two subsections we have seen that for $\phi > 0$, the model exhibits 3 types of stability regions whilst varying either θ or ψ . In the mono-stable region there is a single, stable homogeneous steady state. In the bistable region, period-2 spatial patterns can form, and in the quad-stable region, two pairs of stable branches are present for the same parameter value.

Firstly, we look at the combined effect of feedback via VEGFR-2 production ($\theta > 0$) and a VEGF gradient ($\psi > 0$) using the parameters from Table 4.1. By varying both ψ and

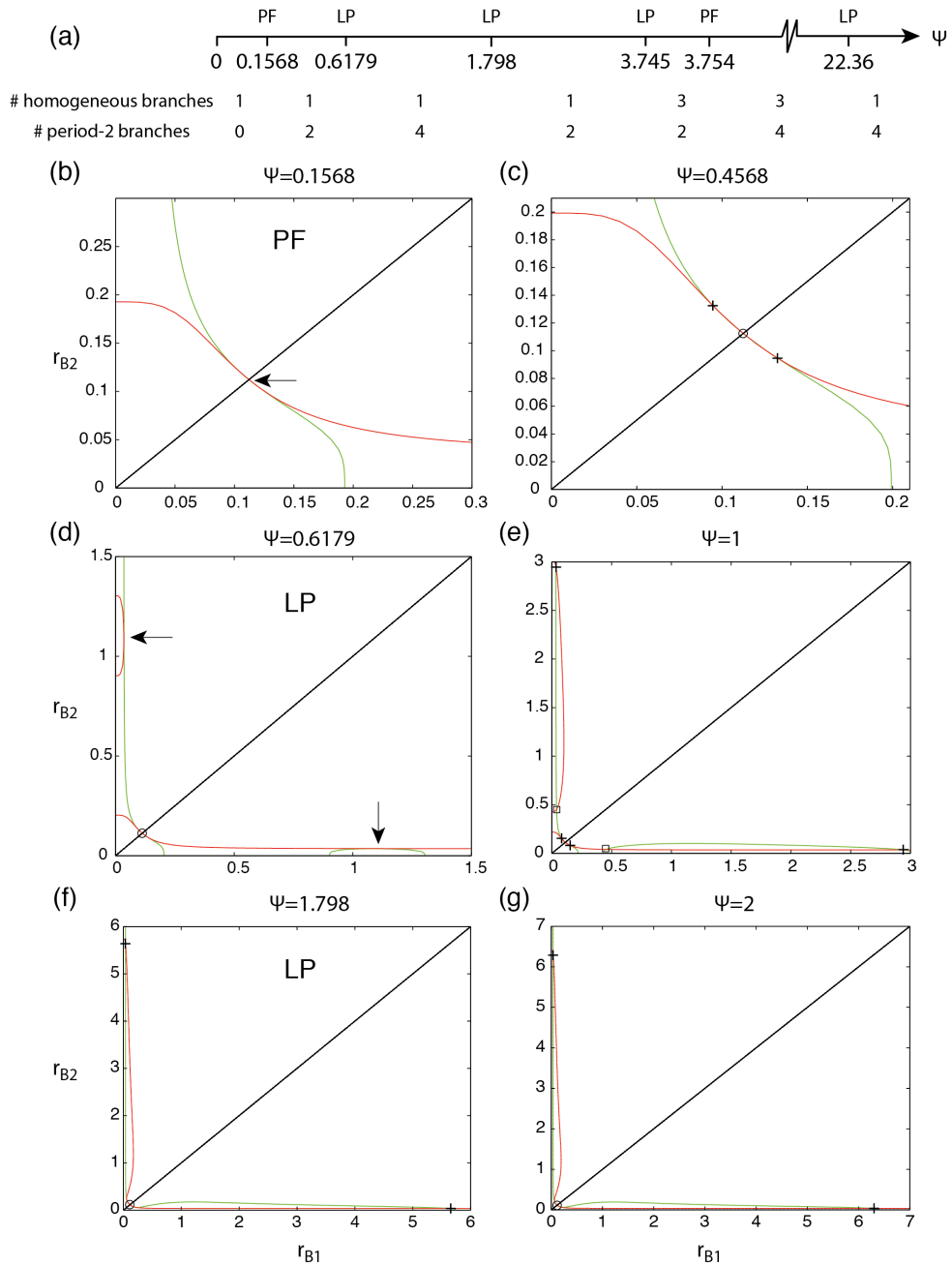


Figure 4.10: Homogeneous and period-2 patterning steady state solutions of the ODE model considering filopodia growth in equations (4.1.11)-(4.1.16). These correspond to on and off-diagonal intersections, respectively, of the green and red curves. Plots were constructed by simultaneously solving equations (4.2.7) and (4.2.8) for $\psi = 0.1568, 0.4568, 0.6179, 1, 1.798, 2$. (a) shows the bifurcation structure of the model and the number of homogeneous/patterning branch solutions (see also Figure 4.9) Key: PF=Pitchfork, and LP=Limit point (or fold) bifurcations (both marked with arrows); +: stable period-2 solutions, open circles: unstable homogeneous solutions, squares: unstable non-patterning branches connecting the inner and outer patterning branches between the limit points at $\psi \approx 0.6179$ and $\psi \approx 1.798$.

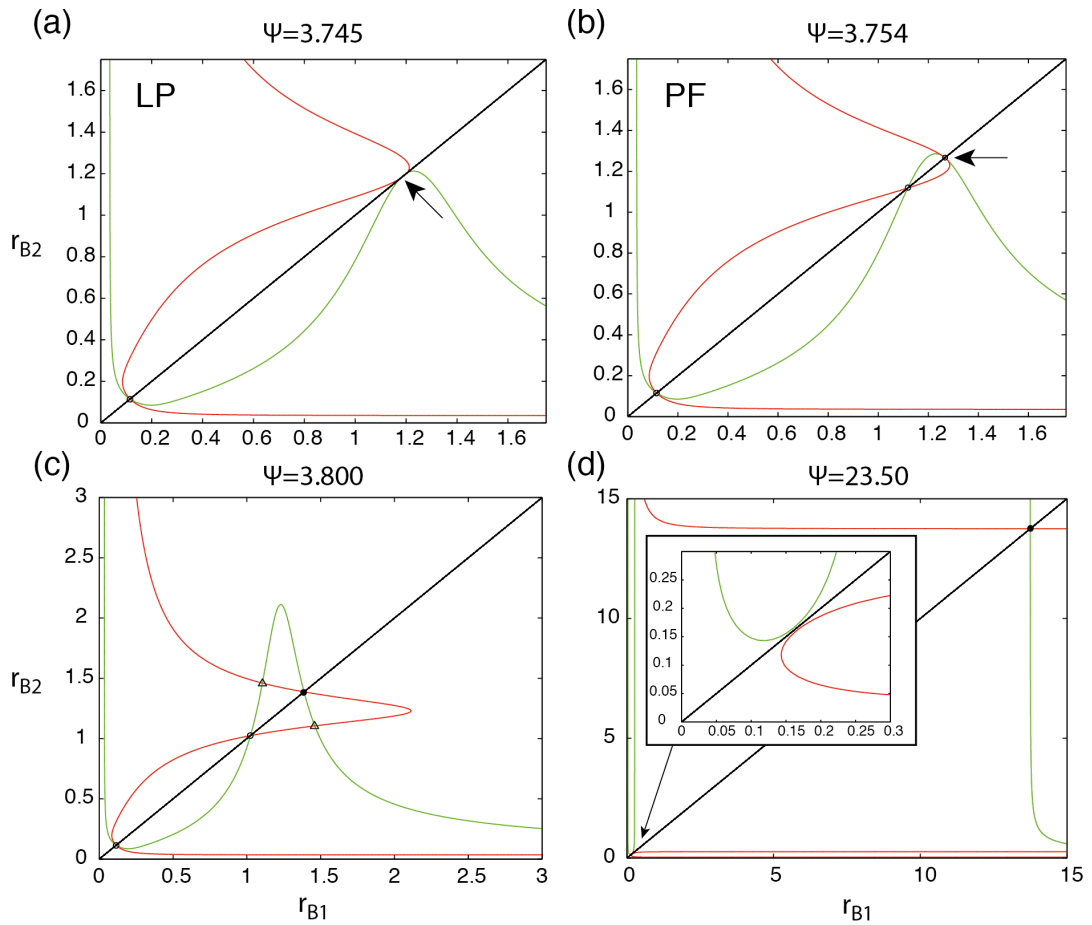


Figure 4.11: Steady state solutions of the ODE model in equations (4.1.11)-(4.1.16), defined and calculated as described in Figure 4.10 for $\psi > 2$. See Figures 4.10(a) and 4.9 for locations of bifurcations. (a) shows the limit point at $\psi = 3.745$ where both curves are tangent to the line $r_{B1} = r_{B2}$. (b) shows the subcritical pitchfork bifurcation at $\psi = 3.754$ where both curves have slope -1 at the point of intersection (arrow). (c) shows the presence of an unstable period-2 patterning solution (triangles) which emerges from the pitchfork bifurcation in (b). (d) shows the presence of a single homogeneous solution after the destruction of two solutions at the LP at $\psi \approx 22.36$ (see zoom inset). Both pairs of period-2 patterning solutions are large amplitude for large ψ . Key: triangles: unstable, period-2 patterning branches; closed(open) circles correspond to stable(unstable) homogeneous solutions. Note that there are 2 stable, period-2 patterning solutions for large r_{B1}, r_{B2} not shown in (a),(b),(c) and 2 stable and 2 unstable in (d).

θ we follow the pitchfork and fold bifurcations in Figure 4.7a to get the two parameter diagram shown in Figure 4.12a. The limit points move closer together as $\psi \rightarrow 0$. At $\psi = 0$ Figure 4.6(a) represents a slice through the two-parameter diagram in Figure 4.12a. Here the system is quadstable only for a small range of values of θ . Thus the solutions may be able to move between the bistable and quadstable patterning regions in response to perturbations in parameter values or changes in parameter values due to development or disease in the embryo. The difference between the equilibrium value of the “inner” and “outer” solution branches is not significant for values of θ in the quadstable region of Figure 4.6. This is not the case in Figure 4.7 where the “inner” and “outer” branches are spaced further apart.

We also follow the pitchfork and fold bifurcations into (ψ, ϕ) space in Figure 4.12b. We find that there are still 4 distinct stability regions: one monostable, two bistable and a quadstable region. Together these results suggest that the stability regions in $\phi - \psi - \theta$ space may be bounded by curved surfaces.

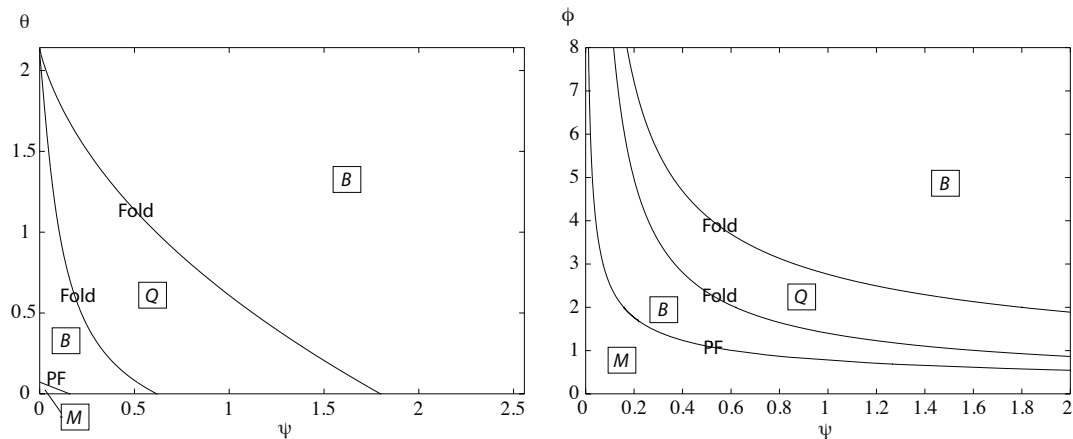


Figure 4.12: Two parameter bifurcation diagrams for the two-cell model defined by equations (4.1.11)-(4.1.16). Continuation of the pitchfork (PF) and fold (Fold) bifurcations in (a) θ - ψ space and (b) ϕ - ψ space. The bifurcations separate the monostable (M), bistable (B) and quadstable (Q) regions of the system. In (a) the θ -axis is equivalent to a slice corresponding to Figure 4.6(a) and the ϕ -axis is equivalent to a slice representing Figure 4.7(a).

4.4 Linear stability analysis

In this section we use linear stability analysis to compare how the models with and without filopodia pattern in terms of the feedback strengths of VEGFR-2 production

(A) and Dll4 ligand production (B). We begin with the dimensionless system in (4.1.11)-(4.1.16) and, following our steps from the model neglecting filopodia growth (see §3.5), assume a quasi-steady state for bound VEGF receptors which gives

$$r_{Bj} = r_{Ue} \left(V_0 + \frac{\psi}{2} \frac{F_e(t)^2}{1 + F_e(t)} \right).$$

This makes the following analysis more tractable and is motivated by the idea that binding processes occur on a faster timescale than transcriptional and translational processes. We remark that a conservation of Notch receptors in their bound and unbound forms has been assumed in equation (4.1.16) giving $n_j = 1 - b_j$. We linearise about the homogeneous steady state, given by the $O(1)$ terms $(F_e, r_{Ue}, \delta_e, b_e)$. We substitute $F_j = F_e + \epsilon \hat{F}_j$, $r_{Uj} = r_{Ue} + \epsilon \hat{r}_{Uj}$, $\delta_j = \delta_e + \epsilon \hat{\delta}_j$ and $b_j = b_e + \epsilon \hat{b}_j$ (for $0 < \epsilon \ll 1$) and retain $O(\epsilon)$ terms giving:

$$\frac{d\hat{F}_j}{dt} = \{ \phi w'(p_G(F_e) r_{Ue}) r_{Ue} p'_G(F_e) - \gamma \} \hat{F}_j + \phi w'(p_G(F_e) r_{Ue}) r_{Ue} p'_G(F_e) \hat{r}_{Uj}, \quad (4.4.1)$$

$$\frac{d\hat{r}_{Uj}}{dt} = (1 + \theta F_e) f'(b_e) \hat{b}_j + \theta f(b_e) \hat{F}_j - \lambda \hat{r}_{Uj}, \quad (4.4.2)$$

$$\begin{aligned} \frac{d\hat{\delta}_j}{dt} = & g_{max} g'(p_G(F_e) r_{Ue}) r_{Ue} p'_G(F_e) \hat{F}_j + \bar{g}_{max} g'(p_G(F_e) r_{Ue}) p_G(F_e) \hat{r}_{Uj}, \\ & - (\mu + k_B(1 - b_e)) \hat{\delta}_j + (k_{-B} + k_B \delta_e) \langle \hat{b}_j \rangle, \end{aligned} \quad (4.4.3)$$

$$\frac{d\hat{b}_j}{dt} = k_B(1 - b_e) \langle \hat{\delta}_j \rangle - (k_{-B} + k_B \delta_e) \hat{b}_j, \quad (4.4.4)$$

where the $w(\cdot)$ is as per equation (4.1.2) and

$$p_G(F_e) = V_0 + \frac{\psi}{2} \frac{F_e^2}{1 + F_e}, \quad (4.4.5)$$

is the dimensionless concentration of VEGF at the homogeneous steady state. We again look for solutions of the form $\hat{u}_j = \hat{u}_j \cdot \exp(ikj + \sigma t)$, where $u_j = F_j, r_{Uj}, \delta_j, b_j$ and k, σ and the $\langle \rangle$ notation are as defined in the no filopodia model. We substitute this ansatz into the linearised system (4.4.1)-(4.4.4). This gives $\sigma \mathbf{v} = M \mathbf{v}$ where $\mathbf{v} = [\hat{F}_j, \hat{r}_{Uj}, \hat{\delta}_j, \hat{b}_j]^\top$ and M is the Jacobian matrix of the filopodia system given by

$$M = \begin{bmatrix} \phi U V r_{Ue} - \gamma & \phi U p_G(F_e) & 0 & 0 \\ \theta f(b_e) & -\lambda & 0 & (1 + \theta F_e) A \\ g_{max} B V r_{Ue} & g_{max} B p_G(F_e) & -(k_B(1 - b_e) + \mu) & (k_{-B} + k_B \delta_e) K \\ 0 & 0 & k_B(1 - b_e) K & -(k_{-B} + k_B \delta_e) \end{bmatrix}, \quad (4.4.6)$$

with $K = \cos(k)$ and

$$A = f'(b_e), \quad B = g'(p_G(F_e) r_{Ue}), \quad U = w'(p_G(F_e) r_{Ue}), \quad V = p'_G(F_e) \quad (4.4.7)$$

The parameters A, B, U and V represent four types of feedback at the homogeneous steady state: feedback via VEGF receptor inhibition (A); feedback via ligand activation (B); feedback via filopodia growth U ; and feedback via a VEGF gradient V .

The stability of the system is determined by the roots of the characteristic polynomial which is a quartic equation in σ given by

$$P(\sigma; K) = \sigma^4 + a_1\sigma^3 + a_2\sigma^2 + a_3\sigma + a_4. \quad (4.4.8)$$

Expressions for the coefficients, a_i ($i = 1, 2, 3, 4$), are given in Appendix C.

The Routh-Hurwitz conditions for a quartic equation of this form are given by

$$a_1 > 0, \quad (4.4.9)$$

$$a_1a_2(K) - a_3(K) > 0, \quad (4.4.10)$$

$$a_3(K) [a_1a_2(K) - a_3(K)] - a_1^2a_4(K) > 0. \quad (4.4.11)$$

$$a_4(K) > 0. \quad (4.4.12)$$

For fixed values of U and V , these inequalities can be used to delimit stability regions in the A - B plane for this model (see Figure 4.13).

4.5 Modulation of stability regions by filopodia feedback

The linearised system of ODEs (4.4.1)-(4.4.4) contains 4 feedbacks terms (see (4.4.7)). The new terms in the filopodia model relate to U and V . However, V depends only on ψ which fixes the steady state values r_{Ue} , F_e and r_{Be} (see equations (E.0.7), (E.0.8) and (E.0.10)). Hence it is not possible to vary V independently of A , B and U without changing the steady state. Therefore we focus on unfolding our analysis of the A - B plane by varying the strength of filopodia production, U . This is done by fixing ψ and θ (and hence the homogeneous steady state and the feedback strength, V), whilst varying $U \propto q$. In appendix E we show how to choose β , α , C and g_{max} such that the feedback strengths A , B and U can be varied without changing the homogeneous steady state.

Figure 4.13 (a),(b) shows that varying U in the absence of filopodia feedback ($\phi > 0$, $\theta = \psi = 0$) has no effect on the patterning regions in the A - B plane (see Figure 3.9) as the ODE for filopodia growth decouples. For non-zero values of θ and ψ the underlying homogeneous steady state, r_{Be} , changes (see Figure 4.13(o)). Rows (c)-(f), (g)-(j) and (k)-(n) relate to cases which lie on the same contour line in Figure 4.13(o) and hence give rise to the same homogeneous steady state $r_{Be} = 0.66$. Increasing the filopodia feedback

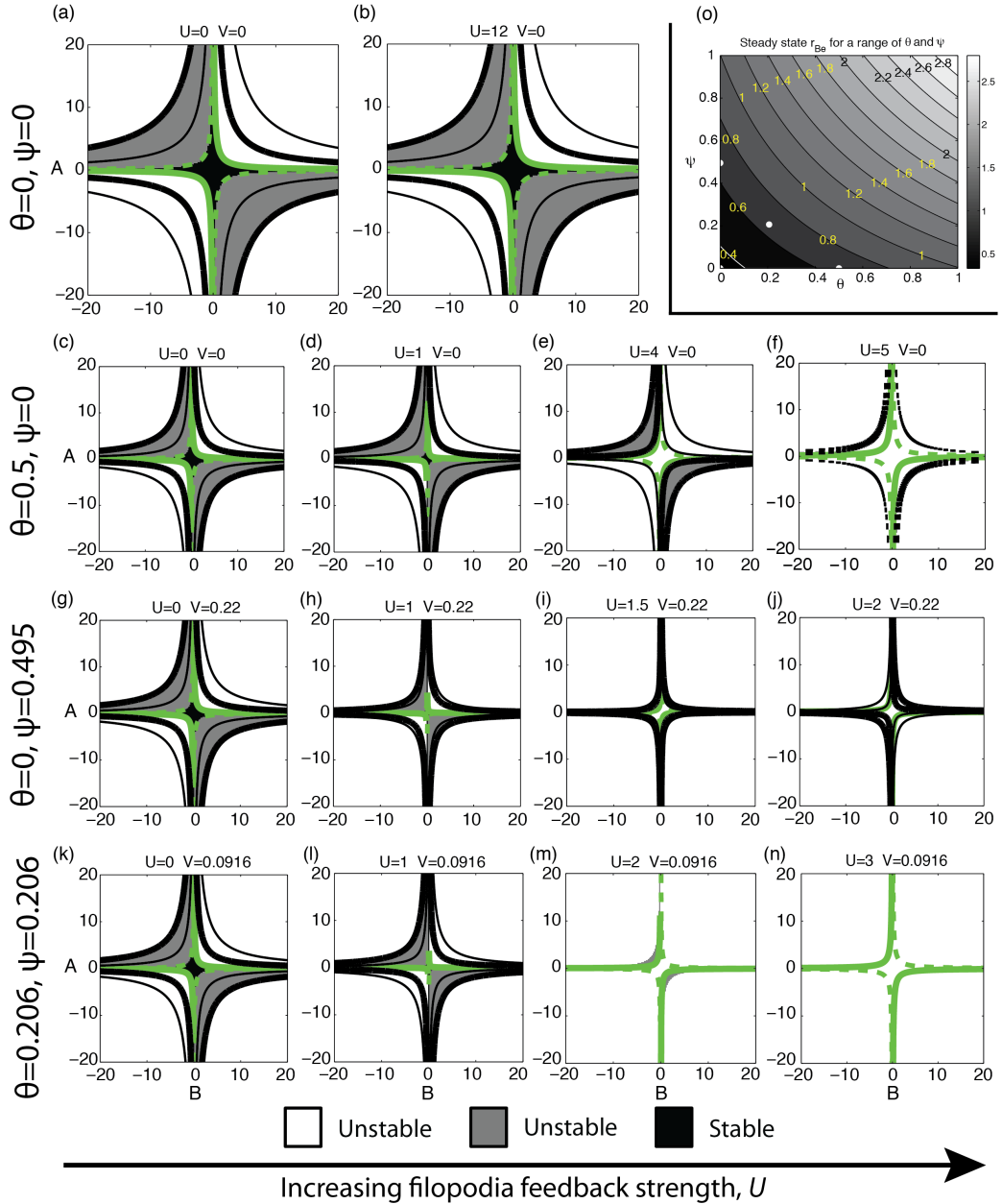


Figure 4.13: Stability plots in the A - B plane for the quasi-steady filopodia system using parameter values as per Table E.1 unless otherwise specified. We fix values of θ and ψ in each row: (a)-(b) $\theta = 0, \psi = 0$ (c)-(f) $\theta = 0.5, \psi = 0$ (g)-(j) $\theta = 0, \psi = 0.495$ (k)-(n) $\theta = 0.206, \psi = 0.206$. (o) The contour plot shows how the homogeneous steady state, r_{Be} , varies with θ and ψ . Traversing each row from left to right corresponds to increasing the feedback strength of filopodia production, U , which is achieved by varying the Hill coefficient, q . For each pair of fixed θ, ψ , increasing the strength of filopodia production, U , causes at first, the stable black region, and then the grey region to disappear. Key: Solid and dashed green lines depict equality of the condition (4.4.12) at $K = \pm 1$ respectively; Thick and thin black lines depict equality of the condition (4.4.11) at $K = \pm 1$ respectively.

strength, U , causes the stable black region to shrink and ultimately vanish. For stronger feedback strengths, similar behaviour is exhibited by the unstable grey region until the only remaining region is the unstable (white) one. When the homogeneous steady state becomes unstable, the system exhibits stable period-2 spatial patterns.

4.5.1 Loss of the black stable region

In each row of Figure 4.13 the vanishing of the black region coincides with the violation of $a_4(K) > 0$ (for $K = -1, 1$) $\forall A, B$. In the $A - B$ plane, $a_4(K = \pm 1)$ take the hyperbolic forms

$$AB = \pm c_0(U) = \frac{\mu [\lambda(\gamma - UV\phi r_{Ue}) - U\theta f(b_e)p_G(F_e)\phi] (k_{-B} + k_B\delta_e)}{\gamma k_B(1 - b_e)g_{max}p_G(F_e)(1 + \theta F_e)} \quad (4.5.1)$$

respectively (shown as solid and dashed green curves) where $c_0(U)$ is a constant parameterised by U . As U increases, it causes c_0 to change sign which is responsible for violating $a_4(K = \pm 1) > 0 \forall A, B$. The parameter values in Table E.1 give $c_0(1) > 0$ and $c_0(1.5) < 0$. Since $c_0(U)$ is a smooth linear function of U and hence continuous on $[1, 1.5]$, by the intermediate value theorem $\exists U_0 \in [1, 1.5]$ such that $c_0(U_0) = 0$. As U passes through U_0 , $a_4(K = 1) = 0$ (the solid green curve) transitions from the $A, B > 0$ quadrant to the $A < 0 < B$ quadrant. The dashed green curve, $a_4(K = -1) = 0$ simultaneously switches in the opposite direction.

Stability of the homogeneous steady state demands the system lie simultaneously below the solid green and above the dashed green curves for $B > 0$ and vice versa for $B < 0$ which is not possible after c_0 changes sign.

Equivalently we examine $a_4(K)$, for fixed A and B of different signs (i.e. in a patterning quadrant), which is quadratic in K :

$$\alpha_0 K^2 + \beta_0 K + \gamma_0, \quad (4.5.2)$$

and is explicitly given in (C.0.4). The coefficients α_0 and γ_0 are functions of U . When $U = 0$, $\alpha_0(U = 0) < 0$ and $\gamma_0(U = 0) > 0$ so (4.5.2) is concave downwards and has a turning point for $K < 0$. As U is increased through some critical $U = U_0$, $\alpha_0(U)$ becomes positive and $\gamma_0(U)$ becomes negative. Hence $a_4(K)$ is concave upwards with a turning point for $K > 0$. At the transition point, $\alpha_0(U_0), \gamma_0(U_0) = 0$ and $a_4(K)$ is linear in K , passing through the origin.

4.5.2 Loss of the grey patterning region

Figure 4.13 also shows that the vanishing of the grey patterning region, in which the homogeneous steady state is unstable to non-homogeneous perturbations, happens

after the destruction of the black stable region, when the filopodia feedback strength, U is further increased. This is because increasing U changes the functional form of the Routh-Hurwitz condition in (4.4.11), corresponding to the black curves in Figure 4.13. For fixed K ,

$$a_3(K) [a_1 a_2(K) - a_3(K)] - a_1^2 a_4(K) = 0 \Leftrightarrow A^2 B^2 + c_1(U) AB + c_2(U) = 0, \quad (4.5.3)$$

where $c_1(U)$ and $c_2(U)$ are constants parameterised by U . The explicit form of this Routh-Hurwitz condition is algebraically intractable but numerical plots (see black curves in Figure 4.13 (i) and (j)) suggest that the disappearance of the grey region coincides with a switching of the thick black curve (which has $K = 1$) from the quadrant with $A < 0 < B$ to the quadrant with $A, B < 0$. This is attributable to a sign change in the coefficient c_2 . In Figure 4.13 (i) numerical calculations give both $c_1(U = 1.5)$, $c_2(U = 1.5) < 0$ whereas in (j), $c_1(U = 2) < 0 < c_2(U = 2)$. Consequently, the homogeneous steady state is no longer stable to homogeneous perturbations $\forall A, B$.

4.5.3 Numerical simulations

In this subsection we take a fixed point in the $A - B$ plane of Figure 4.13 (g),(h) and (j) and, using the parameter values therein, show the effect of increasing the filopodia feedback strength, U , using numerical simulations of a two-cell, quasi-steady filopodia system. As the filopodia feedback strength, U , increases, the Routh-Hurwitz hyperbolae for $a_4(K = \pm 1)$ come together shrinking the black region until it disappears and the fixed point in the $A-B$ plane, which was in the stable black region in (g), transitions to the unstable grey region in (h) and finally the unstable white region in (j). Both of the grey and white regions have stable period-2 patterns. Hence increasing the filopodia feedback strength, U facilitates pattern formation by moving the boundaries of the stability regions.

Using the parameter values from Figure 4.13 (g), (h) and (i) again, we simulate the quasi steady filopodia system in a ring of $N = 30$ cells. The two cell-system exhibits no patterning when it lies in the black stable region (see Figure 4.15 (a)) but does exhibit patterns when it lies in the grey and white unstable regions (see Figure 4.15 (b) and (c)). These patterns are not very robust and contain “errors” since the system at the fixed point in the $A - B$ plane does not have particularly strong feedback strengths A, B . Hence it takes a long time for solutions to reach a robust pattern. Stronger feedback strengths reach a robust pattern in a comparable timeframe to the simulations in Figure 4.15 and can even correct “errors” (not shown).

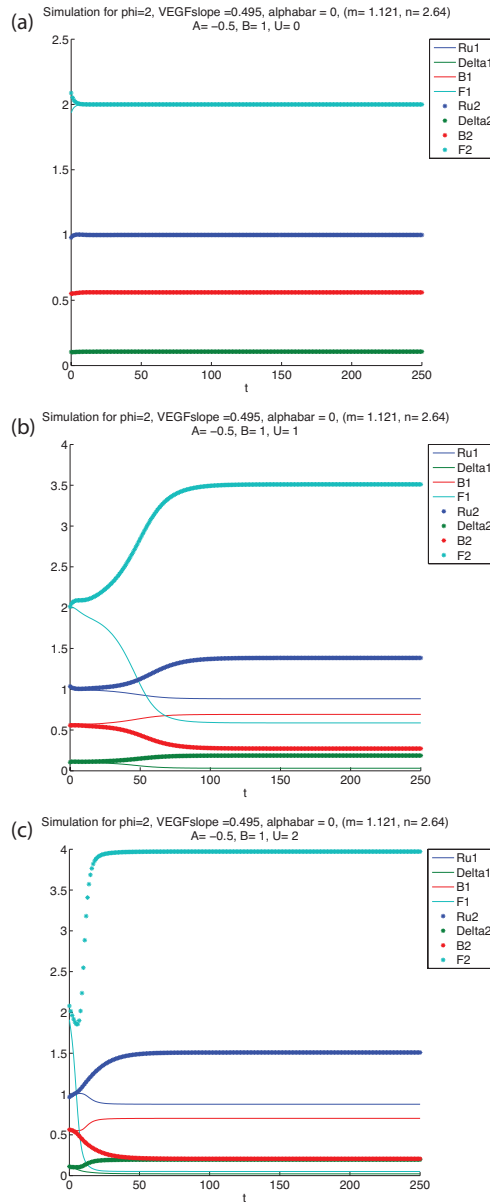


Figure 4.14: Numerical simulations of the quasi-steady filopodia system with $\theta = 0$ and $\psi = 0.495$. $A = -0.5$ and $B = 1$ are fixed whilst U is varied (using the Hill coefficient q) as shown in plot titles. (a,b,c) correspond to simulations from the stability plots in (g,h,j) respectively, in Figure 4.13 with parameters identical to those used therein. In each case, initial conditions are a random perturbation about the homogeneous steady state. As the filopodia feedback strength, U , is made stronger, the two-cell system is able to pattern (b,c) where it could not before (a).

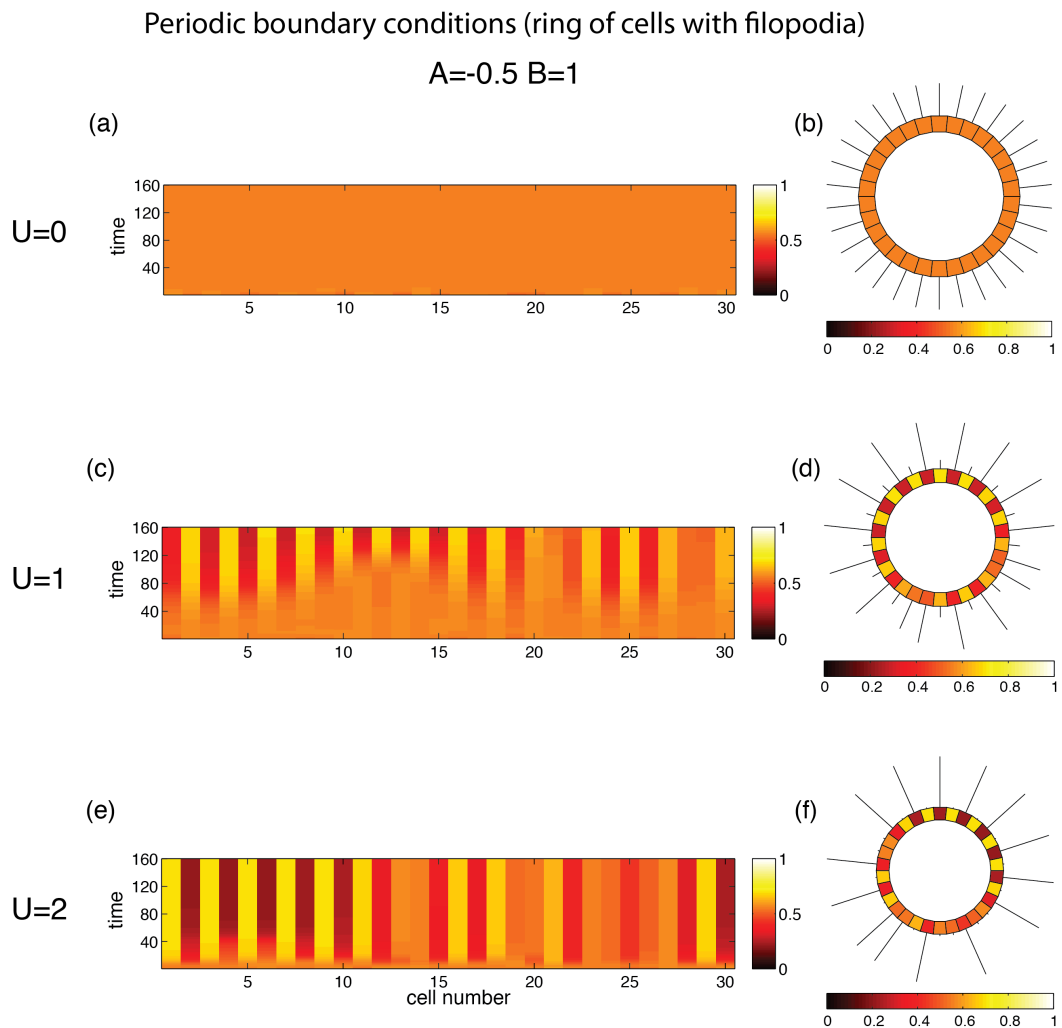


Figure 4.15: Numerical simulations of the quasi-steady filopodia system for a ring of $N = 30$ cells with $\theta = 0$ and $\psi = 0.495$. $A = -0.5$ and $B = 1$ are fixed whilst U is varied (using the Hill coefficient q) as shown in plot titles. (a,c,e) are space-time plots showing the level of bound Notch, b_j , in each cell in the ring and correspond to simulations from the stability plots in (g,h,j) respectively, in Figure 4.13. In each case, initial conditions are a random perturbation about the homogeneous steady state. As the filopodia feedback strength, U , is made stronger, the string of cells is able to admit patterning: (c-f), where it could not before: (a,b). (b,d,f) show the level of b_j at the end of the simulations in (a,c,e) respectively.

4.6 Discussion

We incorporate filopodia growth into our ODE model of Chapter 3, allowing their growth in a linear gradient of extracellular VEGF to give cells with a filopodium an advantage by either increasing their production of VEGFR-2 (via the θF_j term in equation (4.1.12)) and/or allowing them to bind more VEGF (via the term multiplying ψ in equations (4.1.12) and (4.1.13)). These two mechanisms act as part of a positive feedback loop, enabling further elongation of filopodia in these ECs. Our model predicts that filopodia facilitate spatial pattern formation, by either amplifying an existing pattern or inducing one which was not present in the absence of filopodia (see Figure 4.5). Interestingly, our model predicts that patterning is still possible even in the absence of a linear gradient of VEGF ($\psi = 0$). In this case induction or amplification of a pattern needs to occur due to feedback onto VEGFR-2 production ($\theta > 0$) (see Figure 4.4). This is consistent with the agent based model of Bentley et al. [81].

Due to the incorporation of an equation for filopodia growth: (4.1.3); the VEGF receptor feedback term in equation (4.1.4); and the inclusion of a linearly increasing VEGF gradient, ψ ; the equations of this model are more non-linear and much more heavily coupled than for the system of ODEs in Chapter 3. In this model, period-2 steady state solutions were found by simultaneously solving equations (4.2.7) and (4.2.8) whereas in the model without filopodia growth, period-2 solutions corresponded to finding the fixed points of the function $h \circ h(x)$ (see equation 3.3.7). Simultaneous solution of equations (4.2.7) and (4.2.8) for a range of values for the VEGF gradient, ψ , shows that the filopodia growth terms can introduce an extra ‘bump’ in these curves which is responsible for producing the large amplitude (outer branch) pattern (see Figure 4.10d). This also allows the small amplitude pattern to be destroyed at another pair of folds (see Figure 4.10f). Biologically, this gives a mechanism to induce large amplitude patterns that cannot be obtained without filopodia.

For large values of the VEGF gradient, ψ , our model exhibited multiple homogeneous steady states. The fixed points of equation (4.2.6) corresponded to homogeneous steady states. We found that the filopodia growth terms arising from a non-zero value for the VEGF gradient, ψ , or receptor feedback, θ , were capable of introducing a ‘bulge’ in the curve corresponding to equation (4.2.6) allowing multiple fixed points. We confirmed these predictions using bifurcation analysis (see Figure 4.9).

Bifurcation analysis, varying the filopodia feedback parameters ψ and θ using XPPAUT, also confirmed the coexistence of large and small amplitude patterns as predicted by steady state analysis. The large amplitude pattern corresponded to cells having one

very long and one extremely short filopodium (see Figure 4.8). The long filopodia may be able to reach further afield and help cells explore their environment more efficiently. Such a large amplitude pattern may allow communication between ECs many cell diameters away, using long filopodia. Two parameter continuation, using XPPAUT, also showed the movement of the pitchfork and fold bifurcations in $\psi - \theta$ and $\psi - \phi$ parameter space (see Figure 4.12).

The introduction of an equation for filopodia growth made linear stability analysis more difficult than in Chapter 3 (see coefficients of equation (4.4.8) in Appendix C). The extra Routh-Hurwitz condition arising from the filopodium equation marked the grey-white boundary in the stability plots (see black curves in Figure 4.13). Linear analysis showed that increasing the filopodia feedback strength, U , caused the stable regions of A - B parameter space to shrink and vanish. This caused the homogeneous steady state, for a fixed point in the A - B plane, to become destabilised (see Figure 4.13). Numerical analysis, in which we increased the filopodia feedback strength, U , by increasing the Hill coefficient, q , in the production function, $w(\cdot)$, for filopodia growth, confirmed the predictions of the linear analysis. In this model also, the onset of patterning did not depend on the specific functional forms of the feedbacks $f(\cdot)$, $g(\cdot)$, or $w(\cdot)$; only on their respective slopes, A , B , U , at the homogeneous steady state.

A natural way of extending this work would be to allow multiple filopodia to grow per cell or to incorporate recovery delays representing the time before gene expression returns to normal [81]. Other extensions could involve allowing the cells to divide and migrate away from the vessel, though this would necessitate the need for a spatial geometry. Allowing the VEGF concentration to vary in the j direction, parallel to the string of cells, could be another interesting avenue for further work. Zygmunt et al., have shown that Semaphorin-Plexin signalling, between zebrafish somitic cells and ECs of the DA, can induce DA cells, away from somite boundaries, to secrete soluble flt1, which limits signalling via the VEGF–VEGFR-2 interactions we have studied here [58]. Thus Semaphorin-Plexin signalling represents one possible way in which an external signalling pathway may modulate the spatial distribution of VEGF in the j direction.

A Partial Differential Equation Model for Intramembrane VEGF Receptor Transport-Regulated Filopodia Extension

The trafficking of proteins and receptors is known to be important for moving proteins from their sites of synthesis to their sites of action [120]. Coupling of receptors with effector molecules, other receptors, cytoskeletal elements and other membrane associated components requires diffusion within the cell membrane bilayer. This process has been investigated using experimental techniques such as *fluorescence recovery after photobleaching* (FRAP) [121, 122]. Transmembrane proteins such as receptors may, in certain cases, be required to establish polarity across or between cells [72, 123]. Similarly, the dynamics of cells stimulated by spatially varying signals, (for example, a gradient of extracellular VEGF), may differ from those of cells exposed to a spatially homogeneous signal.

In this chapter we formulate a model to investigate how the VEGF–Delta–Notch signalling system is modulated by filopodia growth. We account for spatial variation in VEGFR-2 along the filopodium and cell membrane which is caused by spatial gradients of extracellular VEGF. We formulate model in which the concentrations of unbound and bound VEGFR-2 are spatially resolved. PDEs describing the spatiotemporal evolution of unbound and bound VEGFR-2 are coupled to ODEs describing the time evolution of whole cell variables: the cellular concentrations of Delta ligands and Notch receptors. We use this framework to explore the effects of receptor diffusion, and filopodia growth, on the pattern forming potential of a string of discrete, coupled

cells.

5.1 PDE model framework and model equations

We consider Delta-Notch interactions in terms of whole cell variables (as in Collier et al [67, 68, 71, 74]. Bound VEGF receptors upregulate production of Delta ligand which binds to Notch receptors on neighbouring cells. Consequently, the bound Notch receptors on the neighbouring cells downregulate their production of (unbound) VEGFR-2. Thus we assume that the VEGF-regulated production of Delta ligand is an increasing function of the bound VEGFR-2 concentration at the cell body. There are alternative choices for coupling between whole cell and local variables: these are discussed below.

The geometry for our model, in the discrete cell direction, is identical to that shown in Figure 4.1 with j defined as the discrete cell variable. The spatial geometry in the direction of the cell membrane and filopodia is shown in Figure 5.1 for a single cell. The cell body has a fixed length, L_0 , and the growing filopodium has time-dependent length $F_j(t)$. The cell body is located in a constant concentration of VEGF and the filopodia extend into a linearly increasing gradient.

The model variables for VEGF, unbound and bound VEGFR-2 are the concentrations (densities) of ligands and receptors as a function of distance along the membrane, measured from the bottom of cells that extend filopodia ‘upwards’ or equivalently in the x direction (see Figure 5.1).

The local variables are given by:

$\rho_{Uj}(x, t)$, the density of R_{Uj} , VEGFR-2 receptors on cell j

$\rho_{Bj}(x, t)$, the density of R_{Bj} , bound VEGFR-2 receptors on cell j .

The whole cell variables are given by:

$\delta_j(t)$, the density of Δ_j , (unbound) Dll4 in cell j

$n_j(t)$, the density of N_j , (unbound) Notch in cell j

$b_j(t)$, the density of B_j , bound Delta-Notch compound, Notch from cell j

$F_j(t)$, the length of the filopodia projecting from cell j ,

and the extracellular VEGF concentration is

$$V(x) = V_0 + \psi(x - L_0) ,$$

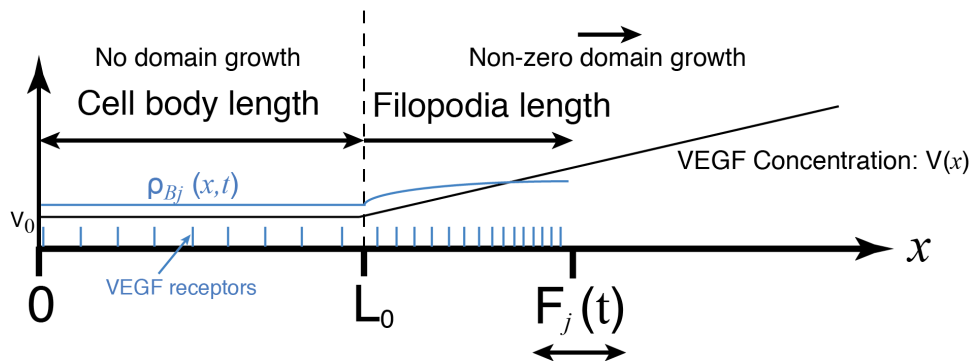


Figure 5.1: Schematic showing the spatial aspect in the filopodia (or x) direction of a single cell for the PDE model. The geometry in the string (or cell) direction remains the same as earlier (see Figure 4.1). The cell body has fixed length L_0 and the filopodium has time-dependent length $F_j(t)$. The extracellular VEGF distribution, $V(x)$, (superimposed in black) assumes that the cell body is located in a constant concentration of VEGF and that the filopodia extend into a linearly increasing gradient which extends perpendicularly away from the cell. In this model VEGFR-2 (blue lines) can diffuse and advect in the cell membrane. A sketch of their spatial distribution is plotted in blue, $\rho_{B_j}(x,t)$. The local strain rate is defined to be zero at the cell body, and hence the domain does not grow for $0 < x < L_0$. The strain rate is some function of bound VEGFR-2 for $L_0 < x \leq L_0 + F_j$, and here the domain grows causing advection of receptors along the filopodium.

where L_0 is the length of the fixed cell membrane and ψ is the linearly increasing gradient of VEGF, which initiates from the upper surface of the string of ECs.

The equations for Delta and Notch are similar to those used in the ODE model of §4 (see equations (4.1.14)-(4.1.16)):

$$\frac{d\delta_j}{dt} = g_{max}g(\tilde{R}_{Bj}) + k_{-B} \left(\frac{b_{j-1} + b_{j+1}}{2} \right) - k_B \left(\frac{n_{j-1} + n_{j+1}}{2} \right) \delta_j - \mu\delta_j, \quad (5.1.1)$$

$$\frac{db_j}{dt} = k_B \left(\frac{\delta_{j-1} + \delta_{j+1}}{2} \right) n_j - k_{-B}b_j, \quad (5.1.2)$$

$$n_j = 1 - b_j. \quad (5.1.3)$$

The variable $\tilde{R}_{Bj} = \tilde{R}_{Bj}(t)$ is some spatially averaged measure of the total amount of VEGF bound to cell j . For example, we might consider the global average receptor concentration:

$$\tilde{R}_{Bj}(t) = \bar{R}_{Bj}(t) = \frac{\int_0^{L_0+F_j(t)} \rho_{Bj}(x, t) dx}{L_0 + F_j(t)}. \quad (5.1.4)$$

The biological justification for this choice would be if signal transduction from all VEGFR-2 was integrated by the cell. An alternative might be that signal transduction depends on the concentration of bound VEGFR-2 close to the nucleus or indeed the concentration at any single point on the cell membrane, $x \in [0, L_0]$. For simplicity, we proceed using the concentration of bound VEGFR-2 at the bottom/proximal end of the cell where $x = 0$, $\tilde{R}_{Bj}(t) = \rho_{Bj}(0, t)$.

We assume that VEGFR-2 can bind and unbind with extracellular VEGF at association and dissociation rates, k_{VR} and k_{-VR} , respectively. We also assume that unbound VEGF receptors decay linearly with rate μ and that their production is downregulated by bound Notch receptors. Hence, the equations for $\rho_{Uj}(x, t)$ and $\rho_{Bj}(x, t)$, defined on the domain $x \in [0, L_0 + F_j(t)]$ as follows,

$$\begin{aligned} \frac{\partial \rho_{Uj}}{\partial t} = & (1 + \hat{\theta}F_j(t))f(b_j) + k_{-VR}\rho_{Bj} - k_{VR}\rho_{Uj}V(x) - \lambda\rho_{Uj} \\ & + \underbrace{D_U \frac{\partial^2 \rho_{Uj}}{\partial x^2}}_{\text{Diffusion}} - \underbrace{\frac{\partial}{\partial x} (v_j \rho_{Uj})}_{\text{Advection}}, \end{aligned} \quad (5.1.5)$$

$$\frac{\partial \rho_{Bj}}{\partial t} = k_{VR}\rho_{Uj}V(x) - k_{-VR}\rho_{Bj} + D_B \frac{\partial^2 \rho_{Bj}}{\partial x^2} - \frac{\partial}{\partial x} (v_j \rho_{Bj}). \quad (5.1.6)$$

D_U and D_B represent the diffusivity of unbound and bound VEGF receptors in the cell membrane, and the $\frac{\partial}{\partial x} (v_j \rho)$ term represents the advective transport of receptors in the filopodia with local advective velocity $v_j(x, t)$ which is determined by constitutive laws that we define later in this chapter. Each law assumes domain growth is localised

in the filopodia (zero domain growth at the cell body). Thus a Dirichlet condition at $x = 0$ matching the velocity at the cell body is specified under the assumption that the proximal end remains fixed:

$$v_j(0, t) = 0. \quad (5.1.7)$$

The remaining terms represent VEGFR-2 production and linear degradation, and VEGF-VEGFR-2 binding and unbinding as specified in the ODE model earlier (see equations (4.1.4) and (4.1.5)). In this model however, the VEGF concentration at position x is given by

$$V(x) = L_0 + \psi(x - L_0), \quad (5.1.8)$$

rather than being approximated by an integral, as per the ODE model in Chapter 4 (see equation (4.1.10)).

The boundary conditions for ρ_{Uj} and ρ_{Bj} are zero flux at $x = 0$ and $x = L_0 + F_j(t)$:

$$\frac{\partial \rho_{Uj}}{\partial x}(0, t) = 0 = \frac{\partial \rho_{Uj}}{\partial x}(L_0 + F_j(t), t), \quad (5.1.9)$$

$$\frac{\partial \rho_{Bj}}{\partial x}(0, t) = 0 = \frac{\partial \rho_{Bj}}{\partial x}(L_0 + F_j(t), t). \quad (5.1.10)$$

This ensures that VEGF receptors are not lost at the domain boundaries. Furthermore, the velocity at the end of the filopodia defines the overall growth rate of the filopodia domain:

$$\frac{dF_j}{dt} = v_j(L_0 + F_j(t), t). \quad (5.1.11)$$

The initial conditions are specified when conducting numerical simulations. Thus far, the dimensional model is specified by the ODEs in equations (5.1.1)-(5.1.3); the PDEs in equations (5.1.5)-(5.1.6) with boundary conditions in equations (5.1.9)-(5.1.10) and filopodia length as per equation (5.1.11). It remains to determine the flow, $v_j(x, t)$ which has boundary condition in equation (5.1.7). We consider several examples in the sections that follow.

5.2 Domain growth laws

Growth is driven by local expansion of the cell membrane which leads to the transport of material comprising the membrane and filopodia (lipids, proteins and actin, for example). In our model, membrane extension, specifically in the filopodia, is stimulated by bound VEGFR-2. In the cell body, there may be constant membrane turnover due to endocytosis which is balanced by production but for convenience we define the local strain rate in the cell body to be zero. In the filopodia, we suppose that the local strain

depends on the local concentration of bound VEGFR-2 and the filopodium length minus some constant which accounts for membrane turnover or endocytosis. Thus the general form of the local strain rate is

$$\frac{\partial v_j}{\partial x} = \begin{cases} 0, & 0 \leq x < L_0 \\ \Gamma(\rho_{Bj}(x, t), F_j(t)) - \gamma, & L_0 \leq x \leq L_0 + F_j(t) \end{cases}, \quad (5.2.1)$$

where Γ is an operator for domain growth which takes the form of a function of the bound VEGFR-2 concentration, $\rho_{Bj}(x, t)$, and the filopodium length, $F_j(t)$. This is to be a local function in the case where growth depends on locally bound VEGFR-2, or a function of an integral in the case where growth depends on the global average concentration of bound VEGFR-2 (see equation (5.1.4)). We consider these two cases and a third case, in which the growth depends on the receptor concentration at a single point ($x = 0$), individually, and compare the form of the ODE for filopodia growth predicted by the PDE model of this section and the ODE model of §4.

In the sections that follow, we consider both filopodia length independent and dependent forms for Γ . In §5.2.1-5.2.3 we consider a form of local growth which is independent of the filopodia length:

$$\Gamma(\rho_{Bj}(x, t), F_j(t)) = \Phi(\rho_{Bj}(x, t)), \quad (5.2.2)$$

and in §5.2.4-5.2.5 we consider filopodia length-dependent growth:

$$\Gamma(\rho_{Bj}(x, t), F_j(t)) = \frac{\Phi(\rho_{Bj}(x, t))}{F_j(t)}. \quad (5.2.3)$$

5.2.1 Local strain dependent on the local bound VEGFR-2 concentration

In this case the local strain rate, $\partial v_j / \partial x$, is assumed to be zero in the cell body due to the assumption of zero growth and decay there. In the filopodia, Γ is some filopodium length-independent function, Φ , of the local receptor concentration, $\rho_{Bj}(x, t)$. Hence the local strain rate is given by:

$$\frac{\partial v_j}{\partial x} = \begin{cases} 0, & 0 \leq x < L_0 \\ \Phi(\rho_{Bj}(x, t)) - \gamma, & L_0 \leq x \leq L_0 + F_j(t) \end{cases}. \quad (5.2.4)$$

Integrating this with respect to x and applying the boundary condition gives

$$v_j(x, t) = \begin{cases} 0, & 0 \leq x < L_0 \\ \int_{L_0}^x \Phi(\rho_{Bj}(x, t)) dx - \gamma(x - L_0), & L_0 \leq x \leq L_0 + F_j(t) \end{cases}, \quad (5.2.5)$$

and in particular,

$$\frac{dF_j}{dt} = v_j(L_0 + F_j(t), t) = \int_{L_0}^{L_0+F_j(t)} \Phi(\rho_{B_j}(x, t)) dx - \gamma F_j(t). \quad (5.2.6)$$

We also note that if Φ were a linear operator e.g. $\Phi(y) = \zeta y$, then using equation (5.1.4),

$$\frac{dF_j}{dt} = \zeta \int_{L_0}^{L_0+F_j(t)} \rho_{B_j}(x, t) dx - \gamma F_j \quad (5.2.7)$$

$$= \zeta \left((L_0 + F_j) \bar{R}_{B_j} - \int_0^{L_0} \rho_{B_j}(x, t) dx \right) - \gamma F_j, \quad (5.2.8)$$

which is in contrast to the growth rate, $w(\cdot)$, used in the phenomenological ODE model of §4 (see equation 4.1.3). This is due to the multiplying factor $(L_0 + F_j)$ in equation (5.2.8) which we expect will lead to unbounded growth (this is shown later) and the correcting integral due to the zero contribution from $[0, L_0]$ in this model. We do, however, obtain the general property, similar to the ODE model of chapter (see equation (4.1.3)), that the filopodia elongation rate should be some function of bound VEGFR-2 density minus decay.

5.2.2 Local strain dependent on the global average bound VEGFR-2 concentration

If Γ is another filopodia length-independent function, Φ , of the global average bound VEGFR-2 concentration, $\bar{R}_{B_j}(t)$, then the strain rate, $\partial v_j / \partial x$, is given by

$$\frac{\partial v_j}{\partial x} = \begin{cases} 0, & 0 \leq x < L_0 \\ \Phi(\bar{R}_{B_j}(t)) - \gamma, & L_0 \leq x \leq L_0 + F_j(t) \end{cases}. \quad (5.2.9)$$

This can be integrated directly as the right-hand side is (piecewise) spatially independent and after applying the boundary conditions we obtain

$$v_j(x, t) = \begin{cases} 0, & 0 \leq x < L_0 \\ (\Phi(\bar{R}_{B_j}(t)) - \gamma)(x - L_0), & L_0 \leq x \leq L_0 + F_j(t) \end{cases}, \quad (5.2.10)$$

and in particular,

$$\frac{dF_j}{dt} = v_j(L_0 + F_j(t), t) = (\Phi(\bar{R}_{B_j}(t)) - \gamma) F_j(t). \quad (5.2.11)$$

The growth function, Φ , multiplying $F_j(t)$ may be problematic given the kind of form we expect, (compare with equation (4.1.3)), because, similarly to the growth law in §5.2.1, the $\Phi(\bar{R}_{B_j}(t)) F_j(t)$ term is likely to lead to the unbounded growth of $F_j(t)$.

5.2.3 Local strain dependent on the VEGFR-2 concentration at the proximal end of the cell ($x = 0$)

This section considers a specific case in which domain growth depends on the bound VEGFR-2 concentration at a single point and is independent of the filopodium length. A growth law of this type may be appropriate if the cell nucleus co-ordinated transport of actin for filopodia growth is determined by the VEGF signal at the cell body. This could be a point close to the nucleus, for instance. However, choosing the point $x = 0$ is both analytically and numerically tractable. The strain rate becomes integrable and allows us to validate our method of numerical integration in the sections that follow. The strain rate is given by

$$\frac{\partial v_j}{\partial x} = \begin{cases} 0, & 0 \leq x < L_0 \\ \Phi(\rho_{Bj}(0, t)) - \gamma, & L_0 \leq x \leq L_0 + F_j(t) \end{cases}. \quad (5.2.12)$$

Since this is spatially independent, it can be directly integrated to give

$$v_j(x, t) = \begin{cases} 0, & 0 \leq x < L_0 \\ (\Phi(\rho_{Bj}(0, t)) - \gamma)(x - L_0), & L_0 \leq x \leq L_0 + F_j(t) \end{cases}, \quad (5.2.13)$$

which yields an equation for filopodia growth of the form

$$\frac{dF_j}{dt} = v_j(L_0 + F_j(t), t) = (\Phi(\rho_{Bj}(0, t)) - \gamma)F_j(t). \quad (5.2.14)$$

The issue of unbounded growth due to the $\Phi(\rho_{Bj}(0, t))F_j(t)$ term arises again for this case. In fact, the form of equation (5.2.14) is very similar to equation (5.2.11).

5.2.4 Filopodia length-dependent local bound VEGFR-2 dependent growth model

In this section, we consider a form for Γ which is dependent on the filopodia length as given in equation (5.2.3). A biological justification for this could be that there is limited material for growth which has to be distributed over the length of the filopodium and hence division of the local growth term by the filopodium length in equation (5.2.3). We show that provided we assume a large receptor diffusivity, we can obtain an equation for F_j , which is identical to the one belonging to the ODE model of Chapter 4 (see equation (4.1.3)).

We assume that the operator Γ takes the form

$$\frac{\Phi(\cdot)}{F_j(t)}. \quad (5.2.15)$$

Now the strain rate in (5.2.4) changes to

$$\frac{\partial v_j}{\partial x} = \begin{cases} 0, & 0 \leq x < L_0 \\ \frac{\Phi(\rho_{B_j}(x,t))}{F_j} - \gamma, & L_0 \leq x \leq L_0 + F_j(t) \end{cases}. \quad (5.2.16)$$

Integrating this and applying the boundary condition gives

$$v(x, t) = \begin{cases} 0, & 0 \leq x < L_0 \\ \frac{\int_{L_0}^x \Phi(\rho_{B_j}(x,t)) dx}{F_j} - \gamma(x - L_0), & L_0 \leq x \leq L_0 + F_j(t) \end{cases}. \quad (5.2.17)$$

By assuming large receptor diffusivity, we have an approximate spatially homogeneous distribution of bound VEGFR-2:

$$\rho_{B_j}(x, t) \approx \bar{R}_{B_j}(t), \quad (5.2.18)$$

which allows us to evaluate the integral in equation (5.2.17) which is now given by

$$\begin{aligned} \frac{dF_j}{dt} &= \Phi(\bar{R}_{B_j}(t)) \frac{\int_{L_0}^{L_0+F_j(t)} dx}{F_j(t)} - \gamma F_j(t) \\ &= \Phi(\bar{R}_{B_j}(t)) - \gamma F_j(t) \end{aligned} \quad (5.2.19)$$

which is in agreement with the ODE in equation (4.1.3).

5.2.5 Filopodia length-dependent global average and proximal end VEGFR-2 dependent growth models

In this section we again consider a form for Γ which is dependent on the filopodia length as given in equation (5.2.3) with biological justification as given in §5.2.4.

We show that the models assuming growth dependent on the global average and proximal end bound VEGFR-2 concentrations each give an ODE: $v_j(L_0 + F_j, t) = \frac{dF_j}{dt}$ in agreement with equation (4.1.3) of the ODE model. For the model considering global average VEGFR-2 dependent growth we obtain the following strain rate

$$\frac{\partial v_j}{\partial x} = \begin{cases} 0, & 0 \leq x < L_0 \\ \frac{\Phi(\bar{R}_{B_j}(t))}{F_j} - \gamma, & L_0 \leq x \leq L_0 + F_j(t) \end{cases}, \quad (5.2.20)$$

which can be integrated to give

$$v_j(x, t) = \begin{cases} 0, & 0 \leq x < L_0 \\ \left(\frac{\Phi(\bar{R}_{B_j}(t))}{F_j} - \gamma \right) (x - L_0), & L_0 \leq x \leq L_0 + F_j(t) \end{cases}, \quad (5.2.21)$$

and in particular

$$\frac{dF_j}{dt} = v_j(L_0 + F_j(t), t) = \Phi(\bar{R}_{B_j}(t)) - \gamma F_j(t), \quad (5.2.22)$$

which agrees with the form of equation (4.1.3).

The same steps can be taken for the model considering proximal end bound VEGFR-2 from equation (5.2.12). Therefore the algebra is omitted here but yields the following ODE for filopodia growth:

$$\frac{dF_j}{dt} = v_j(L_0 + F_j(t), t) = \Phi(\rho_{B_j}(0, t)) - \gamma F_j(t), \quad (5.2.23)$$

which is also of the required form (matching equation (4.1.3)).

We note that for both global average and proximal end dependent models, the assumption of large receptor diffusivity is not necessary to obtain the form of $\frac{dF_j}{dt}$ matching equation (4.1.3).

We note that for a growth operator of the form

$$\Gamma = \frac{\Phi(\cdot)}{F_j(t)}, \quad (5.2.24)$$

which depends on the filopodium length F_j , both global average bound VEGFR-2 and proximal end bound VEGFR-2 dependent growth models give ODEs for filopodia extension which agree with those of the ODE model. We also expect the local bound VEGFR-2 model to agree with the ODE model when VEGFR-2 diffusivity is rapid. Without this condition we do not obtain the same form of ODE for filopodia growth as used in the ODE model of Chapter 4.

5.3 Numerical simulation

In this section we simulate equations (5.1.1)-(5.1.11) for the following growth laws:

- proximal end bound VEGFR-2 dependent growth divided by filopodia length (see equation (5.2.12)) ,
- local bound VEGFR-2 dependent growth divided by filopodia length (see equation (5.2.16)) ,
- local bound VEGFR-2 dependent growth divided by the entire domain length (as equation (5.2.16) but divided by $L_0 + F_j$) ,
- global average bound VEGFR-2 dependent growth (see equation (5.2.20)) ,

- local bound VEGFR-2 dependent growth (no division by filopodia length; see equation (5.2.16)) .

Numerical simulations are performed, in the order listed above, The order in which the models are simulated is different to the order in which they were first presented in §5.2. In this section, we simulate the models in order of increasing complexity required to numerically implement each model. We start by considering the model with proximal end VEGFR-2 dependent growth as it is the simplest to set up. This model has fewer PDEs (2 second order PDEs in equations (5.1.5) and (5.1.6)) which are easier to solve than equations for local and global average bound VEGFR-2 dependent growth laws. This is because, for growth depending on VEGFR-2 at a single point, the PDE for the strain rate decouples from equations (5.1.5) and (5.1.6).

We then simulate model variants with local bound VEGFR-2 dependent growth. The spatially dependent strain rate involves coupling an extra PDE for the strain rate, $\frac{\partial v_j}{\partial x}$, to the 2 second order PDEs. We simulate local VEGFR-2 dependent growth divided by the filopodia length, followed by local VEGFR-2 dependent growth divided by the entire domain length. This latter case corresponds to a different ODE model for filopodia growth and we compare the steady state behaviour and bifurcation structure of the two models.

Following this, we simulate growth depending on the global average bound VEGFR-2 as it is the most complicated model to implement. By introducing an extra variable representing the cumulative number of bound VEGFR-2, we are able to track the global average concentration of receptors.

Finally we consider local growth without dividing by the filopodia or entire domain lengths to demonstrate that filopodia lengths can grow unbounded depending on the parameters used. This justifies dividing the growth terms by $F_j(t)$ in the previous sections so that our models exhibit physically realistic solutions.

Numerical simulations of two-cell systems with periodic boundary conditions (with respect to the cell number, j) are carried out using the Fortran/NAG routines D03PHF and D03PKF (details are given in §5.3.2). These two solvers require the domain size to be fixed. Hence we begin by mapping the equations in (5.1.5)-(5.1.11) onto a fixed domain. Finite element method solvers, which work directly on deforming or adapting meshes, offer another possible way of integrating these equations directly, without rescaling onto a fixed domain but we proceed using the former [124].

Before mapping the equations to a fixed domain, we non-dimensionalise the model in equations (5.1.1)-(5.1.11) to allow for comparison with the ODE model of Chapter

4. Equations (5.1.5)-(5.1.6) and the boundary conditions in (5.1.9)-(5.1.10) are non-dimensionalised in the same way as averaged bound and unbound VEGF receptors are in Chapters 3 and 4 (see Appendix B). The new variables, $\rho_{Uj}, \rho_{Bj}, x, v_j$ have the following scalings:

$$\rho_{Uj} = \frac{R_{U0}}{k_{-VR}} \rho_{Uj}^*, \quad \rho_{Bj} = \frac{R_{U0}}{k_{-VR}} \rho_{Bj}^*, \quad x = L_0 x^*, \quad v = L_0 k_{-VR} v^* \quad (5.3.1)$$

where the stars, on the dimensionless variables are dropped for convenience. The new dimensionless diffusion coefficients of the PDE model are as follows:

$$D_U^* = L_0^2 k_{-VR} D_U, \quad D_B^* = L_0^2 k_{-VR} D_B. \quad (5.3.2)$$

The stars on the dimensionless parameters are dropped for convenience here too.

5.3.1 Transforming PDEs to a fixed domain

The governing equations are solved using the Fortran/NAG routines, D03PHF and D03PKF on a spatial domain of fixed length. However, since the filopodia in our model dynamically extend and retract, the domain length evolves over time making this a moving boundary problem. Thus the PDEs in equations (5.1.5) and (5.1.6), the boundary conditions, (5.1.9) and (5.1.9), and the growth law, $\frac{\partial v_j}{\partial x}$, must all be transformed onto a fixed domain. We do this following Crampin et al [101].

We use the uniform spatial scaling given by

$$\xi_j(x, t) = \frac{x}{r_j(t)} \quad \text{where} \quad r_j(t) = L_0 + F_j(t), \quad (5.3.3)$$

to transform the spatial co-ordinate in cell j , $x \in [0, L_0 + F_j]$, to the unit interval $[0, 1]$.

We rewrite equations (5.1.5) and (5.1.6) as

$$\frac{\partial \rho_{Uj}}{\partial t} = \eta_{Uj}(\rho_{Uj}, \rho_{Bj}, x, b_j, F_j(t)) + D_U \frac{\partial^2 \rho_{Uj}}{\partial x^2} - \frac{\partial}{\partial x} (v_j \rho_{Uj}), \quad (5.3.4)$$

$$\frac{\partial \rho_{Bj}}{\partial t} = \eta_{Bj}(\rho_{Uj}, \rho_{Bj}, x) + D_B \frac{\partial^2 \rho_{Bj}}{\partial x^2} - \frac{\partial}{\partial x} (v_j \rho_{Bj}), \quad (5.3.5)$$

where

$$\eta_{Uj} = (1 + \hat{\theta} F_j(t)) f(b_j) + k_{-VR} \rho_{Bj} - k_{VR} \rho_{Uj} V(x) - \lambda \rho_{Uj}$$

$$\eta_{Bj} = k_{VR} \rho_{Uj} V(x) - k_{-VR} \rho_{Bj}$$

Using the transformation in (5.3.3) the time derivatives become

$$\frac{\partial}{\partial t} = \frac{\partial}{\partial t} + \frac{\partial}{\partial \xi_j} \frac{\partial \xi_j}{\partial t} = \frac{\partial}{\partial t} - \frac{\partial}{\partial \xi_j} \frac{x}{r_j^2} \frac{dr_j}{dt} = \frac{\partial}{\partial t} - \frac{\xi_j}{r_j} \frac{\partial}{\partial \xi_j} \frac{dr_j}{dt}, \quad (5.3.6)$$

and the spatial derivatives become

$$\frac{\partial}{\partial x} = \frac{\partial}{\partial \xi_j} \frac{\partial \xi_j}{\partial x} = \frac{\partial}{\partial \xi_j} \frac{1}{r_j}. \quad (5.3.7)$$

Applying these to equations (5.1.5) and (5.1.6), and denoting the transformed variables for unbound and bound VEGF receptors by $\tilde{\rho}_U(\xi_j(x, t), t)$ and $\tilde{\rho}_B(\xi_j(x, t), t)$, we obtain

$$\frac{\partial \tilde{\rho}_{Uj}}{\partial t} = \eta_{Uj}(\rho_{Uj}, \rho_{Bj}, x, b_j, F_j(t)) + \frac{1}{r_j} \frac{\partial}{\partial \xi_j} \left(D_U \frac{1}{r_j} \frac{\partial \tilde{\rho}_{Uj}}{\partial \xi_j} - v_j \rho_{Uj} \right) + \frac{1}{r_j} \xi_j \frac{\partial \tilde{\rho}_{Uj}}{\partial \xi_j} \frac{dr_j}{dt}, \quad (5.3.8)$$

$$\frac{\partial \tilde{\rho}_{Bj}}{\partial t} = \eta_{Bj}(\rho_{Uj}, \rho_{Bj}, x, b_j, F_j(t)) + \frac{1}{r_j} \frac{\partial}{\partial \xi_j} \left(D_U \frac{1}{r_j} \frac{\partial \tilde{\rho}_{Bj}}{\partial \xi_j} - v_j \rho_{Bj} \right) + \frac{1}{r_j} \xi_j \frac{\partial \tilde{\rho}_{Bj}}{\partial \xi_j} \frac{dr_j}{dt}, \quad (5.3.9)$$

and the zero flux boundary conditions in equations (5.1.9) and (5.1.10) are given by

$$\frac{1}{r_j} \frac{\partial \rho_{Uj}}{\partial \xi_j}(0, t) = 0 = \frac{1}{r_j} \frac{\partial \rho_{Uj}}{\partial \xi_j}(1, t), \quad (5.3.10)$$

$$\frac{1}{r_j} \frac{\partial \rho_{Bj}}{\partial \xi_j}(0, t) = 0 = \frac{1}{r_j} \frac{\partial \rho_{Bj}}{\partial \xi_j}(1, t). \quad (5.3.11)$$

In general, the flow, $v_j(x, t)$, is determined by integrating the local strain rate, $\frac{\partial v_j}{\partial x}(x, t)$ which we define and transform, case-by-case, in the examples that follow.

5.3.2 Numerical solvers and numerical continuation methodology

We integrate the models outlined at the beginning of 5.3 using two Fortran/NAG routine methods. The first method, D03PHF, integrates linear or non-linear systems of parabolic PDEs in one space dimension coupled to ODEs. The PDEs are solved using the method of lines by which they are discretised using finite difference methods, converting them to ODEs, and then solved using a backward differentiation formula. This method is used to implement the proximal end bound VEGFR-2 dependent growth law because in this case the model comprises two second order, reaction-diffusion equations.

The D03PKF solver integrates systems of first order PDEs in one space dimension, coupled to ODEs. The solver uses a Keller box scheme to discretise and reduce the PDEs to ODEs which are then solved in the same way as D03PHF. We use this method when the first order PDE cannot be integrated directly, when we consider local bound VEGFR-2 dependent growth, for example. In such cases, we convert our second order PDEs for $\rho_{Uj}(x, t)$ and $\rho_{Bj}(x, t)$ to a system of 4 first order PDEs. These are coupled to the first order PDE for the velocity, v_j , giving 5 PDEs coupled to 3 ODEs which are solved using the local VEGFR-2 dependent growth model.

For each model, we compare the steady state solutions and bifurcations of the PDE model with the steady states and bifurcations of the ODE model from Chapter 4. We focus on the sensitivity of our model solutions to variations in the VEGF gradient, ψ , and thus compare steady state solutions for bound Notch receptors, b_1, b_2 , and filopodia lengths, F_1, F_2 , in two-cell systems of the ODE and PDE models using parameter values from Table 4.1. We already have the steady states for the ODE model (see Figure 4.7a). To produce the equivalent bifurcation diagram for the PDE model, we perform semi-automated numerical continuation.

For a particular value of the parameter ψ , we impose initial conditions close to the homogeneous steady state and integrate equations (5.1.1)-(5.1.11), with the appropriate growth law, forwards in time. To determine whether the system has reached steady state, we calculate the relative change in the L2-norm of the solution vector, corresponding to the ODE variables, and terminate integration when the relative change in the norm was $< 1 \times 10^{-9}$. The parameter ψ was then increased, and integration repeated, using as initial conditions, the steady state for the previous value of ψ . In this way we established the locations of the steady state branches in parameter space.

One of the challenges in assigning initial conditions corresponding to the final solution following integration from the previous run was that initial conditions usually began on a steady state branch. When the system moved beyond the pitchfork bifurcation, the initial conditions corresponded to being on the stable manifold of the unstable homogeneous branch of solutions. Therefore we added a perturbation to the initial conditions so the system could move away from the unstable homogeneous steady state and settle at a period-2 spatial pattern.

By varying $\psi \in [0, 2]$, we were able to capture the pitchfork bifurcation (of the ODE model) at $\psi \approx 0.157$ and the inner (low amplitude) patterning branches. When the system reached the pair of fold bifurcations at $\psi \approx 1.80$, it moved to the outer (large amplitude) patterning branches. In order to find the outer patterning branches for $0.618 < \psi < 1.80$ (the quadstable region) we decreased ψ from 2 to 0 as the system only moved to the inner pair of patterning branches at the pair of fold bifurcations at $\psi \approx 0.618$. We term finding the steady state solutions of the PDE model in this way, by increasing and decreasing the bifurcation parameter, a *forward* and *reverse run*, respectively.

Since D03PHF and D03PKF solve PDEs on a fixed domain, when plotting the spatial distribution of VEGF receptors, we transform back from the scaled/fixed domain $\xi_j \in [0, 1]$ to the growing domain which extends to the filopodium tip $x \in [0, L_0 + F_j]$.

5.4 Simulation of proximal end bound VEGFR-2 dependent filopodia growth

In this section we assume that the growth of the domain at position x depends on $\rho_{Bj}(0, t)$, the concentration of bound VEGFR-2 at the proximal end of the domain ($x = 0$), as defined in §5.2.3 and define the local strain rate as

$$\frac{\partial v_j}{\partial x} = \begin{cases} 0, & 0 \leq x < L_0 \\ \frac{\phi w(\rho_{Bj}(0, t))}{F_j(t)} - \gamma, & L_0 \leq x \leq L_0 + F_j(t) \end{cases}, \quad (5.4.1)$$

where $w(\cdot)$ is as defined in equations (4.1.1) and (4.1.2), which, using the transformation in equation (5.3.3), gives

$$\frac{\partial v_j}{\partial \xi_j} = \begin{cases} 0, & 0 \leq \xi_j < \frac{L_0}{L_0 + F_j(t)} \\ \left(\frac{\phi w(\rho_{Bj}(0, t))}{F_j(t)} - \gamma \right) (L_0 + F_j(t)), & \frac{L_0}{L_0 + F_j(t)} \leq \xi_j \leq 1 \end{cases}. \quad (5.4.2)$$

In this case, an arbitrary point along the cell membrane could be chosen to define the growth rate at position x , however choosing the point $x = 0$ makes sense from a numerical point of view as it is invariant under the transformation in equation (5.3.3) making it the simplest spatial coupling point to use.

5.4.1 Simulation with algebraically defined velocity profile

Since the form of the local strain rate in equation (5.4.1) is independent of the spatial variable, x , it can be integrated to find an explicit algebraic expression for the velocity given by

$$v_j(x, t) = \begin{cases} 0, & 0 \leq x < L_0 \\ \left(\frac{\phi w(\rho_{Bj}(0, t))}{F_j(t)} - \gamma \right) (x - L_0), & L_0 \leq x \leq L_0 + F_j(t) \end{cases}. \quad (5.4.3)$$

The corresponding scaled velocity can be found by either transforming equation (5.4.3) (using 5.4.1) or by integrating equation (5.4.2), and is given by

$$v_j(\xi_j, t) = \begin{cases} 0, & 0 \leq \xi_j < \frac{L_0}{L_0 + F_j(t)} \\ \left(\frac{\phi w(\rho_{Bj}(0, t))}{F_j(t)} - \gamma \right) (\xi_j(L_0 + F_j(t)) - L_0), & \frac{L_0}{L_0 + F_j(t)} \leq \xi_j \leq 1 \end{cases}. \quad (5.4.4)$$

Equations (5.1.1)-(5.1.11), with velocity as per equation (5.4.3), are integrated to steady state for values of $\psi \in [0, 2]$ using the numerical continuation method described in §5.3.2. In Figure 5.2 we show that the steady state solution branches for bound Notch

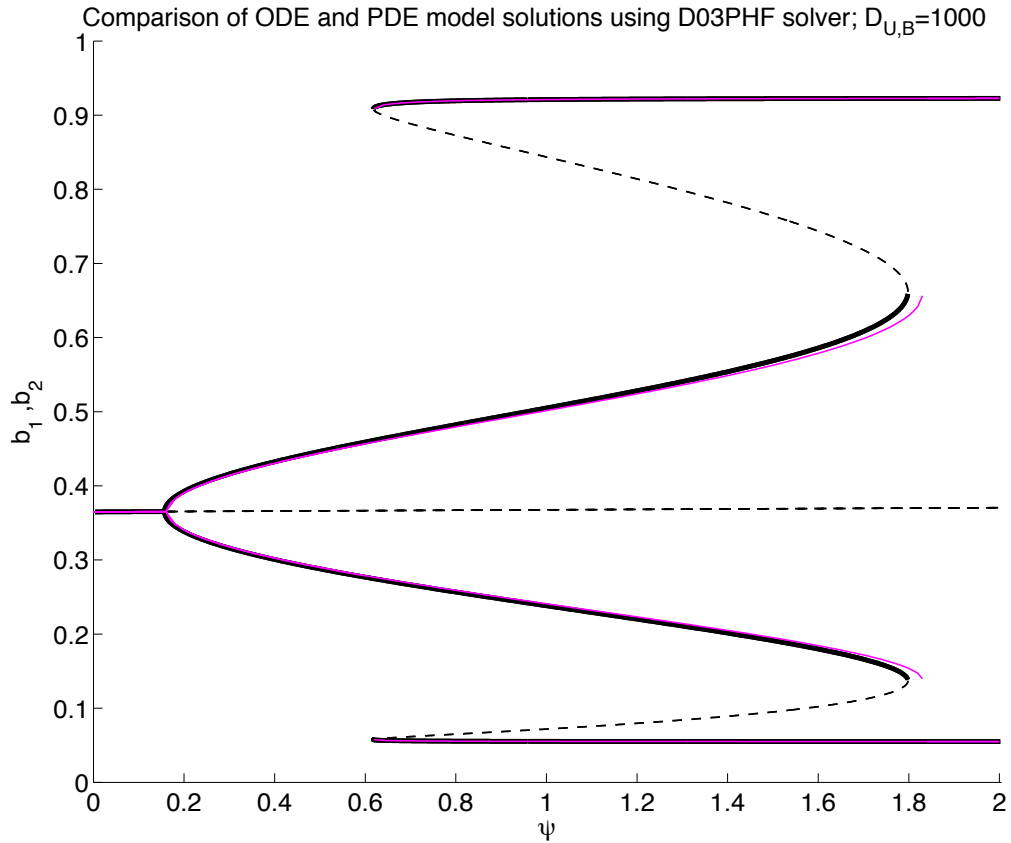


Figure 5.2: Bifurcation diagram constructed by integrating equations (5.1.1)-(5.1.11), using the algebraically defined velocity profile in equation (5.4.3) arising from the growth law in equation (5.4.1), to steady state and plotting steady solutions for bound Notch receptors, b_1, b_2 , for $\psi \in [0, 2]$ (plotted in magenta). This is superimposed with the corresponding bifurcation diagram from the ODE model with filopodia grown given in equations (4.1.11)-(4.1.16) (plotted in black; also see Figure 4.7). For a large receptor diffusivity, in this case $D = 1000$, the steady states of the PDE and ODE models match up very well.

receptors, b_1, b_2 , from the PDE model using the parameter values in Table 4.1, closely match the steady state solutions of the corresponding ODE model (see Figure 4.7)

The PDE model's solutions appear to deviate slightly from the ODE model solutions for $\psi \in [1.5, 1.8]$. This deviation decreases when the number of spatial mesh points used to discretise the PDEs is increased or when the diffusion coefficients for unbound and bound VEGF receptors, D_U and D_B , are increased. Figure 5.3 shows that, for $\psi = 1.7$, increasing the diffusion coefficients beyond $D_U, D_B = 300$ does not significantly affect convergence of the two model solutions. A finer spatial mesh, however, does further improve the agreement between the two models.

We therefore fix the diffusion coefficients at $D_U, D_B = 300$, and run simulations of the PDE model to steady state, for increasing numbers of spatial mesh points. We find that the steady state solutions of the PDE model converge to the steady state solutions of the ODE model (see Figure 5.4).

5.4.2 Simulation with a coupled PDE for the strain rate

In this section, we simulate the same model for domain growth based on the VEGFR-2 level at the proximal end of the cell, as per equation (5.4.1). However, instead of using the algebraic form for the advection velocity, given in equation (5.4.3), we couple the strain rate, $\frac{\partial v_j}{\partial x}$, to the remaining equations and allow the solver to determine the advection velocity at each integration step. We do this to develop simulations that can be applied to the more complex growth laws for which algebraic expressions for $v_j(x)$ are not available. In this way we can test the numerical methods against the results in §5.4.1 and verify that D03PKF integrates the PDE for $v(x, t)$ correctly.

In order to use the Fortran/NAG routine, D03PKF, we first converted equations (5.1.5) and (5.1.6) to a system of first order PDEs (as described in §5.3.2) to integrate an equivalent system of equations with $\frac{\partial v_j}{\partial x}$ used to determine the advection velocity.

In this section we show that the two numerical methods used to solve the model with proximal-end ($x = 0$) bound VEGFR-2 dependent growth, one using an algebraically defined velocity profile (see (5.4.3)) and the other using a PDE for the velocity, agree well. This gives us faith in the solution profiles calculated by D03PKF. By running the model to steady state, whilst varying ψ , we find that this simulation model has an equivalent bifurcation diagram to the method used in §5.4.1 when the diffusion coefficients D_U, D_B are large (compare Figures 5.2 and 5.5).

Since it is only the numerical method which changes, and not the growth law, we also expect the two methods to give equivalent steady state bifurcation diagrams when the

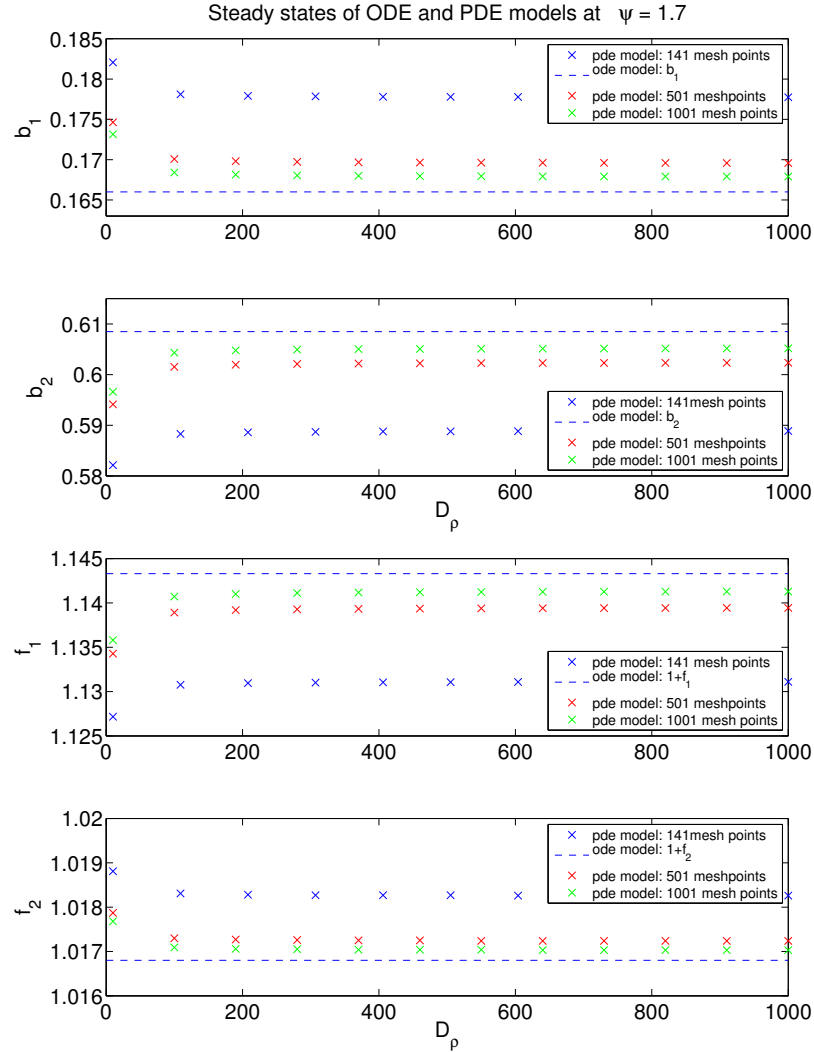


Figure 5.3: Convergence of the steady state PDE model solutions to the ODE model's steady state solutions as the diffusion coefficients, $D_U = D_B$, are varied (D_ρ is shorthand for both). PDE model solutions are found by integrating equations (5.1.1)-(5.1.11) for a two-cell system with the algebraic expression for the advection velocity given in equation (5.4.3). Simulations of the two cell system were run using extracellular VEGF gradient parameter, $\psi = 1.7$ (where agreement between the ODE and PDE model solutions is relatively poor with small numbers of spatial mesh points) and diffusion coefficients, $D_\rho \in [10, 1000]$. For 141 mesh points, as D_ρ is increased, the steady state of bound Notch receptors in each cell of the PDE model, b_1, b_2 (shown as blue crosses in upper two plots), approaches, but does not reach, the steady state of bound Notch receptors in the ODE model (blue dashed line in upper two plots). Increasing the number of mesh points improves the agreement between the PDE (red and green crosses in upper two plots) and ODE models. Similar convergence is seen for the filopodia lengths (lower two plots). In all cases, the PDE solutions do not change significantly beyond $D_\rho = D_U = D_B = 300$.

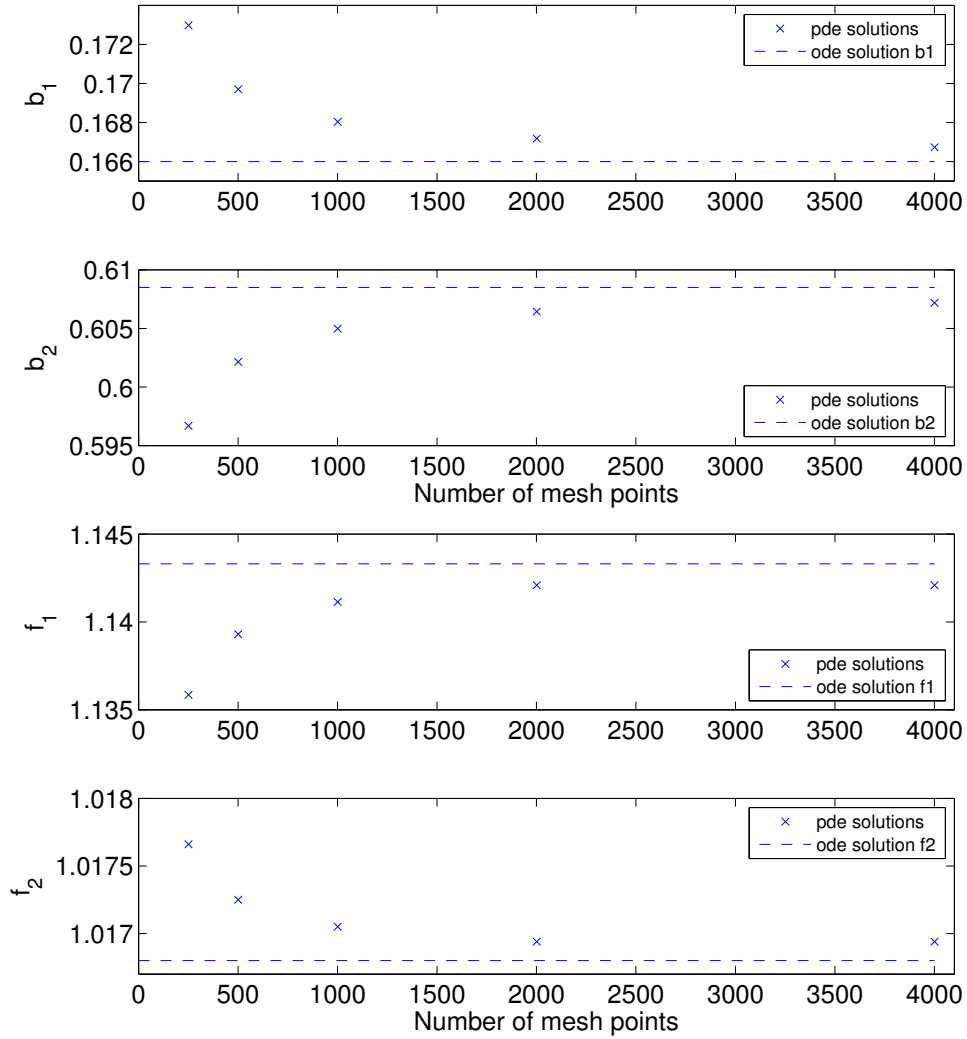


Figure 5.4: Convergence of the PDE model's steady state solutions to the steady states of the ODE model for increasing number of mesh points used in the discretisation of the PDE model. PDE model solutions were calculated by integrating equations (5.1.1)-(5.1.11) with the algebraically defined velocity profile in equation (5.4.3). Simulations of the two-cell system were run using extracellular VEGF slope parameter, $\psi = 1.7$ (where convergence to the ODE model's steady states is relatively poor with small numbers of spatial mesh points), and diffusion coefficients, $D_U = D_B = 300$. As the number of spatial mesh points is increased, the steady state of bound Notch receptors in each cell of the PDE model, b_1, b_2 (shown as blue crosses in upper two plots), approaches the steady state of bound Notch receptors in the ODE model in equations (4.1.11)-(4.1.16) (blue dashed lines in upper two plots). Similar convergence is seen for the filopodia lengths (lower two plots).

receptor diffusivity is small. Figure 5.5 shows that for $D_U, D_B = 1$, the agreement with the ODE model in equations (5.2.14)-(4.1.16) is not as good. The figure also shows that the fold bifurcations at $\psi \approx 0.618$ shift to the right.

We also show numerical simulations of the two-cell system for a particular value of the VEGF gradient, ($\psi = 1.95$), at which the model exhibits a single, large amplitude stable period-2 patterning solution (corresponding to the outer pair of solution branches) in which one cell has a very long filopodium and the other a very short one (see Figure 4.8). At $\psi = 1.95$, our simulations give steady state filopodia lengths $F_1 \approx 3.9$ and $F_2 \approx 0.0049$, as opposed to the lengths $F_1 \approx 0.066$ and $F_2 \approx 0.037$ when $\psi = 0.4$ (inner pair of patterning branches). When the diffusion coefficients D_U, D_B are large, the steady state distribution of unbound and bound VEGFR-2 on both cells is approximately spatially uniform (see Figures 5.7a and 5.7c). Cell 1 has a long filopodium which extends relatively far into the VEGF gradient. This results in high of VEGF-VEGFR-2 binding near the filopodium tip. Due to the large diffusion coefficient, the receptors quickly redistribute themselves along the filopodium and cell body, attaining a fairly spatially uniform distribution (blue plot in Figures 5.7a and 5.7c). Cell 2, however, has a very short filopodium which does not extend far into the VEGF gradient. Hence most of the VEGF-VEGFR-2 binding occurs in a constant concentration of VEGF and consequently the concentration of bound receptors is almost spatially uniform (red plot).

For smaller diffusion coefficients, the receptors move less quickly in the cell membrane, leading to spatially non-uniform steady state distributions of receptors along the filopodium and cell body (see Figures 5.7b and 5.7d). This is most apparent in cell 1 (blue plot in Figure (5.7)b), which has a long filopodium reaching far into the VEGF gradient. Since most binding occurs near the end of the filopodium, where the VEGF concentration is highest, the concentration of bound receptors increases along the filopodium, away from the cell. In contrast, despite the smaller diffusion coefficients, the receptor distribution in the cell with the shorter filopodia (see 5.7b and 5.7d) is almost homogeneous, since most of the binding occurs in the cell body, where the VEGF concentration is fixed at a constant value.

The agreement between the models in this section and §5.4.1 gives us confidence that the D03PKF solver correctly calculates the advection velocity by integrating the strain rate. Thus we can begin exploring more interesting and biologically realistic growth laws for which the strain rate is not analytically integrable.

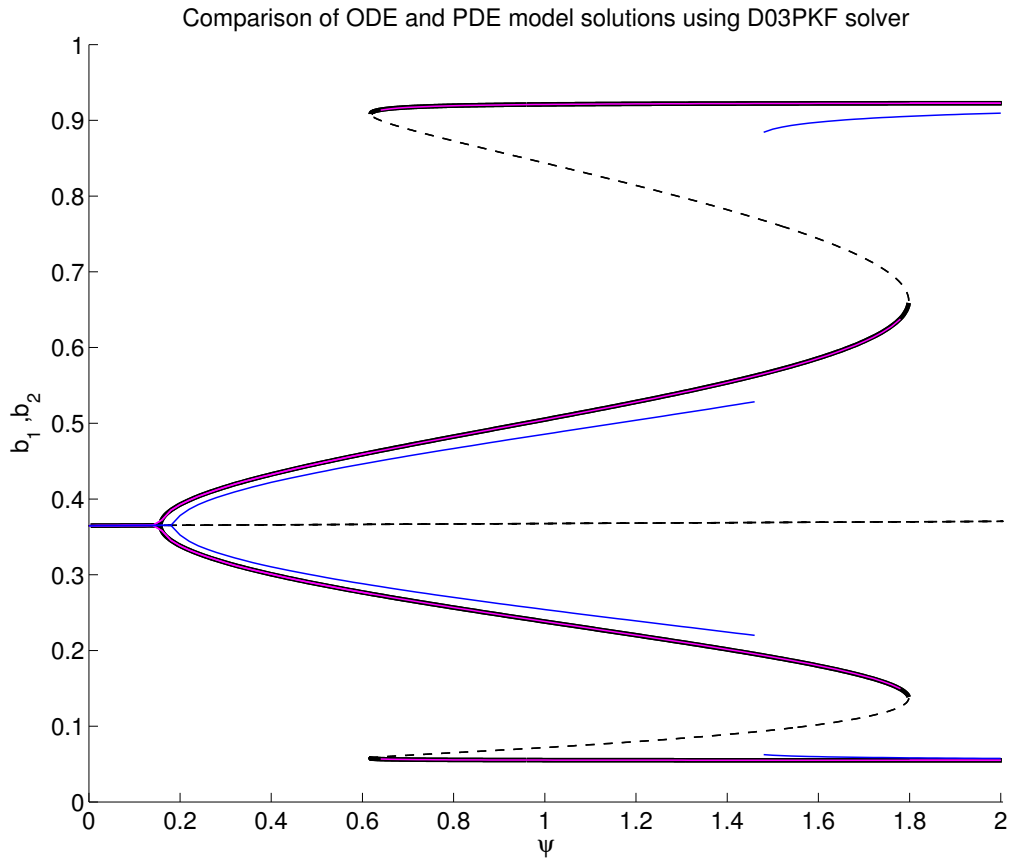


Figure 5.5: Bifurcation diagram showing steady state PDE model solutions (magenta) for bound Notch, b_j (shown in magenta) as the VEGF gradient ψ is varied. Solutions were obtained by integrating equations (5.1.1)-(5.1.11) subject to the proximal end bound VEGFR-2 dependent growth law (with a coupled PDE for the strain rate in (5.4.1)) to steady state. The equations were integrated using the DO3PKF routine for systems of first order PDEs. This numerical method produces very similar results to the D03PHF routine which was used to investigate the equations of the same model, with an algebraically defined velocity profile (compare with Figure 5.2). Good agreement with the ODE model solutions (superimposed in black) is observed, particularly near the fold bifurcations at $\psi \approx 1.80$ using this numerical integrator (compare with Figure 5.2). Parameter values used to integrate the PDEs are identical to those used to calculate the ODE model's steady states in Figure 4.7. PDE model solutions for $D_U, D_B = 1$ (blue), as described in §5.3.2, show that when receptor diffusivity is small enough, the agreement with the ODE model is not so good.

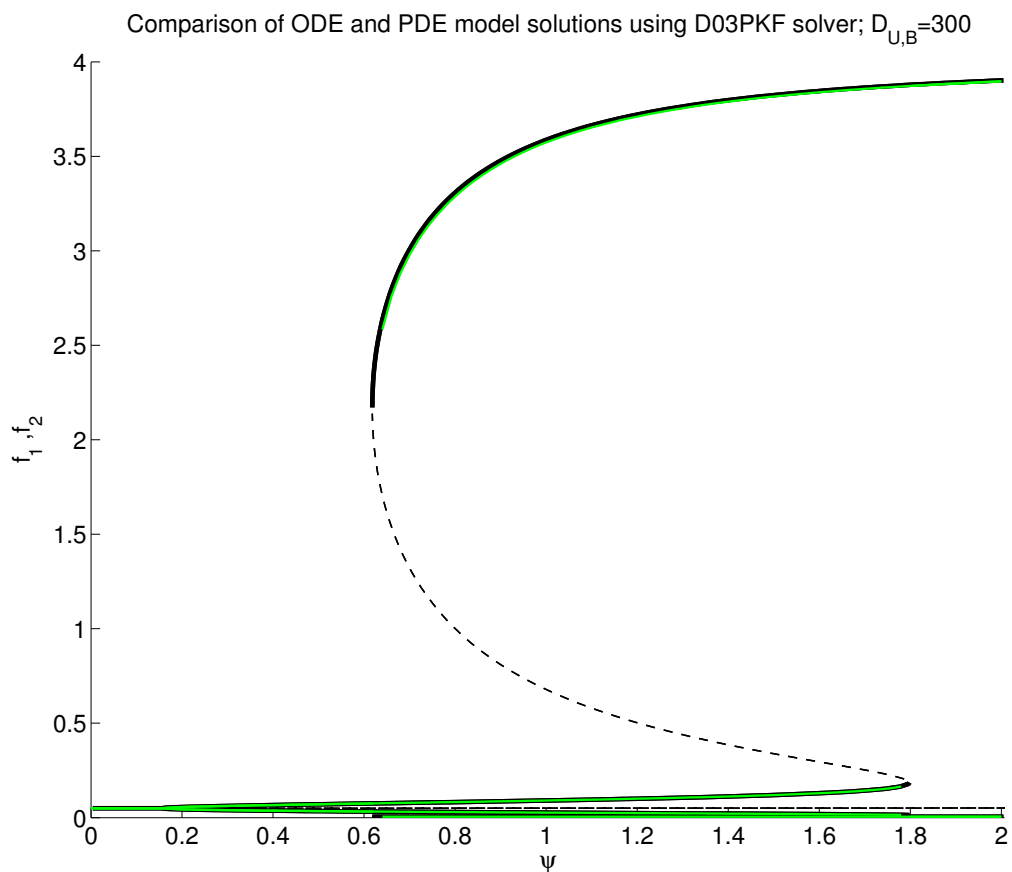


Figure 5.6: Bifurcation diagram showing steady state PDE model solutions for the filopodia lengths, F_1, F_2 (shown in green) as the VEGF gradient $\psi \in [0, 2]$ is varied. The equivalent bifurcation diagram from the ODE model is superimposed in black. This Figure was generated in the same way as Figure 5.5, but is used to demonstrate that the agreement between the ODE and PDE models for the filopodia length variables is also good.

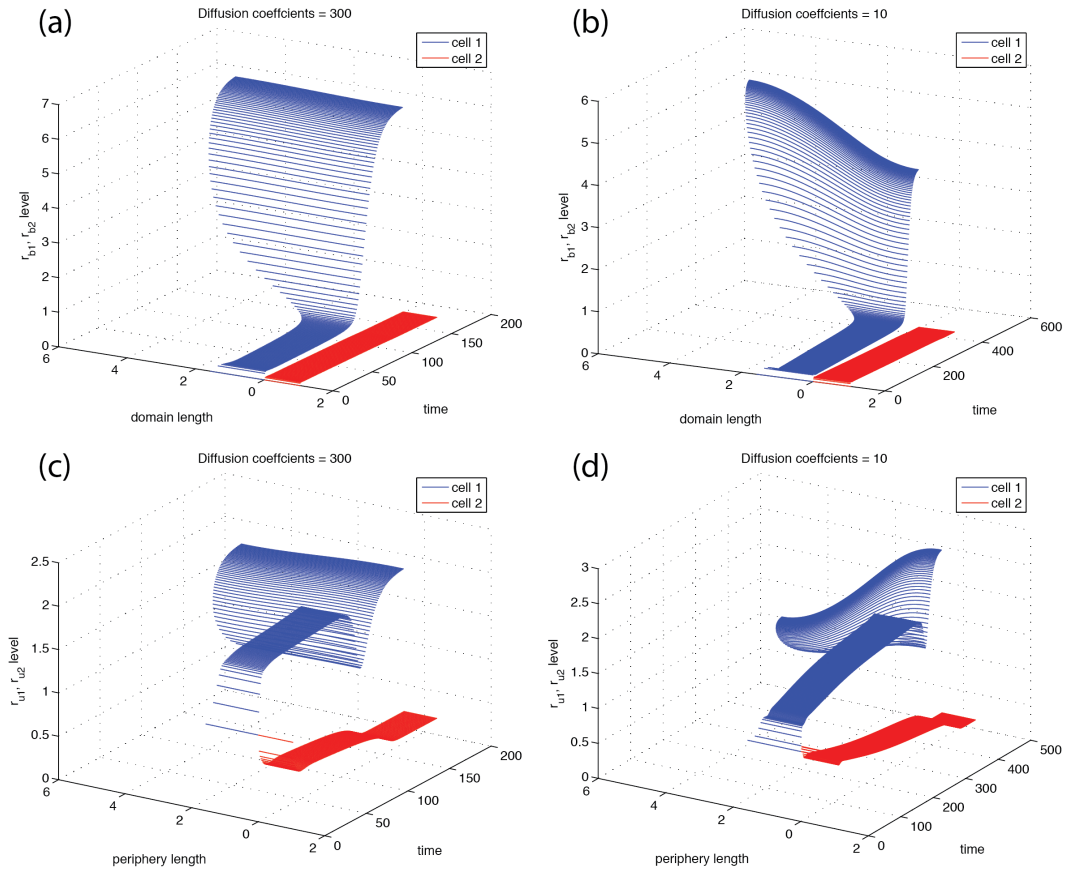


Figure 5.7: Spatial solution profiles of bound VEGFR-2, r_{Bj} in (a,b), and unbound VEGFR-2 in (c,d) for a two-cell system defined by equations (5.1.1)-(5.1.11) with VEGF slope parameter $\psi = 1.95$ and domain growth depending on the proximal VEGFR-2 concentration (see equation (5.4.1)). (a,c) When $D_U, D_B = 300$ so that receptor diffusivity is large, the steady state distribution of VEGFR-2 over the cell membrane and filopodium is almost homogeneous. However, in (b,d) $D_U, D_B = 10$ (and diffusivity is small), the steady state distribution of VEGFR-2 is spatially inhomogeneous. (b) shows that the highest concentration of bound VEGFR-2 is at the filopodia tip where the extracellular VEGF concentration is greatest. (c) shows the highest concentration of unbound VEGFR-2 is along the cell body ($x \in [0, L_0]$) where the VEGF concentration is lowest. Both cell 1 and 2 have proximal ends at $x = 0$. The co-ordinate systems for cells 1 and 2 increase to the left and right, respectively. Initial conditions are close to the homogeneous steady state and model parameters are as per Figure 4.7 unless otherwise stated.

5.5 Simulation with growth dependent on local bound VEGFR-2 concentration divided by the filopodia length

In this section, we assume domain growth based on $\rho_{Bj}(x, t)$, the local concentration of bound VEGFR-2. We use a local strain rate of the form

$$\frac{\partial v_j}{\partial x} = \begin{cases} 0, & 0 \leq x < L_0 \\ \frac{\phi w(\rho_{Bj}(x, t))}{F_j(t)} - \gamma, & L_0 \leq x \leq L_0 + F_j(t) \end{cases}. \quad (5.5.1)$$

Using the transformation in equation (5.3.3), equation (5.5.1) scales to

$$\frac{\partial v_j}{\partial \xi_j} = \begin{cases} 0, & 0 \leq \xi_j < \frac{L_0}{L_0 + F_j(t)} \\ \left(\frac{\phi w(\rho_{Bj}(\xi_j(x, t), t))}{F_j(t)} - \gamma \right) (L_0 + F_j(t)), & \frac{L_0}{L_0 + F_j(t)} \leq \xi_j \leq 1 \end{cases}. \quad (5.5.2)$$

Equation (5.5.1) rate cannot, in general, be integrated directly. Instead we couple the strain rate in (5.5.1) to equations (5.1.1)-(5.1.11) and integrate the system in this section in the same way as the model in §5.4.2.

To compare this growth law with the growth law in equation (5.4.1), we integrate equations (5.1.1)-(5.1.11) to steady state for $\psi \in [0, 2]$ using parameters identical to those used in Figure 4.7(a) and diffusion coefficients, $D_U, D_B = 300$. The resulting bifurcation diagram is presented in Figure 5.8 and is in excellent agreement with the diagram of the equivalent ODE model (see Figure 4.7).

At $\psi = 1.95$, we anticipate that one of the cells in a two-cell system will have a larger filopodium than the other cell. To confirm this, we ran a two-cell simulation using the growth law in equation (5.5.1). Figure 5.9 shows that this growth law produces solution profiles which are almost identical to those for the growth law which depends on bound VEGFR-2 at the proximal end of the cell (compare Figures 5.9 and 5.7).

5.5.1 Small diffusion

Both the proximal end and locally bound VEGFR-2 dependent filopodia growth laws exhibit spatially non-uniform steady states for receptor diffusivity values, $D_U = 10$ and $D_B = 10$ (see Figure 5.9). However, for the local growth law of this section, the bifurcation diagram obtained, by varying ψ while holding the other parameters fixed at the values used in Figure 5.9, looks identical to that obtained in the limit of large diffusion: $D_U, D_B = 300$, (see Figure 5.8). Therefore we omit the bifurcation diagram for $D = 10$ and seek to determine how small we have to make the diffusion coefficients in order to modulate the bifurcation structure seen in Figure 5.8.

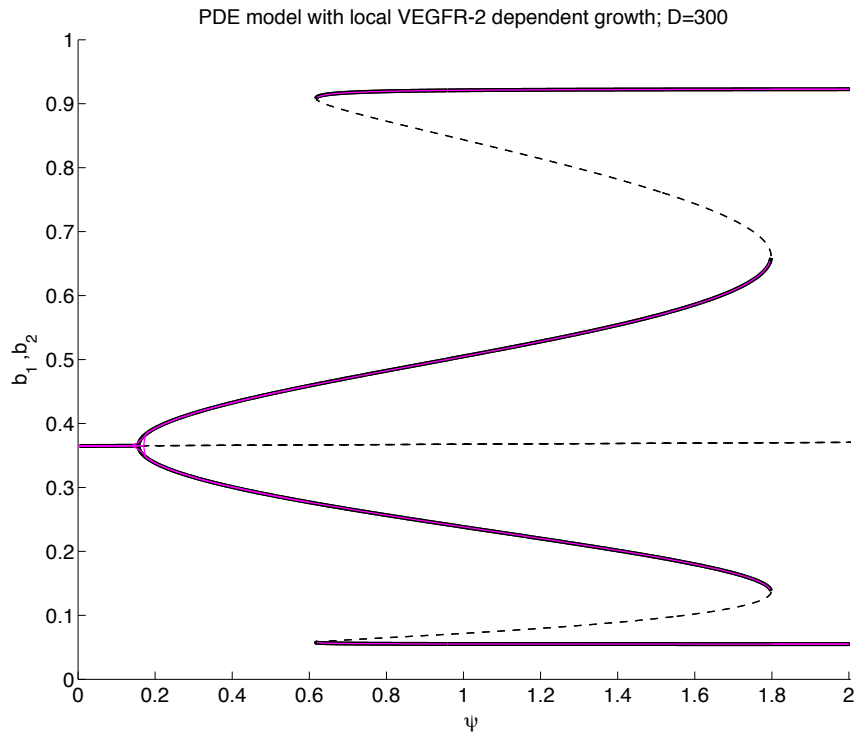


Figure 5.8: Bifurcation diagram showing steady state PDE model solutions for bound Notch, b_j (shown in magenta) as the VEGF gradient, ψ , is varied. Solutions were obtained by integrating equations (5.1.1)-(5.1.11) and the growth law considering the local bound VEGFR-2 concentration in equation (5.5.1) to steady state. Superimposed (in black) is the corresponding bifurcation diagram from the ODE model in (4.1.11)-(4.1.16) considering filopodia growth (see Figure 4.7). Parameter values used to integrate the PDEs are identical to those used to calculate the ODE model's steady states in Figure 4.7 with diffusion coefficients for unbound and bound VEGFR-2, $D_U, D_B = 300$. For large diffusivity the PDE model steady states and bifurcations agree well with the ODE model.

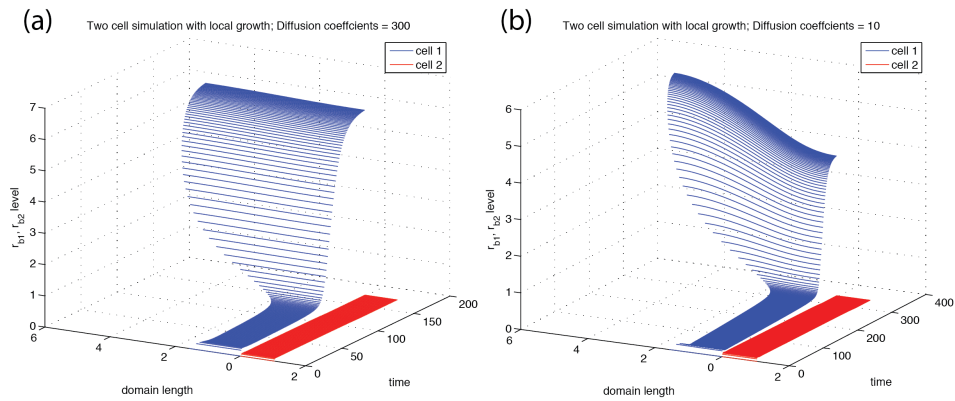


Figure 5.9: Spatial solution profile for bound VEGF receptors, r_{Bj} , in a two-cell system defined by equations (5.1.1)-(5.1.11) with VEGF slope parameter $\psi = 1.95$ and domain growth depending on the local VEGFR-2 concentration as defined in equation 5.5.1. (a) uses $D_U, D_B = 300$ and shows that when receptor diffusivity is large, the final steady state distribution of VEGFR-2 over the cell membrane and filopodium is almost homogeneous, whereas (b) uses $D_U, D_B = 10$ and shows that when diffusivity is small, the final steady state distribution of VEGFR-2 over the cell membrane and filopodium is spatially inhomogeneous. For $D_U, D_B = 300$ and $D_U, D_B = 10$ the spatiotemporal solution profiles for this growth law look identical to the solution profiles from the proximal end VEGFR-2 two-cell simulations (compare with Figure 5.7a,b).

Figure 5.10 shows the steady state level of bound Notch receptors after a perturbation of the unstable homogeneous steady state at $\psi = 0.4$ whilst varying $D_U, D_B \leq 10$. For $D_U, D_B \leq 0.1$, the system is no longer in the patterned state, suggesting that the pitchfork bifurcation has shifted to the right.

Hence we simulate equations (5.1.1)-(5.1.11) to steady state whilst varying ψ for different values of the diffusion coefficients, D_U, D_B . We superimpose the resulting bifurcation diagrams using $D_U, D_B = 0.5, 0.25, 0.1$ with the bifurcation diagram for the equivalent ODE model (see Figure 5.11). The agreement between the PDE and ODE models, breaks down when D_U, D_B are small. The pitchfork and fold bifurcations move towards each other and the outer patterning branches begin to move towards the underlying homogeneous steady state. Calculation of similar bifurcation diagrams, for smaller diffusion coefficients becomes computationally expensive but our analysis suggests that when diffusion is small, strings of cells are less likely to pattern (due to the steeper gradient required) and the resulting patterns have smaller amplitudes.

5.6 Simulation with growth dependent on the locally-bound VEGFR-2 concentration divided by the total domain size

In this section, we assume that domain growth depends on the local concentration of bound VEGFR-2, $\rho_{Bj}(x, t)$, scaled by the total domain size, $L_0 + F_j$, rather than the filopodia length alone, as was previously assumed. Growth is then governed by a local strain rate of the form

$$\frac{\partial v_j}{\partial x} = \begin{cases} 0, & 0 \leq x < L_0 \\ \frac{\phi w(\rho_{Bj}(x, t))}{L_0 + F_j(t)} - \gamma, & L_0 \leq x \leq L_0 + F_j(t) \end{cases}. \quad (5.6.1)$$

In this case the ODE for filopodia length becomes

$$\frac{dF_j}{dt} = \phi w(r_{Bj}) \frac{F_j}{1 + F_j} - \gamma F_j. \quad (5.6.2)$$

Dividing the growth by the entire domain length could be biologically justified if the material for growth was shared out over the whole cell membrane. When F_j is large, we expect this model to give similar results to the growth laws in which we divide by the filopodia length. To analyse the effect of this growth law, we integrate the system of equations (5.1.1)-(5.1.11) to steady state for $\psi \in [0, 2]$ for the model parameters in Table 4.1 and diffusion coefficients, $D_U, D_B = 300$. The resulting bifurcation diagrams for bound Notch receptors and filopodia lengths are shown in Figure 5.12. The diagrams show that although the homogeneous solutions for the two models coincide for $0 <$

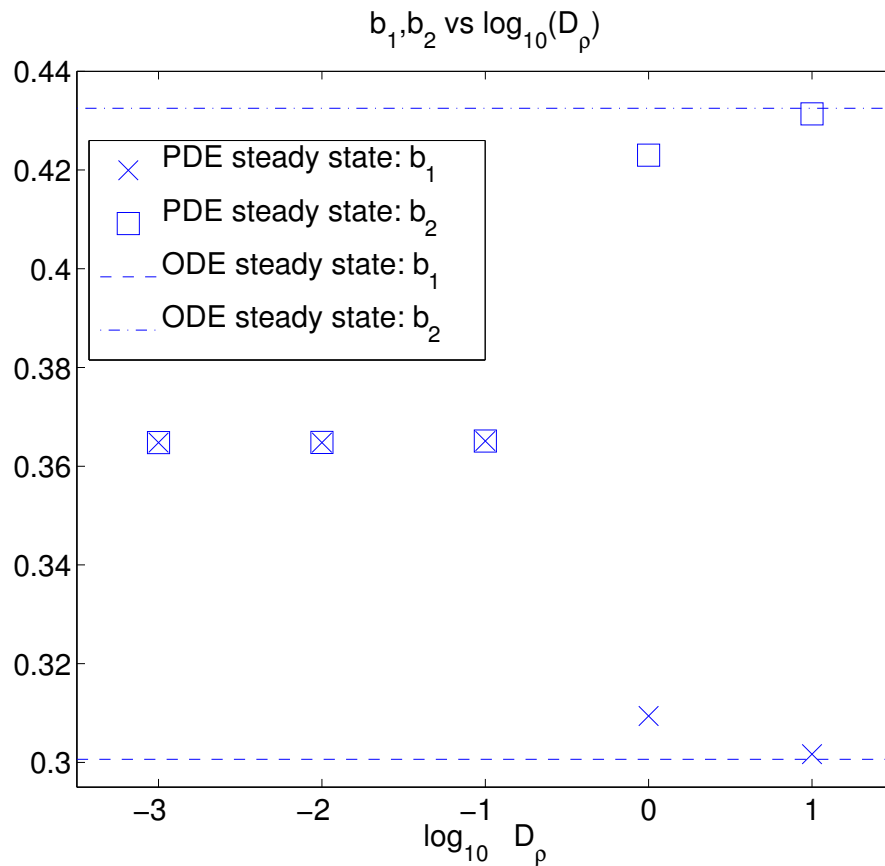


Figure 5.10: Comparison of steady state solutions of a two-cell system for bound Notch, b_1, b_2 , in the ODE model in equations (4.1.11)-(4.1.16) (dashed and dot-dashed line), and the PDE model (crosses and squares) for $D_U, D_B = 10^{-3}, 10^{-2}, 10^{-1}, 1, 10$ at $\psi = 0.4$ (a VEGF gradient for which the equivalent ODE model exhibits a period-2 pattern). Simulations were started close to the homogeneous steady state. For $D_U, D_B = 1, 10$, the PDE model exhibits a patterned state in which cells 1 and 2 have high and low levels of bound Notch respectively. For smaller diffusion coefficients, perturbations of the homogeneous steady state of the PDE model decay back to, $b_1, b_2 = 0.3648$. This implies that the pitchfork bifurcation, at which patterning first occurs, moves to the right when decreasing the diffusion coefficient. Model parameters are as Figure 4.7 unless otherwise stated.

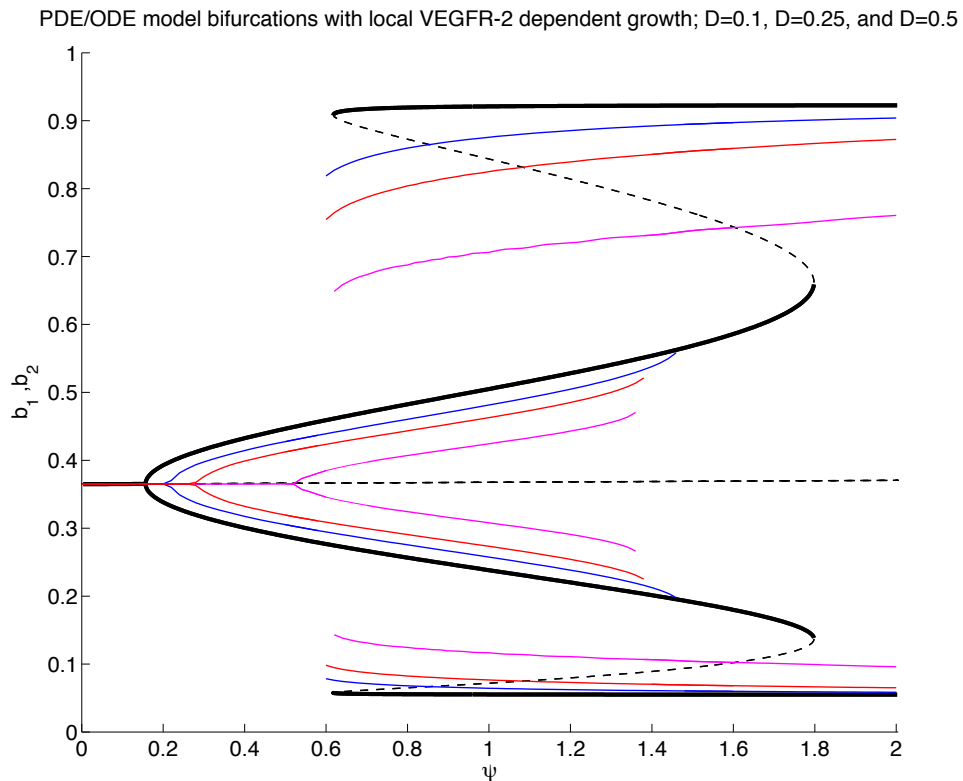


Figure 5.11: Bifurcation diagram showing how steady state solutions of bound Notch, b_1, b_2 , in a two cell system vary with the VEGF gradient, ψ . Coloured solution branches were calculated by integrating the PDE model in equations (5.1.1)-(5.1.11) and growth law depending on the local bound VEGFR-2 concentration in equation (5.5.1) (as described in §5.3.2) to steady state for $\psi \in [0, 2]$ and fixed values of the diffusion coefficients: blue ($D_U, D_B = 0.5$), red ($D_U, D_B = 0.25$) and magenta ($D_U, D_B = 0.1$). Superimposed in black is the bifurcation diagram for the corresponding ODE model in equations (4.1.11)-(4.1.16) from Figure 4.7a. The diagram suggests that as the diffusion coefficients are reduced, the outer branches move towards the homogeneous steady state, the pitchfork bifurcation moves to the right and the fold bifurcations at $\psi \approx 1.80$ move to the left. Hence, the agreement between the ODE and PDE models collapses as the diffusion coefficients are decreased. Model parameters are as in Figure 4.7 unless otherwise stated.

$\psi < 1.173$, there is no agreement for $\psi > 1.173$. For $\psi > 1.173$, the large-amplitude (outer) patterning branches of the two models coincide, but for $\psi < 1.173$ there are no such branches. There is no pitchfork bifurcation and thus no small amplitude (inner branch) pattern for this model.

5.7 Simulation for growth depending on the average bound VEGFR-2 concentration

In this section we simulate the PDE model with the domain growth dependent on the global average value of bound VEGFR-2:

$$\frac{\partial v_j}{\partial x} = \begin{cases} 0, & 0 \leq x < L_0 \\ \frac{\phi w(\bar{R}_{Bj})}{F_j(t)} - \gamma, & L_0 \leq x \leq L_0 + F_j(t) \end{cases}. \quad (5.7.1)$$

The global average is calculated, in our simulations, by introducing a variable representing the cumulative amount of bound VEGFR-2, $\hat{r}_B(x, t)$ which is defined by the following PDE:

$$\frac{\partial \hat{r}_B}{\partial x} = \rho_B(x). \quad (5.7.2)$$

Thus,

$$\hat{r}_B(x) = \int_0^x \rho_B(x) dx, \quad (5.7.3)$$

and the global average is given by

$$\bar{R}_{Bj} = \frac{\hat{r}_B|_{x=1+F_j}}{1+F_j}. \quad (5.7.4)$$

Since the domain length in the rescaled model is $\xi_j(L_0 + F_j, t) = 1$, the global average in the rescaled model is given by

$$\bar{R}_{Bj} = \hat{r}_B|_{\xi_j=1}, \quad (5.7.5)$$

and we track this variable at each timestep and couple it to the equation for domain growth (see equation 5.7.1).

We investigate the effect of domain growth that depends on the average receptor concentration by integrating equations (5.1.1)-(5.1.11) and equation 5.7.1 to steady state for $\psi \in [0, 2]$. The resulting bifurcation diagram is shown in Figure 5.13 and shows that there is excellent agreement with the ODE model when the diffusion coefficients are large. When diffusion is small ($D_U, D_B = 0.25$) the agreement with the equivalent ODE model is less good.

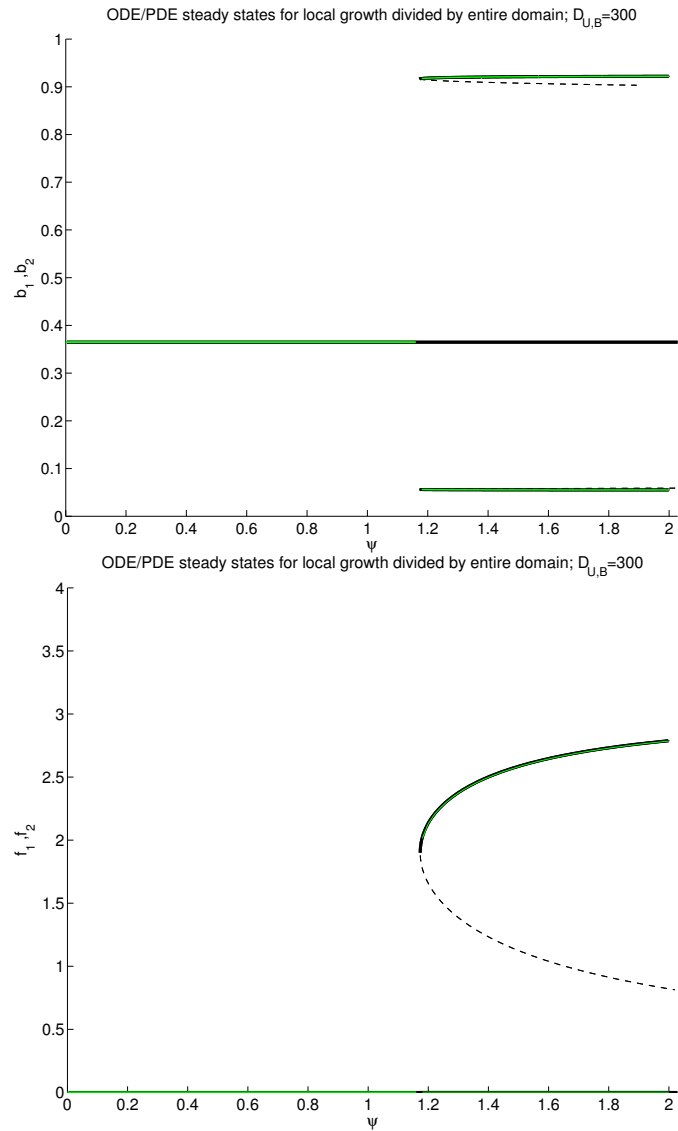


Figure 5.12: Bifurcation diagram showing the steady state solutions for bound Notch receptors, b_1, b_2 , of the PDE model (in green) as the VEGF gradient, ψ is varied. Solutions were obtained by integrating equations (5.1.1)-(5.1.11) and growth law depending on the local bound VEGFR-2 concentration divided by the entire domain length in 5.6.1 (as described in §5.3.2) for diffusion coefficients $D_U, D_B = 300$ and the parameters in Table 4.1. Superimposed is the bifurcation diagram for the corresponding ODE model defined by equations (5.6.2) and (4.1.12)-(4.1.16) (in black) calculated using XPPAUT. The two models have different bifurcations, for instance, the PDE model does not have a pitchfork bifurcation for the chosen parameters and the outer branches only coincide for certain values of $\psi > 1.173$ (a fold bifurcation). The lower diagram shows that the homogeneous steady state filopodia lengths are $F_j = 0$ for $\psi \in [0, 2]$ and for $\psi > 1.173$ one filopodium remains at zero while the other takes non-zero length, coinciding with the PDE steady state.

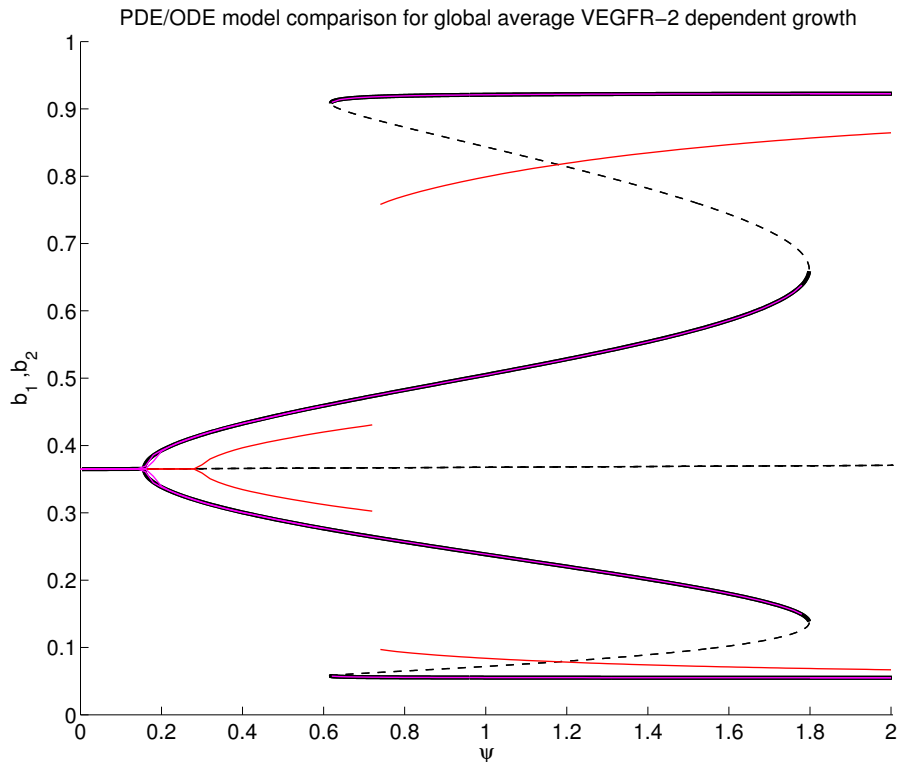


Figure 5.13: Bifurcation diagram for equations (5.1.1)-(5.1.11) using the growth law in equation (5.7.1) which assumes that domain growth depends on the global average of bound VEGFR-2, \bar{R}_{Bj} . The figure shows how the steady state concentration of bound Notch receptors, b_1, b_2 , varies with the VEGF slope parameter ψ for diffusion coefficients $D_U, D_B = 300$ (magenta curve). Superimposed is the corresponding bifurcation diagram from the ODE model in equations (4.1.11)-(4.1.16) (see Figure 4.7a). The figure shows that there is a very good agreement between this model and the equivalent ODE model when the diffusion coefficients are large. When receptor diffusivity is small ($D_U, D_B = 0.25$), the agreement between the ODE and PDE models is less good. Model parameters are as per Figure 4.7, unless otherwise stated.

5.8 Growth depends on local VEGFR-2 concentration without scaling

In this section, we again study domain growth which depends on the local bound VEGFR-2 concentration. Here however, the domain growth rate is not scaled by either the filopodia or total domain lengths, in contrast to §5.5 and §5.6 respectively. Thus, the growth is governed by

$$\frac{\partial v_j}{\partial x} = \begin{cases} 0, & 0 \leq x < L_0 \\ \phi w(\rho_{B_j}(x, t)) - \gamma, & L_0 \leq x \leq L_0 + F_j(t) \end{cases}. \quad (5.8.1)$$

Using the transformation in equation (5.3.3), equation (5.5.1) scales to

$$\frac{\partial v_j}{\partial \xi_j} = \begin{cases} 0, & 0 \leq \xi_j < \frac{L_0}{L_0 + F_j(t)} \\ (\phi w(\rho_{B_j}(\xi_j(x, t), t)) - \gamma) (L_0 + F_j(t)), & \frac{L_0}{L_0 + F_j(t)} \leq \xi_j \leq 1 \end{cases}. \quad (5.8.2)$$

The choice of parameter values in this model determines the steady state concentration distribution for $\rho_{B_j}(x, t)$. Thus for certain parameter values, we expect the filopodia to grow quickly since the $\phi w(\rho_{B_j}(x, t))$ term is multiplied by $F_j(t)$. Figure 5.14, which simulates equations (5.1.1)-(5.1.11) shows this to be the case for the parameter values in Table E.1.

We can also expect similar choices of parameter values, used with other growth laws (proximal and global average dependent growth) to give unbounded filopodia growth. We confirm that dividing the growth terms in the strain rate by the filopodia length, to give the same ODE for filopodia growth as the ODE model of equations (5.1.11) - (4.1.16), gives bounded solutions for the filopodia lengths.

5.9 Comparison of models with growth dependent on local, global average and proximal end VEGFR-2 concentrations

We have shown that the proximal, local and global average VEGFR-2 dependent growth laws give exactly the same bifurcation diagram when the receptor diffusivity is large, that is one that has an excellent agreement with the corresponding ODE bifurcation diagram from Figure 4.7. When the diffusivity is small, we expect the growth law depending on the proximal end bound VEGFR-2 concentration to deviate the most from the ODE model. This is because, for small receptor diffusivities, the bound VEGFR-2 steady state distribution is inhomogeneous (see Figures 5.7 and 5.9) and lowest at

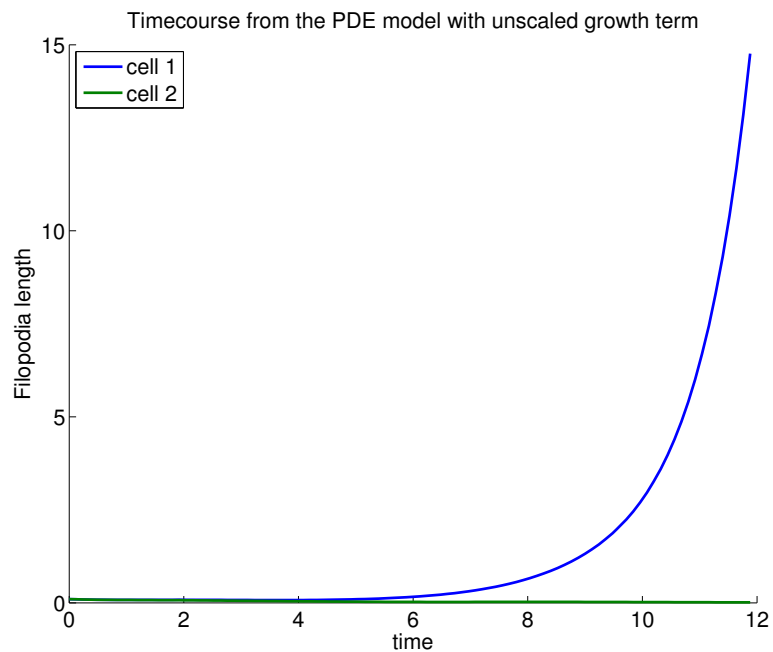


Figure 5.14: Two cell simulation of equations (5.1.1)-(5.1.11) using the growth law in equation (5.8.1) in which filopodia growth depends on the local concentration of bound VEGFR-2 without being divided by either the filopodia or entire domain lengths. Initial conditions used are close to the homogeneous steady state. Simulations show that, unlike the other model variables, for the parameter values in Table E.1 except for $\psi = 0.5$ and $m = n = 30$, the filopodia lengths do not settle to steady state but instead, filopodia grow without bound. The unbounded growth is dependent on the parameters. We found that for the parameter values as per Table 4.1 (which were also used in simulations of all the other growth laws), the filopodia do not grow without bound.

$x = 0$:

$$\rho_{Bj}(0, t) < \rho_{Bj}(x, t) \quad \forall x \in (0, L_0 + F_j]. \quad (5.9.1)$$

Figure 5.15 confirms that the proximal end VEGFR-2 dependent model deviates the most from the ODE model and the local growth model deviates the least. The differences between the three models are most apparent near $\psi \approx 2$ where the filopodia lengths are the longest. Where the filopodia are short, for example, on the inner branch solution near the pitchfork bifurcation, the three models show almost identical behaviour with overlapping steady states.

Figure 5.16 shows that if we make the diffusion coefficients smaller, there are much bigger differences between all 3 types of model (compare Figures 5.15 and 5.16). These are, again, most apparent when the filopodia lengths are large, i.e. in the vicinity of the (outer branch) large amplitude pattern. Since diffusion is even smaller in this Figure, differences can be distinguished even where the filopodia lengths are small (see inset zoom of Figure 5.16). As the diffusion coefficients are decreased beyond $D_U, D_B = 0.25$, we expect the differences between the local and global average dependent growth models to also increase.

5.10 Conclusions and further work

In this chapter we have developed a PDE model to investigate the role of VEGF-modulated Delta-Notch signalling in angiogenic tip cell selection in order to properly take account of the spatial distributions of VEGFR-2 that spatially-averaged ODE models cannot address. This is done by separately developing PDEs for unbound and bound VEGF receptors which allow both diffusive and advective transport of VEGF receptors along the cell membrane and filopodia. Our motivation for studying this came from the fact that inhomogeneous distributions of proteins and receptors commonly occur and epithelial structures are often oriented with polarity. We have shown that, for sensible choices of growth laws governing filopodia extension, and receptor diffusivity spanning many orders of magnitude, the ODE model of Chapter 4 gives an excellent approximation to a problem with a significant spatial aspect. We also demonstrate the extent to which our ODE model gives good approximations. We show that paying explicit attention to the spatial details can be crucial as, in the limit of small diffusion, our PDE model can produce dynamics which differ from those of the equivalent ODE models which ignore such details.

To begin, we outlined the model equations and considered three types of constitutive

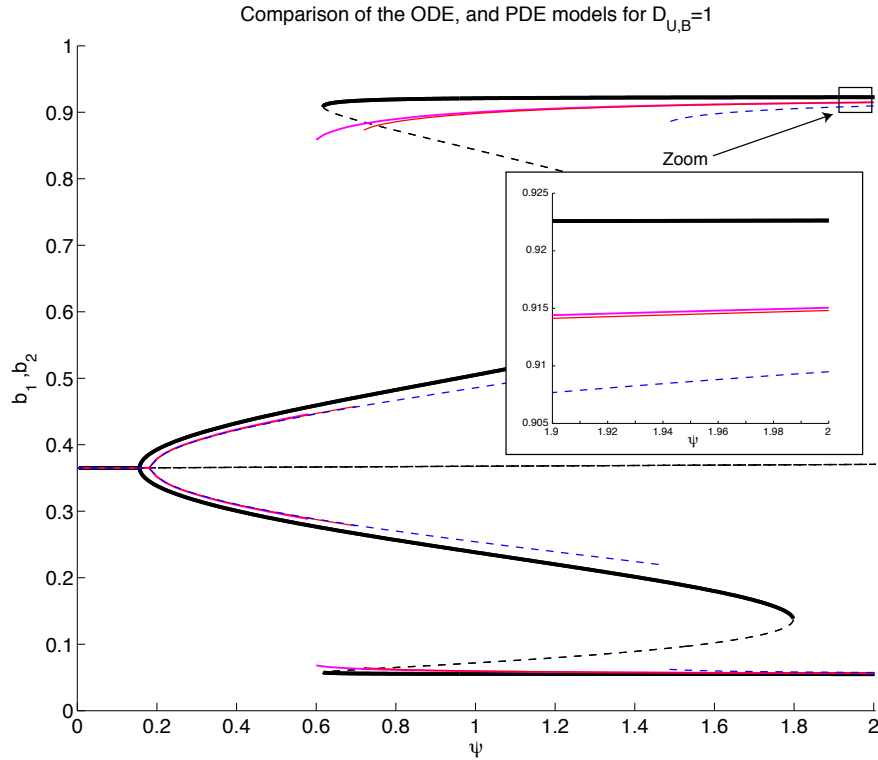


Figure 5.15: Bifurcation diagrams for the PDE model with receptor diffusivity $D_U, D_B = 1$ using the local (magenta) and global average (red) and proximal (blue dashed) growth laws in equations (5.4.1), (5.5.1) and (5.7.1) respectively and parameter values as in Figure 4.7. The location of the curves was calculated by integrating the system to steady state for $\psi \in [0, 2]$ using reverse runs as described in §5.3.2. The curves show the local VEGFR-2 dependent model has the closest match with the ODE model (superimposed in black) followed by the global average VEGFR-2 dependent model, followed by the proximal end bound VEGFR-2 dependent growth model (see the ‘zoom’ inset). For the receptor diffusivity used in this Figure, the pitchfork bifurcations approximately coincide at $\psi \approx 0.18$ for all three models as the filopodia lengths are small here.

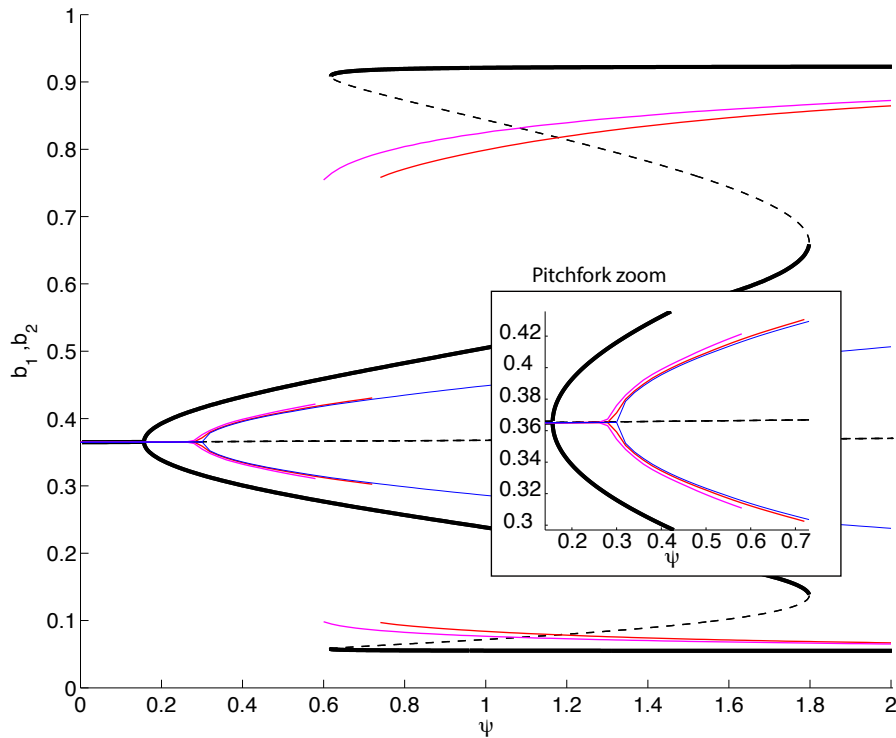


Figure 5.16: Bifurcation diagrams for the PDE model with receptor diffusivity $D_U, D_B = 0.25$ using the local (magenta) and global average (red) and proximal (blue) growth laws in equations (5.4.1), (5.5.1) and (5.7.1) respectively and parameter values as per Figure 4.7. The location of the curves was calculated by integrating the system to steady state for $\psi \in [0, 2]$ using reverse runs as described in §5.3.2. The curves show that the local VEGFR-2 dependent model has the closest match with the ODE model followed by the global average VEGFR-2 dependent model. For the diffusivity used, we could not find large amplitude (outer branch) solutions for $\psi \leq 2$ in the proximal end VEGFR-2 dependent model (blue). However, this model's pitchfork bifurcation shifts furthest from the ODE model's pitchfork bifurcation (see 'Pitchfork zoom' inset), suggesting this model agrees least well with the ODE model.

growth laws formulated in terms of the local strain rate, $\frac{\partial v_j}{\partial x}$. Filopodia growth laws which depend on local, global average and proximal end VEGFR-2 concentrations were considered. In each case, we compared the form of the filopodia extension rate derived from the advection velocity (see equation (5.1.11)) with the equivalent rate from the ODE model in equation (4.1.3).

Our analysis showed that filopodia length-independent growth laws, for the three cases of growth depending on the proximal, local and global average concentrations of VEGFR-2, produced ODEs for filopodia growth which were different to the corresponding ODE for the filopodia extension rate in Chapter 4. Our numerical simulations showed that filopodia could grow without bound in such cases and the unbounded growth was dependent on the parameter values used. When the growth terms were inversely proportional to filopodia length, the models with growth laws considering the global average concentration gave rise to an ODE of the same form as equation (4.1.3). In contrast, although the model considering local bound VEGFR-2 levels also gave an equivalent ODE to equation (4.1.3) for the filopodia extension rate, the whole PDE model only had solutions equivalent to the ODE model when the additional assumption of large receptor diffusivity was made. In this case, receptor concentrations equilibrated rapidly, became spatially uniform and were almost equivalent to the global average concentration.

Our numerical analysis began by exploring the model using proximal-end bound VEGFR-2 dependent growth. We were able to find an analytical expression for the velocity, $v_j(x, t)$, and verify that the numerical integrator correctly integrated the strain rate. This then gave credence to the upcoming numerical simulations of models with spatially dependent strain rates in §5.5,5.6,5.7,5.8. For large receptor diffusivity, we expected this model to coincide with the ODE model as homogeneity implied $\rho_{Bj}(0, t) = \bar{R}_{Bj}(t)$ and numerical simulations confirmed this (see Figure 5.2).

Using numerical simulations of a two-cell system we were able to verify the consistency of the local and global average VEGFR-2 dependent models with the ODE model, for large receptor diffusivity, by comparing the bifurcation structure of each model (see Figures 5.8 and 5.13). When the receptor diffusivity became small enough, the numerical results in Figure 5.11 predicted that the pitchfork bifurcation would occur for larger values of the VEGF gradient and that the patterning branches would move towards the homogeneous steady state. This suggested that it becomes more difficult for cells to pattern when receptor diffusivity is small enough, because a larger VEGF gradient is needed to shift the system past the pitchfork and into the low amplitude patterning window (inner branches). The compression of these branches also suggested that the

patterns generated for small receptor diffusivity would be smaller in amplitude.

The inner and outer pairs of stable patterning branches on the bifurcation diagrams in Figures 5.5, 5.8 and 5.13 corresponded to small and large amplitude patterns respectively. The small amplitude pattern had alternating cells with longer and shorter filopodia, albeit of comparable length. This contrasted to the large amplitude pattern, in which alternating cells had one very long and one very short filopodium. In this case the long filopodium reached further into the field of extracellular VEGF and numerical simulations suggested that the distribution of receptors would be homogeneous (inhomogeneous) for large (small) diffusion coefficients. Our models showed that, for some cases, where diffusion is small enough to give inhomogeneous distributions of VEGFR-2 the agreement between the ODE and PDE models is still good.

Gerhardt and co-workers have shown that VEGF–VEGFR-2 signalling is necessary for filopodia extension. Thus it is likely that the local growth rate may depend on the local concentration of bound VEGFR-2. We, however, have scaled the growth by the filopodium length whilst it remains unclear as to how or why the local growth rate should have information about this global property.

In §5.6, we scaled the growth by the total domain length, $L_0 + F_j$ and confirmed that although the steady state solutions for bound Notch receptors in the ODE and PDE models match in certain places, their bifurcation structures varies remarkably. In particular, for the parameter values used, we found no pitchfork bifurcation or low amplitude (inner branch) pattern. These differences can be attributed to the fact that this growth law corresponds to an ODE for filopodia extension which is different to the ODE in (4.1.3). By generating the bifurcation diagram for the ODE model in XPPAUT, we have shown that the PDE model agrees with the equivalent ODE model but the behaviour of this model for smaller receptor diffusivity remains to be tested.

In summary, our numerical analysis suggested that for the three models in §5.4, 5.5 and 5.7, which use sensible filopodia growth laws, the ODE model of §4 provides an excellent approximation, when the receptor diffusivity is large, for predicting the onset of patterning and the corresponding steady state solutions, including the new large amplitude patterns that arise due to the inclusion of filopodia growth. It is only when the VEGFR-2 diffusivity is sufficiently small, does the PDE model offer fresh insight into the behaviour of the system and its bifurcation structure. However, since it is currently unclear whether biologically realistic VEGFR-2 diffusivity is small enough to warrant using the PDE models of this section, we conclude that the simpler ODE model is sufficient for studying pattern formation in cells extending filopodia without the extra complexity of the PDE models.

Our numerical bifurcation analysis also predicted that for sufficiently small receptor diffusivity, where there is a discrepancy between the ODE and corresponding PDE models, the proximal end bound VEGFR-2 model least agreed with the ODE model of Chapter 4. The local bound VEGFR-2 dependent growth model had the best agreement followed by the global average bound VEGFR-2 dependent model (see Figure 5.15).

In order to generate bifurcation diagrams for our PDE model, we performed semi-automated numerical continuation as described in §5.3.2. Using this method we saw that for small receptor diffusivity there is some discrepancy between the ODE and PDE model bifurcations. It would be interesting to locate the unstable branches of the system and conduct two-parameter continuation, for instance, and follow the fold bifurcations in $\psi - D_U, D_B$ space. However, this would be a big challenge as we would need to formulate our PDEs into a numerical continuation routine that calculates the Jacobian of the system at each step and makes use of techniques such as pseudo arc-length continuation to locate unstable branches.

We conclude this chapter by stating that the PDE and ODE models of this chapter and Chapter 4, respectively, give qualitatively similar results. Thus, our PDE model justifies using the ODE model in reasonable cases regarding filopodia growth and receptor diffusivity.

5.10.1 Further work

One way in which we could further extend the work from this chapter, would be to consider the effect of other relevant growth laws such as apical growth. For this law, the growth would be zero everywhere except in a small layer of length l from the tip of the filopodium.

Other important analysis that remains to be done is applying linear stability analysis to this system, although it is unclear under which circumstances an underlying homogeneous steady state would exist from which the system could diverge from, given that it initiated from the stable manifold. Should such a steady state exist, an appropriate coordinate system to use would be (x, j) , i.e. (position along the cell membrane, position along the string) and perturbations could be written in the form

$$\tilde{u}(x, t) = \exp(ikx + i\kappa j + \sigma t), \quad (5.10.1)$$

which implies a dispersion relation for σ in terms of the wavenumbers k and κ in the filopodia (x) and string (j) directions respectively.

Thus far, the ECs in our models have remained stationary. A natural way to proceed further with this work would be to include the effects of cell growth, proliferation and

migration up the spatial gradient of VEGF. Allowing cells to extend multiple filopodia is also another possibility. The model could also be used to test the effect of VEGF or VEGF receptor inhibitors on the ability of ECs to sprout tip cells. Lastly allowing the VEGF gradient to vary in the j direction would also be an interesting way to extend this work.

Conclusions

The establishment of a functional and perfused network of blood vessels is essential for the transport of oxygen, nutrients, immune system cells and the removal of waste products from tissues in, both, the growing embryo and the adult organism. Initially, blood vessels are formed in a process called vasculogenesis in which endothelial precursor cells coalesce together and undergo arteriovenous specification so that blood circulation may ensue in an organised fashion. Subsequently, tube formation hollows these primitive vessels before the onset of blood circulation.

In order to meet the metabolic demands of growing tissues, or to alleviate stresses caused by wound healing, for example, the primary vasculature remodels itself by angiogenesis: the formation of new blood vessels from pre-existing ones. Angiogenesis begins with the selection of particular endothelial cells to become tip cells which respond to extracellular cues, such as growth factors, by sprouting from the primary blood vessel and migrating towards the source of growth factor.

Haematopoietic stem cells (HSCs), which are derived from the same blood vessels that undergo sprouting hours earlier in the zebrafish embryo, are responsible for the replenishment of the components of the blood system, such as, red blood cells, myeloid and lymphoid cells. HSCs play this role in both the developing embryo and in the adult where they are necessary for homeostasis and the ability to invoke an immune response.

The aim of this thesis was to develop our understanding of how Notch signalling controls each of the following processes in the dorsal aorta of zebrafish embryos:

- Arterial specification at 18hpf ,
- Tip cell selection at 21hpf ,
- HSC specification at 24hpf .

We began in Chapter 1, by providing an overview of these processes, and reviewed key published works which have provided us with an insight into the biological mechanisms underpinning them. Key biological observations from the literature included a Hedgehog–VEGF–Notch signalling cascade which has shown to be necessary for both arterial and HSC specification in cells of the DA [22, 25]; and an intimate connection between the VEGF and Notch signalling pathways influencing the response of ECs to VEGF and thereby allowing the selection of tip cells for angiogenic sprouting from an initially equivalent population of cells [9, 13, 23, 50, 56, 110]. This was followed by a review of existing mathematical models used to study juxtacrine cell signalling, angiogenic sprouting and tip cell selection and models of Notch signalling in other contexts. Chapter 2, uses a combination of mathematical modelling and experimental data to investigate arterial and HSC specification in ECs. Experimental data implicate *efnb2a* and *runx1* as markers of arterial and HSC identity, respectively, during development [21, 25, 30, 33]. *In-situ* hybridisation results from the Gering lab show that knockdown of Notch signalling in the *mindbomb* mutant results in a loss of *efnb2a* and *runx1* whereas knockdown with the γ -secretase inhibitor, DAPT, results in a loss of *runx1* only (see Figure 2.4). In addition, the transgenic zebrafish Notch reporter line, $12\times\text{CSL}:\text{Venus}$ has low expression of the fluorescent protein, Venus, in the DA at 18hpf, when *efnb2a* is first detected and higher expression at 24hpf, when *runx1* expression is first detected and when *flt4* expression is downregulated (see Figure 2.5). This led to the hypothesis that Notch signalling was needed at two distinct time points: at 18hpf at a low level which is capable of inducing *efnb2a* expression and at 24 hpf at a higher level which is sufficient to drive *runx1* expression.

To test this hypothesis we used three ODE models to simulate the responses of *gata2*, *efnb2a* and *runx1* to a prescribed, increasing input signal of NICD. The first model used Michaelis-Menten kinetics to model their responses, and provided that conditions on parameter values associated with promoter sensitivity were met, was capable of delaying the *runx1* mRNA expression level, relative to *efnb2a* (see Figure 2.11). The last two models introduced a sigmoidal response in the pathway activating *runx1* and demonstrated that it could increase the delay time in the induction of *runx1* by effectively making it less sensitive to NICD. We sought to determine whether incorporating Delta-Notch coupling upstream of NICD and allowing a prescribed VEGF input to drive the system could amplify the average level of *runx1* in cells after the induction of *efnb2a*. Delta-Notch signalling invokes the lateral inhibition mechanism which characteristically generates salt-and-pepper patterns with a wavelength of two cells. We showed that our model can exhibit this behaviour but is dependent on the parameter values

used (see Figures 2.16 and 2.19).

We also outlined the experimental procedures that I carried out in the Gering laboratory in order to obtain gene expression data for *efnb2a*, *runx1*, and *flt4*. The experiments were much more challenging than expected. Our data showed that *flt4* was not downregulated in *gfp^{high}* cells (assumed arterial) (see Table 2.6). Hence, we concluded that using the *flk1:gfp* transgenic line was not sufficient to reliably isolate arterial cells. Further work would need to use a different combination of transgenic lines to successfully isolate the appropriate ECs. The shortcomings of our current methodology could also be remedied by performing qPCR on RNA isolated from individually FAC sorted cells. This would prevent the effects of analysing RNA from a mixed population of arterial and venous ECs. The *runx1* and *efnb2a* qPCR data showed the appropriate trend and increased from 20-27hpf. For proof of concept, we fitted the parameters of our simple feed-forward model of §2.2.3 with sigmoidal *runx1* response to *gata2*, to this experimental data. The parameter fitting highlighted the possible need for including basal transcription into the model and the use of statistical methods for model selection. In conclusion more reliable data, a greater number of replicates at each time point, fine-tuned models, and further knowledge of the genetic interactions are required to make further progress in determining the role of Notch in arterial and HSC specification.

The following three chapters focused on modelling the process of tip cell selection in strings of ECs. In Chapter 3, we analysed the VEGF–Delta–Notch signalling processes in the absence of filopodia growth, VEGF gradients or transport of receptors. In this model extracellular binding of VEGF to its receptor VEGFR-2 upregulated the production of the ligand Dll4 which subsequently bound Notch receptors on adjacent cells (see Figure 3.1). The bound Notch receptors, in adjacent cells, caused downregulation of VEGFR-2 in those cells. Consequently, these cells had a reduced response to VEGF and were specified as stalk cells, whereas cells with high levels of VEGFR-2 were fated as tip cells. We implemented this feedback into an ODE modelling framework and subsequently studied it using analytical and numerical approaches. Numerical simulations, in a system of two coupled cells, initially close to the homogeneous steady state, showed that the model was, by itself, capable of generating patterns for particular parameter values. Manipulating the Hill coefficients in the production functions for Dll4 ligand and VEGFR-2 allowed the formation of period-2 spatial patterns by increasing the non-linearity of the production responses. Using steady state analysis, we implicated parameters corresponding to the extracellular level of VEGF, V^* , and the maximal production rate of Dll4 ligand, g_{max} , to allow patterning. Analysis using the bifurcation package, XPPAUT, confirmed that the model could indeed exhibit patterns

for a range of V^* and g_{max} (see Figure 3.4).

We investigated the onset of patterning by analysing the linear stability of the homogeneous steady state. The patterning instability was of Turing type such that the homogeneous steady state was stable to homogeneous perturbations and unstable to spatially varying perturbations. Our analysis suggested that patterning occurred when a real eigenvalue of the linearised system changed sign. Furthermore, we used the Routh-Hurwitz conditions formulated for a reduced system of equations in which we assumed a quasi-steady state for bound VEGFR-2 and conservation of Notch receptors. We found that the Routh-Hurwitz conditions were always quadratic (as a function of the cosine of the wavenumber) with negative leading coefficient. Violation of these conditions, corresponding to a patterning instability, indicated that the first mode to become unstable was the period-2 patterning mode (see Figures 3.7 and 3.8). By formulating the Routh-Hurwitz conditions in terms of the feedback strengths of Dll4 ligand, A , and VEGFR-2, B , we identified regions of parameter space which admitted the period-2 spatial pattern (see Figure 3.9). The Routh-Hurwitz conditions, delimiting these regions, retain their positions relative to each other in response to changes in the model parameters. Furthermore, this meant that the homogeneous steady state always became unstable to admit patterning when a real eigenvalue changed sign and never due to a pair of complex conjugates crossing the imaginary axis. Numerical integration and continuation of steady state solutions validated the predictions of our linear analysis (see Figures 3.15 and 3.17). We also explored the effects of different boundary conditions and found that if cells at the boundary did not receive the correct amount of inhibition, the instability spreads into the domain, causing the system to pattern. We also observed travelling waves for $A, B < 0$ and $A, B > 0$ where our system admits multiple homogeneous steady states (see Figure 3.20).

Chapter 4 extended the ODE model of chapter 3 by incorporating filopodia growth using a variable representing the length of the filopodium on cell j . The ODE for filopodia growth was coupled to ODEs for the spatially averaged concentrations of unbound and bound VEGF receptors, Delta ligand (Dll4) and a conserved concentration of Notch receptors per cell. The cells were exposed to a gradient of VEGF which the filopodia grew into. The growth of filopodia was induced by the number of VEGF receptors which were assumed to be located both in the cell membrane and the filopodium and in turn, VEGF receptor production was enhanced by the filopodia length in that cell. The effects of receptor feedback, θ , and the linear gradient of VEGF, ψ , were investigated using numerical simulations and bifurcation analysis. The analysis suggested that the feedbacks introduced by filopodia growth facilitated pattern formation

in strings of cells. They did this by increasing the range of values in parameter space for which the system could admit patterning, thus creating regions of parameter space in which systems of cells with filopodia could pattern, unlike equivalent systems of cells without filopodia growth. This was confirmed using numerical simulations. Steady state analysis also suggested that the model would be able to exhibit multiple homogeneous and period-2 patterning solutions which could coexist in particular regions of parameter space. This was confirmed using numerical continuation, as θ or ψ were varied (see Figures 4.6 and 4.7). Notably, filopodia growth allowed the existence of a large amplitude pattern in which one cell had an extremely long filopodium and the other cell a very short filopodium. This differed from the small amplitude pattern for which the filopodia were of a relatively similar size. Further feedback via the growth terms could also destroy the small amplitude pattern. The system also exhibited hysteresis effects due to the coexistence of the two patterns. Lastly we used linear stability analysis to determine how filopodia feedback modulates the growth rate of perturbations of the homogeneous steady state. For a fixed point in the A - B plane, our linear analysis showed that increasing the feedback strength, U , which corresponded to the slope of the production function for filopodia growth, shrinks the stable region and the unstable patterning region of parameter space, until the homogeneous steady state is unstable to perturbations of all wavelengths (see Figure 4.13). Thus filopodia growth acts to facilitate patterning by destabilising the homogeneous steady state. These predictions were also confirmed using numerical analysis (see Figure 4.14).

Chapter 5 aimed to understand the conditions under which the spatially averaged model in Chapter 4 could be used to study the effects of filopodia growth on tip cell selection. The model is discrete in the string (j) direction, consisting of whole cell variables for the concentrations of Delta ligand and Notch receptors, and is spatially resolved in the direction of filopodia growth (x). We used PDEs to describe the spatiotemporal evolution of unbound and bound VEGFR-2 in the cell membrane and filopodia. VEGF receptors were allowed to diffuse in the cell membrane and filopodia, and advection of receptors was determined by three types of constitutive law defining domain growth: growth depending on the local bound VEGFR-2 concentration, the global average VEGFR-2 concentration, and the concentration of VEGFR-2 at the proximal end of the cell. The growth laws defined a local strain rate: $\frac{dv_j}{dx}$ which was integrated analytically to obtain an expression for the advection velocity. The filopodia growth rate, $\frac{dF_j}{dt}$, was defined as the velocity at the end of the domain: $v(x, t)|_{x=L_0+F_j}$. We found that all three growth laws gave expressions for the filopodia growth rate which could potentially exhibit exponential growth, which we later confirmed for the local VEGFR-2 dependent growth law using a numerical simulation (see Figure 5.14). To avoid expo-

nentially growing filopodia lengths in our PDE model, we divided the growth terms by the filopodia length. This was justified by assuming that the local growth rate would be smaller for a larger filopodium due to distribution of material for growth throughout the filopodium. This led to ODEs for the filopodia growth rate which were equivalent to the corresponding ODE from Chapter 4.

Using numerical continuation (described in §5.3.2) we showed that the steady states and bifurcation structure of the PDE model, for each of the growth laws, coincided with the bifurcation structure of the ODE model from Chapter 4 when the receptor diffusivity was large. Numerical simulation of cells exhibiting the large amplitude pattern, with a long filopodium extending far into the gradient of VEGF, showed that rapid equilibration of receptors lead to an almost spatially homogeneous distribution of VEGF receptors in the membrane. In contrast, when the receptor diffusivity was small, the steady state distribution of VEGFR-2 was inhomogeneous, with a higher concentration of bound receptors at the filopodium tip than at the cell body (see Figure 5.7). In addition, for small VEGFR-2 diffusivity, the steady states and bifurcations of the PDE models were different to the those of the equivalent ODE model from Chapter 4. We found that the model using proximal end VEGFR-2 dependent growth agreed least of all three growth laws, whereas the local bound VEGFR-2 dependent growth law gave the best agreement (see Figures 5.15 and 5.16). In conclusion, we found that different growth laws were capable of exhibiting almost identical solutions to the ODE model of Chapter 4 when the receptor diffusivity was large. It remains to be determined whether physically realistic values for the diffusion coefficients would necessitate the use of PDE model of this chapter over the ODE model of Chapter 4.

In this thesis we have developed both ODE and PDE models to investigate the role of Notch signalling in the processes of arterial specification, tip cell selection during angiogenic sprouting, and HSC specification. We began by using experimental results and observations to guide mathematical models to better understand how Notch signalling can induce arterial and HSC gene induction in the developing zebrafish embryo. We then developed three models to study tip cell selection in angiogenic sprouting and found that filopodia growth and the spatial distribution of VEGF receptors are important factors in tip cell selection. We have also highlighted several prospects for future work which may shed further light on the role of Notch signalling in the developmental processes studied herein.

Non-dimensionalisation and scalings for the model without filopodia growth: (3.2.10)-(3.2.14)

We non-dimensionalise the model in (3.2.10)-(3.2.14) by scaling the variables with typical time and concentration scales of the model as follows,

$$t = \frac{1}{k_{-VR}} \tau, \quad (\text{A.0.1})$$

$$N_j = N_{tot} n_j \quad (\text{A.0.2})$$

$$B_j = N_{tot} b_j, \quad (\text{A.0.3})$$

$$\Delta_j = N_{tot} \delta_j, \quad (\text{A.0.4})$$

$$R_{Uj} = \frac{R_{U0}}{k_{-VR}} r_{Uj}, \quad (\text{A.0.5})$$

$$R_{Bj} = \frac{R_{U0}}{k_{-VR}} r_{Bj}. \quad (\text{A.0.6})$$

The two functions f and g are scaled in the following way,

$$f(x) = \frac{R_{U0}}{1 + (bx)^m},$$

$$g(x) = \frac{g_{max} x^n}{x^n + a^n}.$$

Hence

$$f(B_j) = f(b_j N_{tot}) = R_{U0} \frac{1}{1 + (b N_{tot} b_j)^m}, \quad (\text{A.0.7})$$

$$g(R_{Bj}) = g\left(\frac{R_{U0}}{k_{-VR}} r_{Bj}\right) = g_{max} \frac{\left(\frac{R_{U0}}{k_{-VR}} r_{Bj}\right)^n}{\left(\frac{R_{U0}}{k_{-VR}} r_{Bj}\right)^n + a^n}. \quad (\text{A.0.8})$$

We define

$$\beta = \frac{1}{bN_{tot}} \quad \text{and} \quad \alpha = \frac{ak_{-VR}}{R_{U0}}, \quad (\text{A.0.9})$$

and rewrite (A.0.7) and (A.0.8) as:

$$f(B_j) = R_{U0}\tilde{f}(b_j) \quad \text{and} \quad g(R_{Bj}) = g_{max}\tilde{g}(r_{Bj}), \quad (\text{A.0.10})$$

where \tilde{f} and \tilde{g} are normalised to have maximum value equal to 1 and are given, in terms of the dimensionless parameters, β and α , as

$$\tilde{f}(b_j) = \frac{1}{1 + \left(\frac{b_j}{\beta}\right)^m} \quad \text{and} \quad \tilde{g}(r_{Bj}) = \frac{r_{Bj}^n}{r_{Bj}^n + \alpha^n}. \quad (\text{A.0.11})$$

The non-dimensional model contains 10 dimensionless parameters altogether:

$$V^* = \frac{k_{VR}}{k_{-VR}}V, \quad (\text{A.0.12})$$

$$\bar{\lambda} = \frac{\lambda}{k_{-VR}}, \quad (\text{A.0.13})$$

$$\bar{g}_{max} = \frac{g_{max}}{k_{-VR}N_{tot}}, \quad (\text{A.0.14})$$

$$\bar{k}_{-B} = \frac{k_{-B}}{k_{-VR}}, \quad (\text{A.0.15})$$

$$\bar{k}_B = \frac{k_B N_{tot}}{k_{-VR}}, \quad (\text{A.0.16})$$

$$\bar{\mu} = \frac{\mu}{k_{-VR}}, \quad (\text{A.0.17})$$

as well as β and α as defined in (A.0.9) and the two Hill coefficients, m and n .

For notational simplicity we drop the bars on parameters (A.0.13)-(A.0.17) and the tildes on the production functions in equation (A.0.11). The full dimensionless system is given in equations (3.2.10)-(3.2.14).

Non-dimensionalisation and scalings for the model considering filopodia growth: (4.1.3)-(4.1.5)

We non-dimensionalise the model in equations (4.1.3)-(4.1.8) using the appropriate scalings below. The new model introduces a single variable, F_j , for the length of a filopodium on cell j , which is scaled with the fixed length of the cell body membrane, L_0 , as follows,

$$F_j = L_0 F_j^* . \quad (\text{B.0.1})$$

For R_{Uj} , R_{Bj} , Δ_j , N_j and B_j we use the same scalings as in Appendix A. The Hill functions $f(B_j)$ and $g(r_{Bj})$ have also been non-dimensionalised as in Appendix A. The filopodia growth function $w(r_{Bj})$ is non-dimensionalised in the same way as the function g previously. The four new dimensionless parameters \bar{C} , θ , $\bar{\gamma}$ and $\bar{\phi}$ are defined as follows

$$\bar{C} = \frac{C k_{-VR}}{R_{U0}} , \quad (\text{B.0.2})$$

$$\theta = L_0 \hat{\theta} , \quad (\text{B.0.3})$$

$$\bar{\gamma} = \frac{\gamma}{k_{-VR}} , \quad (\text{B.0.4})$$

$$\bar{\phi} = \frac{\phi}{L_0 k_{-VR}} \quad (\text{B.0.5})$$

For convenience we drop the star from the dimensionless F_j in (B.0.1) and the bars on C , γ and ϕ .

We next non-dimensionalise the term from equations (4.1.4) and (4.1.5) involving the non-constant VEGF field

$$- \frac{k_{VR}}{k_{-VR}} \frac{\int_0^{L_0+F_j(t)} V(x) dx}{(L_0 + F_j(t))} r_{Uj}. \quad (\text{B.0.6})$$

Here the scaling for \bar{R}_{Uj} has already been cancelled and $\frac{1}{k_{-VR}}$ is the scaling for time. We substitute in the expression for the integrated form of $V(x)$ from (4.1.10) to obtain

$$- \frac{k_{VR}}{k_{-VR}(L_0 + F_j(t))} \left(V_0(L_0 + F_j(t)) + \frac{\psi}{2} F_j(t)^2 \right) r_{Uj} \quad (\text{B.0.7})$$

Choosing the scaling in (B.0.1) for $F_j(t)$ and cancelling $L_0 + F_j(t)$ we get

$$- \left(\tilde{V}_0 + \frac{\psi}{2} \frac{F_j^*(t)^2}{(1 + F_j^*(t))} \right) r_{Uj} \quad (\text{B.0.8})$$

which has the following two dimensionless parameters

$$\tilde{V}_0 = V_0 \frac{k_{VR}}{k_{-VR}}, \quad (\text{B.0.9})$$

$$\tilde{\psi} = \psi L_0 \frac{k_{VR}}{k_{-VR}}. \quad (\text{B.0.10})$$

Henceforth, for convenience, we drop the tildes from \tilde{V}_0 and $\tilde{\psi}$, and the star on $F_j(t)$.

Routh Hurwitz conditions for the filopodia system

The characteristic polynomial for (4.4.6) is a quartic of the form $\sigma^4 + a_1\sigma^3 + a_2(K)\sigma^2 + a_3(K)\sigma + a_4(K)$ where the coefficients are given by

$$a_1 = \gamma + \lambda + \mu + k_B(1 - b_e) + k_{-B} + k_B\delta_e - UV\phi r_{Ue}, \quad (\text{C.0.1})$$

$$\begin{aligned} a_2(K) = & -k_B(1 - b_e)(k_{-B} + k_B\delta_e)K^2 + \lambda(\gamma - UV\phi r_{Ue}) \\ & + (\gamma + \lambda - UV\phi r_{Ue})(\mu + k_B(1 - b_e) + k_{-B} + k_B\delta_e) \\ & + (\mu + k_B(1 - b_e))(k_{-B} + k_B\delta_e) - U\theta f(b_e)p_G(F_e)\phi, \end{aligned} \quad (\text{C.0.2})$$

$$\begin{aligned} a_3(K) = & -k_B(1 - b_e)(k_{-B} + k_B\delta_e)(\gamma + \lambda - UV\phi r_{Ue})K^2 \\ & - k_B(1 - b_e)AB\bar{g}_{max}p_G(F_e)(1 + \theta F_e)K \\ & + (\gamma + \lambda - UV\phi r_{Ue})(k_{-B} + k_B\delta_e)(\mu + k_B(1 - b_e)) \\ & + (\mu + k_B(1 - b_e) + k_{-B} + k_B\delta_e) [\lambda(\gamma - UV\phi r_{Ue}) - U\theta f(b_e)p_G(F_e)\phi], \end{aligned} \quad (\text{C.0.3})$$

$$\begin{aligned} a_4(K) = & -k_B(1 - b_e)(k_{-B} + k_B\delta_e) [\lambda(\gamma - UV\phi r_{Ue}) - U\theta f(b_e)p_G(F_e)\phi] K^2 \\ & - k_B(1 - b_e)AB\bar{g}_{max}p_G(F_e)(1 + \theta F_e)\gamma K \\ & + (\mu + k_B(1 - b_e))(k_{-B} + k_B\delta_e) [\lambda(\gamma - UV\phi r_{Ue}) - U\theta f(b_e)p_G(F_e)\phi]. \end{aligned} \quad (\text{C.0.4})$$

The four Routh-Hurwitz conditions for the quartic characteristic polynomial of the filopodia model are given by

$$a_1 > 0, \quad (\text{C.0.5})$$

$$a_1 a_2(K) - a_3(K) > 0, \quad (\text{C.0.6})$$

$$a_3(K) [a_1 a_2(K) - a_3(K)] - a_1^2 a_4(K) > 0, \quad (\text{C.0.7})$$

$$a_4(K) > 0. \quad (\text{C.0.8})$$

Condition (C.0.5) is identical for both the filopodia and no-filopodia models. We here show that the Routh-Hurwitz conditions in equations (C.0.6) and (C.0.8) reduce to their analogues in the no-filopodia model.

Consider (C.0.8) at $K = -1$ which gives

$$\begin{aligned} a_4(-1) &= \mu(k_{-B} + k_B \delta_e) [\lambda(\gamma - UV\phi r_{Ue}) - U\theta f(b_e) p_G(F_e) \phi] \\ &\quad + k_B(1 - b_e) AB \bar{g}_{max} p_G(F_e) (1 + \theta F_e) \gamma. \end{aligned} \quad (\text{C.0.9})$$

This reduces to the condition in (3.5.18) as $\phi \rightarrow 0$. It should be noted that $F_e \rightarrow 0$ and $p_G(F_e) \rightarrow V_0$ as $\phi \rightarrow 0$ (see (4.4.5)). Thus

$$\begin{aligned} \lim_{\phi \rightarrow 0} a_4(-1) &= \gamma [(k_{-B} + k_B \delta_e) \lambda \mu + k_B(1 - b_e) AB \bar{g}_{max} V_0], \\ &= \gamma \tilde{a}_3(-1), \end{aligned}$$

where \tilde{a}_3 is the constant coefficient of the characteristic polynomial for the no-filopodia model (see equation (3.5.12)). Similarly

$$\begin{aligned} \lim_{\phi \rightarrow 0} (a_1 a_2(1) - a_3(1)) &= k_B(1 - b_e) (k_{-B} + k_B \delta_e) (a_1 - \lambda) \\ &\quad + k_B(1 - b_e) AB \bar{g}_{max} V_0 + (\gamma + a_1) (k_{-B} + k_B \delta_e) (\mu + k_B(1 - b_e)) \\ &\quad (\gamma + \lambda) [(\gamma + a_1) (a_1 - \lambda) - (k_{-B} + k_B \delta_e) (\mu + k_B(1 - b_e) + \lambda \gamma)]. \end{aligned} \quad (\text{C.0.10})$$

For this condition we also need to assume that γ is negligible, which gives

$$\begin{aligned} \lim_{\phi \rightarrow 0, \gamma \rightarrow 0} (a_1 \cdot a_2(1) - a_3(1)) &= \\ &= (a_1 - \lambda) [\lambda a_1 + \mu(k_{-B} + k_B \delta_e)] + k_B(1 - b_e) AB \bar{g}_{max} V_0, \end{aligned} \quad (\text{C.0.11})$$

such that imposing $a_1 \cdot a_2(1) - a_3(1) > 0$ recovers the equivalent condition from the no-filopodia model given in (3.5.17) with $V_0 = V^*$.

Parameter choices for the no-filopodia model

We here show how to choose the parameters g_{max} , α and β so that we can vary the values of A and B to move around the plane in Figure 3.9 without changing the value of the homogeneous steady state or the positions of the Routh-Hurwitz hyperbolae. We begin by considering the quasi-steady system outlined in (3.5.1)-(3.5.3) at the homogeneous steady state (r_{Ue}, δ_e, b_e) . Adding (3.5.2) and (3.5.3) at steady state gives

$$g_{max} g(V^* r_{Ue}) = \mu \delta_e,$$

which fixes the value of g_{max} in terms of δ_e , r_{Ue} and the remaining model parameters as

$$g_{max} = \mu \delta_e \frac{\alpha^n + (V^* r_{Ue})^n}{(V^* r_{Ue})^n}. \quad (\text{D.0.1})$$

Here the steady state values of r_{Ue} and δ_e are determined by b_e as follows. Equation (3.5.1) at steady state gives

$$f(b_e) = \lambda r_{Ue},$$

so that

$$r_{Ue} = \frac{1}{\lambda} \frac{\beta^m}{\beta^m + b_e^m}. \quad (\text{D.0.2})$$

and equation (3.5.3) fixes δ_e as

$$\delta_e = \frac{k_{-B} b_e}{k_B (1 - b_e)}. \quad (\text{D.0.3})$$

Substituting (D.0.3) and (D.0.2) into (D.0.1) defines the parameter g_{max} in terms of b_e . Next we would like to make the slopes of f and g independent of the homogeneous steady state as these are the key regulators of the model behaviour.

The slope of f is given by

$$f'(b_e) = \frac{-m \beta^m b_e^{m-1}}{(\beta^m + b_e^m)^2} \quad (\text{D.0.4})$$

but if we choose $\beta = b_e$ then

$$A = f'(b_e) = \frac{-m b_e^{2m-1}}{4b_e^{2m}} = -\frac{m}{4b_e}. \quad (\text{D.0.5})$$

Similarly, when $\beta = b_e$ the slope of g is given by

$$\begin{aligned} g'(V^* r_{Ue}) &= g' \left(\frac{V^* \beta^m}{\lambda(\beta^m + b_e^m)} \right) \Big|_{\beta=b_e} = g' \left(\frac{V^*}{2\lambda} \right) \\ &= \frac{n\alpha^n \left(\frac{V^*}{2\lambda} \right)^{n-1}}{\left(\alpha^n + \left(\frac{V^*}{2\lambda} \right)^n \right)^2}. \end{aligned}$$

By choosing $\alpha = \frac{V^*}{2\lambda}$ we have

$$B = g'(V^* r_{Ue}) = \frac{n \left(\frac{V^*}{2\lambda} \right)^{2n-1}}{4 \left(\frac{V^*}{2\lambda} \right)^{2n}} = \frac{\lambda}{2V^*} n. \quad (\text{D.0.6})$$

Both (D.0.5) and (D.0.6) are linear functions of m and n for a fixed b_e and our choices of α and β give us entire ranges for $A, B \in (-\infty, \infty)$.

In summary, we choose and fix b_e and all model parameters except g_{max} , β and α , which are specified in terms of these as described above. (See the non-shaded rows of Table E.1 for parameter values used with $b_e = 0.5605$).

Parameter values for the filopodia model

We use an approach similar to that of Webb and Owen [71] in choosing our parameters. When analysing the system in the A - B plane, all parameters are fixed except for two free parameters, m and n in the no-filopodia system. These are the Hill coefficients of f and g , describing the rate of production for VEGF receptors and Delta ligand respectively. The free parameters can be interpreted as a measure of the response strengths of ligand and receptor production. Similarly, in the system which includes filopodia growth, q is the free parameter indicating the response strength, U , of filopodia growth.

We here show how to choose the parameters g_{max} , α , β and C in the filopodia system such that we can vary the free parameters m , n and q without changing the underlying homogeneous steady state. This is important as it allows us to compare the behaviour of the model using different response strengths.

The system of equations at the homogeneous steady state is given by

$$0 = \phi w(r_{Be}) - \gamma F_e, \quad (\text{E.0.1})$$

$$0 = (1 + \theta F_e) f(b_e) + r_{Be} - r_{Ue} \left(V_0 + \frac{\psi}{2} \frac{F_e^2}{1 + F_e} \right) - \lambda r_{Ue}, \quad (\text{E.0.2})$$

$$0 = r_{Ue} \left(V_0 + \frac{\psi}{2} \frac{F_e^2}{1 + F_e} \right) - r_{Be}, \quad (\text{E.0.3})$$

$$0 = g_{max} g(r_{Be}) + k_{-B} b_e - k_B (1 - b_e) \delta_e - \mu \delta_e, \quad (\text{E.0.4})$$

$$0 = k_B \delta_e (1 - b_e) - k_{-B} b_e, \quad (\text{E.0.5})$$

where F_e , r_{Ue} , r_{Be} , δ_e and b_e are the steady state values of the model variables. We fix

the equilibrium level of bound Notch receptors, b_e and choose

$$\beta = b_e, \quad \alpha = r_{Be}, \quad C = r_{Be}. \quad (\text{E.0.6})$$

where r_{Be} is the homogeneous steady state of bound VEGF receptors to be determined in terms of the model parameters. Substituting these into the steady state system fixes the Hill functions: $f(b_e) = g(r_{Be}) = w(r_{Be}) = \frac{1}{2}$ and gives

$$F_e = \frac{\phi}{2\gamma}, \quad (\text{E.0.7})$$

$$r_{Ue} = \frac{1}{2\lambda}(1 + \theta F_e) = \frac{1}{2\lambda}\left(1 + \theta \frac{\phi}{2\gamma}\right), \quad (\text{E.0.8})$$

$$\delta_e = \frac{k_{-B}b_e}{k_B(1 - b_e)}. \quad (\text{E.0.9})$$

Substituting (E.0.8) into (E.0.3) defines the steady state of bound VEGF receptors

$$r_{Be} = \frac{1}{2\lambda} \left(1 + \frac{\theta\phi}{2\gamma}\right) \left(V_0 + \frac{\tilde{m}}{2} \frac{\phi^2}{4\gamma^2 + 2\phi\gamma}\right), \quad (\text{E.0.10})$$

(in terms of the fixed model parameters $\lambda, \mu, \theta, \phi, \gamma, V_0, \psi, k_B$ and k_{-B}). Substituting the expression for δ_e (E.0.9) into (E.0.4)+(E.0.5) defines the model parameter g_{max} as

$$g_{max} = \frac{2\mu k_{-B}b_e}{k_B(1 - b_e)}, \quad (\text{E.0.11})$$

which is equivalent to (D.0.1) with $\alpha = \frac{V^*}{2\lambda}$, r_{Ue} as in (D.0.2) and δ_e as in (D.0.3).

The expression for r_{Be} in (E.0.10) defines α and C as

$$\alpha = \frac{1}{2\lambda} \left(1 + \frac{\theta\phi}{2\gamma}\right) \left(V_0 + \frac{\tilde{m}}{2} \frac{\phi^2}{4\gamma^2 + 2\phi\gamma}\right) \quad (\text{E.0.12})$$

$$C = \frac{1}{2\lambda} \left(1 + \frac{\theta\phi}{2\gamma}\right) \left(V_0 + \frac{\tilde{m}}{2} \frac{\phi^2}{4\gamma^2 + 2\phi\gamma}\right) \quad (\text{E.0.13})$$

Hence, choosing the parameters as in (E.0.6) is sufficient for the choices of g_{max} , α and C in (E.0.11)-(E.0.13) but not necessary as for certain values of m and n , our model exhibits multiple homogeneous steady states. The slopes of the production functions are given by

$$f'(b_e) = \frac{-m\beta^m b_e^{m-1}}{(\beta^m + b_e^m)^2}, \quad g'(r_{Be}) = \frac{n\alpha^n r_{Be}^{n-1}}{(\alpha^n + r_{Be}^n)^2}, \quad w'(r_{Be}) = \frac{nC^n r_{Be}^{n-1}}{(C^n + r_{Be}^n)^2}, \quad (\text{E.0.14})$$

however, after applying our parameter choices from (E.0.6), these become

$$A = f'(b_e) = \frac{-m}{4b_e}, \quad B = g'(r_{Be}) = \frac{n}{4r_{Be}}, \quad U = w'(r_{Be}) = \frac{q}{4r_{Be}}. \quad (\text{E.0.15})$$

Hence varying the values of m , n and q allows us to change the feedback strengths A , B and U but doesn't change the value of the homogeneous steady state parameterised by b_e and r_{Be} in (E.0.10). It should be noted that A is the same as in the no-filopodia model, (D.0.5), and $B = \frac{n}{4} \frac{2\lambda}{V_0}$ when $\phi = 0$ which is equivalent to the expression from the no-filopodia model, (D.0.6), with $V_0 = V^*$. All parameter choices are summarised in Table E.1.

Parameter	Numerical Value
V_0	0.33
λ	0.5
k_{-B}	0.25
k_B	3
μ	1
β	0.5605
ϕ	2
γ	0.5
ψ	0
θ	0
g_{max}	(E.0.11) \implies 0.2126
α	(E.0.12) \implies 0.33
C	(E.0.13) \implies 0.33
m	-
n	-
q	-

Table E.1: Table of dimensionless parameter values for A - B plane analysis of the no-filopodia model (unshaded rows) and filopodia model (shaded rows). The parameter V_0 is the filopodia model equivalent to V^* (used in the model without filopodia) and m, n and q (filopodia model) are free parameters used to vary the feedback strengths whilst keeping a fixed homogeneous steady state of $b_e = 0.5605$ and $r_{Be} = 0.33$.

References

- [1] R.J. D'Amato, M.S. Loughnan, E. Flynn, and J. Folkman. Thalidomide is an inhibitor of angiogenesis. *Proceedings of the National Academy of Sciences*, 91(9):4082–4085, 1994.
- [2] C.J. Drake. Embryonic and adult vasculogenesis. *Birth Defects Research Part C: Embryo Today: Reviews*, 69(1):73–82, 2003.
- [3] K. Kissa and P. Herbomel. Blood stem cells emerge from aortic endothelium by a novel type of cell transition. *Nature*, 464(7285):112–115, 2010.
- [4] G. Swiers, M. de Bruijn, and N.A. Speck. Hematopoietic stem cell emergence in the conceptus and the role of Runx1. *Int. J. Dev. Biol*, 54:1151–1163, 2010.
- [5] J.Y. Bertrand, N.C. Chi, B. Santoso, S. Teng, D.Y.R. Stainier, and D. Traver. Haematopoietic stem cells derive directly from aortic endothelium during development. *Nature*, 464(7285):108–111, 2010.
- [6] C. Lengerke and G.Q. Daley. Autologous blood cell therapies from pluripotent stem cells. *Blood reviews*, 24(1):27–37, 2010.
- [7] A.S. Chung and N. Ferrara. Developmental and pathological angiogenesis. *Annual review of cell and developmental biology*, 27:563–584, 2011.
- [8] H.U. Wang, Z.F. Chen, and D.J. Anderson. Molecular distinction and angiogenic interaction between embryonic arteries and veins revealed by ephrin-b2 and its receptor Eph-b4. *Cell*, 93(5):741–753, 1998.
- [9] M. Hellström, L.K. Phng, J.J. Hofmann, E. Wallgard, L. Coultas, P. Lindblom, J. Alva, A.K. Nilsson, L. Karlsson, N. Gaiano, K. Yoon, J. Rossant, M.L. Iruela-Arispe, M. Kalén, H. Gerhardt, and C. Betsholtz. Dll4 signalling through Notch1 regulates formation of tip cells during angiogenesis. *Nature*, 445(7129):776–780, 2007.

REFERENCES

- [10] K. Kumano, S. Chiba, A. Kunisato, M. Sata, T. Saito, E. Nakagami-Yamaguchi, T. Yamaguchi, S. Masuda, K. Shimizu, T. Takahashi, S. Ogawa, Y. Hamada, and H. Hirai. Notch1 but not Notch2 is essential for generating hematopoietic stem cells from endothelial cells. *Immunity*, 18(5):699–711, 2003.
- [11] L.T. Krebs, J.R. Shutter, K. Tanigaki, T. Honjo, K.L. Stark, and Thomas Gridley. Haploinsufficient lethality and formation of arteriovenous malformations in Notch pathway mutants. *Genes & development*, 18(20):2469–2473, 2004.
- [12] B.K. Hadland, S.S. Huppert, J. Kanungo, Y. Xue, R. Jiang, T. Gridley, R.A. Conlon, A.M. Cheng, R. Kopan, and G.D. Longmore. A requirement for Notch1 distinguishes 2 phases of definitive hematopoiesis during development. *Blood*, 104(10):3097–3105, 2004.
- [13] L.K. Phng and H. Gerhardt. Angiogenesis: a team effort coordinated by Notch. *Developmental cell*, 16(2):196–208, 2009.
- [14] M. Gering and R. Patient. Notch signalling and haematopoietic stem cell formation during embryogenesis. *Journal of cellular physiology*, 222(1):11–16, 2010.
- [15] S.J. Bray. Notch signalling: a simple pathway becomes complex. *Nature reviews Molecular cell biology*, 7(9):678–689, 2006.
- [16] A. Louvi and S. Artavanis-Tsakonas. Notch signalling in vertebrate neural development. *Nature Reviews Neuroscience*, 7(2):93–102, 2006.
- [17] B.A. Osborne and L.M. Minter. Notch signalling during peripheral t-cell activation and differentiation. *Nature Reviews Immunology*, 7(1):64–75, 2006.
- [18] A.P. Weng, A.A. Ferrando, W. Lee, J.P. Morris, L.B. Silverman, C. Sanchez-Irizarry, S.C. Blacklow, A.T. Look, and J.C. Aster. Activating mutations of Notch1 in human T-cell acute lymphoblastic leukemia. *Science*, 306(5694):269–271, 2004.
- [19] M.F.T.R. de Bruijn, N.A. Speck, M.C.E. Peeters, and E. Dzierzak. Definitive hematopoietic stem cells first develop within the major arterial regions of the mouse embryo. *The EMBO journal*, 19(11):2465–2474, 2000.
- [20] T.P. Zhong, S. Childs, J.P. Leu, and M.C. Fishman. Gridlock signalling pathway fashions the first embryonic artery. *Nature*, 414(6860):216–220, 2001.
- [21] N.D. Lawson, N. Scheer, V.N. Pham, C.H. Kim, A.B. Chitnis, J.A. Campos-Ortega, and B.M. Weinstein. Notch signaling is required for arterial-venous differentiation during embryonic vascular development. *Development*, 128(19):3675–3683, 2001.

REFERENCES

- [22] N.D. Lawson, A.M. Vogel, and B.M. Weinstein. Sonic hedgehog and vascular endothelial growth factor act upstream of the Notch pathway during arterial endothelial differentiation. *Developmental cell*, 3(1):127–136, 2002.
- [23] C. Roca and R.H. Adams. Regulation of vascular morphogenesis by Notch signaling. *Genes & development*, 21(20):2511–2524, 2007.
- [24] J. Grego-Bessa, L. Luna-Zurita, G. del Monte, V. Bolós, P. Melgar, A. Arandilla, A.N. Garratt, H. Zang, Y.S. Mukouyama, H. Chen, W. Shou, E. Ballestar, M. Esteller, A. Rojas, J.M. Pérez-Pomares, and J.L. de la Pompa. Notch signaling is essential for ventricular chamber development. *Developmental cell*, 12(3):415–429, 2007.
- [25] M. Gering and R. Patient. Hedgehog signaling is required for adult blood stem cell formation in zebrafish embryos. *Developmental cell*, 8(3):389–400, 2005. ISSN 1534-5807.
- [26] N.W. Gale, M.G. Dominguez, I. Noguera, L. Pan, V. Hughes, D.M. Valenzuela, A.J. Murphy, N.C. Adams, H.C. Lin, J. Holash, G. Thurston, and G.D. Yancopoulos. Haploinsufficiency of Delta-like 4 ligand results in embryonic lethality due to major defects in arterial and vascular development. *Proceedings of the National Academy of Sciences of the United States of America*, 101(45):15949–15954, 2004.
- [27] L.R. You, F.J. Lin, C.T. Lee, F.J. DeMayo, M.J. Tsai, and S.Y. Tsai. Suppression of Notch signalling by the COUP-TFII transcription factor regulates vein identity. *Nature*, 435(7038):98–104, 2005.
- [28] J.M. Rowlinson and M. Gering. Hey2 acts upstream of Notch in hematopoietic stem cell specification in zebrafish embryos. *Blood*, 116(12):2046, 2010.
- [29] S.P. Herbert, J. Huisken, T.N. Kim, M.E. Feldman, B.T. Houseman, R.A. Wang, K.M. Shokat, and D.Y.R. Stainier. Arterial-venous segregation by selective cell sprouting: an alternative mode of blood vessel formation. *Science*, 326(5950):294–298, 2009.
- [30] C.E. Burns, D. Traver, E. Mayhall, J.L. Shepard, and L.I. Zon. Hematopoietic stem cell fate is established by the Notch–Runx pathway. *Genes & development*, 19(19):2331, 2005.
- [31] C.B. Kimmel, W.W. Ballard, S.R. Kimmel, B. Ullmann, and T.F. Schilling. Stages of embryonic development of the zebrafish. *Developmental dynamics*, 203(3):253–310, 1995.

REFERENCES

- [32] E. Ellertsdóttir, A. Lenard, Y. Blum, A. Krudewig, L. Herwig, M. Affolter, and H.G. Belting. Vascular morphogenesis in the zebrafish embryo. *Developmental biology*, 341(1):56–65, 2010.
- [33] M.L. Kalev-Zylinska, J.A. Horsfield, M.V.C. Flores, J.H. Postlethwait, M.R. Vitas, A.M. Baas, P.S. Crosier, and K.E. Crosier. Runx1 is required for zebrafish blood and vessel development and expression of a human RUNX1-CBF2T1 transgene advances a model for studies of leukemogenesis. *Development*, 129(8):2015–2030, 2002.
- [34] W.T. Nottingham, A. Jarratt, M. Burgess, C.L. Speck, J.F. Cheng, S. Prabhakar, E.M. Rubin, P.S. Li, J. Sloane-Stanley, J. Kong-a-San, and M.F.T.R. de Bruijn. Runx1-mediated hematopoietic stem-cell emergence is controlled by a Gata/Ets/SCL-regulated enhancer. *Blood*, 110(13):4188–4197, 2007.
- [35] À. Robert-Moreno, L. Espinosa, J.L. de la Pompa, and A. Bigas. Rbpj κ -dependent Notch function regulates gata2 and is essential for the formation of intra-embryonic hematopoietic cells. *Development*, 132(5):1117–1126, 2005.
- [36] J. Guiu, R. Shimizu, T. D’Altri, S.T. Fraser, J. Hatakeyama, E.H. Bresnick, R. Kageyama, E. Dzierzak, M. Yamamoto, L. Espinosa, and A. Bigas. Hes repressors are essential regulators of hematopoietic stem cell development downstream of Notch signaling. *The Journal of experimental medicine*, 210(1):71–84, 2013.
- [37] W.K. Clements, A.D. Kim, K.G. Ong, J.C. Moore, N.D. Lawson, and D. Traver. A somitic Wnt16/Notch pathway specifies haematopoietic stem cells. *Nature*, 474(7350):220–224, 2011.
- [38] I. Kobayashi, J. Kobayashi-Sun, A.D. Kim, C. Pouget, N. Fujita, T. Suda, and D. Traver. Jam1a-Jam2a interactions regulate haematopoietic stem cell fate through Notch signalling. *Nature*, 512(7514):319–323, 2014.
- [39] A.J. Singer, and R.A.F. Clark. Cutaneous wound healing. *New England journal of medicine*, 341(10):738–746, 1999.
- [40] A. Martin, M.R. Komada, and D.C. Sane. Abnormal angiogenesis in diabetes mellitus. *Medicinal research reviews*, 23(2):117–145, 2003.
- [41] A.E. Koch. Angiogenesis as a target in rheumatoid arthritis. *Annals of the rheumatic diseases*, 62(suppl 2):ii60–ii67, 2003.
- [42] A.P. Adamis, D.T. Shima, M.J. Tolentino, E.S. Gragoudas, N. Ferrara, J. Folkman, P.A. D’Amore, and J.W. Miller. Inhibition of vascular endothelial growth factor

REFERENCES

- prevents retinal ischemia-associated iris neovascularization in a nonhuman primate. *Archives of ophthalmology*, 114(1):66–71, 1996.
- [43] P. Carmeliet. Angiogenesis in life, disease and medicine. *Nature*, 438(7070):932–936, 2005.
- [44] D. Ribatti, B. Nico, and E. Crivellato. The role of pericytes in angiogenesis. *International Journal of Developmental Biology*, 55(3):261, 2011.
- [45] J.J. Walter and D.C. Sane. The role of smooth muscle cells and pericytes in angiogenesis. *Angiogenesis Inhibitors and Stimulators*, page 27, 2000.
- [46] A. Armulik, A. Abramsson, and C. Betsholtz. Endothelial/pericyte interactions. *Circulation research*, 97(6):512–523, 2005.
- [47] S. Suchting, C. Freitas, F. le Noble, R. Benedito, C. Bréant, A. Duarte, and A. Eichmann. The Notch ligand Delta-like 4 negatively regulates endothelial tip cell formation and vessel branching. *Proceedings of the National Academy of Sciences*, 104(9):3225–3230, 2007.
- [48] T. Tammela, G. Zarkada, E. Wallgard, A. Murtomäki, S. Suchting, M. Wirzenius, M. Waltari, M. Hellström, T. Schomber, R. Peltonen, C. Freitas, A. Duarte, H. Isoniemi, P. Laakkonen, G. Christofori, S. Ylä-Herttuala, M. Shibuya, B. Pytowski, A. Eichmann, C. Betsholtz, and K. Alitalo. Blocking VEGFR-3 suppresses angiogenic sprouting and vascular network formation. *Nature*, 454(7204):656–660, 2008.
- [49] J.D. Leslie, L. Ariza-McNaughton, A.L. Bermange, R. McAdow, S.L. Johnson, and J. Lewis. Endothelial signalling by the Notch ligand Delta-like 4 restricts angiogenesis. *Development*, 134(5):839–844, 2007.
- [50] A.F. Siekmann and N.D. Lawson. Notch signalling limits angiogenic cell behaviour in developing zebrafish arteries. *Nature*, 445(7129):781–784, 2007.
- [51] L. Jakobsson, K. Bentley, and H. Gerhardt. VEGFRs and Notch: a dynamic collaboration in vascular patterning. *Biochemical Society Transactions*, 37(6):1233, 2009.
- [52] G. Thurston, I. Noguera-Troise, and G.D. Yancopoulos. The Delta paradox: Dll4 blockade leads to more tumour vessels but less tumour growth. *Nature Reviews Cancer*, 7(5):327–331, 2007.
- [53] I. Noguera-Troise, C. Daly, N.J. Papadopoulos, S. Coetzee, P. Boland, N.W. Gale, H.C. Lin, G.D. Yancopoulos, and G. Thurston. Blockade of Dll4 inhibits tumour

REFERENCES

- growth by promoting non-productive angiogenesis. *Nature*, 444(7122):1032–1037, 2006.
- [54] M.A. Thompson, D.G. Ransom, S.J. Pratt, H. MacLennan, M.W. Kieran, H.W. Detriche, B. Vail, T.L. Huber, B. Paw, A.J. Brownlie, A.C. Oates, A. Fritz, M.A. Gates, A.A. Amores, N. Bahary, W.S. Talbot, H. Her, D.R. Beier, J.H. Postlethwait, and L.I. Zon. The cloche and spadetail genes differentially affect hematopoiesis and vasculogenesis. *Dev Biol*, 197:248–269, 1998.
- [55] L.D. Covassin, J.A. Villefranc, M.C. Kacergis, B.M. Weinstein, and N.D. Lawson. Distinct genetic interactions between multiple VEGF receptors are required for development of different blood vessel types in zebrafish. *Proceedings of the National Academy of Sciences*, 103(17):6554–6559, 2006.
- [56] B.M. Hogan, R. Herpers, M. Witte, H. Heloterä, K. Alitalo, H.J. Duckers, and S. Schulte-Merker. VEGF-C/Flt4 signalling is suppressed by Dll4 in developing zebrafish intersegmental arteries. *Development*, 136(23):4001–4009, 2009.
- [57] N.D. Lawson, J.W. Mugford, B.A. Diamond, and B.M. Weinstein. phospholipase c gamma-1 is required downstream of vascular endothelial growth factor during arterial development. *Genes & development*, 17(11):1346, 2003.
- [58] T. Zygmunt, C.M. Gay, J. Blondelle, M.K. Singh, K.M.C. Flaherty, P.C. Means, L. Herwig, A. Krudewig, H.G. Belting, M. Affolter, J.A. Epstein, J. Torres-Vázquez. Semaphorin-plexinD1 signaling limits angiogenic potential via the VEGF decoy receptor sflt1. *Developmental cell*, 2011.
- [59] J. Krueger, D. Liu, K. Scholz, A. Zimmer, Y. Shi, C. Klein, A. Siekmann, S. Schulte-Merker, M. Cudmore, A. Ahmed, and F. le Noble. Flt1 acts as a negative regulator of tip cell formation and branching morphogenesis in the zebrafish embryo. *Development*, 138(10):2111–2120, 2011.
- [60] L. Jakobsson, C.A. Franco, K. Bentley, R.T. Collins, B. Ponsioen, I.M. Aspalter, I. Rosewell, M. Busse, G. Thurston, A. Medvinsky, S. Schulte-Merker, and H. Gerhardt. Endothelial cells dynamically compete for the tip cell position during angiogenic sprouting. *Nature cell biology*, 12(10):943–953, 2010.
- [61] J. Bussmann, S.A. Wolfe, and A.F. Siekmann. Arterial-venous network formation during brain vascularization involves hemodynamic regulation of chemokine signaling. *Development*, 138(9):1717–1726, 2011.

REFERENCES

- [62] I.B. Lobov, R.A. Renard, N. Papadopoulos, N.W. Gale, G. Thurston, G.D. Yancopoulos, and S.J. Wiegand. Delta-like ligand 4 (Dll4) is induced by VEGF as a negative regulator of angiogenic sprouting. *Proceedings of the National Academy of Sciences*, 104(9):3219–3224, 2007.
- [63] Z.J. Liu, T. Shirakawa, Y. Li, A. Soma, M. Oka, G.P. Dotto, R.M. Fairman, O.C. Velazquez, and M. Herlyn. Regulation of Notch1 and Dll4 by vascular endothelial growth factor in arterial endothelial cells: implications for modulating arteriogenesis and angiogenesis. *Molecular and cellular biology*, 23(1):14–25, 2003.
- [64] H.M. Byrne. Dissecting cancer through mathematics: from the cell to the animal model. *Nature Reviews Cancer*, 10(3):221–230, 2010.
- [65] G. von Dassow, E. Meir, E.M. Munro, and G.M. Odell. The segment polarity network is a robust developmental module. *Nature*, 406(6792):188–192, 2000.
- [66] C.J. Tomlin and J.D. Axelrod. Biology by numbers: mathematical modelling in developmental biology. *Nature Reviews Genetics*, 8(5):331–340, 2007.
- [67] J.R. Collier, N.A.M. Monk, P.K. Maini, and J.H. Lewis. Pattern formation by lateral inhibition with feedback: a mathematical model of Delta-Notch intercellular signalling. *Journal of Theoretical Biology*, 183(4):429–446, 1996.
- [68] M.R. Owen and J.A. Sherratt. Mathematical modelling of juxtacrine cell signalling. *Mathematical biosciences*, 153(2):125–150, 1998.
- [69] M.R. Owen, J.A. Sherratt, and H.J. Wearing. Lateral induction by juxtacrine signaling is a new mechanism for pattern formation. *Developmental Biology*, 217(1): 54–61, 2000.
- [70] H.J. Wearing, M.R. Owen, and J.A. Sherratt. Mathematical modelling of juxtacrine patterning. *Bulletin of Mathematical Biology*, 62(2):293–320, 2000.
- [71] S.D. Webb and M.R. Owen. Oscillations and patterns in spatially discrete models for developmental intercellular signalling. *Journal of mathematical biology*, 48(4): 444–476, 2004.
- [72] S.D. Webb and M.R. Owen. Intra-membrane ligand diffusion and cell shape modulate juxtacrine patterning. *Journal of theoretical biology*, 230(1):99–117, 2004.
- [73] M. Santillán. On the use of the hill functions in mathematical models of gene regulatory networks. *Mathematical Modelling of Natural Phenomena*, 3(02):85–97, 2008.

REFERENCES

- [74] D. Sprinzak, A. Lakhanpal, L. LeBon, L.A. Santat, M.E. Fontes, G.A. Anderson, J. Garcia-Ojalvo, and M.B. Elowitz. Cis-interactions between Notch and Delta generate mutually exclusive signalling states. *Nature*, 465(7294):86–90, 2010.
- [75] D. Sprinzak, A. Lakhanpal, L. LeBon, J. Garcia-Ojalvo, and M.B. Elowitz. Mutual inactivation of Notch receptors and ligands facilitates developmental patterning. *PLoS computational biology*, 7(6):e1002069, 2011.
- [76] D. Balding and D.L.S. McElwain. A mathematical model of tumour-induced capillary growth. *Journal of theoretical biology*, 114(1):53–73, 1985.
- [77] H.M. Byrne and M.A.J. Chaplain. Mathematical models for tumour angiogenesis: numerical simulations and nonlinear wave solutions. *Bulletin of mathematical biology*, 57(3):461–486, 1995.
- [78] M.E. Orme and M.A.J. Chaplain. Two-dimensional models of tumour angiogenesis and anti-angiogenesis strategies. *Mathematical Medicine and Biology*, 14(3):189–205, 1997.
- [79] F. Milde, M. Bergdorf, and P. Koumoutsakos. A hybrid model for three-dimensional simulations of sprouting angiogenesis. *Biophysical journal*, 95(7):3146–3160, 2008.
- [80] N.V. Mantzaris, S. Webb, and H.G. Othmer. Mathematical modeling of tumor-induced angiogenesis. *Journal of mathematical biology*, 49(2):111–187, 2004.
- [81] K. Bentley, H. Gerhardt, and P.A. Bates. Agent-based simulation of Notch-mediated tip cell selection in angiogenic sprout initialisation. *Journal of Theoretical Biology*, 250(1):25–36, 2008.
- [82] K. Bentley, G. Mariggi, H. Gerhardt, and P.A. Bates. Tipping the balance: robustness of tip cell selection, migration and fusion in angiogenesis. *PLoS computational biology*, 5(10):e1000549, 2009.
- [83] R.M.H. Merks and J.A. Glazier. Dynamic mechanisms of blood vessel growth. *Nonlinearity*, 19(1):C1, 2006.
- [84] H.A. Levine, S. Pamuk, B.D. Sleeman, and M. Nilsen-Hamilton. Mathematical modeling of capillary formation and development in tumor angiogenesis: penetration into the stroma. *Bulletin of mathematical biology*, 63(5):801–863, 2001.
- [85] H.A. Levine, A.L. Tucker, and M. Nilsen-Hamilton. A mathematical model for the role of cell signal transduction in the initiation and inhibition of angiogenesis. *Growth Factors*, 20(4):155–175, 2003.

REFERENCES

- [86] M. Cohen, M. Georgiou, N.L. Stevenson, M. Miodownik, and B. Baum. Dynamic filopodia transmit intermittent Delta-Notch signaling to drive pattern refinement during lateral inhibition. *Developmental cell*, 19(1):78–89, 2010.
- [87] E. Meir, G. von Dassow, E. Munro, and G.M. Odell. Robustness, flexibility, and the role of lateral inhibition in the neurogenic network. *Current Biology*, 12(10):778–786, 2002.
- [88] H. Momiji and N.A.M. Monk. Oscillatory Notch-pathway activity in a delay model of neuronal differentiation. *Physical Review E*, 80(2):021930, 2009.
- [89] E.M. Özbudak and J. Lewis. Notch signalling synchronizes the zebrafish segmentation clock but is not needed to create somite boundaries. *PLoS genetics*, 4(2):e15, 2008.
- [90] N. Geard and K. Willadsen. Dynamical approaches to modeling developmental gene regulatory networks. *Birth Defects Research Part C: Embryo Today: Reviews*, 87(2):131–142, 2009.
- [91] S.H. Strogatz. *Nonlinear dynamics and chaos: with applications to physics, biology and chemistry*. Perseus publishing, 2001.
- [92] C.G. Moles, P. Mendes, and J.R. Banga. Parameter estimation in biochemical pathways: a comparison of global optimization methods. *Genome research*, 13(11):2467–2474, 2003.
- [93] N. Metropolis, A.W. Rosenbluth, M.N. Rosenbluth, A.H. Teller, and E. Teller. Equation of state calculations by fast computing machines. *The journal of chemical physics*, 21(6):1087–1092, 1953.
- [94] J.A. Nelder and R. Mead. A simplex method for function minimization. *The computer journal*, 7(4):308–313, 1965.
- [95] J.H. Holland. Genetic algorithms. *Scientific american*, 267(1):66–72, 1992.
- [96] P. Venkataraman. *Applied optimization with MATLAB programming*. John Wiley & Sons, 2009.
- [97] D.W. Marquardt. An algorithm for least-squares estimation of nonlinear parameters. *Journal of the Society for Industrial & Applied Mathematics*, 11(2):431–441, 1963.
- [98] B. Ermentrout. *Simulating, analyzing, and animating dynamical systems: a guide to XPPAUT for researchers and students*, volume 14. Siam, 2002.

REFERENCES

- [99] N. Noykova, T.G. MuÈller, M. Gyllenberg, and J. Timmer. Quantitative analyses of anaerobic wastewater treatment processes: identifiability and parameter estimation. *Biotechnology and bioengineering*, 78(1):89–103, 2002.
- [100] M. Rodriguez-Fernandez, J.A. Egea, and J.R. Banga. Novel metaheuristic for parameter estimation in nonlinear dynamic biological systems. *BMC bioinformatics*, 7(1):483, 2006.
- [101] E.J. Crampin, W.W. Hackborn, and P.K. Maini. Pattern formation in reaction-diffusion models with nonuniform domain growth. *Bulletin of mathematical biology*, 64(4):747–769, 2002.
- [102] J. Crank. *Free and moving boundary problems*. Oxford: Clarendon press, 1984.
- [103] A.A. Neville, P.C. Matthews, and H.M. Byrne. Interactions between pattern formation and domain growth. *Bulletin of mathematical biology*, 68(8):1975–2003, 2006.
- [104] M. Itoh, C.H. Kim, G. Palardy, T. Oda, Y.J. Jiang, D. Maust, S.Y. Yeo, K. Lorick, G.J. Wright, L. Ariza-McNaughton, A.M. Weissman, J. Lewis, S.C. Chandrasekharappa, and A.B. Chitnis. Mind bomb is a ubiquitin ligase that is essential for efficient activation of Notch signaling by Delta. *Developmental cell*, 4(1):67–82, 2003.
- [105] A.V. Gore, M.R. Swift, Y.R. Cha, B. Lo, M.C. McKinney, W. Li, D. Castranova, A. Davis, Y.S. Mukoyama, and B.M. Weinstein. Rspo1/Wnt signaling promotes angiogenesis via VEGF-C/VEGFR-3. *Development*, 138(22):4875–4886, 2011.
- [106] H. Hirai, I.M. Samokhvalov, T. Fujimoto, S. Nishikawa, J. Imanishi, and S.I. Nishikawa. Involvement of Runx1 in the down-regulation of fetal liver kinase-1 expression during transition of endothelial cells to hematopoietic cells. *Blood*, 106(6):1948–1955, 2005.
- [107] K.J. Livak and T.D. Schmittgen. Analysis of relative gene expression data using real-time quantitative pcr and the $2^{-\Delta\Delta C_t}$ method. *Methods*, 25(4):402–408, 2001.
- [108] J. Folkman and H. Brem. Angiogenesis and inflammation. *Inflammation: Basic Principles and Clinical Correlates, Second Edition*.(eds. JI Gallin, IM Goldstein and R. Dnyderman), New York, Raven Press, 1992.
- [109] R. Blanco and H. Gerhardt. Vegf and Notch in tip and stalk cell selection. *Cold Spring Harbor perspectives in medicine*, 3(1), 2013.

REFERENCES

- [110] H. Gerhardt, M. Golding, M. Fruttiger, C. Ruhrberg, A. Lundkvist, A. Abramson, M. Jeltsch, C. Mitchell, K. Alitalo, D. Shima, and C. Betsholtz. VEGF guides angiogenic sprouting utilizing endothelial tip cell filopodia. *The Journal of cell biology*, 161(6):1163–1177, 2003.
- [111] C. Ruhrberg, H. Gerhardt, M. Golding, R. Watson, S. Ioannidou, H. Fujisawa, C. Betsholtz, and D.T. Shima. Spatially restricted patterning cues provided by heparin-binding VEGF-A control blood vessel branching morphogenesis. *Genes & development*, 16(20):2684–2698, 2002.
- [112] P. Carmeliet, V. Ferreira, G. Breier, S. Pollefeyt, L. Kieckens, M. Gertsenstein, M. Fahrig, A. Vandenhoeck, K. Harpal, C. Eberhardt, C. Declercq, J. Pawling, L. Moons, D. Collen, W. Risau, and A. Nagy. Abnormal blood vessel development and lethality in embryos lacking a single VEGF allele. *Nature*, 380(6573):435–439, 1996.
- [113] A. Duarte, M. Hirashima, R. Benedito, A. Trindade, P. Diniz, E. Bekman, L. Costa, D. Henrique, and J. Rossant. Dosage-sensitive requirement for mouse Dll4 in artery development. *Genes & development*, 18(20):2474–2478, 2004.
- [114] A.M. Turing. The chemical basis of morphogenesis. *Bulletin of mathematical biology*, 52(1):153–197, 1990.
- [115] N.A.M. Monk. Restricted-range gradients and travelling fronts in a model of juxtacrine cell relay. *Bulletin of mathematical biology*, 60(5):901–918, 1998.
- [116] M.R. Owen. Waves and propagation failure in discrete space models with non-linear coupling and feedback. *Physica D: Nonlinear Phenomena*, 173(1):59–76, 2002.
- [117] J.P. Keener. Propagation and its failure in coupled systems of discrete excitable cells. *SIAM Journal on Applied Mathematics*, 47(3):556–572, 1987.
- [118] Y.J. Jiang, B.L. Aerne, L. Smithers, C. Haddon, D. Ish-Horowicz, and J. Lewis. Notch signalling and the synchronization of the somite segmentation clock. *Nature*, 408(6811):475–479, 2000.
- [119] F. Giudicelli and J. Lewis. The vertebrate segmentation clock. *Current opinion in genetics & development*, 14(4):407–414, 2004.
- [120] C.G. Lau and R.S. Zukin. Nmda receptor trafficking in synaptic plasticity and neuropsychiatric disorders. *Nature Reviews Neuroscience*, 8(6):413–426, 2007.

REFERENCES

- [121] D.A. Lauffenburger and J.J. Linderman. *Receptors: models for binding, trafficking, and signaling*, volume 365. Oxford University Press New York, 1993.
- [122] D. Axelrod, D.E. Koppel, J. Schlessinger, E. Elson, and W. Webb. Mobility measurement by analysis of fluorescence photobleaching recovery kinetics. *Biophysical journal*, 16(9):1055–1069, 1976.
- [123] A. Tomlinson and G. Struhl. Decoding vectorial information from a gradient: sequential roles of the receptors frizzled and Notch in establishing planar polarity in the drosophila eye. *Development*, 126(24):5725–5738, 1999.
- [124] L. Demkowicz. *Computing with hp-ADAPTIVE FINITE ELEMENTS: Volume 1 One and Two Dimensional Elliptic and Maxwell problems*. CRC Press, 2006.